Multimodal photoacoustic remote sensing (PARS) microscopy combined with swept-source optical coherence tomography (SS-OCT) for in-vivo, non-contact, functional and structural ophthalmic imaging applications.

by

Zohreh Hosseinaee

A thesis
presented to the University of Waterloo
in fulfillment of the
thesis requirement for the degree of
Doctor of Philosophy
in
System Design Engineering

Waterloo, Ontario, Canada, 2021

Examining Committee Membership

The following served on the Examining Committee for this thesis. The decision of the Examining Committee is by majority vote.

External Examiner	Michael C. Kolios Professor, Department of Physics Ryerson University
Supervisor(s)	Parsin Haji Reza Assistant Professor, System Design Engineering Department University of Waterloo
Internal Member	Paul Fieguth Professor, System Design Engineering Department University of Waterloo
Internal Member	Alexander Wong Professor, System Design Engineering Department University of Waterloo
Internal-external Member	Chris Hudson Professor, School of Optometry & Vision Science University of Waterloo

AUTHOR'S DECLARATION

This thesis consists of material all of which I authored or co-authored: see Statement of Contributions included in the thesis. This is a true copy of the thesis, including any required final revisions, as accepted by my examiners.

I understand that my thesis may be made electronically available to the public.

Statement of Contributions

Chapter 2:

Zohreh Hosseinaee, Alexander James Tummon Simmons, Parsin Haji Reza. "Dual-modal photoacoustic imaging and optical coherence tomography." Frontiers in Physics 8 (2021): 635.

Author contributions

Zohreh Hosseinaee read and collected the reference papers, organized the content of the review paper, sub-categorized the techniques, compiled the article, prepared the figures, and wrote the main manuscript.

Alexander James Tummon Simmons edited parts of the article.

Parsin Haji Reza was the principal investigator, set the article scope, and proofread the article.

All authors contributed to the final version for publication.

Chapter 3:

Zohreh Hosseinaee, Martin Le, Kevan Bell, and Parsin Haji Reza "Towards non-contact photoacoustic imaging." Photoacoustics (2020): 100207.

Author contributions

Zohreh Hosseinaee read and collected the reference papers, organized the content of the review paper, sub-categorized the non-contact photoacoustic imaging techniques, compiled the article, prepared the figures and wrote the main manuscript.

Martin Le edited parts of the article and helped in reviewing some of the references.

Kevan Bell edited parts of the article.

Parsin Haji Reza was the principal investigator, set the article scope, and proofread the article.

All authors contributed to the final version for publication.

Chapter 4:

Zohreh Hosseinaee, Layla Khalili, James A. Tummon Simmons, Kevan Bell, and Parsin Haji Reza, "Label-free, non-contact, in vivo ophthalmic imaging using photoacoustic remote sensing microscopy," Opt. Lett. 45, 6254-6257 (2020)

Author contributions

Zohreh Hosseinaee co-designed with supervisor the optical system for PARS suitable for imaging the eye, prepared and ordered the optical and digital components of the system, constructed the PARS system, conducted the experiments, processed the images, contributed to interpreting the data, prepared the figures, and wrote the main manuscript.

James A. Tummon Simmons helped in constructing the PARS system.

Kevan Bell helped with hardware and software of the PARS system.

Layla Khalili assisted with animal imaging experiments.

Parsin Haji Reza conceived the study, contributed to the interpretation of all results, and acted as the primary investigators.

All authors contributed to the final version for publication.

Chapter 5:

Zohreh Hosseinaee, Benjamin Ecclestone, Nicholas Pellegrino, Layla Khalili, Lyazzat Mukhangaliyeva, Paul Fieguth, and Parsin Haji Reza, "Functional photoacoustic remote sensing microscopy using a stabilized temperature-regulated stimulated Raman scattering light source," Opt. Express 29, 29745-29754 (2021)

Author contributions

Zohreh Hosseinaee co-designed with supervisor the optical system for PARS, collected background information on the topic, conducted the experiments, collected the data, processed the PARS data, prepared the figures, and wrote the main manuscript.

Benjamin Ecclestone helped with processing the data and conducting the experiments.

Nicholas Pellegrino developed and implemented the signal unmixing method.

Layla Khalili and **Lyazzat Mukhangaliyeva** developed the chicken embryo model.

Paul Fieguth contributed to the interpretation of the results and provide guidance.

Parsin Haji Reza proposed the idea, conceived the study, contributed to the interpretation of all results, and acted as the primary investigators.

All the authors reviewed the manuscript.

Chapter 6:

Zohreh Hosseinaee, Nima Abbasi F., Nicholas Pellegrino, Layla Khalili, Lyazzat Mukhangaliyeva, Parsin Haji Reza, " Functional and structural ophthalmic imaging using noncontact multimodal photoacoustic remote sensing microscopy and optical coherence tomography " *Sci Rep* **11,** 11466 (2021).

Author contributions

Zohreh Hosseinaee co-designed with supervisor the optical system for PARS-OCT suitable for imaging the eye, investigated and lead the digital control requirements for the system, prepared and ordered the optical and digital components of the PARS-OCT system, constructed the PARS-OCT system, investigated and lead image processing for the SS-OCT system, conducted the experiments, processed the images, contributed to the interpretation the data, prepared the figures, and wrote the main manuscript.

Nima Abbasi constructed the software of the OCT system.

Nicholas Pellegrino developed and implemented the signal unmixing method.

Layla Khalili and **Lyazzat Mukhangaliyeva** assist with animal handling and conducting imaging experiments.

Parsin Haji Reza proposed the idea, conceived the study, contributed to the interpretation of all results, and acted as the primary investigators.

All the authors reviewed the manuscript.

Chapter 7:

Zohreh Hosseinaee, Nicholas Pellegrino, Nima Abbasi, Tara Amiri, James A. Tummon Simmons, Paul Fieguth, Parsin Haji Reza " *In vivo* functional and structural retina imaging using multimodal photoacoustic remote sensing microscopy and optical coherence tomography " (*submitted to Scientific Reports*)

Author contributions

Zohreh Hosseinaee studied and designed the modifications required for retina imaging, co-designed with supervisor the SO_2 accuracy experiments, conducted the experiments, processed the images, contributed to the interpretation the data, prepared the figures, and wrote the main manuscript.

Nicholas Pellegrino developed and implemented the signal unmixing method.

Nima Abbasi constructed the software of the OCT system.

Tara Amiri assisted with conducting SO_2 validation experiments.

Alexander James Tummon Simmons helped with designing the rat eye model phantom.

Paul Fieguth contributed to the interpretation of the results and provide guidance.

Parsin Haji Reza proposed the idea, conceived the study, contributed to the interpretation of all results, and acted as the primary investigators.

All the authors reviewed the manuscript.

Peer review journals, conference, and patent contributions:

1. Benjamin Ecclestone, **Zohreh Hosseinaee**, Nima Abbasi, Kevan Bell, Deepak Dinakaran, John R. Mackey, and Parsin Haji Rez “Three-dimensional virtual histology in unprocessed resected tissues with photoacoustic remote sensing (PARS) microscopy and optical coherence tomography (OCT)”. Sci Rep **11,** 13723 (2021).

2. **Zohreh Hosseinaee**, Nima Abbasi, Layla Khalili, Lyazzat Mukhangaliyeva, Anne Mei, Nicholas Pallegrino, Parsin Haji Reza, “Non-contact, in-vivo, functional, and structural ophthalmic imaging using dual-modal photoacoustic remote sensing microscopy and optical

coherence tomography", The Association for Research in Vision and Ophthalmology (ARVO) conference, 2021.

3. **Zohreh Hosseinaee,** Nima Abbasi, Alex Tummon Simmons, Layla Khalil, Kevan L Bell, Parsin Haji Reza, "Dual-modality photoacoustic remote sensing (PARS) microscopy and swept-source optical coherence tomography (SS-OCT) for in-vivo imaging", SPIE Photonics West, 2021

4. Parsin Haji Reza, Kevan Bell, **Zohreh Hosseinaee,** Benjamin Ecclestone, Saad Abbasi, "PARS imaging methods", US Patent. Patent number: US 11,122,978 B1

5. Parsin Haji Reza, Kevan Bell, **Zohreh Hosseinaee,** Benjamin Ecclestone, Saad Abbasi, "Dual-modality Photoaocustic remote sensing and optical coherence tomography (PARS-OCT), and thermally enhance photoacoustic remote sensing microscopy (TE-PARS)", Provisional Patent. Application number: 63/040,866

Abstract

Ophthalmic imaging has long played an important role in the understanding, diagnosis, and treatment of a wide variety of ocular disorders. Currently available clinical ophthalmic imaging instruments are primarily optical-based, including slit-lamp microscopy, fundus photography, confocal microscopy, scanning laser ophthalmoscopy, and optical coherence tomography (OCT). The development of these imaging instruments has greatly extended our ability to evaluate the ocular environment. Studies have shown that at least 40% of blinding disorders in the United States are either preventable or treatable with timely diagnosis and intervention.

OCT is a state-of-the-art imaging technique extensively used in preclinical and clinical applications for imaging both anterior and posterior parts of the eye. OCT has become a standard of care for the assessment and treatment of most ocular conditions. The technology enables non-contact, high-speed, cross-sectional imaging over a large field of view with submicron resolutions.

In eye imaging applications, functional extensions of OCT such as spectroscopic OCT and Doppler OCT have been applied to provide a better understanding of tissue activity. Spectroscopic OCT is usually achieved through OCT systems in the visible spectral range, and it enables the amount of light absorption inside the ocular environment to be measured. This indirect optical absorption measurement is used to estimate the amount of ocular oxygen saturation (SO_2) which is a well-known biomarker in prevalent eye diseases including diabetic retinopathy, glaucoma, and retinal vein occlusions. Despite all the advancements in functional spectroscopic OCT methods, they still rely primarily on measuring the backscattered photons to quantify the absorption of chromophores inside the tissue. Therefore, they are sensitive to

local geometrical parameters, such as retinal thickness, vessel diameters, and retinal pigmentation, and may result in biased estimations.

Of the various optical imaging modalities, photoacoustic imaging (PAI) offers unique imaging contrast of optical absorption because PAI can image any target that absorbs light energy. This unique imaging ability makes PAI a favorable candidate for various functional and molecular imaging applications as well as for measuring chromophore concentration.

Over the past decade, photoacoustic ophthalmoscopy has been applied for visualizing hemoglobin and melanin content in ocular tissue, quantifying ocular SO_2, and measuring the metabolic rate of oxygen consumption (MRO_2). Despite all these advantages offered by PAI devices, a major limitation arises from their need to be in contact with the ocular tissues. This physical contact may increase the risk of infection and cause patient discomfort. Furthermore, this contact-based imaging approach applies pressure to the eye and introduces barriers to oxygen diffusion. Thus, it has a crucial influence on the physiological and pathophysiological balance of ocular vasculature function, and it is not capable of studying dynamic processes under normal conditions. To overcome these limitations and to benefit from the numerous advantages offered by photoacoustic ophthalmoscopy, non-contact detection of photoacoustic signals has been a long-lasting goal in the field of ocular imaging.

In 2017 Haji Reza et al. developed photoacoustic remote sensing (PARS) for non-contact, non-interferometric detection of photoacoustic signals. PARS is the non-contact, all-optical version of optical-resolution photoacoustic microscopy (OR-PAM), where the acoustically coupled ultrasound transducer is replaced with a co-focused probe beam. This all-optical detection scheme allows the system to measure the photoacoustic pressure waves at the subsurface origin

where the pressure is at a maximum. In a very short time, PARS technology has proven its potential for various biomedical applications, including label-free histological imaging, SO_2 mapping, and angiogenesis imaging. PARS is an ideal companion for OCT in ophthalmic applications, where the depth-resolved, detailed scattering information of OCT is well complemented by rich absorption information of PARS. This combined multimodal imaging technology has the potential to provide chromophore selective absorption contrast in concert with depth-resolved scattering contrast in the ocular environment.

The main goals of this PhD project are to:

- Develop a photoacoustic remote sensing microscopy system for *in-vivo*, non-contact ophthalmic imaging. This is the first time a non-contact photoacoustic imaging has been used for *in-vivo* imaging of the eye.
- Develop a robust and temporally stable multiwavelength light source for functional photoacoustic imaging applications.
- Develop a multimodal PARS-OCT imaging system that can image *in-vivo* and record, simultaneously, functional, and structural information in the anterior segment of a rodent eye. This is the first time a multiwavelength non-contact photoacoustic system is used for *in-vivo* measurement of oxygen saturation in the ocular environment.
- Develop and modify the multimodal PARS-OCT imaging system for non-contact, *in-vivo*, functional, and structural imaging of the posterior part of the rodent eye.

Acknowledgements

These years will be the cherished treasure of my life and I would like to acknowledge the people who were of great importance to me during that time. This study would not have been possible without your generous support.

First, I would like to thank Dr. Parsin Haji Reza, my supervisor as well as mentor, for nourishing me with knowledge and training me to be a scientist. He is always both positive and constructively critical to the ideas I came up with. Those challenges and encouragements helped me to grow into an independent researcher. Dr. Haji Reza provided a wonderful atmosphere in the lab that encouraged both independent studies and teamwork. He has been a wonderful supervisor, a great mentor, and an awesome friend during these years. I am very fortunate to have been one of the researchers in his lab and gained a lot of support scientifically and mentally from him and all my colleagues. I also want to thank Dr. Haji Reza for financially supporting my research and providing funding for journal publications and international conferences. Dr. Haji Reza helped me to get my motivation and confidence back when I've been through the rough days of Covid-19 quarantine. He helped me to make those days productive by encouraging me to write two review papers and patents directly related to my PhD dissertation.

Second, I like to appreciate the advice I received from Dr. Luigina Sorbara, who unfortunately passed away and is no longer with us. I will always remember her with her kind smile and beautiful heart. I want to thank Dr. Chris Hudson for stepping in during our time of need and kindly accepting to be on the committee board to review my thesis. I am also fortunate enough to have Dr. Paul Fieguth and Dr. Alexander Wong as my committee members throughout my PhD study. Their valuable advice and constructive feedback were precious experience for me. I want to take this chance to thank Jean Flanagan from the University of Waterloo Central Animal Facility for her help and continuous support for all animal experiments. Last but certainly not the least, I would like to thank Professor Kostadinka Bizheva for her continuous support, mentorship, and precious help during these years.

I want to thank my friends and colleagues at PhotoMedicine Labs. I want to thank Dr. Kevan Bell for his mentorship and patience in answering all my questions. Also, I am thankful to Nima Abbasi for helping me with experiments and his continued encouragement and creating joyful atmosphere during the experiments! Last, but certainly not least, I want to thank Layla Khalili, Lyazzat Mukhangaliyeva, Benjamin Ecclestone, Nicholas Pellegrino, and James Alexander Tummon Simmons for their selfless support, encouragements, and precious help.

I would like to acknowledge all our funding partners. This research was gratefully funded by Natural Sciences and Engineering Research Council of Canada, Canada Foundation for Innovation, Mitacs Accelerate, University of Waterloo, Centre for Bioengineering and Biotechnology, illumiSonics Inc and New frontiers in research fund exploration.

Finally, I want to thank my parents, my beloved brother and sisters, and my friends, Mehdi and Shaghayegh, for gracious support of my choice to become a scientist and throughout my PhD training. I am very grateful for the support you offered during the difficult times of my PhD training and for celebrating my every single success regardless of how small it may have been. I could not even begin my PhD study in the first place without your understanding and non-hesitant support.

Dedication

To my mom and Dad, for their endless love and support.

Table of Contents

List of Figures

List of Abbreviations

AMD	Age-Related Macular Degeneration
ANSI	American National Standards Institute
AR-PAM	Acoustic-Resolution Photoacoustic Microscopy
CAM	Chicken Embryo Chorioallantois Membrane
CL	Collimating
DC	Dispersion Compensator
DR	Diabetic Retinopathy
ELM	External Limiting Membrane
FA	Fluorescein Angiography
FD-OCT	Fourier domain OCT
FL	Focusing Lens
FOV	Field of View
FWHM	Full Width Half Maximum
GCL	Ganglion Cell Layer
ICG	Indocyanine Green
IFT	Inverse Fourier Transform
INL	Inner Nuclear Layer
IOP	Intraocular Pressure
IOS	Intrinsic Optical Signal
IPL	Inner Plexiform Layer
IS	Inner Segment
M	Mirror
MIP	Maximum Intensity Projections
MRO_2	Metabolic Rate of Oxygen Consumption
MPE	Maximum permissible exposure
NA	Numerical Aperture
NIR	Near-Infrared
OCT	Optical Coherence Tomography
OCTA	Optical Coherence Tomography Angiography
ONH	Optic Nerve Head

ONL	Outer Nuclear Layers
OR-PAM	Optical-Resolution Photoacoustic Microscopy
OPD	Optical Path Difference
OS	Outer Segment
PAI	Photoacoustic Imaging
PAE	Photoacoustic Endoscopy
PARS	Photoacoustic remote sensing
PAT	Photoacoustic Tomography
PBS	Plarized beam splitter
PC	Polarization Controllers
PD	Photodiode
PM	Polarization Maintaining
PSF	Point Spread Function
RGC	Retinal Ganglion Cell
RMS	Root Mean Square
RPE	Retina Pigmental Epithelium
SD-OCT	Spectral-Domain OCT
SLD	Superluminescent Diode
SLO	Scanning Laser Ophthalmascopy
SM	Single Mode
SNR	Signal to Noise Ratio
SO_2	Oxygen Saturation
SRS	Stimulated Raman Scattering
SS-OCT	Swept Source Optical Coherence Tomography
TD-OCT	Time-Domain OCT
VCSEL	Vertical Cavity Surface Emitting Laser

List of Tables

Chapter 1
Introduction

Humans might have seen the world for centuries, but the world has only been able to see inside the living human eye for the last 170 years. Until the invention of the ophthalmoscope in 1851, the structure of the living human eye was an inaccessible mystery. Since that time, there have been many exciting breakthroughs in the field of ophthalmic imaging, including but not limited to fluorescein angiography (FA), scanning laser ophthalmoscopy (SLO), optical coherence tomography (OCT) and photoacoustic ophthalmoscopy. The development of these imaging instruments has greatly extended our ability to evaluate ophthalmic diseases. Studies have shown that at least 40% of blinding diseases in the United States are either preventable or treatable with timely diagnosis and intervention[1].

The human eye is a complex organ of numerous components (Figure 1-1). The eye can be broadly classified into two main parts: anterior and posterior segments. The anterior segment of the eye is composed of the cornea, conjunctiva, sclera, aqueous humor, lens, and iris. The posterior segment contains the inner side of the choroid, vitreous humor, retina, and optic nerve. The ability to image both anterior and posterior segments of the eye play a crucial role in early detection, monitoring, and treatment of common blinding eye diseases such as glaucoma, diabetic retinopathy, and macular degeneration.

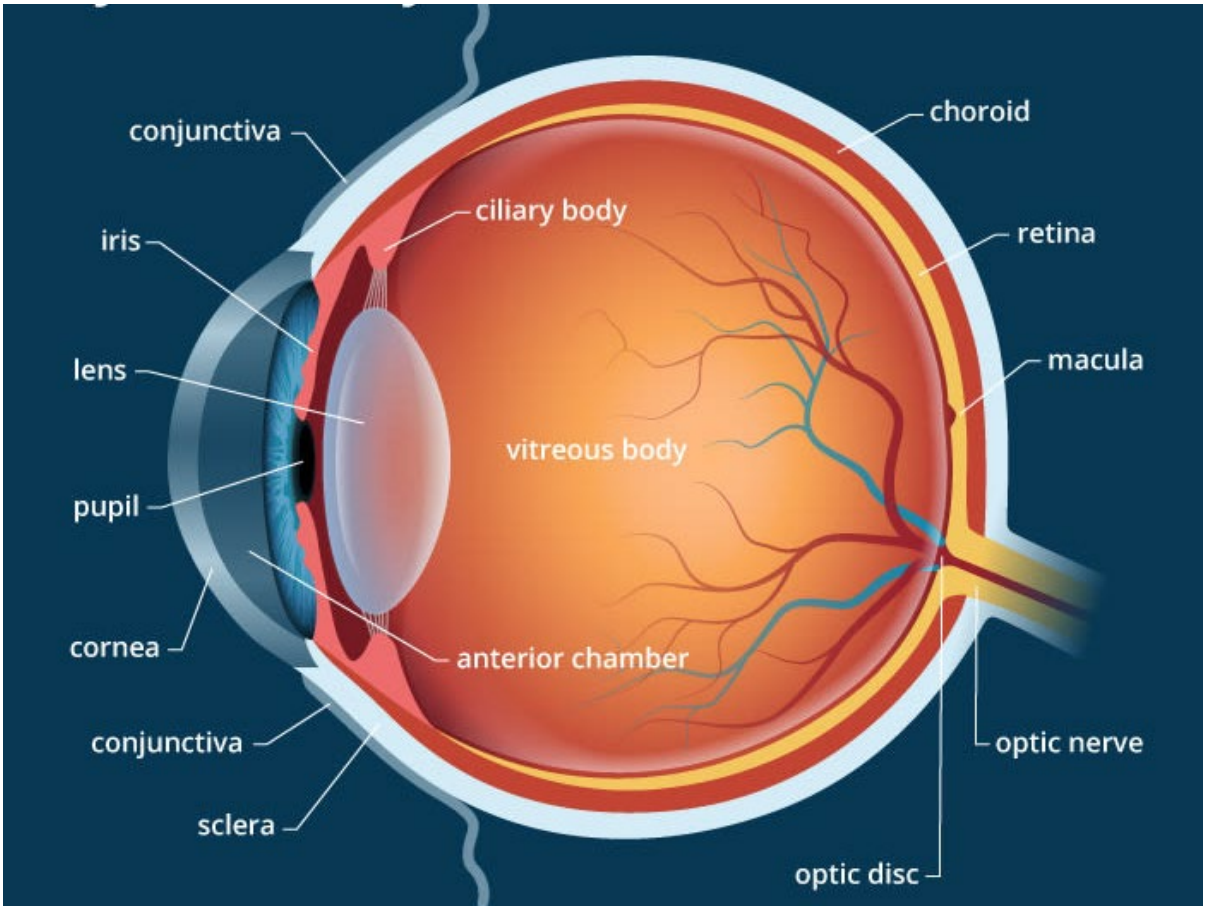

Figure 1-1 Side view of the eye (reproduced from allaboutvision's website [https://www.allaboutvision.com/resources/anatomy.htm])

1.1 A Brief History of ophthalmic imaging

The invention of the ophthalmoscope by Helmholtz in 1851 inaugurated the modern era in ophthalmology[2]. The design consisted of a partially reflecting mirror that directed light from a source onto the retina. The back-reflected light was then magnified to form an image. Helmholtz's ophthalmoscope equipped scientists with a tool for examining the retina. In 1886, Jackman and Webster recorded the first *in-vivo* human retinal photograph, showing the optic disc and larger blood vessels[3]. In 1920, such en-face retinal photography known as fundus photography was commercialized by Zeiss (Zeiss-Nordenson)[4]. Initially, due to its slow film

speed and long exposure time, it had limited clinical use. However, in the 1950s, the invention of the electronic flash made the technology a more common tool in clinics. Shortly after, in 1961, the first successful fluorescein angiography was administered in human eye. Through intravenous injection of fluorescein dyes, FA became the main diagnostic tool for study of retinal circulation[5]. In both fundus photography and fluorescein angiography, the choroid is not usually visible due to the strong scattering and absorption of the retinal pigment epithelium above it. By the early 1990s, indocyanine green angiography gained clinical acceptance for the study of choroidal circulation. The dye has infrared emittance and excitation spectra which facilitates penetration into the choroid. In the early 1980s, Webb's invention of the scanning laser ophthalmoscope thrust the field of fundus imaging into a new era[6]. Instead of capturing the image as a whole, the SLO samples the retina point by point in a raster-like scanning mode. The SLO's high light efficiency allows the laser beam to penetrate better into the lens and corneal opacities, resulting in improved spatial resolution and image contrast.

One of the greatest modern developments in ophthalmic imaging is the ability to evaluate posterior microanatomy in three dimensions. To this end, in 1987, the aforementioned SLO was combined with confocal optics[7]. In addition to obtaining higher contrast by reducing scattered light from other ocular structures, the confocal SLO was capable of depth-sectioning and enabled en-face fundus imaging with micron-scale resolution. Meanwhile, ultrasound techniques were widely used clinically for quantitative measurements of intraocular distances. Ultrasound determines distances within the eye from the echo delay of sound waves. Unfortunately, the ultrasound measuring device (transducer) requires direct contact with the cornea or immersion of the eye in a liquid to facilitate transmission of sound waves. Standard

ultrasound offers axial resolution ~150 μm; higher-frequency ultrasound can offer higher resolution approaching 20 μm, however, its application is only limited to imaging the anterior segment[8]. Furthermore, other methods such as computed tomography and magnetic resonance imaging are limited to the resolutions of hundreds of microns[9]. None of these techniques have sufficient depth resolution to provide useful three-dimensional images of retinal structure. In 1991 optical coherence tomography was introduced into the field of optical imaging. In comparison to the other imaging modalities, OCT provides high resolution (<10 μm) cross-sectional images of the eye in a non-invasive and non-contact manner. It became the standard of care in clinics for various ophthalmic imaging applications and provides detailed structural and three-dimensional images of both anterior and posterior parts of the eye[10].

Despite all the advances in OCT and other ophthalmic imaging modalities, there remains a gap in the amount of functional and physiological information that they can provide for the accurate diagnosis of common eye diseases. The structural information offered by these modalities is usually limited in clinical diagnostic value, and they often require additional techniques to examine physiologic changes related to the structural abnormalities. Recently, photoacoustic ophthalmoscopy techniques have been developed for pre-clinical trials and imaging both anterior and posterior segments in animal eye models. Photoacoustic imaging modalities provide the unique imaging contrast of optical absorption. In the ocular environment, hemoglobin and melanin are the two main optical absorbers. Photoacoustic imaging techniques can potentially quantify the amount of oxygenated, de-oxygenated hemoglobin, oxygen saturation (SO_2), and concentration of melanin in the ocular tissue. These functional

measurements can be achieved based on the differences in optical absorption of these chromophores[11]. Studies have demonstrated that variations in retinal blood oxygen saturation and melanin concentration play an important role in several prevalent blinding eye diseases[12], [13]. Over the last decade, photoacoustic ophthalmoscopy of both the anterior and posterior segments have been reported[14]. However, a major limitation that prevents the technology from moving to clinics is its contact-based imaging approach [11]. This contact-based detection mechanism can increase the risk of infection, abrasion and may cause patient discomfort. Furthermore, it applies pressure to the eye and has a crucial influence on the physiological and pathophysiological balance of ocular vasculature function.

In this thesis we develop a non-contact photoacoustic imaging system based on photoacoustic remote sensing (PARS) for imaging the ocular tissue. The technology enables non-contact photoacoustic imaging of the ocular environment for the first time, and it also provides functional information of the eye. It is further combined with OCT, the state-of-the-art ophthalmic imaging technique, to provide complementary information of optical absorption and optical scattering in both anterior and posterior segments of animal eye models.

1.2 Chapter overview

This thesis is organized based on several journal manuscripts (published or currently in review):

Chapter 2 reviews the importance of dual-modal imaging and discusses the combination of photoacoustic imaging and optical coherence tomography for ophthalmic applications. The impact the dual-modal imaging in the field of ophthalmology is discussed in this chapter.

Chapter 3 explains the importance of non-contact photoacoustic imaging and how it is important in ophthalmic imaging applications. It provides an overview of the different methods applied to achieve non-contact photoacoustic imaging alongside with the advantages and disadvantage of each method. The chapter also introduces photoacoustic remote sensing microscopy and discusses some of its potential applications.

Chapter 4 focuses on the non-contact imaging of the murine eye using photoacoustic remote sensing microscopy.

Chapter 5 discusses the development of a temporally stable multiwavelength light source and its application in functional photoacoustic imaging.

Chapter 6 discusses a multimodal photoacoustic remote sensing microscopy combined with swept source optical coherence tomography for functional and structural imaging in the anterior segment of the eye.

Chapter 7 discusses the modifications of the multimodal system in Chapter 6 and examines its applications for in vivo functional and structural imaging of rat retina.

Chapter 8 discusses the ocular light safety for the multimodal PARS-OCT system.

Chapter 9 Summarizes the results from this PhD thesis and discusses potential future studies.

Chapter 2
Dual-modal photoacoustic imaging and optical coherence tomography

Notes and Acknowledgement

This chapter reviews the importance of dual-modal photoacoustic imaging combined with optical coherence tomography for biomedical applications and ophthalmic imaging. The content of this chapter is based on the following journal manuscript:

Zohreh Hosseinaee, Alexander James Tummon Simmons, Parsin Haji Reza. "Dual-modal photoacoustic imaging and optical coherence tomography." Frontiers in Physics 8 (2021): 635.

Author contributions

Zohreh Hosseinaee read and collected the reference papers, organized the content of the review paper, sub-categorized the techniques, compiled the article, prepared the figures and wrote the main manuscript.

Alexander James Tummon Simmons edited parts of the article.

Parsin Haji Reza was the principal investigator, set the article scope, and proofread the article.

All authors contributed to the final version for publication.

2.1 Introduction

The field of medical imaging has continued to grow quickly since the turn of the century, with many new modalities introduced to perform critical steps in a variety of different disease care pathways. Novel imaging technologies continue to be developed to access valuable functional and morphological information. Each imaging modality has its own specific strength and intrinsic limitations, such as spatial resolution, penetration depth, contrast mechanism, and sensitivity, leading to precise and reliable images correlated with a true anatomy. To compensate for the weak aspects of different modalities, multimodal imaging concepts have been considered in recent years[15]–[17]. Multimodal imaging can play an important role in the clinical care of various diseases by improving the clinician's ability to monitor, surveil, stage, diagnose, plan and guide therapy, screen therapy efficacy, and evaluates recurrence [16]. Multimodal imaging systems have been widely used in medical research and clinical practice, such as for cardiovascular diseases [18], [19], neuropsychiatric diseases [20], Alzheimer's [21] and tumor resection surgeries [22].

Photoacoustic imaging (PAI) is one recent example of a successful novel optical imaging modality. PAI uses the absorption characteristics of specific endogenous or exogenous biomarkers to generate targeted image contrast with a wide scalable range of spatial resolution and penetration depths [23], [24]. The rich absorption information that PAI provides would be well complemented by an imaging modality that offers detailed scattering information. Optical coherence tomography (OCT) is a well-established imaging technology which provides excellent depth-resolved morphological information. OCT is currently used in a broad range of clinical applications and is a standard of care in the field of ophthalmology for the diagnosis

of various critical eye diseases [25]–[27]. OCT is considered as an ideal companion for PAI because it provides complementary imaging contrast, which has strongly motivated the development of multi-modal PAI and OCT systems. While OCT can image microanatomy of biological tissues, PAI devices could provide detailed molecular and metabolic information of the sample [28]–[30]. This multimodal system could provide access to valuable information about biological tissues and has the potential to impact a broad range of clinical and pre-clinical imaging applications, including but not limited to oncology, neurology, dermatology, and ophthalmology. Here, we first introduce the basic mechanisms of PAI and OCT and discuss their current applications. Then we compare PAI and OCT, contrasting the strengths and limitations of each modality while highlighting the potential applications of a multimodal system. Finally, we review the development of existing dual modal systems, emphasizing their strengths along with the challenges that need to overcome before such modalities move to the clinic.

2.2 Photoacoustic imaging: Principles and applications

Photoacoustic imaging is among the most rapidly growing technologies in biomedical imaging [24], [31]. The modality is based on the photoacoustic effect, which was discovered by Bell in 1880[32]. In general, once the tissue is irradiated by short laser pulses, endogenous or exogenous chromophores inside the tissue absorb the photon's energy. This absorbed energy then induces a transient local temperature rise, which in turn generates pressure waves through thermoelastic expansion. These pressure waves, which propagate in tissue as ultrasound signals, can be captured by acoustic detectors to form images of the chromophore's distribution inside the sample[33]. Depending on the spatial scales of optical absorbers, the frequency

content of generated ultrasound signals might extend to several tens or even hundreds of megahertz[34]. The bandwidth of this signal and corresponding spatial resolution is not limited by the PA generation process. Instead, the tissue frequency-dependent acoustic attenuation limits the maximum frequency content of PA wave, and therefore defines the achievable spatial resolution. As a result, the spatial resolution in PAI scales with depth. In addition, ultrasound detector's properties such as bandwidth, center frequency, element size, and detection aperture can limit the spatial resolutions of PAI devices [35].

Based on the way images are formed, PAI can be split into two main categories: photoacoustic tomography (PAT), which uses reconstruction-based image formation, and photoacoustic microscopy (PAM) which uses focused-based image formation [36]. In photoacoustic tomography, usually a wide-field unfocused excitation beam is used together with an array of ultrasonic detectors which measure the generated ultrasound waves in multiple positions simultaneously [37]–[39]. It can provide large field of view (FOV) images, and has been used in applications such as whole-body imaging of small animals[40] and breast cancer studies[41]. In contrast to PAT, PAM is based on raster-scanning of optical and acoustic foci and forms images directly from recorded depth-resolved signals [42]. Generally, PAM is the preferred configuration for use in applications which require high-resolution over deep penetration depth, for example in single cell imaging [43]. PAM can be further divided into acoustic-resolution PAM (AR-PAM), where the acoustic focusing is tighter than optical focusing[44], and optical-resolution PAM (OR-PAM), where the optical focusing dominates the resolution[45]. Figure 2-1 demonstrates the imaging setup for different possible configurations of photoacoustic imaging systems. Photoacoustic endoscopy (PAE) can be considered as a sub-

category of both PAM and PAT (depending on the implementation), which is applied for imaging internal tissue/organs and usually provides micron-scale spatial resolution and millimeter-scale imaging depth [46].

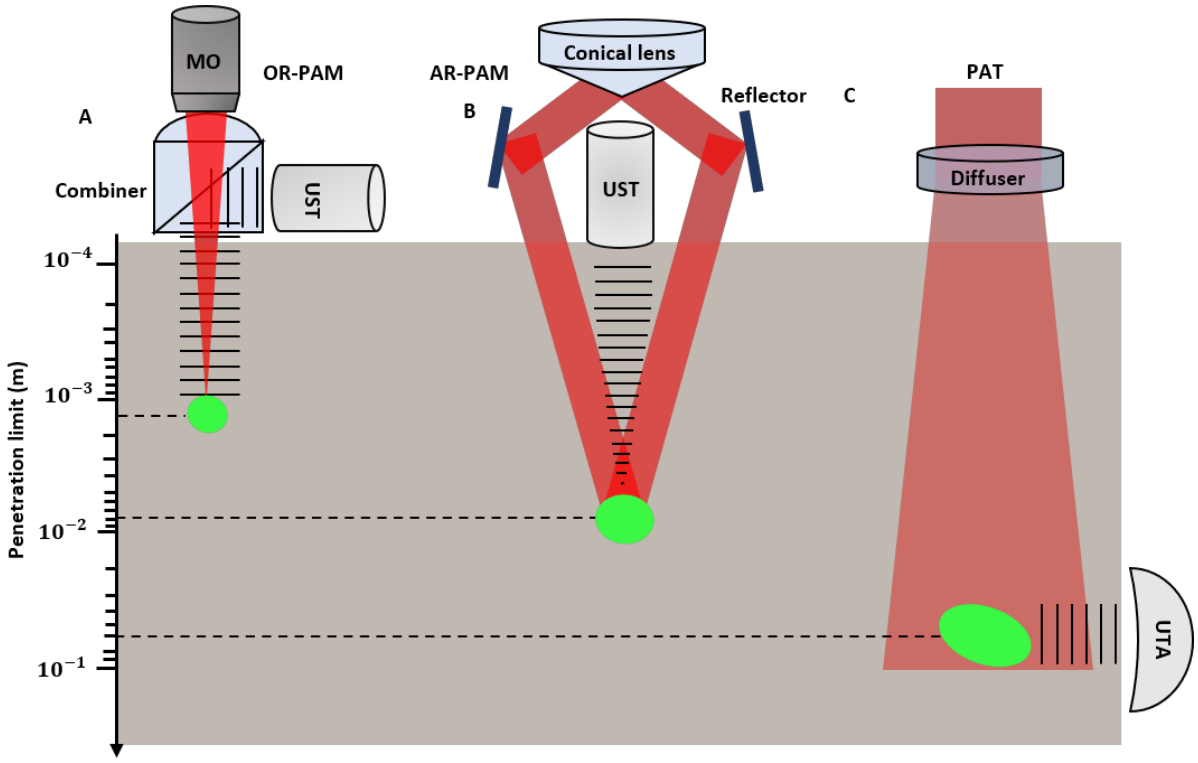

Figure 2-1. Signal generation and detection in different implementations of PAI and penetration limits in scattering tissue. (A) Reflection-mode OR-PAM system with an optical–acoustic combiner that transmits light but reflects sound. (B) AR-PAM system where the laser light is poorly focused. (C) PAT system with ultrasonic transducer array (UTA). The laser beam is expanded and homogenized by a diffuser to provide widefield illumination.

Photoacoustic imaging devices offer two distinct advantages which primarily stem from the combination of optical excitation and acoustic detection. First, they provide the unique imaging contrast of optical absorption. As a result, PAI enables high sensitivity detection of endogenous chromophores which are weakly fluorescent and difficult or impractical to be labeled with exogenous fluorophores, including but not limited to hemoglobin, melanin, collagen, cytochrome and lipid[47]. This complements established imaging technologies including

fluorescence imaging, which is currently one of the leading technologies for in-vivo optical molecular imaging [48]. Second, PAI enables a wide scalable range of spatial resolution and penetration depths across macroscopic (i.e. 100-400 μm resolution at the depth of several centimeters)[24], mesoscopic (i.e. tens of micrometer resolution at the depth of 1-10 mm)[49] and microscopic (i.e. micrometer resolution at the depth of sub-millimeter)[50]. Additionally, the modality has practical functional and molecular imaging capabilities making it a powerful tool for biomedical investigations [35]. One of these well-known capabilities is photoacoustic spectroscopy which is based on the ability to selectively image specific chromophores by tuning the excitation wavelength [51]. Here, by acquiring images at multiple wavelengths and undertaking spectroscopic analysis, the concentration of specific chromophores can be quantified. For example, in the visible and NIR wavelength, the absorption spectrum of blood is highly dependent on its oxygen saturation (SO_2), and consequently the significant spectral difference between oxyhemoglobin (HbO_2) and deoxyhemoglobin (Hb). Using this spectral difference, it is possible to quantify the concentration of HbO_2 and Hb and estimate SO_2 which is an important physiological parameter related to several pathophysiological processes and inflammatory conditions. Other functional extensions of PAI such as Doppler flowmetry [52], [53] and photoacoustic thermometry [54], [55] have enabled measurement of blood flow velocity and acquiring maps of temperature distributions in tissue, respectively.

These unique and important imaging advantages offered by PAI make it the preferred modality for a broad range of functional and molecular imaging applications. It has been used in numerous pre-clinical and clinical applications including but not limited to blood oxygen saturation imaging[56], [57], brain vasculature and functional imaging [58], [59], gene

expression[60], vulnerable atherosclerotic plaques diagnosis[61], skin melanomas[62], histology-like tissue imaging [63], [64], longitudinal tumor angiogenesis studies [65], imaging and detection of protein interactions[66], ophthalmic imaging [67], and tissue engineering scaffolds[68].

2.3 Optical coherence tomography: Principles and applications

Optical coherence tomography is an optical imaging technique with high resolution structural content. Unlike photoacoustic imaging, OCT obtains its imaging contrast from optical scattering of internal tissue microstructures, and can be considered as an optical analogy to ultrasound pulse echo imaging [69]. The modality is based on the principles of low-coherence interferometry, where a low-coherence light beam is directed on to the targeted tissue. The backscattered light is combined with a reference beam, which was split off from the original light beam. The resulting interference patterns are used to reconstruct cross-sectional images, which represent the reflectivity profile of the tissue along the beam path[70], [71].

The first generation of OCT known as time domain OCT (TD-OCT) was developed in 1990s[69]. The technology required acquisition of a depth scan for every location and subsequently suffered from slow imaging speed and poor image quality that limited adoption of the technology. The introduction of Fourier domain OCT (FD-OCT) overcame these limitations by providing a more efficient implementation of low-coherence interferometry principles[72]. Unlike TD-OCT, FD-OCT uses spectral information to generate a depth profile without the need for mechanical scanning of the optical path length[73]. It offers >100x improvement of the image acquisition rate and >20 dB signal-to-noise ratio (SNR) compared to TD-OCT systems.

Depending on whether spectral information in FD-OCT is separated at the system's input (tunable laser), or system's detection end (spectrometer), FD-OCT systems can be classified into two major groups: Spectral-domain OCT (SD-OCT) in which a broad bandwidth light source is used as the interferometer input and a spectrometer with a linear array camera at the interferometer output, or swept-source OCT (SS-OCT), which uses a tunable laser as the interferometer input and a single photodiode at the interferometer output[74]. Figure 2-2 depicts schematic of different OCT modalities.

OCT technology has enabled non-contact, high speed, cross-sectional imaging over a large field of view with submicron resolution in biological tissues. It is currently the preferred technology in ophthalmology for corneal imaging, as well as retinal structural and vascular imaging[75]–[77]. Various functional extensions of OCT have been developed including: Doppler OCT [78], OCT angiography (OCTA) [79], polarization sensitive OCT (PS-OCT) [80], OCT elastography [81], and spectroscopic OCT [82]. Besides ophthalmic applications, OCT has been applied in other clinical applications such as brain imaging [83], [84], tissue engineering[85], cardiology and cardiovascular imaging [86], skin imaging[87], neuroimaging[88], gynecology[89], oncology [90] and dental imaging[91].

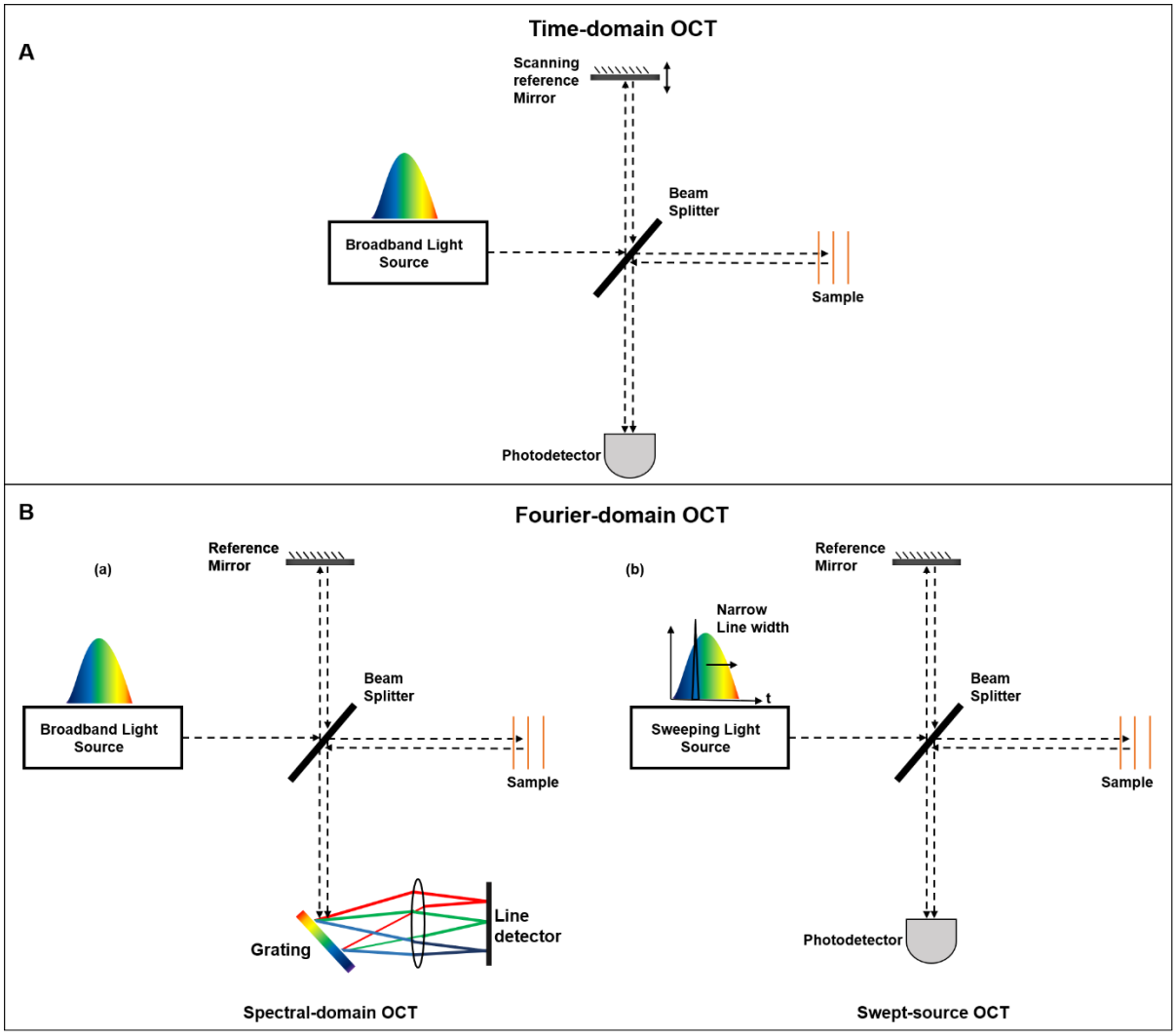

Figure 2-2. Schematic of different OCT modalities. OCT systems can be classified into (A) time domain (TD) and (B) Fourier domain (FD) systems. FD-OCT systems can be further divided into (a) spectrometer based and (b) swept source-based systems.

To describe OCT mathematically, we can consider a simple Michelson interferometer illuminated by a broad-band light source with input electric field given by $E_i = s(k,\omega)\exp[i(kz-\omega t)]$, where $s(k,\omega)$ is the field amplitude dependent on wavenumber $k=\frac{2\pi}{\lambda}$ and angular frequency ω at a given wavelength λ. Considering the sample to be compromised of discrete reflectors of the form $r_S(z_S)=\sum_{n=1}^{N} r_{S,n}\delta(z_S - z_{S,n})$, where $r_{S,n}$ are the electric field reflectors at a distance $z_{S,n}$ from the beam splitter. The electric field from the

sample arm at the 50:50 beam splitter is given by $E_S=(E_i/\sqrt{2})\sum_{n=1}^{N} r_{S,n}\exp(i2kz_{S,n})$. The electric field from a mirror reflector with reflectivity r_R is $E_R = (E_i/\sqrt{2})\, r_R exp(i2kz_R)$ where z_R is the distance of the reference mirror from the beam splitter. The factor of $1/\sqrt{2}$ is due to the splitting of power into half due to 50:50 beam splitter. The interference signal recorded by the square law detector is given by:

$$I_D(k,\omega) = \frac{\rho}{2}\langle|E_R+E_S|^2\rangle \qquad \text{Equation 2-1}$$

Where ρ is the detector responsivity and $\langle . \rangle$ is the average over detector response time. The factor of $1/2$ is due to the double pass of fields through beam splitter. Equation 2-1 can be extended as:

$$I_D(k) = \frac{\rho}{4} S(k)\left(R_R + \sum_{n=1}^{N} R_{S,n}\right)$$

$$+ \frac{\rho}{4}\left\{S(k)\sum_{n\neq m=1}^{N}\sqrt{R_{S,n}R_{S,m}}\left[e^{i2k(z_{S,n}-z_{S,m})} + e^{-i2k(z_{S,n}-z_{S,m})}\right]\right\} \qquad \textbf{Equation 2-2}$$

$$+ \frac{\rho}{4}\left\{S(k)\sum_{n=1}^{N}\sqrt{R_R R_{S,n}}\left[e^{i2k(z_R-z_{S,n})} + e^{-i2k(z_R-z_{S,n})}\right]\right\}$$

Where $S(k) = \langle|s(k,\omega)|^2\rangle$, $R_{S,n}= |r_{S,n}|^2$ and $R_R = |r_R|^2$. The averaging of the signal over the detector response time causes the terms dependent on the temporal angular frequency $\omega=2\pi\nu$ to be eliminated in Equation 2-2. This is due to the fact that in practice, the optical frequency ν oscillates much faster than the detector response time. Equation 2-2 can be further simplified to:

$$I_D(k) = \frac{\rho}{4} S(k)\left(R_R + \sum_{n=1}^{N} R_{S,n}\right) \quad "DC\ term"$$

$$+ \frac{\rho}{4}\left\{S(k)\sum_{n\neq m=1}^{N}\sqrt{R_{S,n}R_{S,m}}\cos\left[2k(z_{S,n}-z_{S,m})\right]\right\} \text{"Autocorrelation term"} \quad \textbf{Equation 2-3}$$

$$+ \frac{\rho}{2}\left\{S(k)\sum_{n=1}^{N}\sqrt{R_R R_{S,n}}\cos\left[2k(z_R-z_{S,n})\right]\right\}. \text{"Cross-correlation term"}$$

The first term in Equation 2-3 is the DC off-set or the constant component, independent of any optical pathlength, whose amplitude is proportional to the sum of the power reflectivity of the reference mirror and the power reflectivity's of the sample. The second term is the auto-correlation term, which is due to the interference between the sample reflectors. The amplitude of this term is usually low compared to the DC term in OCT as it depends linearly on the power reflectivity of the sample reflections, which is much lower than reference power reflectivity. The third term is the signal of interest in OCT referred to as the cross-correlation component, and it depends on the optical pathlength difference between the reference arm and the sample reflectors. Amplitudes of these components are proportional to the square root of the sample power reflectivity's scaled by the square root reference power reflectivity. Although the amplitudes are lower than the DC component, the square root dependence implies logarithmic gain over direct measurement of sample reflectivity's. All the three terms are scaled by the wavenumber spectrum of the light source. Based on Equation 2-3, the measurement of the sample reflections at different depth can be done in both the time domain and Fourier domain. Since Fourier domain OCT is the focus of the present work, a brief description of its principle is discussed here.

As mentioned earlier, there are primarily two ways to get OCT measurement in Fourier domain OCT, SD-OCT, and SS-OCT. In both cases the reference path length is fixed. Once the spectrum of the interference signal, given in Equation 2-3, can be detected spatially or temporally, a simple 1-D Fourier transform $FT_{K\rightarrow Z}\{I_D(k)\}$ gives the reflectivity profile with depth:

$$\tilde{I}_D(k) = \frac{\rho}{8}\gamma(z)\left(R_R + \sum_{n=1}^{N} R_{S,n}\right)$$

$$+ \frac{\rho}{4}\left\{\gamma(z) \otimes \sum_{n\neq m=1}^{N} \sqrt{R_{S,n}R_{S,m}}\ \delta\left[z \pm 2(z_{S,n}-z_{S,m})\right]\right\} \qquad \textbf{Equation 2-4}$$

$$+ \frac{\rho}{8}\left\{\gamma(z)\ \otimes \sum_{n=1}^{N} \sqrt{R_R R_{S,n}}\ \delta\left[z \pm 2(z_R - z_{S,n})\right]\right\}.$$

The sample reflectivity profiles $\sqrt{R_{S,n}}$, scaled by the reference reflectivity $\sqrt{R_R}$, appear at distance $z = +2\,(Z_R - Z_{S,n})$ relative to the reference mirror position and convolved with the complex coherence function $\boldsymbol{\gamma(z)}$. Thus, the axial width of the sample reflectivity profile depends on the coherence length of the light source, which in turn is inversely dependent on the light source bandwidth. Note that the factor of 2 for the path length difference in Equation 2-4 is due to the double pass in Michelson interferometer. The complex conjugate term also appears as distance $z = -2\,(Z_R - Z_{S,n})$, and can be separated from the actual terms of interest by placing the sample completely on one side relative to the reference mirror position. The DC component appears at zero delay, which is the location of the reference mirror. The auto-correlation term appears close to the zero delay, as the pathlength difference between sample reflectors are small in comparison to the pathlength difference between the reference and the sample reflectors[30].

By introducing a pair of galvanometric scanners in the sample arm, the imaging beam can be directed to different positions on the sample, and by moving one of the galvanometric mirrors, the beam would do repetitive A-scans along lateral direction, resulting in a 2D image (B-scan). Similarly, repetitive B-scans along the sample form a three-dimensional stack of images, which provides a morphological profile of the whole sample. Figure 2-3 represents A-scan, B-scan and a 3D dataset recorded from chicken embryo vasculature in our research lab.

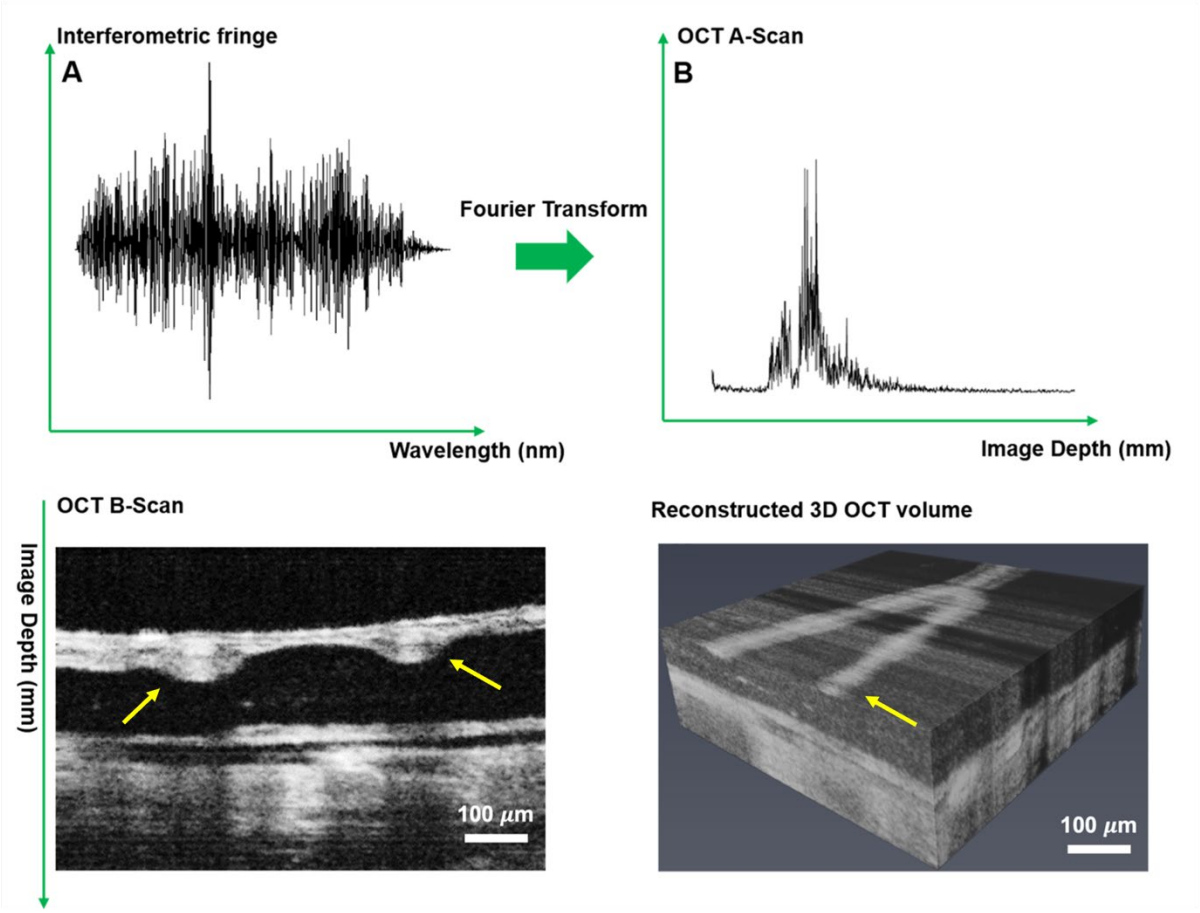

Figure 2-3.(A) Interferometric fringes. (B) An OCT A-scan (1D, depth-dependent reflectivity profile) can be generated by taking the Fourier transform of the interferometric fringe. (C) An OCT B-scan of a vasculature in a chicken embryo model (yellow arrows) generated by stitching the A-scans from different transverse positions. Logarithmic scale with contrast adjustment can be applied for optimal visualization. (D) A volumetric OCT image showing volumetric view of vasculature.

Due to the highly scattering nature of biological tissues and the contrast mechanism of OCT, the penetration depth of OCT devices is limited to be within a few millimeters [26]. In addition, OCT relies on variation in scattering information to derive useful imaging contrast about the sample, making it unable to effectively image interconnected soft tissues with similar scattering properties. To provide additional contrast information, efforts have been made to integrate OCT with other optical imaging modalities such as multiphoton microscopy [92], and confocal microscopy [93]. While these technologies provide new contrast information, they both rely on fluorescence as their contrast mechanism. In addition, they cannot enhance the depth information that OCT devices currently obtain.

2.4 Dual-modal photoacoustic imaging and optical coherence tomography

The performance characteristics of PAI and OCT imaging systems make them a suitable companion for a multimodal imaging system. A brief comparison of important features of both PAI and OCT modalities are given in Table 2-1. The spatial resolution of both modalities is highly dependent on their implementation and can range from sub-micron resolution for OCT [94], [95] and OR-PAM to a few hundreds of microns in PAT systems [24]. While the available imaging depth of OCT is restricted by the optical transport mean free path to ~ 2 mm, AR-PAM and PAT systems can achieve imaging depth of a few millimeters [49] to a few centimeters [41], respectively. In terms of speed, both modalities offer a wide range of imaging speed with sub-milliseconds to a hundred of seconds range [96], [97], that should be chosen based on intended applications.

Table 2-1 Comparison of photoacoustic imaging and optical coherence tomography

Imaging parameter	Photoacoustic imaging	Optical coherence tomography
Axial resolution	Determined by the detected photoacoustic bandwidth, usually several tens of microns	Determined by the central wavelength and coherence length of the light source, generally within a few microns
Lateral resolution	Depending on the implementation can range from ~ 0.3 to 400 μm	Determined by the central wavelength of the light source and imaging" optics, usually within tens of microns
Imaging depth	Depending on the implementation range from ~ 1.5 mm to ~ 7cm	Restricted by the optical transport mean free path ~ 2 mm
Imaging speed	Defined by the laser pulse repetition rate, mechanical scanning speed or the multiplexed data acquisition time	Usually defined by the sweep rate of laser or speed of spectrometers' camera
Contrast mechanism	Absorption	Scattering

The complementary information of PAI and OCT makes them the favoured modality for a wide range of imaging applications. For example, in blood flow imaging, OCT angiography and Doppler OCT could obtain high resolution images based on the backscattering properties of moving red blood cells, while PAI would remain sensitive to all blood cells, regardless of their flowing state. Therefore, the integrated system provides a powerful tool for blood flow imaging in vascular diseases such as stroke, haemorrhage, vascular occlusions or certain pathologies with flow stasis such as tumours [98], [99].

For spectroscopic analysis and blood oxygen saturation measurements, despite recent advances in the spectroscopic OCT [100]–[102] the technology is not background free and suffers from sensitivity to speckle and polarization changes. In addition, the scattering losses alter the spectral signal components and makes it difficult to quantify blood oxygen. On the other hand, spectroscopic PAI methods are well-established for quantifying blood oxygen saturation. This information would be well complemented with Doppler OCT flow measurements and help to quantify metabolic rate of oxygen consumption. This will open a broad range of applications for pathophysiological conditions such as angiogenesis, tissue inflammatory and healing

responses. For example, in ophthalmology measuring metabolic rate of oxygen is a sensitive biomarker for early-stage diagnosis and an indicator for progression of several retinal diseases including glaucoma, diabetic retinopathy, and age-related macular degeneration [103]–[106]. Alternatively, in oncology and metastasis detection, the spectroscopic and metabolic information available through dual-modal PAI-OCT system could reveal changes in endogenous chromophore concentrations and be employed for differentiating normal and pathological tissues [107]. It may facilitate longitudinal assessment of tumour growth and evaluate treatment success of novel therapeutic agents [107], [108]. In brain imaging applications, this metabolic information can be used to extract brain oxygenation and metabolism of oxygen and glucose [109], resting-state connectivity [110] and to study how brain responds to various physiological and pathological conditions [111]. Furthermore, the fine vascular structure and subcellular features available through high spatial resolution of OCT and OR-PAM could facilitate diagnosis of brain disorders such as stroke, epilepsy, and edema [95], [112], [113].

The combination of PAI and OCT is a powerful tool in dermatology by providing detailed morphology and complete description map of skin perfusion. It enables studying the texture of skin and determines the margin of morphological changes caused by skin disorders [114]. The technique may overcome the limitations of histology-based margin assessment methodologies and facilitate tumor resections in surgical rooms [115], [116]. Subsequently, it can be used to improve the rate of complete excision and to reduce the average number of stages during Mohs micrographic surgery [117], [118]. The dual-modal imaging platform can be applied for studying a wide range of skin conditions such as melanoma tumours, vascular lesions, soft

tissue damages such as wounds and burns, inflammatory conditions and other superficial tissue abnormalities characterized by morphology and function of supplying vasculature [119].

The dual-modal PAI-OCT system could have a significant impact for endoscopic applications as well. Currently, most of endoscopic imaging devices rely on wide-field white-light optical methods, which are limited by what the human eye can see and therefore suffer from lack of sensitivity to subsurface and physiological changes. The combination of deep tissue penetration, high resolution along with functional and molecular information make PAI-OCT the favourable endoscope to observe inside the body and visualize physiological processes and microscopic features of tissues [120], [121]. The targeted molecular imaging may allow for the detection of small and invisible lesions in epithelial surfaces that line the internal organs such as gastrointestinal, pulmonary, and ductal. This information can be used to facilitate detecting cancer at early stages [122]. Another important application for endoscopic PAI-OCT would be intravascular atherosclerotic imaging, where PAI subsystem could penetrate deep and provide molecular information about the plaque composition and OCT maintains high resolution, depth-resolved scattering contrast for lipid rich plaques [123].

It is clear there are a diverse set of biomedical applications for a functional multimodal PAI-OCT system. The potential impact of such a broadly applicable technology has motivated the further investigation of possible multimodal system configurations. Here, depending on the photoacoustic imaging system, the multimodal PAI-OCT imaging systems are divided into three main categories of PAT-OCT, PAE-OCT, and PAM-OCT. The developed configurations for each category are reviewed and their advantages and technical challenges are discussed.

2.4.1 Photoacoustic tomography combined with optical coherence tomography.

Due to the high penetration depth benefits, dual-modal PAT-OCT systems are mainly used for applications where depth information is required. For example, in dermatology, while OCT techniques visualize superficial small capillary loops with vessel diameters from 10 to 200 µm to a depth of 1 mm; PAT enables visualization of vasculatures with diameters from 100 µm down to a depth of several centimetres. Therefore, the combination of these modalities could provide a complete perfusion map of the skin [124]. In addition, acquiring PAT and OCT images from overlapping or identical regions has the advantage that highly absorbing structures, which appear as shadow in OCT images (e.g., blood vessels), can be observed in PAT images.

In 2011, Zhang et al.[99] developed a PAT-OCT system and demonstrated in-vivo volumetric images of vasculature and surrounding tissue in mouse and human skin. The schematic of their system is presented in **Figure 2-4**A. The system employed an integrated all-optical detection scheme for both modalities in reflection-mode maintaining a field of view of ~ 13 mm × 13 mm. The photoacoustic waves were detected using a Fabry-Perot sensor place on the surface of the skin. The planar-view PAT system based on Fabry-Perot interferometer is of particular interest in most dual-modal PAT-OCT applications because of the simplicity of sample positioning and optical detection mechanism [125], [126]. The study reported tissue information of vascular structure to a depth of ~ 5 mm. Similar systems were further developed and in-vivo clinical experiments were performed on healthy and pathological skin, [127]–[130] (**Figure 2-4**B). Initial clinical studies demonstrate that the dual modal PAT-OCT systems hold a great potential for applications in dermatology. Recently Liu et al. [119] published a

comprehensive overview of the dual modality PAT-OCT system in the field of dermatology and the challenges and prospects of these two imaging modalities for dermatology were discussed thoroughly.

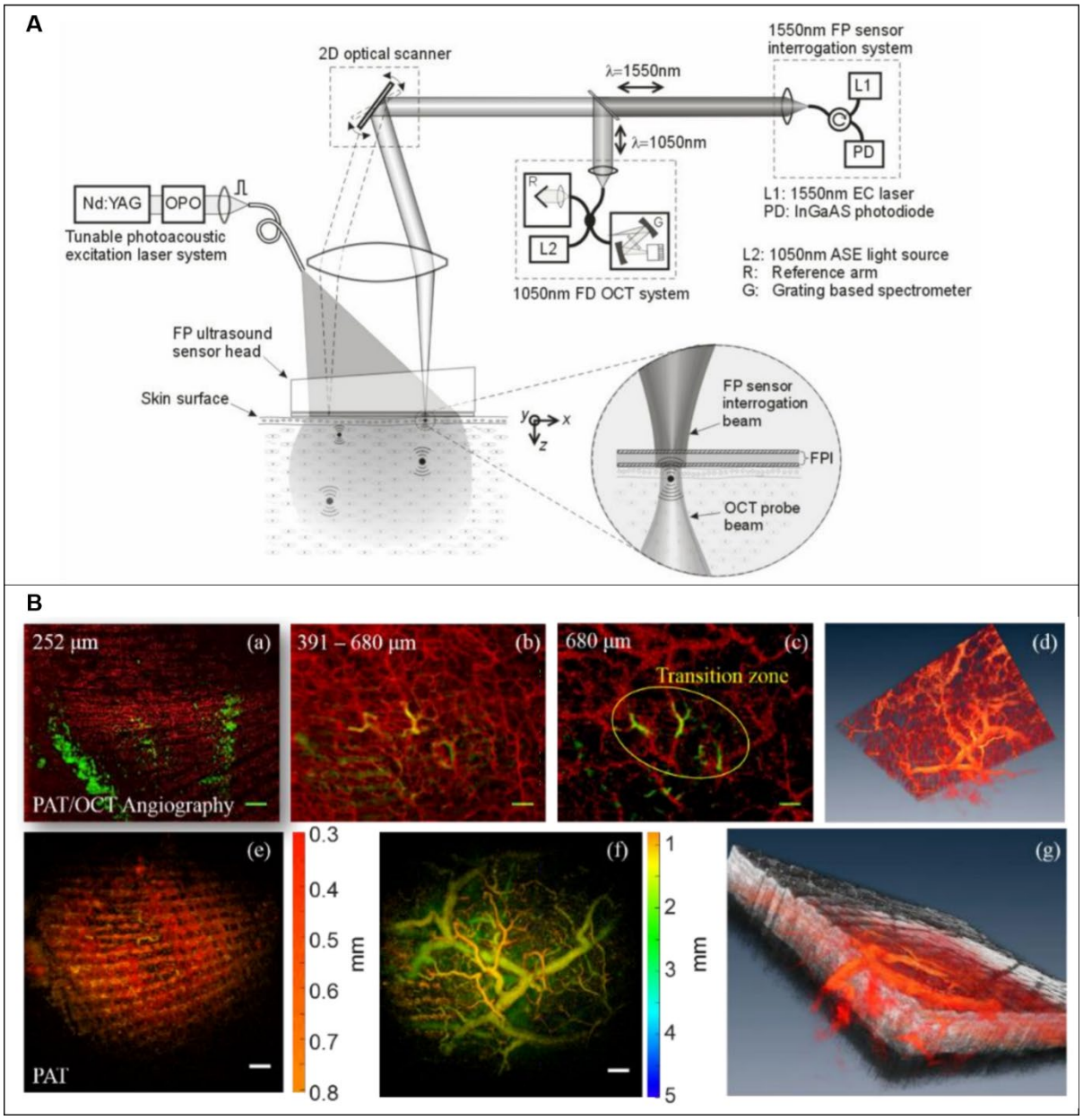

Figure 2-4. (A) Dual modal PAT-OCT scanner. Reprinted with permission from **[99]**. (B) (a-c) overlaid PAT-OCTA images with PAT in the green channel and OCTA in the red channel. (d) Blood vessel network given in volumetric display by fused OCTA and PAT data. (e) PAT image (f) PAT image in deeper region (g) A snapshot of the 3D volume with OCT in gray, OCTA and PAT in red color map. Scale bar = 1 mm. Reprinted with permission from **[127]**.

2.4.2 Photoacoustic endoscopy combined with optical coherence tomography.

Toward realizing dual-modality PAE-OCT, in 2011 Yang et al. [131] made the initial step by integrating ultrasound tomography with photoacoustic and OCT imaging in a single intraoperative probe. The performance of the system was demonstrated on ex-vivo porcine and human ovaries. The OCT subsystem used a swept-source laser centered at ~1300 nm with 110 nm spectral bandwidth and a 20 kHz scan rate and the PAE subsystem had a tunable Ti: Sapphire laser with spectral range of 700 – 950 nm and a 15 Hz repetition rate. The ultrasound transducer operated as both PAI detection and ultrasound transmission and detection. Figure **2-5**A depicts the combined three-modality endoscopic probe. The overall diameter of the endoscope was 5mm and included a ball-lensed OCT sample arm probe, and a multimode fiber to deliver light for photoacoustic imaging. Later, in 2013, Xi et al. [132] reported an endoscopic delivery probe with a diameter of 2.3 mm. The system had a low-frequency unfocused 10 MHz transducer for photoacoustic signal detection and a time-domain OCT system at 1 kHz. The performance of their system could be improved in several ways such as increasing the central frequency of photoacoustic transducer, employing a higher resolution DAQ card, and replacing the time-domain OCT device with a frequency-domain OCT device to enhance the sensitivity. Inspired by one of the initial efforts in the field (Yang et al. [131] study), Dai et al. [133] developed a multimodal miniature probe through which OR-PAM, OCT and pulsed-echo ultrasound images were acquired coaxially and were displayed simultaneously. Figure **2-5**B depicts the schematic of the integrated miniature probe. The 2 mm diameter probe had a 40 MHz unfocused ultrasound transducer for both OR-PAM detection and ultrasound transmission and receiving, and in-vivo images of rat ear were recorded (Figure **2-5**C). The

results show cross-sectional images acquired by OR-PAM, OCT, ultrasound, and combined images, corresponding to the three dashed lines in the respective maximum-amplitude-projection image. Despite offering high imaging resolution, the system suffered from lack of rotational scanning and its imaging speed was limited by the slow repetition rate (20 Hz) of the pulsed laser. Mathews et al. [134] developed a dual-modal intravascular imaging probe using a commercial OCT catheter and a fiber optic ultrasound sensor based on Fabry-Perot cavity. Their experimental setup and the enlarged view of the distal end of the probe is presented in Figure **2-5**D. They demonstrated circumferential PAE-OCT imaging and multispectral PAI on a synthetic phantom. One limitation of their probe configuration was that the stationary fiber optic ultrasound receiver resulted in shielding of the photoacoustic waves by the OCT catheter for certain excitation angles. As a result, the detected photoacoustic signal amplitude varied relatively with respect to the receiving angle in the rotation plane. In general, future direction for multimodal PAE-OCT studies can be focused on improving scanning speed, miniaturizing the probe size, and enhancing detection mechanism.

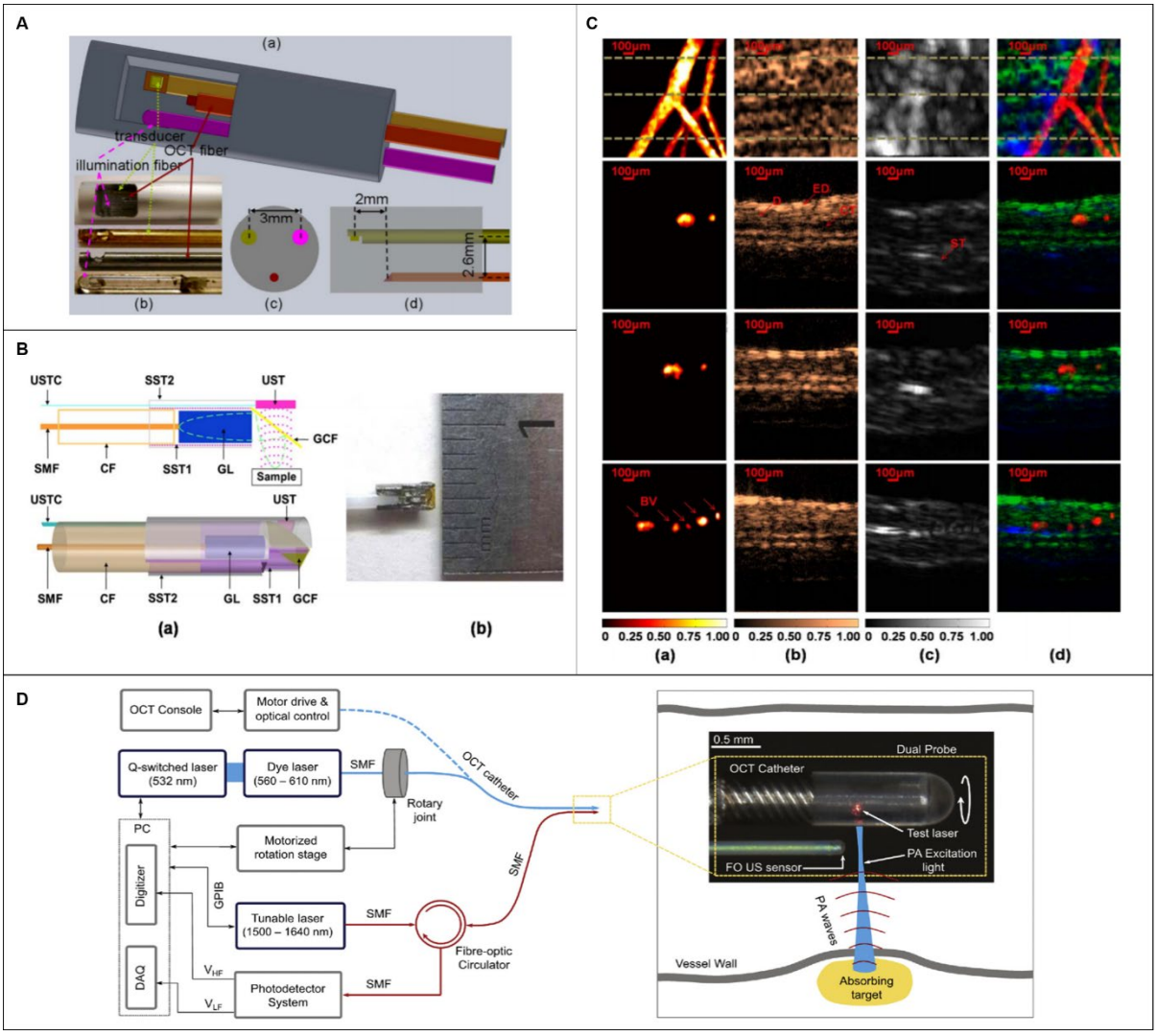

Figure 2-5. (A) Integrated OCT-US-PAI three-modality endoscopic probe. Reprinted with permission from **[131]**. (B) Schematic and photograph of miniature integrated probe. Reprinted with permission from **[133]** (C) In-vivo images of a rat ear. Maximum amplitude projection images (top row) and cross-sectional images (2nd, 3rd, and bottom rows) corresponding to the dotted lines in first row images (a) OR-PAM, (b) OCT, (c) US, and (d) fused images. Reprinted with permission from **[133]**(D) Schematic of the dual-modality PA-OCT system. An enlarged image of the distal end of the probe. Reprinted with permission from **[134]**.

2.4.3. Photoacoustic microscopy combined with optical coherence tomography.

One of the earliest works on the feasibility of multimodal PAM-OCT was demonstrated by Li et al. in 2009 [135]. Their proposed system operated in transmission mode and was only capable of imaging thin samples (Figure **2-6**). The reported penetration depth was ~ 1.5 mm

and 1.8 mm for the PAM and OCT subsystem, respectively. Due to the mechanically translating objective, the system had slow acquisition time which severely limited its in-vivo applications. Despite this limitation, the system was later used to look at the neovascularization of mouse ear [136](Figure **2-6**B). Later Jiao et al. [137]developed a reflection-mode PAM-OCT system, and imaged microvasculature of the mouse ear. The temporal resolution of their dual modal system was limited by the pulse repetition rate of the PAM excitation source (~ 1 kHz). Liu et al. [138] developed a dual modal system where a tunable dye laser was used as excitation source (Figure **2-6**C). It leveraged the spectroscopic measurement capabilities of the PAM subsystem to evaluate total hemoglobin concentration as well as the metabolic rate of oxygen consumption in the mouse ear. Dual modal PAM-OCT systems were further applied on various samples such as animal model of epilepsy progress [139], bovine cartilage osteoarthritis tissue[140], imaging/needle guiding for injection and drug delivery in mouse thigh [141].

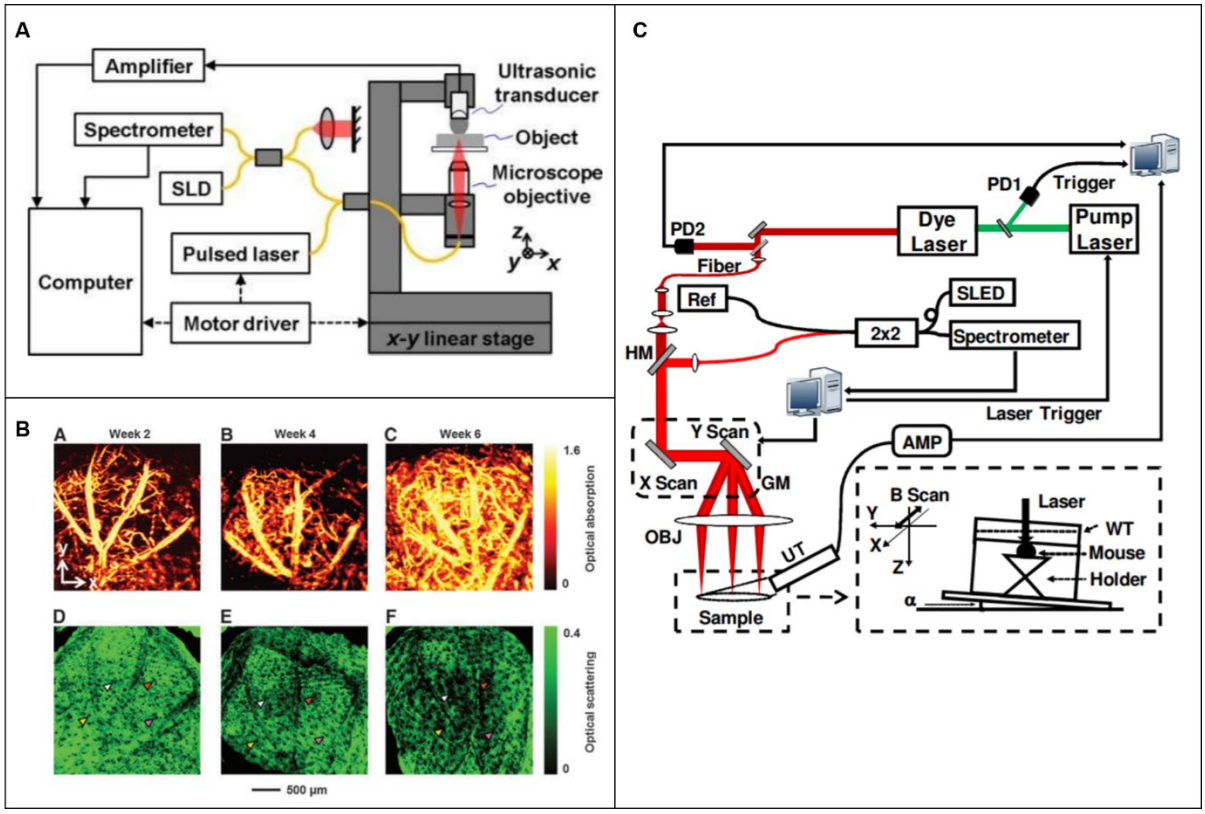

Figure 2-6. (A) Schematic of the combined PAM-OCT. SLD: superluminescent diode. Solid lines represent single-mode optical fibers. Reprinted with permission from **[135]**. (B) PAM and OCT images showing the vasculature and tissue structure for an inverse scaffold with a pore size of 200 μm. (A–C) PAM images showing the development of blood vessels at 2-, 4-, and 6-weeks post implantation, respectively. (D–F) The corresponding OCT images showing the tissue structure. Reprinted with permission from **[136]**. (C) Schematics of the combined PAM and OCT. PD: photodiode; HM: hot mirror; GM: 2D galvanometer; OBJ: objective lens; AMP: amplifier; UT: ultrasonic transducer; WT: water tank; SLED: superluminescent emitting diode; Ref: OCT reference arm. Reprinted with permission from **[138]**.

Qin et al. [142] was among the first to develop portable dual-modal PAM-OCT system. Their system was used for monitoring the recovery of an ulcer wound in human lip. They carried out quantitative analysis by measuring total hemoglobin concentration as well as the size of the ulcer. In-vivo images recorded from healing process of human lip ulcer are shown in Figure **2-7**A. The system offered lateral resolutions of ~ 8 μm for both modalities, and axial resolutions of 116.5 μm for PAM and 6.1 μm for OCT. However, since the system suffered from bulky size, in 2018 the same author demonstrated a handheld version of the system implemented with a MEMS-based optical scanner that offered more flexibility for oral tissue

imaging [143]. The lateral resolutions of the system were improved to 3.7 μm for PAM and 5.6 μm for OCT, sufficient for visualizing morphological features and capillary loops in human oral tissue. Dadkhah et al. [144] took an additional step forward and developed a multimodal imaging system by integrating photoacoustic microscopy, OCT and confocal fluorescence microscopy in one platform. The combination of optical and mechanical scanning together with dynamic focusing improved the sharpness and field of view of the images. The system achieved uniform resolution in a field-of-view of 12 mm × 12 mm with an imaging time of ~ 5 min for simultaneous in-vivo imaging of mouse ear (Figure **2-7**B). The imaging speed of their system was limited by the pulse-repetition-rate of the PAM excitation laser.

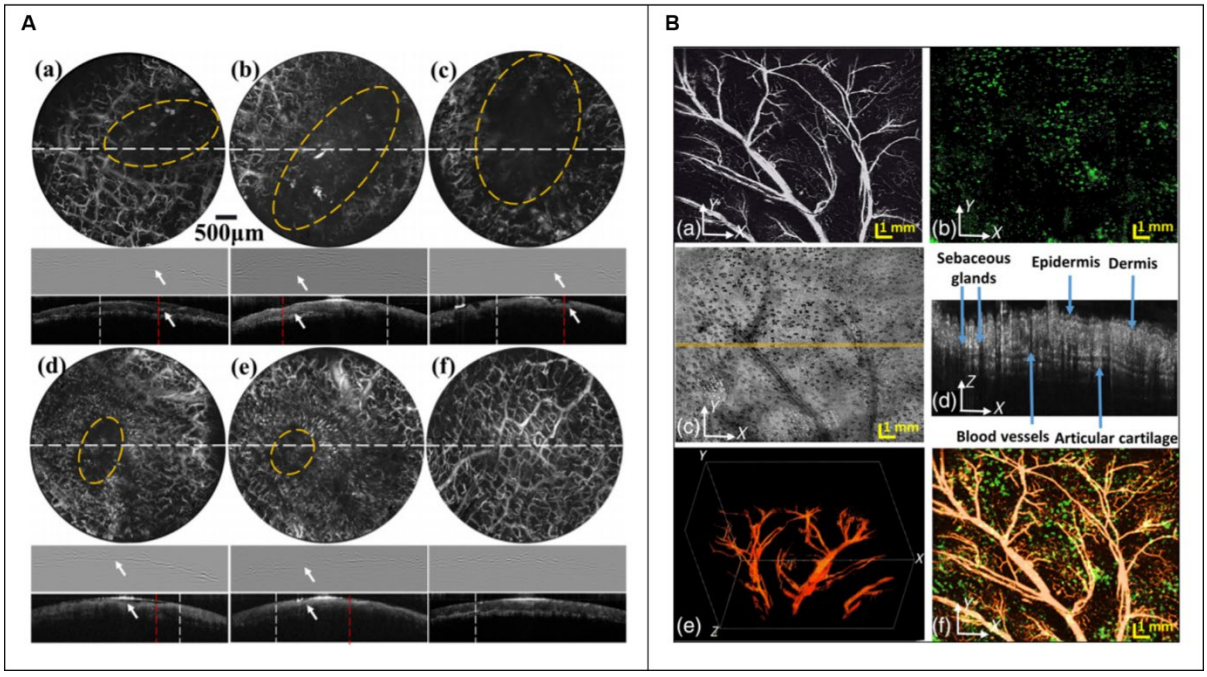

Figure 2-7. (A) PAM and OCT results of the microvascular distribution and microstructures of the lower lip during the healing process of an ulcer wound. Row 1 in PAM images of the lip from day 1 to day 6. Row 2 PAM B-scans of the lip along the dashed white lines in Row1. Row3 OCT B-scans of the lip along the dashed white lines in Row1.The wounds are indicated by the yellow circles in PAM images and the white arrows in PAM B-scans. Scale bars: 500 μm. Reprinted with permission from **[142]**. (B) Simultaneously acquired PAM, confocal microscopy (CFM), and OCT images of a mouse ear with dynamic focusing. (a) PAM image; (b) CFM image; (c) OCT images (d) OCT B-scan at the location marked in panel (c) by a solid line; (e) PAM 3-D image reconstruction; and (f) fused PAM projection and CFM images; bar: 1 mm. Reprinted with permission from **[144]**.

In early 2020, Liu et al. [145] developed a dual-modal system in the NIR range for real-time, in-vivo visualization of the tumor microenvironment changes during chemotherapy. The PAM subsystem utilized an optical parametric oscillation laser which had a wavelength range of 680-1064 nm. The OCT subsystem was based on a commercial system with a center wavelength of ~ 1300 nm, providing 12 μm axial resolution. This study worked to characterize tumor angiogenesis by monitoring changes in the vascular network's density, quantitative total hemoglobin concentration, and oxygen saturation of cancerous tissue. They suggested the dual-modal imaging-guided dose control system as a more efficient technology compared to the presently utilized tumor treatment options.

The majority of PAM-OCT configurations discussed earlier utilized ultrasound transducers for detecting acoustic waves. Despite offering high sensitivity, these transducers pose challenges when integrating PAM and OCT subsystems [146]. In transmission mode, the sample needs to be placed in a water tank or be in contact with ultrasound gel as coupling medium [147]–[149], which limits the application of the technique to thin specimens. In reflection mode, because the opaque transducer obstructs the optical beam path, it needs to be positioned obliquely with respect to the optical axis which causes sensitivity loss [150], [151]. In 2019, Hindl et al. [152] developed a reflection-mode OCT-PAM system using an all-optical akinetic Fabry-Perot etalon sensor. The miniature sensor included a rigid, fiber based Fabry-Perot etalon with a transparent central opening, and enabled linear signal detection over a broad bandwidth[153]. A schematic of the system is presented in Figure 2-8A. The OCT subsystem used a broadband laser centered at 840 nm, with a 5 μm axial resolution and the PAM subsystem used a 532 nm pulsed laser operating at a pulse repetition rate of 50 kHz. This system acquired OCT and PAM

images sequentially. In-vivo images of zebrafish larva's tissue and vascular morphologies were presented (Figure **2-8**B). The system had limited imaging speed due to the use of stepper motors for scanning and the need for signal averaging to provide increased SNR. In addition, the OCT light source combined three superluminescent diodes which were not polarization aligned and resulted in various imaging artifacts and a degraded axial resolution. They recently reported a dual-modal system using a Ti: Sapphire broadband light source and fast laser scanning. The axial resolution was 2.4 μm enabling visualization of retinal layers in zebrafish model. Functional extensions of PAM-OCT system including Doppler OCT and spectroscopic PAM were applied to monitor arterial pulsation and to measure absolute blood flow and oxygen saturation. The in-vivo oxygenation measurement was acquired using a dye laser [154] with a 10 kHz repetition rate at 578 nm, 570 nm, and 562 nm wavelengths. Representative images recorded using the system are presented in Figure **2-8**C&D.

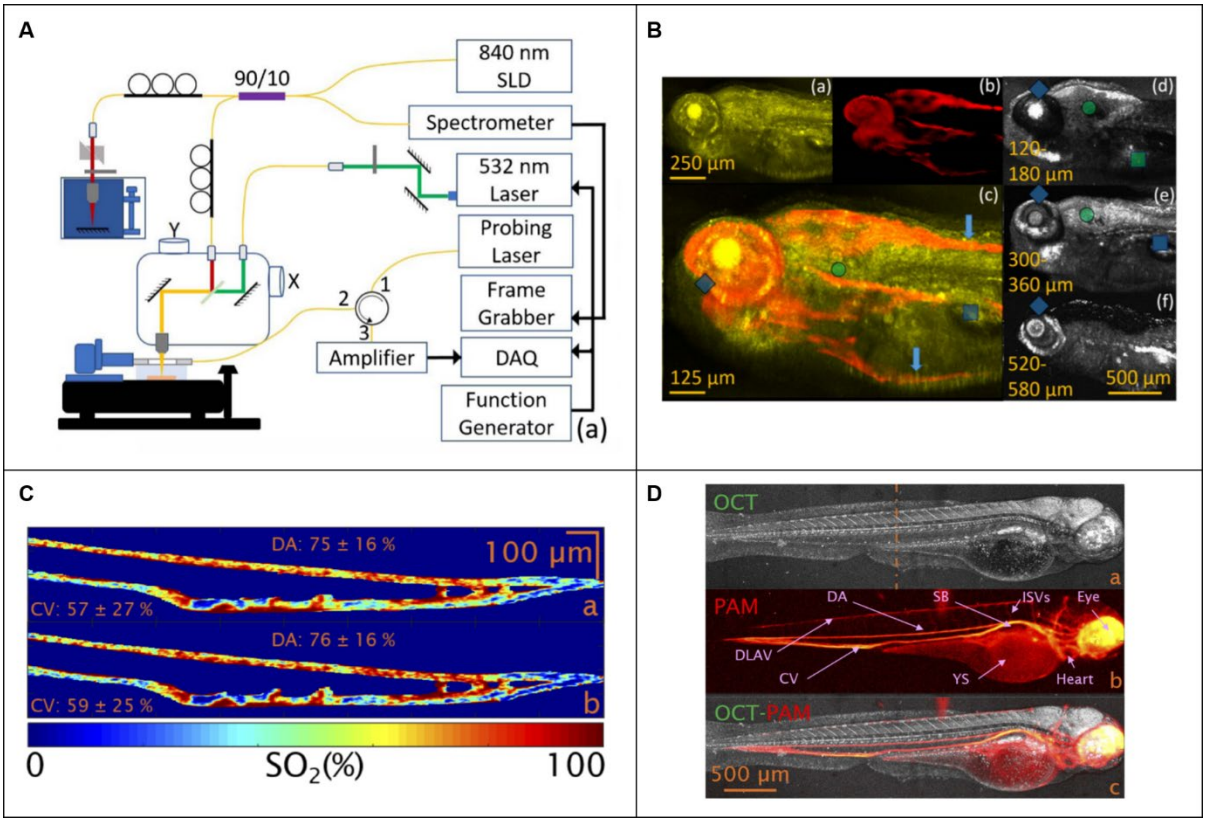

Figure 2-8. (A) Schematic of the reflection mode PAM-OCT system **[152]**. (B) Images of a zebrafish larva. (a) OCT image (b) PAM image (c) Color blended PAM-OCT image using (a) and (b). (d)–(f) Images of OCT integrating 60 µm depth range. Reprinted with permission from **[152]**. (C) Oxygenation map of a zebrafish larval tail. The image is acquired after spectral unmixing using the absorption coefficients of human (a) and zebrafish blood (b), respectively **[154]**. (D) OCT-PAM image of a zebrafish larva. (a) OCT average intensity projection, (b) PAM maximum amplitude projection, (c) multimodal OCT-PAM. Reprinted with permission from **[154]**.

In the system configurations discussed earlier, both PAM and OCT subsystems used their own specific light source. Normally, PAM excitation is based on a narrow band pulsed laser, while OCT requires broadband, continuous light (e.g., superluminescent diode) or virtually continuous light (e.g., Ti: Sapphire laser). The other important difference in their light source is that OCT systems usually use near infrared (NIR) light for deeper penetration, but PAM mainly uses visible light to target the absorption peak of hemoglobin and melanin [155]. However, this apparent difference in wavelength, does not impede applying visible light for OCT or NIR light for PAM. Recent experiments have demonstrated applications of visible

OCT for high resolution imaging and measuring metabolic rate of oxygen for clinical studies [156], [157], while NIR light has been used for imaging lipid and collagen tissues in PAM [157], [158]. Several studies explored the feasibility of using a single light source for PAM excitation and OCT imaging, which would reduce the complexity and costs of the system, in addition, it will generate synchronized and co-registered PAM and OCT images. Zhang et al. [28] demonstrated the first single pulsed light source for PAM-OCT in 2012 and termed the technique optical coherence photoacoustic microscopy (OC-PAM). Experimental setup of the proposed system is demonstrated in Figure **2-9**A. The system was in transmission mode with a custom-designed broadband dye laser centered at 580 nm with 20 nm bandwidth, and a 5 kHz pulse repetition rate. The system was tested on in-vivo mouse ear and promising results were demonstrated; however, the low repetition rate of the light source limited the imaging speed, and the noisy spectrum of the laser degraded the quality of OCT images. Due to their broad spectral bandwidth, supercontinuum (SC) sources were employed in OC-PAM systems as well [159]. In 2016, Shu et al. [151] reported a dual-modality OC-PAM system using a homebuilt fiber-based SC source (Figure **2-9**B). The beam coming from the light source was split into a shorter wavelength band (500 – 800 nm) for PAM and a longer wavelength band (800 – 900 nm) for OCT. The system was tested for in-vivo imaging of mouse ear, and multispectral PAM was performed on ex-vivo porcine retinal sample (Figure **2-9**C).

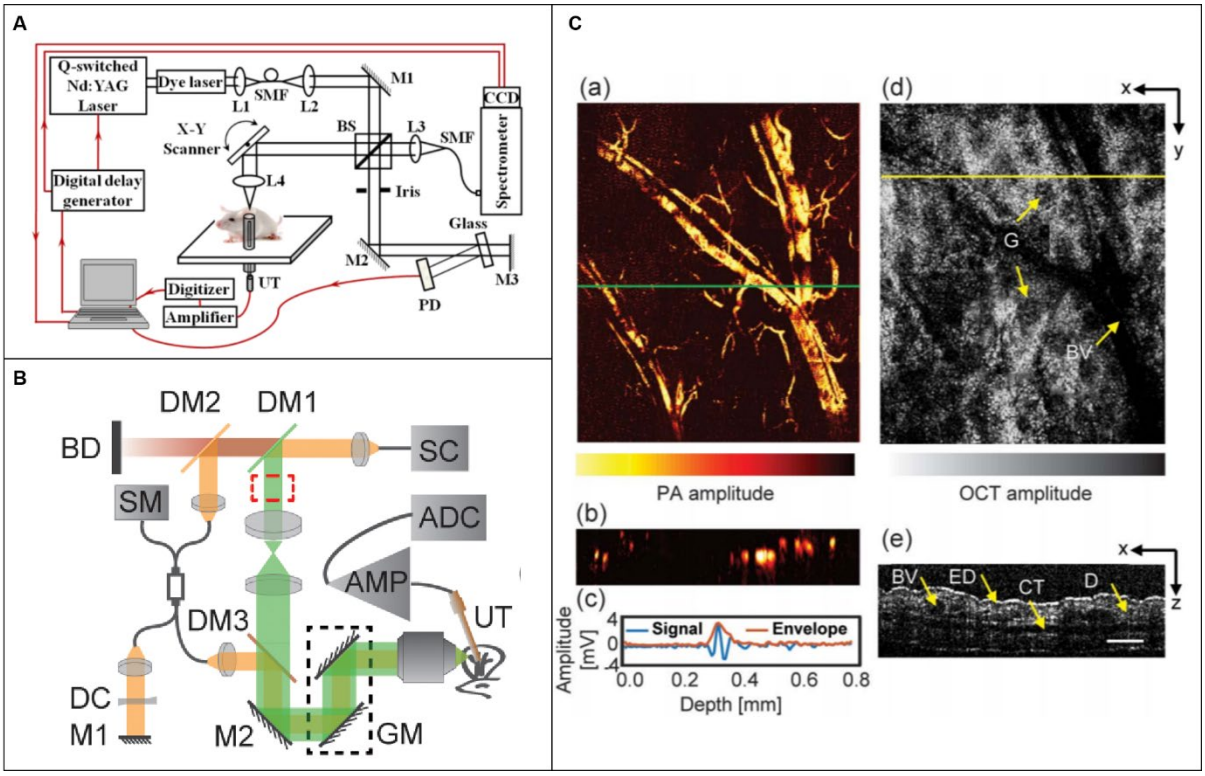

Figure 2-9. (A) Schematic of the experimental system of a free-space OC-PAM. BS: beam splitter; SMF: single mode fiber; PD: photodiode; UT: ultrasonic transducer; L: Lens, M: mirror. Reprinted with permission from **[28]**. (B) Schematic of PAM-OCT system setup. SC, supercontinuum; DM: dichroic mirrors; GM, galvanometer; UT, ultrasound transducer; AMP, amplifier; ADC, digitizer; SM, spectrometer; DC, dispersion compensating slab; M, mirrors; BD, beam dump. Reprinted with permission from **[151]**. (C) Results of in-vivo mouse ear imaging. (a) En-face PAM image (b) PAM B-scan taken from location indicated by the green line in (a). (c) Typical PA A-line and its signal envelope obtained by a Hilbert transform. (d) En face OCT image. G, gland; BV, blood vessel. (e) OCT B-scan taken from location indicated by yellow line in (d). ED, epidermis; CT, cartilage; D, dermis. Scale bar, 150 µm. Reprinted with permission from **[151]**.

2.4.4. Photoacoustic microscopy combined with optical coherence tomography for ophthalmic applications.

Due to the prevalence of OCT imaging for clinical ophthalmology, dual modal PAM-OCT is a natural extension for imaging the eye. In ophthalmic application, access to the absorption information could provide information about the functional and molecular properties of the tissue, such as evaluating the retinal pigment epithelium in diseases like age-related macular degeneration or measuring metabolic rate of oxygen in retinal and choroidal circulations in diabetic retinopathy. In 2010, Jiao et al. [160] reported one of the first multimodal PAM-OCT ophthalmoscope which used an unfocused transducer directly placed on the sclera. The OCT

subsystem was based on a SD-OCT design consisting of a superluminescent diode centred at 870 nm. Experimental results were demonstrated for in-vivo imaging of retinal vessels and retinal pigment epithelium layer in rat eyes, with a laser pulse energy well within the ANSI safety limits. Song et al. [161] further extended this system to include additional modalities like scanning laser ophthalmoscopy and fluorescein angiography and imaged rat retina. They also measured the metabolic rate of oxygen in rat retina [106]. Figure **2-10** illustrates the developed functional imaging system and the combined PAM and OCT scanning pattern on the retina. In 2015, Liu et al. [162] developed an OC-PAM system by using a single pulsed broadband light source with central wavelength of 800 nm. Since the absorption coefficient of haemoglobin is relatively weak at this wavelength, the PAM signals were mainly providing melanin-specific information of the retina. The imaging speed of the system was limited by the 10 kHz pulse repetition rate of the light source, which is not as high as conventional ophthalmic OCT systems. To avoid possible motion artifacts and image blurring/disruption high imaging speed is required. Robinson et al. [163] reported that the eye has a fixation time of ~ 500 ms. Increasing the repetition rate can improve the imaging speed, however it will also increase the average power of the light source which is constrained by existing laser safety limits. This may cause issues in practical applications where there are pulses overlapping in the retina. This highlights the trade-off between pulse repetition rate and pulse energy. Developing a highly sensitive PA detection method is the key for reducing the pulse energy and thus making it safe for clinical eye imaging.

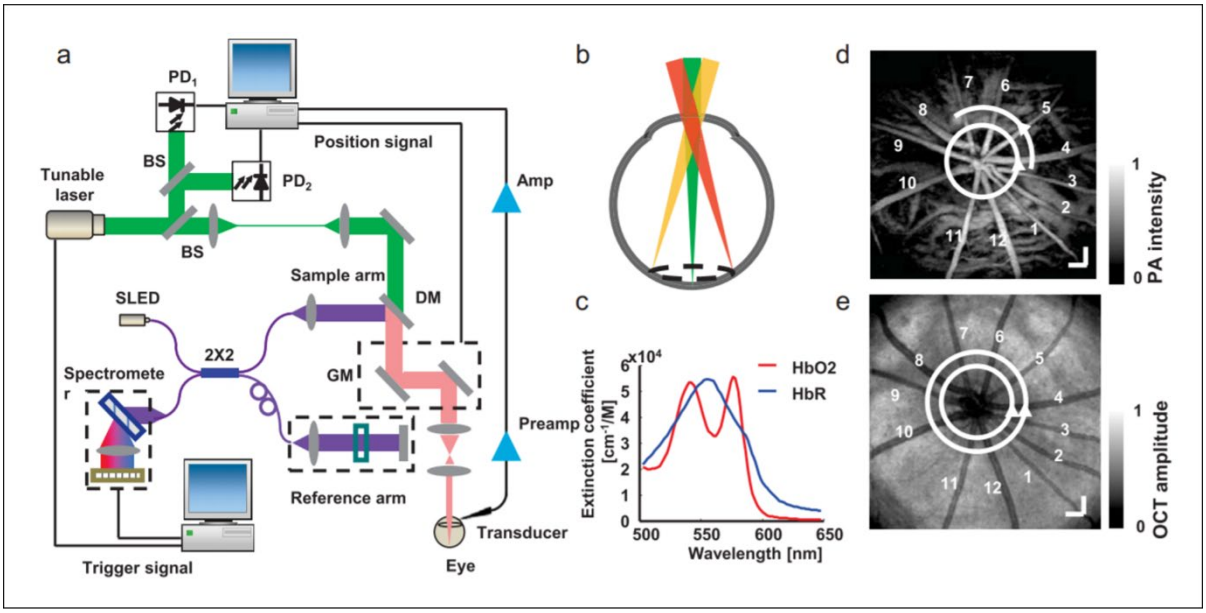

Figure 2-10. Illustration of integrated PAM and SD-OCT to measure retinal metabolic rate of oxygen. (a) Schematic of the experimental setup. (b) Circular scanning pattern on the retina. (c) Molar extinction coefficient spectrum of oxy- and deoxy-hemoglobin. (d) A maximum-amplitude-projection PAM fundus image showing major retinal vessels. Bar: 200 mm. (e) An OCT fundus image of the same rat showed in the panel d. Bar: 200 mm. Reprinted with permission from **[106]**.

Mice and rat eye models have been extensively used in pre-clinical ophthalmic imaging experiments. The eyeballs of these animals are smaller (axial length of mouse eyeballs ~3 mm, rats ~6 mm) compared to humans (~25 mm). Therefore, using animals with larger eyeballs, like rabbits and monkeys are more relevant to human. Tian et al. [164] was among the first groups to demonstrate the application of PAM-OCT system for chorioretinal imaging of rabbit in 2017. They were able to visualize depth-resolved retinal and choroidal vessels using laser exposure well below the ANSI safety limit. A multi-modal imaging system combining PAM, OCT and florescence microscopy was demonstrated by Zhang et al. [165], [166], and it was applied to evaluate angiogenesis in both albino and pigmented live rabbit eyes. The authors claimed that in pigmented rabbits, melanin from the retinal pigment epithelium overlies the choroid and thus possibly block the diffuse choroidal hyperfluorescence and improve the image quality of all the three modalities. Nguyen et al. [108] employed gold nanoparticles as

a contrast agent for both OCT and PAM imaging. They imaged in-vivo rabbit retina, and the exogenous contrast agent improved the efficiency for visualizing capillaries, retinal and choroidal vessel. The speed of the system was defined by 1 kHz pulse repetition rate of the excitation laser. The system was later used to evaluate optical properties of retinal vein occlusion and retinal neovascularization in living rabbits [167]. Spectroscopic PAM was performed at wavelengths ranging from 510 to 600 nm to further evaluate dynamic changes in the retinal morphology [168]. The schematic of the developed system and recorded images using multimodal system are presented in Figure **2-11**A and B, respectively.

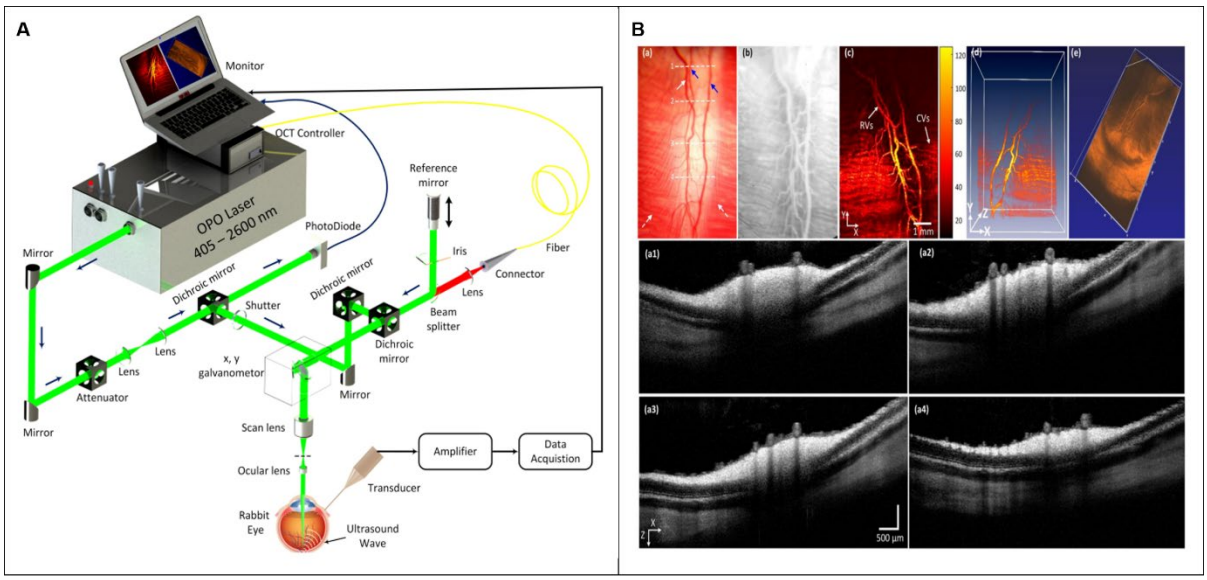

Figure 2-11. (A) Schematic diagram of the integrated PAM and OCT systems for multimodal retinal imaging. Reprinted with permission from **[167]**. (B) images of retinal blood vessels in rabbits: (a) color fundus photography of retina. (b) Fluorescein angiography image showing retinal, choroidal and capillaries. (c) Corresponding maximum amplitude projection PAM images of retina. (d,e) volumetric PAM and OCT image, respectively. (a1–a4) Cross-sectional OCT images acquired along the scanning lines from Figure (a). Reprinted with permission from **[167]**.

In general, PAM devices have relatively low axial resolution compared to OCT systems, and there is a large resolution gap between two modalities. Unlike, OCT whose axial resolution is defined by the spectral bandwidth of the light source, in PAM axial resolution depends on detector's bandwidth and ultrasound attenuation [47]. The typical axial resolution of OCT

systems is less than 10 μm, which corresponds to ~ 100 MHz ultrasound signal frequency. These high frequency signal can rarely survive in some cases where the distance from the source to the detector is long such as retina imaging. Therefore, for ophthalmic PAM-OCT, it is importance to enhance PA detection mechanism to reduce the gap in axial resolution.

2.5. Discussion

The combination of PAI and OCT has drawn a large amount of research interest throughout the past decade. This multi-modal technology has the potential to provide chromophore selective image contrast in concert with depth-resolved scattering contrast. Despite offering several advantages there are still a couple of key challenges to overcome.

One of the major limitations of current systems is the significant imaging speed mismatch between OCT and PAI subsystems. Imaging speed is a critical parameter when it comes to real-time functional studies. Additionally, faster imaging speeds will help systems mitigate image artifacts due to involuntary motion. Thanks to technological developments, current OCT systems are able to reach video rate over a large scanning area [169]–[171]. The same is not true for PAI systems, and as a result the imaging speed of the dual-modal system is defined by the pulse repetition rate of the PA excitation light source or mechanical scanning speed of the PAI probe head. Widespread implementation of PAI-OCT systems will depend on the development and integration of suitable light sources with high repetition rate, stable short pulse illumination, and high output energy at multiple wavelengths. This development would enable PAI-OCT systems to capture real-time large field-of-view images.

The other major constraint in most PAI systems is that most ultrasound detectors are opaque. Therefore, the physical size of the sensor obstructs the optical path required for OCT

acquisition. To overcome this limitation, in some studies the active size of the transducer was reduced, or the transducer was positioned obliquely [153]. However, since the sensitivity of the photoacoustic imaging scales with the active element size of the detector, these methods effect the sensitivity of the photoacoustic images and will degrade image quality [172]. Several studies have investigated optimizing light delivery to improve PA image contrast and signal-to-noise ratio [173]–[175]. Monte Carlo simulations suggest that the optimal PA illumination depends on the optical properties of the sample[176]. Improvements in light delivery have also be investigated through using optically transparent spacer between transducer and sample to directly deliver light to the surface underneath the transducer [177]–[179]. In addition, custom transducers and new materials have been explored to develop different illumination geometries and improve the quality of the PA image [59], [180], [181]. However, these methods require significant modification of the system and cannot be readily integrated into standard clinical scanners[181].

Another important constraint of ultrasound transducers used in most PAI system rise from their need for physical contact with the sample through a coupling medium. This contact-based detection minimizes the acoustic reflection losses at poorly matched interfaces such as tissue and air. However, it is not suitable for several clinical and pre-clinical applications such as wound assessment, brain imaging or ophthalmic imaging [182]. Various approaches have been suggested to overcome this limitation among which optical detection approaches hold the promise to provide high sensitivity over a wide frequency range [183]–[186]. Optical detection methods also offer the opportunity of developing miniaturized and optically transparent ultrasound detectors [146]. Pure optical PAI-OCT system is more attractive nowadays and

offers a better choice for the multimodal imaging. Different studies have been conducted on the performance of pure optical photoacoustic imaging integrated with optical coherence tomography [187], [188]. In [141], authors proposed a resolution-matched reflection mode PAM-OCT system for in-vivo imaging applications. The PAM subsystem is based on a polarization-dependent reflection ultrasonic detection (PRUD), which still requires water as coupling medium and complicated optical alignment. The akinetic sensor employed in [152], is another example of pure optical PA detection sensor, which also suffers from the need for acoustic gel as coupling medium. All-optical PA detection methods have been investigated for non-contact, dual modal PAI-OCT system as well. In the next chapter, we will discuss different methods developed for achieving non-contact PA signal detection with an emphasis on the all-optical methods. Each method is discussed along with its advantages and disadvantages.

Chapter 3
Non-contact photoacoustic imaging

Notes and Acknowledgement

This chapter reviews the importance of non-contact photoacoustic imaging. It overviews the current non-contact photoacoustic detection techniques with an emphasis on all-optical detection methods and their associated physical mechanisms. The content of this chapter is based on the following journal manuscript:

Zohreh Hosseinaee, Martin Le, Kevan Bell, and Parsin Haji Reza "Towards non-contact photoacoustic imaging." Photoacoustics (2020): 100207.

Author contributions

Zohreh Hosseinaee read and collected the reference papers, organized the content of the review paper, sub-categorized the non-contact photoacoustic imaging techniques, compiled the article, prepared the figures, and wrote the main manuscript.

Martin Le edited parts of the article and helped in reviewing some of the references.

Kevan Bell edited parts of the article.

Parsin Haji Reza was the principal investigator, set the article scope, and proofread the article.

All authors contributed to the final version for publication.

3.1. Introduction

Photoacoustic imaging (PAI) is an impactful modality in biomedical optics that has attracted interest from various research communities in the last decade, especially biomedical imaging. The photoacoustic effect was discovered by Bell in 1880[32]. He discovered that sound waves might be generated in solid material when exposed to a pulsed light source. Development of the laser in the 1960s had a significant impact on the field by providing directional, high peak power, and spectrally pure beam that many photoacoustic applications require. Subsequently, the phenomena found popularity in spectroscopy, and in 1964 Amar *et al.* reported the application of PA spectroscopy for *in-vivo* rabbit eye[189] and ex-vivo human eye specimens[190]. Theodore Bowen was among the first to propose the phenomena for soft tissue imaging in 1981[37]. These early studies progressed, culminating in work published in 1993 which demonstrated one of the first *in-vivo* photoacoustic study performed on human finger[191]. Thereafter, the field has seen significant advancements in terms of instrumentation, image reconstruction algorithms, functional imaging, and molecular imaging capabilities.

PAI offers high sensitivity for obtaining optical absorption contrast over a wide range of spatial scales from organelles, cells, tissue, organs, and small animals. Additionally, it is complementary to other imaging modalities in terms of contrast, sample penetration, spatial and temporal resolutions. These unique opportunities were utilized in the last two decades in several pre-clinical and clinical applications including but not limited to blood oxygen saturation imaging[42], [56], [57], brain vasculature and functional imaging[43], [59], [192], gene expression[60], vulnerable atherosclerotic plaques diagnosis[61], skin melanomas[62],

histology-like tissue imaging[63], [64], longitudinal tumor angiogenesis studies[65], imaging and detection of protein interactions[66], multi-modal ocular imaging[67], [182], [193], [194], and tissue engineering scaffolds[31], [68] . In addition, PAI methods have been utilized in different non-medical applications such as non-destructive testing[195], [196] detecting metal surface defects[197], spectroscopy[198], [199], and uncovering hidden features in paintings[200].

Despite offering high sensitivity, novel imaging contrast, and high resolution, photoacoustic microscopy is not generally an all-optical imaging method unlike the other microscopy techniques. One of the significant limitations of photoacoustic microscopes arises from their need to be in physical contact with the sample through a coupling media. This physical contact, coupling, or immersion of the sample is undesirable or impractical for many clinical and pre-clinical applications. This also limits the flexibility of photoacoustic techniques to be integrated with other all-optical imaging microscopes for providing complementary imaging contrast. To overcome these limitations, several non-contact photoacoustic signal detection approaches have been proposed. This chapter presents a brief overview of current non-contact photoacoustic detection techniques with an emphasis on all-optical detection methods and their associated physical mechanisms.

3.2. Physical mechanism of photoacoustic imaging

In general, when biological tissues are irradiated by photons of light, depending on the light wavelength, the photons penetrate to some depths. Inside the tissue, these photons get scattered and absorbed, where the absorption occurs by light-absorbing molecules known as chromophores. The absorbed optical energy induces a local transient temperature rise, which

generates pressure via thermo-elastic expansion. In thermal confinement the photoacoustic equation for an arbitrary absorbing target with an arbitrary excitation source is defined as[33]:

$$\left(\nabla^2 - \frac{1}{v_s^2}\frac{\partial^2}{\partial t^2}\right) p(\vec{r}, t) = -\frac{\beta}{C_p}\frac{\partial H}{\partial t} \qquad \text{Equation 3-1}$$

Where $p(\vec{r}, t)$ denotes the acoustic pressure rise at location $\vec{r}$ at time t, v_s is the speed of sound, β is the thermal coefficient of volume expansion, C_p denotes the specific heat capacity at constant pressure, and H represents the heating function defined as the thermal energy deposited per unit volume and per unit time [201]. Based on this equation, photoacoustic pressure propagation is driven by the first-time derivative of the heating function H. Therefore, time-invariant heating does not generate photoacoustic pressure waves. When both thermal and stress confinements are met, thermal expansion causes a pressure rise (p_0) that can be estimated by [202]:

$$p_0 = \Gamma . \mu_a . F \qquad \text{Equation 3-2}$$

Where p_0 is the initial pressure rise, μ_a is the absorption coefficient ($\frac{1}{cm}$), $\Gamma = \beta v_s^2 / C_p$ is the Grüneisen coefficient[203], [204] representing thermal and mechanical properties of the tissue, and F is the fluence of the irradiated energy ($\frac{J}{cm^2}$). According to the American National Standard Institute (ANSI) safety standard, in the visible spectral region, the maximum permissible fluence on the skin surface is 20 mJ/cm^2. The generated pressure propagates in the form of acoustic waves and can be detected on the surface of the tissue by an ultrasonic transducer or transducer array. These signals form an image that maps the optical energy absorption inside the tissue[47] (Figure **3-1**).

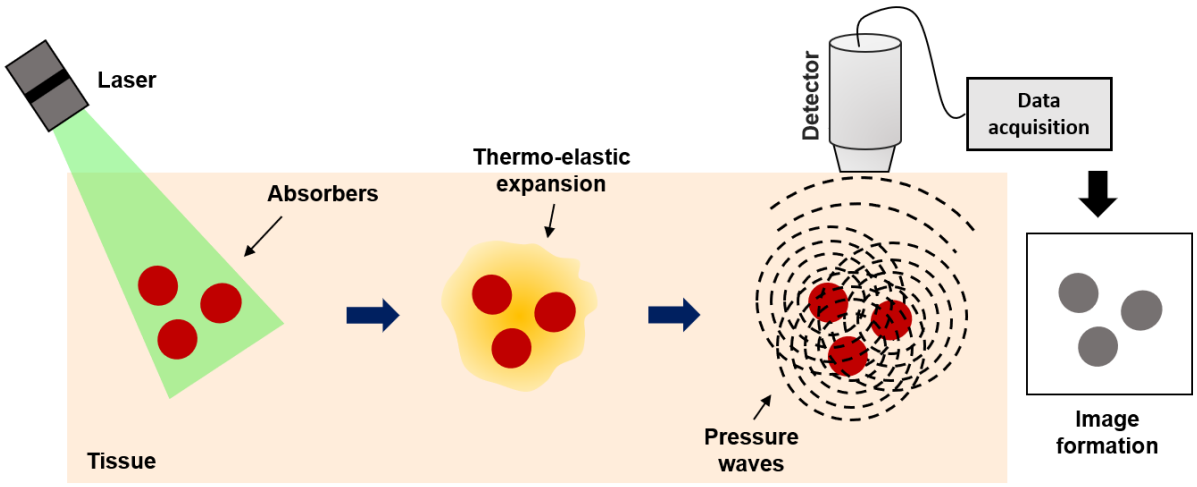

Figure 3-1. General principle of photoacoustic imaging. Targeted chromophores absorb optical energy resulting in a local temperature rise, inducing local pressure rise, which propagates outwards towards an ultrasonic transducer. The recorded signal is reconstructed to map the original optical energy deposition inside the tissue.

3.3. Photoacoustic modalities

PAI can be split into two main categories depending on how the images are formed: photoacoustic tomography (PAT), which uses reconstruction-based image formation and photoacoustic microscopy (PAM), which uses focused-based image formation.

In PAT, an unfocused optical beam excites the region of interest, and an array of ultrasonic transducers measures the generated ultrasound waves in multiple positions[24], [36], [40], [205]. Common detection geometries used in PAT are planar, cylindrical, and spherical. In planar detection mode, a two-dimensional planar, linear, or phased array is used, while cylindrical detection mode uses ring transducer arrays or split ring arrays[206], [207]. Spherical detection has been used for imaging with an arc-shaped transducer array[208], [209] and a hemispherical array[109], [210]. The axial resolution of a PAT system is defined by the bandwidth of the detector, while the lateral resolution is dependent on the detection geometries[211]. PAT imaging depth theoretically is limited to a few centimeters in soft tissue,

where the optical fluence is significantly attenuated due to both absorption and scattering[96]. Previous works have demonstrated 720 μm lateral resolution at a depth of ~7 cm in biological tissue[24]. PAT can be used for various applications ranging from microscopic to macroscopic imaging, and it can provide large field of view (FOV) images. As a result, it has been used in applications such as whole-body imaging of small animals[212] and clinical breast cancer studies[41].

Unlike PAT, PAM employs raster-scanning of optical and acoustic foci and forms images directly from recorded depth-resolved signals[23]. PAM is generally used for applications that require high-resolution rather than deep penetration depth like single-cell imaging[50]. PAM can be further classified into acoustic-resolution PAM (AR-PAM), where the acoustic focusing is tighter than optical focusing[213], and optical-resolution PAM (OR-PAM), where the optical focusing is tighter[44], [214].

Acoustic resolution photoacoustic microscopy (AR-PAM). For AR-PAM, an unfocused beam of light illuminates the tissue, and the induced photoacoustic signals are detected using a focused ultrasound transducer. Since the acoustic focus is limited by the acoustic diffraction limit rather than the optical diffraction limit, the achieved resolution by AR-PAM is on the order of tens of microns[45]. The lateral resolution of AR-PAM is given by[215]:

$$\boldsymbol{\Delta x_{AR-PAM} = 0.71\lambda_a/NA_a} \qquad \text{Equation 3-3}$$

Where λ_a is the acoustic wavelength, and NA_a is the numerical aperture (NA) of the focused ultrasonic transducer. The axial resolution of PAT and AR-PAM is determined by the bandwidth (Δf) of the ultrasonic transducer, which can be described as[216]:

$$\boldsymbol{\Delta z = 0.88c/\Delta f} \qquad \text{Equation 3-4}$$

where *c* is the speed of sound. AR-PAM has been used for the deep-penetration imaging of microvasculature[217] and functional brain imaging with improved penetration depth[218]. For example, an imaging depth of ~ 11 mm has been demonstrated in biological tissue, which is ~10 times higher than the attainable depth of OR-PAM[219]. Another example comes from Moothanchery *et al.* [49], who reported an AR-PAM system with a lateral resolution of 45 μm with an imaging depth of ~7.6 mm for deep vasculature imaging.

Optical resolution photoacoustic microscopy (OR-PAM). The resolution of OR-PAM is limited by the optical diffraction limit of the focused laser beam[220]. Therefore it generates images with higher resolution than AR-PAM; however its penetration depth is restricted by the optical transport mean free path, which is ~ 1.5 mm for visible wavelengths in biological tissues[221], [222]. The lateral resolution of OR-PAM can be defined as[44]:

$$\Delta x_{OR-PAM} = 0.51\lambda_o/NA_o \qquad \text{Equation 3-5}$$

where λ_o is the optical wavelength and NA_o is the NA of the objective lens. In an OR-PAM configuration, the axial and lateral resolutions are defined by the NA of the objective lens. The high lateral resolution makes OR-PAM suitable for a wide range of applications. Zhang *et al.*[50] reported the first subwavelength OR-PAM by employing a 1.23 NA objective lens, obtaining a lateral resolution of 0.22 μm. Here, single-cell imaging was demonstrated on individual melanoma cells and erythrocytes.

3.4. Imaging Contrast

Photoacoustic imaging modalities offer a unique imaging contrast by taking advantage of direct optical absorption. In other words, any imaging target that absorbs light energy, can be

visualized by PAI modalities. In biological tissues, both endogenous and exogenous contrast agents can be exploited as imaging targets. Endogenous contrast agents are ideal targets as they are naturally available in tissue. Therefore, they are non-toxic and do not interfere with the original tissue microenvironment. The most commonly imaged endogenous contrast agents for PAI include DNA/RNA, hemoglobin, melanin, lipids, collagen, and water (Figure **3-2**). Among these, DNA/RNA is commonly used for cell nuclei imaging using an ultraviolet excitation source[223], hemoglobin is widely used for vascular imaging in the visible and near-infrared (NIR) spectral ranges[220], and melanin is used for melanoma tumor imaging in the NIR region[224]. Additionally, in the NIR region, lipids and water are used for atherosclerotic plaque[225] and injury imaging[226], respectively. Since these endogenous contrast agents have different absorption spectra, PAI can differentiate them with spectral measurements when the local optical fluence is known[227]. Exogenous contrast agents also offer the ability to be specifically engineered for maximum detection sensitivity and can be conjugated with target molecules to selectively bind to specific cell surface receptors[228], [229]. Their performance has been demonstrated for several applications such as cancer imaging[230], [231], functional brain imaging[232], [233], and monitoring therapeutic procedures[234], [235].

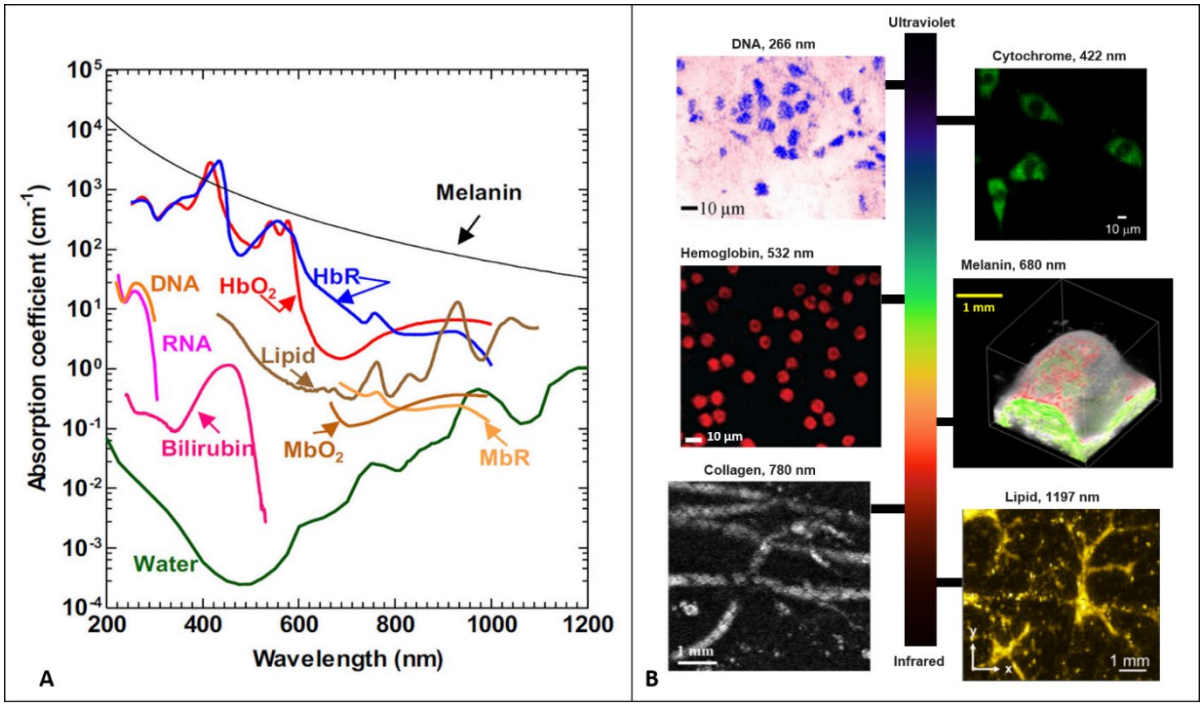

Figure 3-2. (A) Absorption spectra of common endogenous chromophores in biological tissues. Reprinted with permission from**[47]** (B) photoacoustic images acquired from mouse small intestine cells and DNA contrast at 266 nm. Reprinted with permission from**[236]**, fibroblast cytoplasm's with cytochrome contrast at 422 nm, reprinted with permission from **[237]**, PA image of mouse blood smear with hemoglobin contrast at 532 nm, reprinted with permission from**[238]**, tyrosinase tumor expressing with melanin contrast at 680 nm, reprinted with permission from **[60]**, photoacoustic image of mouse paw with skin removed and collagen contrast at 780 nm, reprinted with permission from **[158]**, intramuscular fat photoacoustic image with lipid contrast at 1197 nm, reprinted with permission from **[157]**.

3.5. Photoacoustic signal detection

Photoacoustic signals can be generated by an intensity-modulated continuous-wave (CW) excitation[239] or pulsed excitation[217]. Pulse excitation is more commonly used, since the signal-to-noise ratio (SNR) of photoacoustic signal is higher than that in CW excitation, if the same number of photons are delivered, or ANSI safety limits are considered[240]. Photoacoustic signals are broadband and thus demand the use of wideband ultrasonic transducers. The center frequency and bandwidth of the detector are two significant parameters, and, based on the intended application, the appropriate center frequency and bandwidth must be selected. Popular types of ultrasonic transducers for photoacoustic signal

detection include piezoelectric transducers, Fabry-Perot interferometers (FPI), capacitive micromachined ultrasound transducers (CMUTs), and micro ring resonators (MRRs)[36].

Despite offering several advantages, ultrasonic transducers need to be physically in contact with the sample through a coupling medium. Contact-based detection minimizes acoustic reflection losses at poorly matched interfaces such as between tissue and air. This poorly matched interface would result in pressure wave reflections back into the sample and away from the acoustic transducer. Appropriate acoustic matching is required to produce a conventional PAI device with high sensitivity. Physical contact, coupling, or immersion is not suitable for some applications. For example, ophthalmic imaging applications cannot fully benefit from PAI for structural and functional microvasculature visualization. Currently, in ophthalmic applications, the ultrasonic transducer is placed on the surface of the tissue or conjunctiva[165], increasing the risk of abrasion, infection, and patient discomfort. Additionally, involuntary eye movements may affect the coupling efficiency and degrade image quality[241], [242]. In small animal imaging, immersion in water significantly complicates the procedure and commonly results in sacrificing the animal[241], [243].

Although the skin is potentially the most accessible organ for optical and acoustic imaging, and PAI can be used for clinical dermatological applications, the requirement of physical contact, as opposed to purely optical methods, poses some limitations. In wound assessment and burn diagnostics, a coupling medium and physical contact with the sample increases the risk of pain and infection.

Endoscopic applications would also benefit from a non-contact detection mechanism[244]–[246]. At the moment, most photoacoustic endoscopic systems use miniaturized piezoelectric

transducers, which complicate the design of the endoscopic tip due to their size and opaque nature. The sensitivity and FOV of these transducers will be sacrificed by shrinking their size which adversely affect the achieved image quality. In addition, these transducers require direct contact and an impedance matching medium, resulting in an obstructed view, restricting their imaging capabilities to rotational scanning and side-views. Therefore, the advantages of forward-view imaging for guiding minimally invasive surgical procedures and special imaging applications are not available[247].

Additionally, in brain imaging, when applied to surgical applications, the transducer array must be inserted in a sterile saline solution, which acts as the coupling medium. To keep the solution stable and maintain maximum efficiency, it requires a horizontal working plane which is not convenient to achieve when the patient is on a surgical bed[245].

Moreover, most ultrasound detectors are opaque, which restricts the illumination direction of the excitation laser beam so that the inline configuration of detector and laser is challenging. Furthermore, combining PAI systems with other optical imaging modalities may require a complicated design. Therefore, a non-contact detection approach that avoids these issues opens up new possibilities for clinical applications and multi-modal imaging techniques[35], [160], [188].

Several techniques have been developed to realize non-contact detection of photoacoustic signals. Air-coupled transducers and all-optical detection methods such as interferometric- and non-interferometric-based approaches have been proposed as alternatives to contact-based ultrasonic transducers. Here, an overview of these techniques and their underlying physical mechanisms and reconstruction algorithms are presented.

3.6. Non-contact photoacoustic signal detection

3.6.1. Air-Coupled detection

Coupling transducers through air/gas has been explored to eliminate the need to use coupling media in conventional ultrasound transducers. The approach has been used for a wide range of ultrasound imaging applications, including non-destructive testing[248]–[251], material characterization[252]–[254], secure wireless transmission of data[255], sensing and analysis of cultural heritage[256], water control in agriculture[257], [258], quality control in food industry[259] and computer gesture-base control[260], [261]. A major drawback of the air-coupled ultrasound transducers comes from the impedance mismatch between air and solids, which cause high attenuation of ultrasound signal in the air[262]. Therefore, applications mentioned earlier were possible through improving the design of air-coupled transducers[263]–[266], increasing the excitation energy, low noise amplification, and digital signal processing techniques[267]–[270]. In addition, to further reduce losses and maintain a reasonable SNR, the working frequency is usually below 1 MHz, which is relatively low compared to the tens of MHz frequency range of common ultrasound transducers used in medical photoacoustic imaging applications.

In 2010, Kolkman *et al.*[271] demonstrated the feasibility of air-coupled transducers to detect photoacoustic signals in artificial blood vessels made of a silicon rubber tube filled with human blood. Here, the excitation fluence satisfied the ANSI maximum permissible exposure (MPE) limits and the energy density at the interface was of about 20 mJ/cm^2. Two unfocused transducers with central frequencies at 200 kHz and 1 MHz were placed at 7.5 mm above the phantom interface and recorded photoacoustic time traces (Figure **3-3**A). The achieved axial

resolution of their system was measured as 13 mm for 200 kHz transducer and 4 mm for the 1 MHz one. In 2015, Dean-Ben *et al.*[272] developed a transmission mode PAI system using a custom-designed air-coupled piezoelectric transducer with a central frequency of 800 kHz and bandwidth of 400 kHz. Their experiment followed the excitation light fluence determined by the ANSI safety limits, however, the narrow detection bandwidth of the transducer significantly compromised the system's resolution performance. Images of vessel-mimicking tubes were acquired; and significant averaging was found necessary to properly resolve these structures (Figure **3-3**B). Sathiyamoorthy *et al.*[273] developed an inverted photoacoustic microscope using a low-power CW laser and a kHz-range microphone. Information about the incident power on the imaging sample was not reported for this study. The detector was attached to a custom-designed chamber, and images from red blood cells located inside the chamber were recorded with a lateral resolution of 1.37 μm (Figure **3-3**C). The need for mechanical scanning and a large ensemble of averaging inhibits potential *in-vivo* applications of the air-coupled transducers due to their long acquisition time.

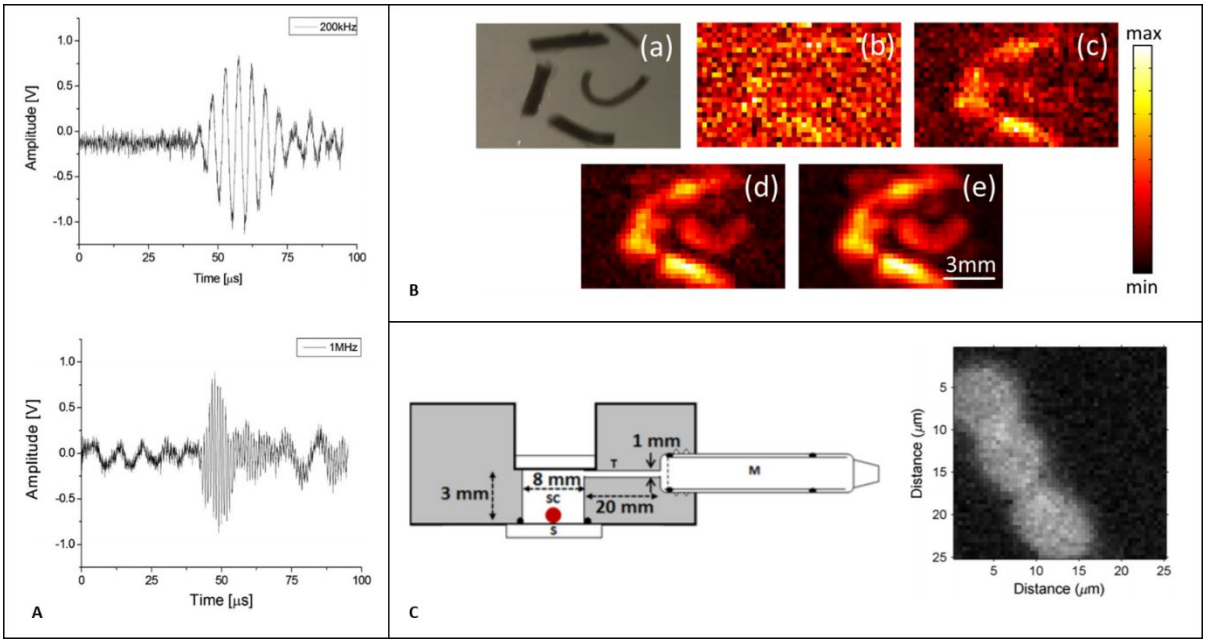

Figure 3-3 (A) Photoacoustic time traces from an artificial blood vessel, recorded with air-coupled ultrasound transducers with center frequency of 200 kHz and 1 MHz (the recorded signals are averaged 512 times), reprinted with permission from **[271]** (B) Photoacoustic images obtained by raster scanning of the air-coupled transducer (a) Photograph of the imaged ink channels. (b)–(e) Photoacoustic images of the phantom after the recorded signals have been averaged 1, 10, 100, and 1000 times respectively, Reprinted from **[272]**, with the permission of AIP Publishing. (C) Schematic diagram of the PA sensor and PA images of red blood cells smeared on a glass substrate, M is the microphone, SC is the sample chamber, S is substrate, reprinted with permission from **[273]**.

3.6.2. Optical detection of Photoacoustic signals

Early studies on optical detection of ultrasound signal began in 1960s[274]. In the last decade, due to the advancement of material science and fabrication technologies, significant progress has been made in developing high-performance optical detectors for ultrasound signals[275]. Optical ultrasound detection methods provide higher sensitivity, and wider frequency bandwidth over conventional piezoelectric devices, and also offer the opportunity of developing miniaturized and optically transparent ultrasound detectors[146]. Contact-based optical photoacoustic detectors like polymer microring resonators and FPIs have been widely used in applications such as bladder tissue vasculature imaging[276], *in-vivo* imaging of the vasculature in human skin[58], [114], [127], [277], endoscopic imaging of

microvasculature[278], [279] and multi-modal imaging[99], [280]. Furthermore, all-optical PAM system based on pressure distribution measurements and probe beam deflection techniques were developed, despite offering high sensitivity and micron scale resolution in these method the sample needs to be submerged in water cell limiting the *in-vivo* applications[281]–[284].

3.6.2.1. Speckle pattern analysis

Speckle is a feature of coherent wave propagation formed when interference occurs between superimposed waves[285]. This effect has been leveraged in several techniques, including laser speckle imaging[286], ultrasonography[287], synthetic aperture radar[288], and optical coherence tomography[289]. When photoacoustic waves arrive at the sample surface, they cause mechanical deformations. When a continuous-wave laser illuminates this region, these surface deformations modulate the speckle patterns of the backscattered beam. By characterizing these patterns, information about the surface deformations, and thus the acoustic pressure, can be extracted[290]–[294].

In 1999, Leveque *et al.* [295] developed a speckle detection scheme where a CCD camera operated as a detector array. This technique could demonstrate one-dimensional images of biological tissue. The system was further modified for acquiring two-dimensional and three-dimensional images[296]–[300] (Figure **3-4**A). Horstmann *et al.* [301] reported a full-field speckle interferometry method where the backscattered light was combined with a reference and imaged onto a high-speed camera. This experimental setup is demonstrated in Figure **3-4**B. Through consecutive measurements, they were able to extract signals from porcine skin phantoms with a 90 μm lateral resolution over a 4 mm penetration depth range. Lengenfelder

et al.[290] performed experiments in both reflection and transmission modes for *ex-vivo* fat tissue imaging. To increase the SNR of the system, the optical exposure was 5-times higher than the ANSI MPE limits for biological tissues. They went on to further apply speckle pattern analysis for endoscopic applications and demonstrated 2.76 μm lateral resolution on phantoms and *ex-vivo* porcine fat tissue using a high frame rate camera (823,500 fps) [247]. Recently, Li *et al.*[302] evaluated the feasibility of delineating the strength of PA signals using a two-beam optical design and a CMOS camera operating at 60 Hz with a 10 μs exposure. A black tape phantom was imaged and by correlating the speckle patterns as a function of time, the strength of PA perturbations was quantified (Figure **3-4**C). In the report, the probe beam was not focused on the sample interface resulting in a reflected speckle pattern that was highly sensitive to surface motion on the sample. As well, the bandwidth of the camera proved insufficient for capturing salient MHz-regime signals limiting its potential efficacy. However, this would need to be balanced against the resulting decrease in SNR brought on by lower integration times. Since any form of motion and mechanical noise can distort the speckle patterns of the probe beam, this method is very sensitive to phase noise and ambient motions and *in-vivo* applications would be extremely limited.

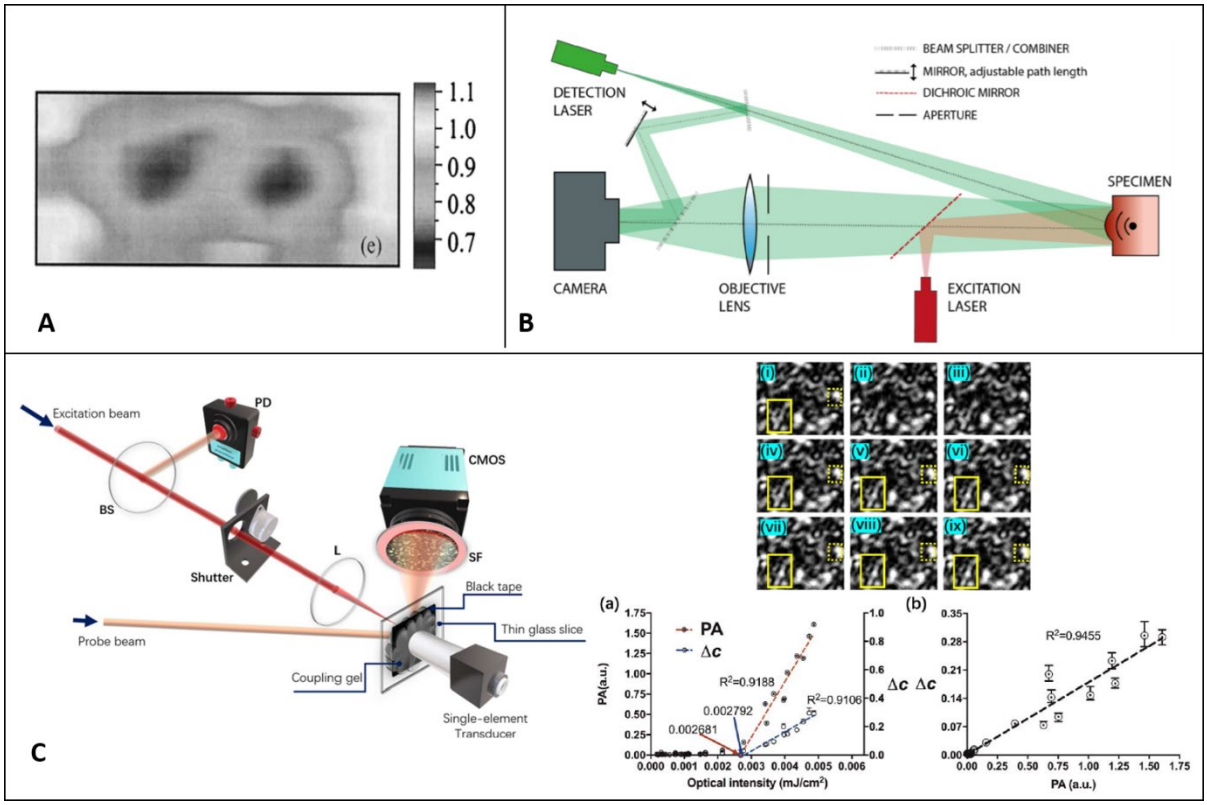

Figure 3-4. (A) Two-dimensional image of chicken breast tissue in which two gizzard objects were buried, reprinted with permission from **[299]**. (B) Interferometric detection of object surface displacement after photoacoustic excitation. © Institute of Physics and Engineering in Medicine. Reproduced by permission of IOP Publishing**[301]**. All rights reserved. (C) Schematic setup for specklegram-based non-contact photoacoustic detection. BS, beamsplitter; CMOS, CMOS camera; L, lens; PD, photodiode; SF, spectral filter. Speckle pattern generated by the probe beam observed for various moments (i)–(ix) in (a). Among them, (i) is the initial speckle pattern, (ii) and (iii) are recorded when the shutter is off, and no excitation beam is illuminated on the sample, and (iv)–(ix) are a sequence of patterns associated with the excitation of PA effect. (a) Measured speckle correlation changes as a function of excitation pulse energy (right axis) and the ultrasound piezoelectric transducer-based PA amplitude as a function of excitation pulse energy (left axis). (b) Linearity between the two detection methods, reprinted with permission from **[302]**.

3.6.2.2. Interferometric PA detection methods

Interferometric approaches have become a popular method for remote detection of photoacoustic signals. They overcome some of the issues brought forward with speckle-based detection by leveraging dedicated interferometers for extraction of phase-contrast from light returning from the sample. Both homodyne and heterodyne architectures have been investigated for ultrasound signal detection[303], [304]. In homodyne mode, interference occurs between beams of the same frequency, and the phase difference of the beams results in

an intensity modulation of the detected light[305]. On the other hand, in heterodyne mode, the interference occurs between beams with different frequencies, generating an interference with one constant component and one oscillating component where the amplitude of the oscillating component is proportional to the product of the interfering beams[306]–[309]. In general, heterodyne interferometers are relatively less sensitive to ambient noise compared with homodyne variants[310]. Each of these methods depends on the tissue surface as well as the stability of the entire detection system, which will be discussed in the following sections.

3.6.2.2.1. Heterodyne detection

In 1968, Massey *et al.*[311] demonstrated the application of an optical heterodyne system for sensing the vibration amplitude distribution on a reflective resonant diaphragm placed in the liquid acoustic medium. The method was further applied for all-optical detection of PA signals in spectroscopy[312], [313] and imaging applications[314], [315]. In 2014, Park *et al.*[316] explored an all-fiber heterodyne interferometer for photoacoustic imaging. They reported 1.7 μm lateral resolution from a miniaturized probe looking at polyethylene terephthalate fibers positioned inside the gelatin-based phantom. However, the excitation fluence used in this study was above ANSI MPE limits. The year after, Eom *et al.*[314] reported a different fiber-optic heterodyne interferometer looking at a chicken chorioallantois membrane (CAM). Blood vessel structures as deep as 2.5 mm were identified with lateral and axial resolutions of 100 μm and 30 μm, respectively (Figure **3-5**A). They further developed the system into a dual-modality imaging technique by integrating the photoacoustic detection with a swept-source optical coherence tomography (OCT) for endoscopic imaging (Figure **3-5**B)[187]. Acoustic waves were detected at the outer surface of the water layer under which the sample was

submerged. The method was also applied for non-contact delineation of stereotactic boundaries of artificial tumor in pig brain tissue and was successful in providing accurate thickness information of the sample[317].

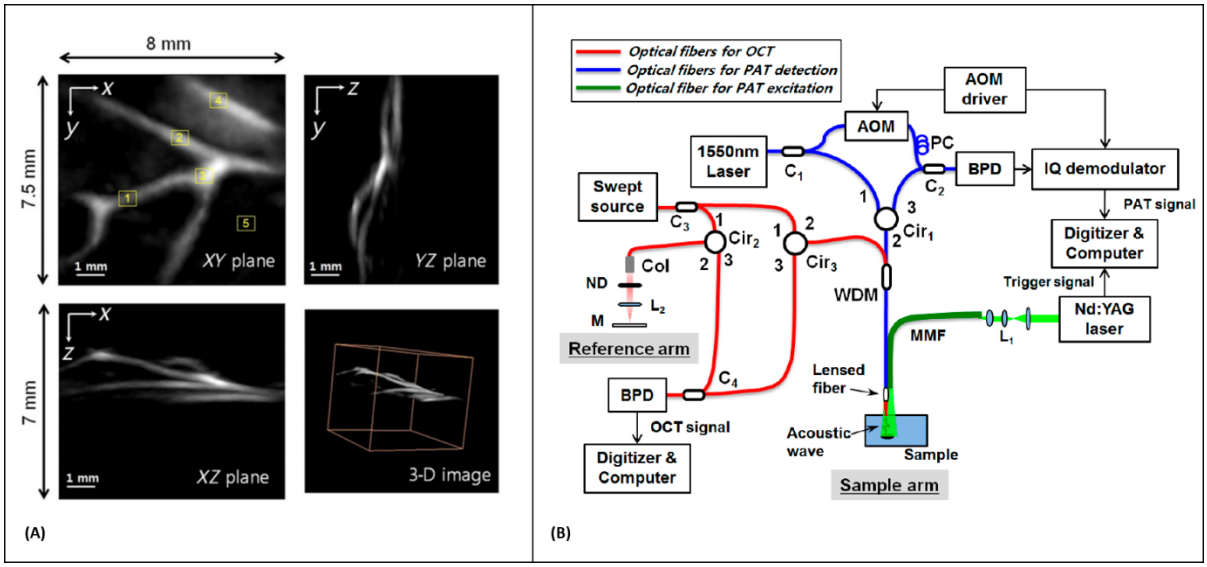

Figure 3-5. (A) 3-D photoacoustic images of the CAM. Top left: XY plane maximum intensity projection (MIP) image. Top right: YZ plane MIP image. Lower left: XZ plane MIP image. Lower right: 3-D image, reprinted with permission from [314] (B) Schematic of all-fiber-based dual modality PA-OCT with miniature common probe. AOM: acousto-optic modulator; PC polarization controller, BPD: balanced photodetector, Col: collimator; ND: neutral density filter; WDM: Wavelength division multiplexer; MMF: multimode fiber, reprinted with permission from [187].

Heterodyne interferometers have difficulty detecting highly scattered probe beams on rough surfaces, and therefore require a thin layer of water or oil above the sample[314], [317]. This provides an appropriate smooth and reflective surface for the interferometer; however, the method can no longer be considered fully non-contact (called quasi non-contact) as the system requires the addition of fluid to the surface of the sample. Much like standard acoustic coupling performed in conventional PAI techniques, this greatly limits potential biomedical applications.

A solution that was explored involved the application of a two-wave-mixing interferometer (TWMI)[318], [319]. In these devices the beams interfere inside a photorefractive nonlinear

crystal, where the beams are amplified and low frequency noises are suppressed so the effect of ambient noises like air disturbance is negligible [320], [321]. While the technique is mainly used for non-destructive testing applications[322], biomedical applications like skin imaging have also been explored[323]–[325]. George *et al.*[326] developed a non-contact photoacoustic microscope utilizing a photorefractive crystal-based interferometer for imaging of red blood cells and *ex-vivo* porcine retinal samples. The schematic diagram of the system and representative images recorded with the system are presented in Figure **3-6**A-C a CW laser with a wavelength of 532 nm operates as the light source for the interferometer, and the sample was irradiated using a diode laser operating at 638 nm. The reference and sample beam were combined inside the $Bi_{12}SiO_{20}$ crystal operating at its drift regime, leading to the formation of a dynamic hologram detected by the photodetector. The resolution of the microscope was estimated to be ~ 5.3 μm. Despite offering a completely non-contact detection scheme for imaging rough tissue surfaces, the excitation exposure was 3 times higher than the safe limit for skin imaging which may impede its application to *in-vivo* studies.

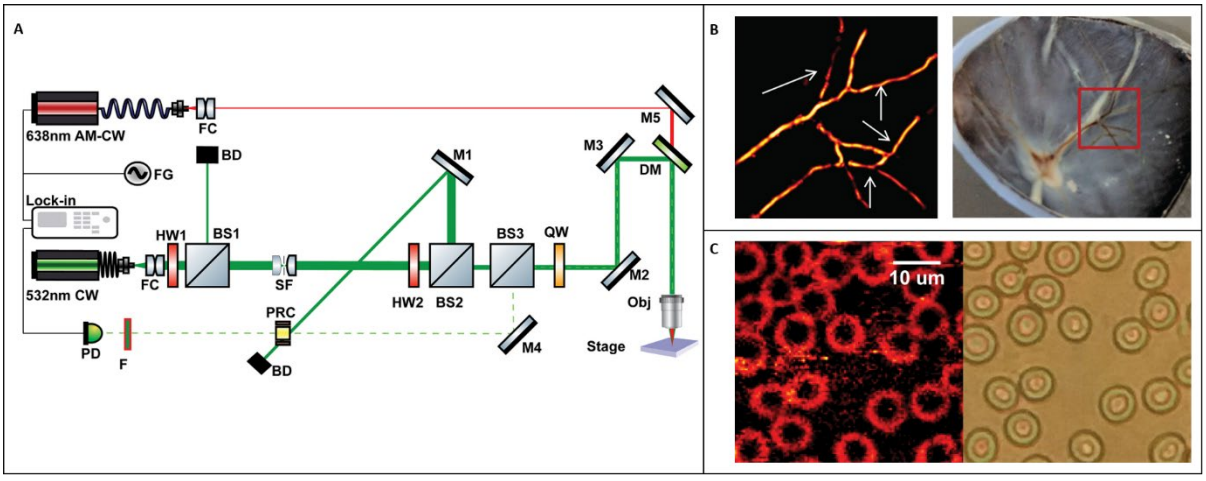

Figure 3-6. (A) Schematic of the PRC-based PAM system. FC: fiber optic collimator, M: Mirror, DM: dichroic mirror, QW: quarter-waveplate, OBJ: objective, BS: beamsplitter, HW: half-waveplate PRC: photorefractive crystal, BD: beam dump, PD: photodetector, F: laser line filter. (B) (left) PAM image of *ex-vivo* retinal samples, (right) Photograph of the sample. (C) (left)

photoacoustic image of blood smear showing RBC; (right) corresponding bright field image. Reprinted with permission from **[326]**.

3.6.2.2.2. Homodyne detection

Depending on the coherence length of the light source used, homodyne interferometers employed for PA detection, can be divided into low-coherence and long-coherence. When a single beam of light is split and interfered with itself, coherent edition will only occur for path lengths which are less than the characteristic coherence length of the source. For low-coherence light sources this is generally on the order of microns, whereas it can reach kilometers for a long-coherence source. Techniques which use low-coherence interferometers generally leverage this low coherence as a means of path length discrimination since the absolute length of a sample path can be determined against a reference path of known length down to single-micron scales.

Low-coherence devices. *For* these devices interference only occurs for path lengths on the scale of the coherence length. This effect can be leveraged to omit scattered signals arising from depths which are far away from the reference path length. The coherence length of typical light sources used in a low-coherence interferometer is on the order of micrometers, and when compared to nanometer scale photoacoustic induced surface displacement, the coherence length of the source is larger by three orders of magnitude. For such small displacements, the sensitivity of the interferometer depends on the initial phase of the system. Since an interference signal varies in a sinusoidal form, the highest sensitivity occurs when the initial phase is at the quadrature-point ($k\pi \pm \pi/2$) of the interferometer. However, it is difficult to maintain the quadrature-point consistently during the whole measurement period, as the system is sensitive to environmental perturbations such as vibration, and room temperature variation.

To overcome this problem, feedback methods are introduced, in which the optical phase of an interferometric signal is adjusted using a motorized stage[327] or by changing the laser wavelength[328]. These feedback methods may slow down the imaging speed or invoke other external perturbations due to the mechanical movement of the stage. Wang *et al.* [184] developed a synchronization detection method, in which only measurements made at quadrature points were analyzed. The system was used for *in-vivo* imaging of blood vessels within the mouse ear. The PA signals were detected in quasi non-contact approach from the oil layer on top of the sample; and the system's axial and lateral resolutions were measured as 60 μm and 30 μm, respectively. The imaging speed was highly limited by the 10 Hz pulse repetition rate of the excitation source, slow scanning mirror in the detection interferometer, and the synchronization system. Chen *et al.*[329] reported a PAM system using an all-fiber low-coherence interferometer. The imaging speed of the system was improved by a piezoelectric actuator driving the reference mirror of the interferometer. The imaging time of collecting one dataset was ~17 minutes which was much faster than the 10 hour imaging time reported by Wang *et al.* [184]. *In-vivo* images of mouse ear microvasculature with 11 μm lateral and ~ 20 μm axial resolution was demonstrated in quasi non-contact mode (Figure **3-7**A). A similar system was developed by Liu *et al.* [330] for PAT. The interferometer had a central wavelength at ~1300 nm and a spectral bandwidth of 46 nm; an axial and lateral resolution of 45 μm and ~15 μm was achieved, respectively for *in-vivo* imaging of mouse ear vasculature. Recently, Park *et al.*[183] employed the intrinsic phase difference of a multiport (3 × 3) interferometer to reconstruct the photoacoustic signal without suffering from the initial phase drift (Figure **3-7**B). The performance of the system was evaluated by imaging human

hairs embedded in polydimethylsiloxane resin block, and isometric resolution of ~ 85 µm over 1.5 mm imaging depth was reported. Generally, in an ideal 3 × 3 coupler, the return ports have an intrinsic phase difference of 120° to each other. Therefore, the quadrature component of the signal measured at one particular return port can be calculated using the measured signal at any other return port of the same coupler[331]. Moreover, the long-term variation of intrinsic phase difference in a 3 × 3 fiber-optic coupler is rather stable; and in it has slight effect on the displacement measurement [332]. The proposed system eliminated the need for any feedback components. However, the imaging speed was again highly limited by the low repetition rate of the excitation laser which prevented *in-vivo* experiments. In general, for a low-coherence interferometer the sensitivity decreases when the optical path difference (OPD) between two arms increases, and it turns to zero when the OPD is greater than the coherence length of the light source[98]. This might not be an issue for imaging thin samples like mouse ear and ex-vivo studies. However, while imaging thick samples or *in-vivo* experiments where motion is unavoidable, it would become a severe issue.

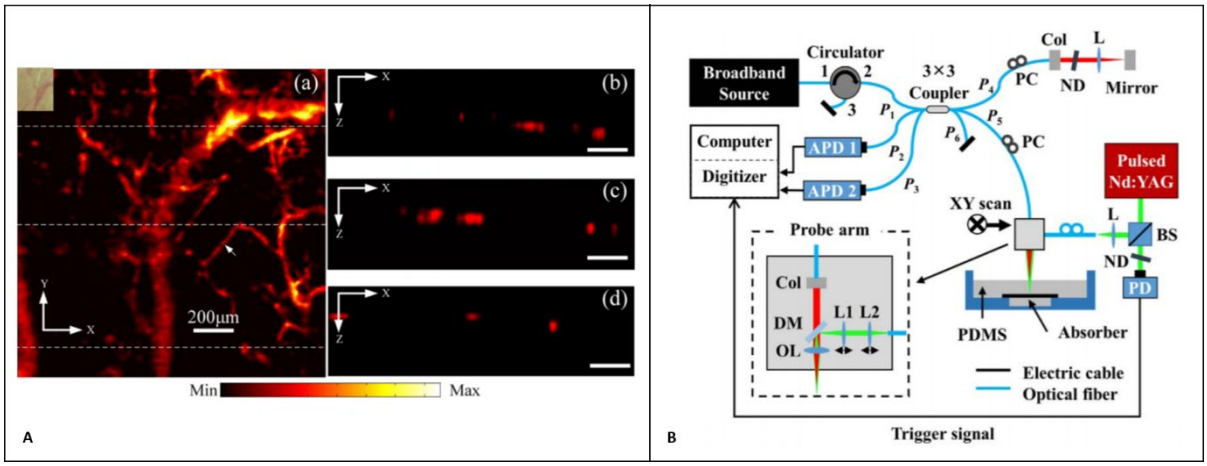

Figure 3-7. (A) In vivo photoacoustic image of microvasculature of a mouse ear. (a) Photoacoustic maximum intensity projection of the microvasculature of a mouse ear. The total time for obtaining the photoacoustic image is 16.7 min. Inset: photograph of the imaging area. (b)–(d) B-scan image of microvasculature corresponding to the three white dotted line in (a) Reprinted from **[329]**, with the permission of AIP Publishing (B) Schematic of the experimental setup. The probe beam and

the excitation beam are combined and scanned together. APD, avalanche photodetector; ND, neutral density filter; Col, collimator; BS, beam splitter; DM, dichroic mirror; L, lens; OL, objective lens; P, fiber-optic coupler port; PC, polarization controller; PD, photodetector, Reprinted with permission from **[183]**.

Long-coherence devices. To overcome the sensitivity dependence of low-coherence interferometers and to maintain constant sensitivity over a large dynamic range of OPDs, long-coherence interferometers can be used. Lu *et al.*[333] utilized a homodyne interferometer with ~ 17 mm coherence length along with a synchronization method to lock the system at its maximum sensitivity. The imaging was performed in quasi non-contact mode using a water layer on top the mouse ear, demonstrating *in-vivo* images of blood vessels. Images with and without a water layer on top of the sample are shown in Figure **3-8**A. It is clear that the water layer on the sample surface plays a crucial role in the method. Ma *et al.*[98] utilized a similar technology and developed a dual-modality imaging system combining spectral-domain OCT with PAM. The system was utilized for *in-vivo* blood flow assessment in the mouse ear. In the PAI subsystem, surface vibrations of the water layer on top of the sample were detected by a homodyne interferometer operating at 1310 nm with a 0.1 nm bandwidth. The vasculature in the mouse ear were imaged with normal and impeded blood circulations. The experimental results indicated that the integrated system could differentiate blood flow states and improved visualization of conditions such as hemorrhage (Figure **3-8**B). Wang *et al.*[185] recently employed a multiport (3 × 3) fiber coupler homodyne interferometer centered at 1310 nm with a coherence length of more than several hundred millimeters (Figure **3-8**C). The multiport interferometer eliminated the influence of initial phase and the phase perturbation from the environment. The intensity changes of the probe beam were used to reconstruct the photoacoustic images. The method offered several advantages including, freedom from the influence of the rough tissue surface and having a confocal configuration to focus both probe

light and excitation light at a common point below the sample surface. The system demonstrated *in-vivo* imaging of the blood vessels of a mouse ear with an excitation fluence well within the ANSI MPE limits (Figure **3-8**D). In general, long coherence devices may suffer from unwanted interferences due to reflection from the optical components and sample structures.

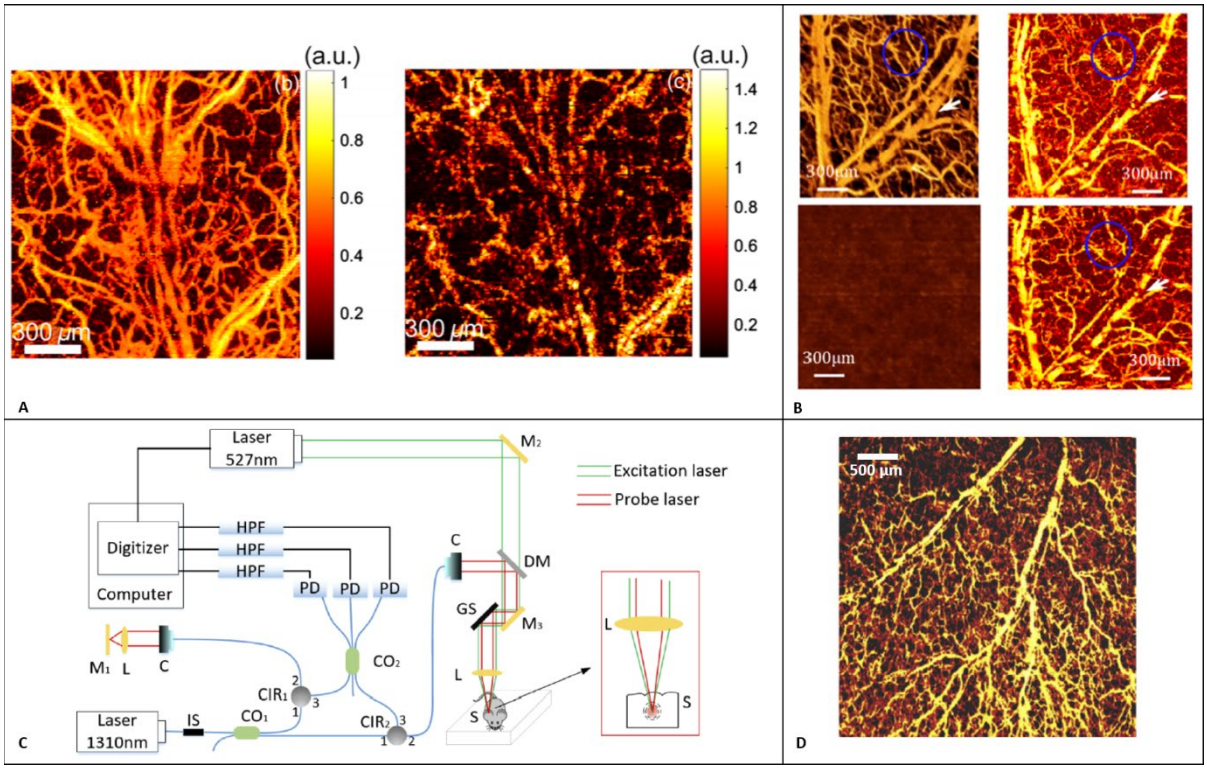

Figure 3-8. (A) In vivo photoacoustic images of blood vessels in the mouse ear (left) with and (right) without water layer on top, Reprinted with permission from **[333]**. (B) differentiation of blood flow states with the dual-modal system. (left) En-face microvasculature image of OCT angiography, (right) photoacoustic image of mouse pinna, (top) images with blood flow, (down) images with blood flow blocked, Reprinted with permission from **[98]**. (C) Schematic of the multiport photoacoustic imaging system. Reprinted with permission from **[185]** (D) Photoacoustic MAP image acquired *in-vivo* from mouse ear. Reprinted with permission from **[185]**.

The interferometric detection of photoacoustic signals has several significant technical limitations. First, the rough tissue surface dramatically affects the quality of the image when directly measuring the vibration of the tissue surface. This motivates the use of a water/oil layer on the surface of the sample. Secondly, in most of these methods except the one proposed

by Wang *et al.*[185], the probe beam is focused on the surface of the sample or water layer, while the excitation beam was focused below the surface. This requires elaborate adjustment of the probe beam, making it difficult to perform *in-vivo* imaging due to the uneven surface of the tissue and motion of the sample. Finally, to maintain the interferometric system at its highest sensitivity, complicated phase stabilization techniques are required, which sacrifice the imaging speed, and limited success could be achieved in well-controlled lab settings[334].

3.6.3. Photoacoustic remote sensing (PARS)

Photoacoustic remote sensing (PARS) was first introduced by Haji Reza *et al.* in 2017 for non-contact non-interferometric detection of photoacoustic signals [335]. Similar to conventional PAI, PARS employs a nanosecond pulsed laser to excite ultrasonic pressures in biological tissues. Unlike other PAI modalities, in PARS the ultrasound transducer is replaced with a second detection laser, which is co-focused with the excitation laser on the sample. The back-reflected beams from the sample are directed towards a photodiode. A long-pass filter is typically placed before the photodiode to block any excitation light and to ensure the detector only measures the detection laser's intensity. If only the detection laser is incident on the sample, the reflected light would have a constant intensity (effectively a DC signal). As an excitation pulse is applied, a small and rapid oscillation is found to be imposed on the back-reflected light. Therefore, the photodiode voltage output is typically high pass filtered to only extract these rapidly oscillating signals and reject the scattering signals. A simplified system diagram of a PARS system is provided in Figure 3-9.

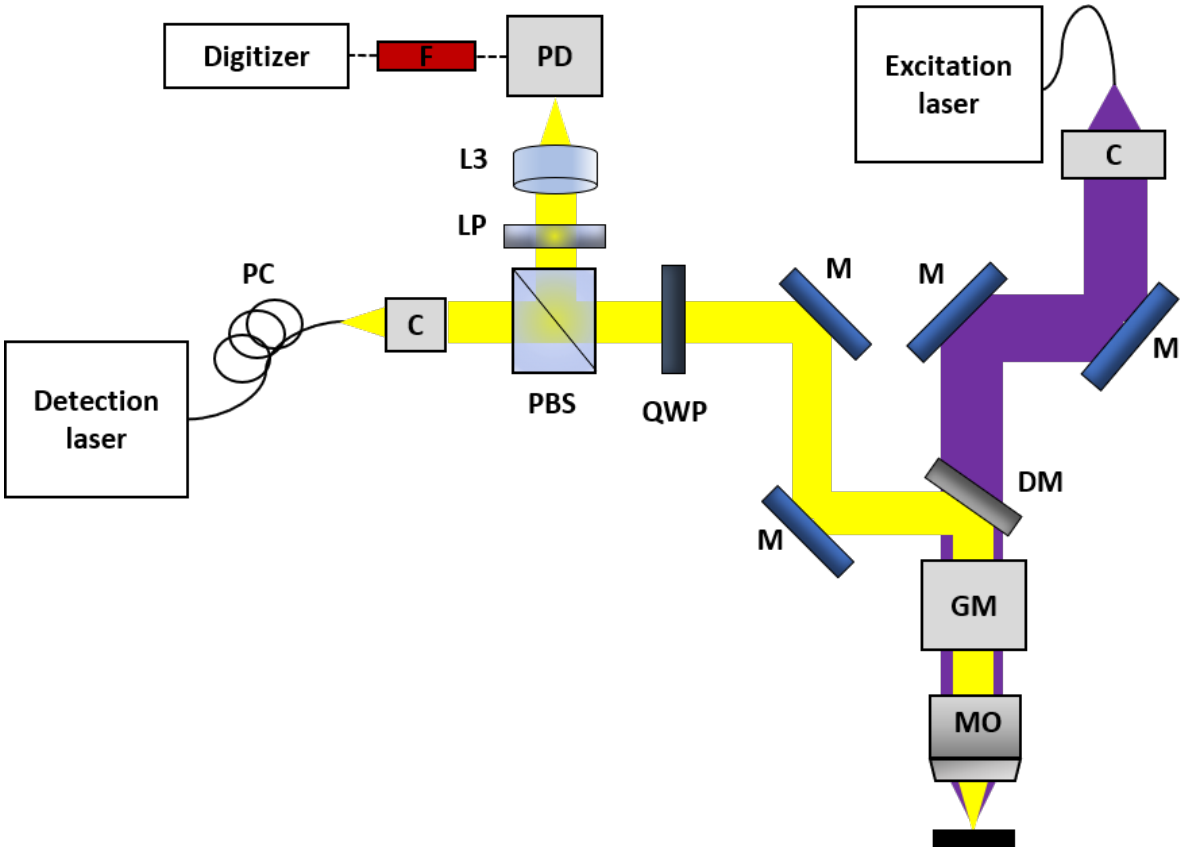

Figure 3-9. simplified schematic of PARS microscopy. F: Filter, PD: Photodiode, LP: Long pass filter, PBS: Polarized beamsplitter, QWP: Quarter waveplate, M: Mirror, DM: Dichroic mirror, C: Collimator, L: Lens, MO: microscope objective, PC: Polarization controller, GM: Galvanometer mirror.

In PARS, the thermoelastic pressure and temperature rise induced by both the excitation and detection beams contribute to the optical absorption and the final signal. By propagating through the sample, they modulate the refractive index of the medium due to the elasto-optic effect[336]. The change in refractive index leads to a change in reflectivity of the sample, which can be observed as fluctuations in the back-reflection intensity of the detection laser. For the case of normally incident light, the reflectivity R, can be calculated using Fresnel equations as $R = |\frac{n_1-n_2}{n_1+n_2}|^2$ where n_1 and n_2 are refractive indices of two media within the tissue. Assuming the excitation laser is incident on an object whose index of refraction is n_1, we can express a slight perturbation in its refractive index as $n_1 + \delta n_1$. The reflectivity can now be

described as R′=$|\frac{n_1+\delta n_1-n_2}{n_1+\delta n_1+n_2}|^2$. As PARS only measures the resulting transient oscillations, we can express the change in reflectivity as $\Delta R = R - R'$. This can be shown to be $\Delta R = \propto \delta(n_1 - n_2)$[335]. The key insight is the fact that the PARS effect is amplified if there is an existing refractive step between the media. Without this pre-existing refractive index contrast, the reflectivity change is subtle. Though this may seem to be of little use in practice, scattering and optical absorption contrast exists prevalently throughout biological tissue. Subsequent works extended this model to include temporal and spatial dimensions[337], [338].

Over the short period of time, PARS has demonstrated its potential for high-resolution *in-vivo* imaging of microvasculature structures [335], deep sensing capabilities [339], label-free histology imaging [340]–[342] and functional imaging [339]. Images acquired *in-vivo* from single red blood cells, oxygen saturation mapping, and deep-vasculatures are presented in Figure **3-10**. Oxygen saturation measurement was achieved by utilizing spectra generated using stimulated Raman scattering (SRS) in a single mode fiber. Additionally, a fully fiber-tetherable design of the system for real-time functional imaging was reported, and characterized by estimating blood oxygen saturation in blood-flow phantoms and with *in-vivo* mouse ear microvasculature[343].

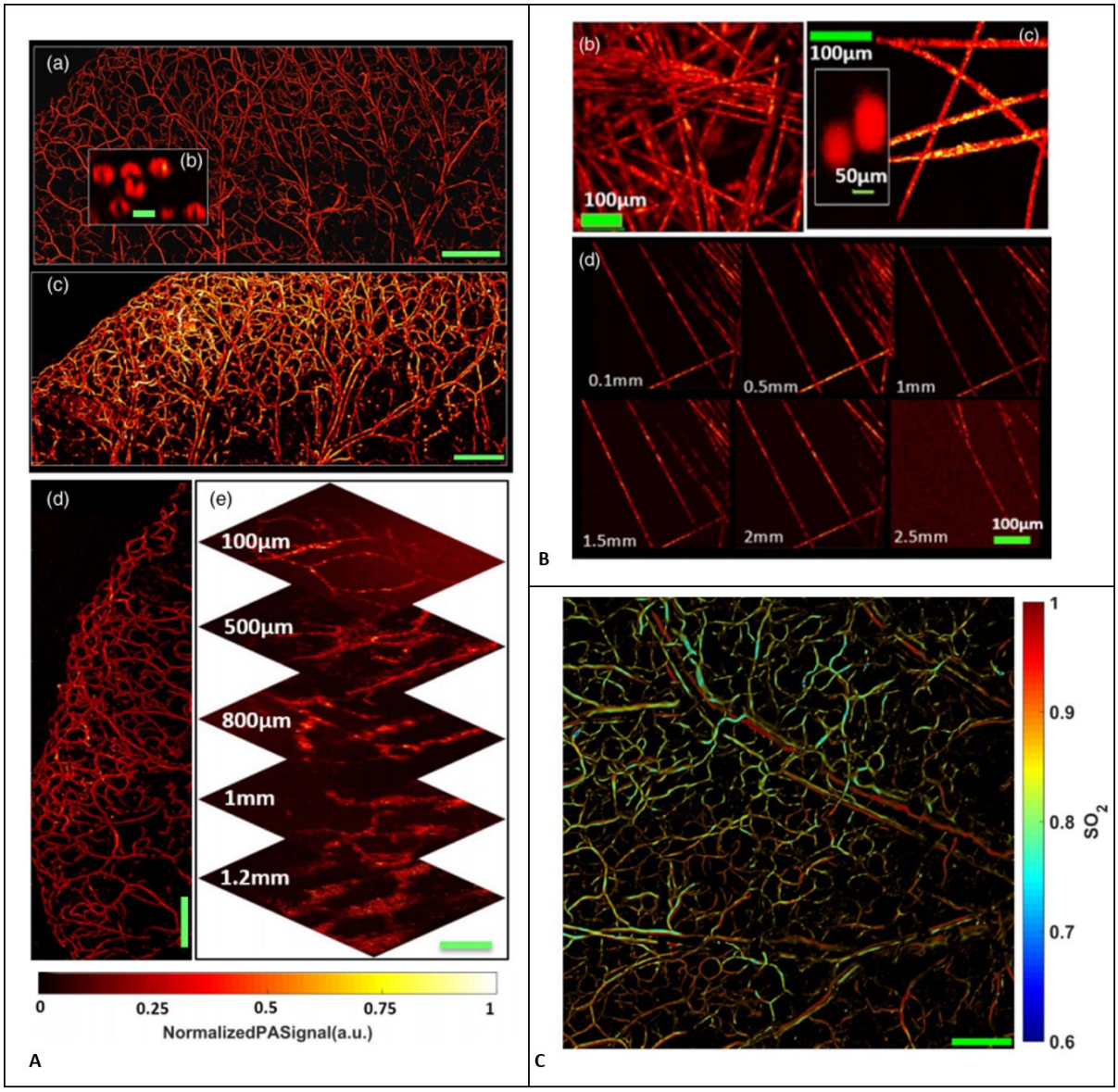

Figure 3-10. (A) In vivo PARS microscopy structural images. (a) Image of en face microvasculature in mouse ear using the high-resolution mode (Scale bar: 500 µm) (b) *In-vivo* image of red blood cells in the mouse ear using the high-resolution mode (Scale bar: 5 µm) (c) Image of mouse ear vasculature using the deep-penetrating mode (Scale bar: 500 µm) (d) Image of en face microvasculature in the tip of a mouse ear using the high-resolution mode (Scale bar: 500 µm) (e) Images of back flank of mouse at various depths using the deep penetrating mode (Scale bar: 100 µm) (B) Image of carbon fiber networks using the deep penetrating imaging mode. (c) Image of carbon fiber networks using the high-resolution imaging mode, as well as an inset image of 100-nm gold nanoparticles. (d) Images of carbon fiber networks at various depths in tissue-mimicking solution. (C) Functional images SO2 measurement of en face microvasculature in the ear of an 8-week-old nude mouse. Reprinted with permission from **[339]**.

Recently, Ecclestone *et al.* [340], [344], [345] utilized the UV absorption peak of DNA to visualize cell nuclei and bulk tissue structure. Representative images of one-to-one comparison

of PARS histological imaging and H&E staining in human breast tissue are presented in Figure **3-11**.

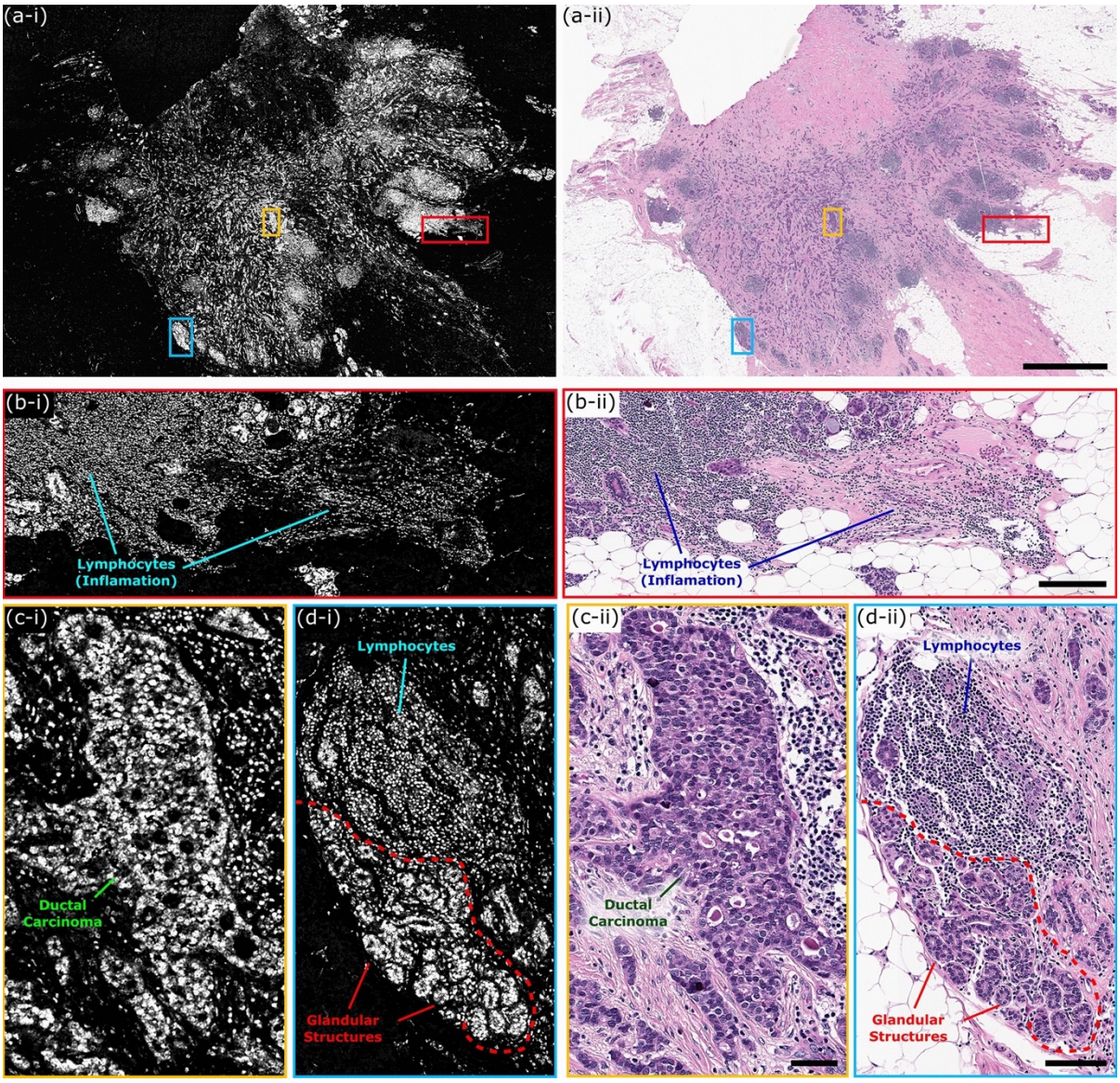

Figure 3-11. One to one comparison of PARS histological imaging and H&E staining. (a) Large field of view (9 mm × 13.25 mm) PARS (780 megapixel) image of nuclear morphology in a thin section of formalin fixed paraffin embedded excised breast tumor tissues. (b–d) (i) Subsections of the large field of view PARS image (a) highlighting regions of interest within the large field scan. (ii) Images of the exact same set of tissues following H&E staining, providing a direct one-to-one comparison between PARS imaging of tissues and the gold standard for histopathology H&E imaging. (a) Scale Bar: 2 mm. (b) Scale Bar: 200 µm. (c) Scale Bar: 50 µm. (d) Scale Bar: 75 µm. Reprinted with permission from [344].

In general, the all-optical detection scheme applied in PARS presents several benefits over previously discussed approaches:

i. PARS usually employs an optical confocal geometry between the excitation and the detection lasers. This confocal geometry is significantly simpler than the conventional OR-PAM devices and does not require additional components between the microscope objective and the target[334]. This all-optical confocal geometry enables high-resolution imaging in a reflection-mode architecture.

ii. The all-optical confocal geometry also eliminates the need for acoustic coupling and provides non-contact detection of photoacoustic pressures. This non-contact detection scheme minimizes the risk of infection in clinical settings and does not require the apparatus to be submerged in water.

iii. The PARS confocal detection mechanism measures the initial pressures and temperature rise local to the targeted absorber. These initial pressure waves dissipate in a few hundred nanoseconds and allow for significantly faster imaging speeds compared to conventional PAI system, potentially in the range of tens of megahertz [81]. However, conventional PAI devices typically require waiting for a minimum interval of time for the ultrasonic pressure waves to propagate through the tissue. The minimum time interval is dependent on the speed of sound in the tissue and the image depth. Assuming that the average speed of sound in the tissue is 1540 mm/s [82], it will take the acoustic waves about 0.65 μs to propagate over an imaging depth of 1 mm. Therefore, the maximum imaging rate is 1.5 MHz. If an excitation pulse is applied before this minimum time interval, acoustic waves within the sample can potentially interfere with each other and degrade the image quality.

iv. Like other PAI devices, PARS takes advantage of intrinsic optical absorption to visualize contrast and does not require the use of exogenous chromophores. This label-free imaging modality can be deployed in clinical settings and may not require special control measures and precautions.

v. The all-optical imaging mechanism enables PARS to be combined with other imaging modalities to capture additional contrasts and yield additional diagnostic information to the clinicians. The all-optical imaging design also enables to be miniaturized to an endoscope and visualize absorption contrast deep within the body.

Employing PARS, the next chapter investigates the application of PARS for non-contact ophthalmic imaging applications. This is the first time a non-contact photoacoustic imaging has been used for *in-vivo* imaging of the eye.

Chapter 4

Photoacoustic remote sensing microscopy for ophthalmic imaging

Notes and Acknowledgement

This chapter summarizes results from a study that showed the first label-free, non-contact, *in-vivo* imaging of the ocular vasculature using a photoacoustic imaging technique. Both anterior and posterior segments of mouse eye were imaged in this study. The content of this chapter is based on the following journal manuscript:

Zohreh Hosseinaee, Layla Khalili, James A. Tummon Simmons, Kevan Bell, and Parsin Haji Reza, "Label-free, non-contact, in vivo ophthalmic imaging using photoacoustic remote sensing microscopy," Opt. Lett. 45, 6254-6257 (2020)

Author contributions

Zohreh Hosseinaee co-designed with supervisor the optical system for PARS suitable for imaging the eye, prepared and ordered the optical and digital components of the system, constructed the PARS system, conducted the experiments, processed the images, contributed to interpreting the data, prepared the figures, and wrote the main manuscript.

James A. Tummon Simmons helped in constructing the PARS system.

Kevan Bell helped with hardware and software of the PARS system.

Layla Khalili assisted with animal imaging experiments.

Parsin Haji Reza conceived the study, contributed to the interpretation of all results, and acted as the primary investigators.

All authors contributed to the final version for publication.

4.1. Introduction

Ophthalmic imaging has long played an important role in the understanding, diagnostic and treatment of a wide variety of ocular disorders. Currently available clinical ophthalmic imaging instruments are primarily optical-based, including slit-lamp microscopy, fundus photography, confocal microscopy, scanning laser ophthalmoscopy and optical coherence tomography (OCT). Despite offering valuable structural and morphological information from ocular tissue, these modalities have limitations providing detailed functional and molecular characteristics of the eye[11]. Access to this information would help with early diagnosis and consequently facilitate the treatment of major eye diseases including age related macular degeneration, glaucoma and diabetic retinopathy[103].

Photoacoustic microscopy (PAM) is among the most rapidly growing optical imaging modalities. The technology is well-known for its practical functional and molecular imaging capabilities. Its unique imaging contrast of optical absorption makes PAM the preferred modality for a wide range of biomedical applications[47]. In ophthalmic imaging, PAM has been used for visualizing hemoglobin and melanin content[216], measuring blood oxygen saturation[349], and quantifying metabolic rate of oxygen in the ocular tissue[106]. Even though PAM offers high sensitivity, unique imaging contrast, and high resolution, it is not generally an all-optical imaging method unlike the other ophthalmic microscopy techniques. One of the significant limitations of photoacoustic microscopes in ophthalmic applications arises from their need to be in physical contact with the sample through a coupling media. This physical contact, coupling, or immersion of the sample is undesirable in ophthalmic applications. It may increase the risk of abrasion, infection, and patient discomfort.

Additionally, involuntary eye movements may affect the coupling efficiency and degrade image quality. In small animal imaging, immersion in water significantly complicates the procedure and commonly results in sacrificing the animal[241].

To overcome the limitations of contact-based PAM devices, in 2017 Haji Reza et. al developed photoacoustic remote sensing (PARS) microscopy for non-contact, non-interferometric detection of photoacoustic signals[335]. The technology has proved its potential over a short period of time in various biomedical applications such as label-free histology imaging[341], [342], SO_2 mapping and angiogenesis imaging[339]. Here, we have successfully extended the application of PARS microscopy for non-contact photoacoustic imaging of ocular tissue. This has been a long-lasting desire in the field of photoacoustic ophthalmoscopy[350]. In this study, we present the first real-time, *in-vivo,* non-contact photoacoustic imaging of the eye. To make this possible, we made significant modifications to make PARS microscopy suitable for ophthalmic imaging. These modifications include employing, eye-friendly 830 nm detection wavelength, suitable scanning pattern and interpolation algorithm, focusing optics and live feedback during *in-vivo* imaging. The 830 nm probe beam improves photoacoustic signal detection in the ocular environment by having lower absorption in water. Additionally, it reduces the amount of chromatic aberration in the system by having close spectral bandwidth to the 532 nm excitation beam. The PARS microscope reported in this study, for the first time has employed a telecentric pair, which provides a uniform image intensity and improves the effective imaging field of view (FOV) of the optical scanning. We have also showed the first live feedback imaging in the eye which is beneficial for accurate alignment and to select the right imaging location. The system is used

for imaging different regions of the ocular tissue including, iris, scleral and retinal vasculature. To best of our knowledge this is the first study showing non-contact photoacoustic imaging conducted on ocular tissue.

4.2. Method

Figure **4-1** illustrates the experimental setup used in this study. The excitation source is 532-nm 1 ns pulse-width, ytterbium-doped fiber laser (IPG Photonics) capable of pulse repetition rates from 20 kHz to 600 kHz. The detection arm uses an 830-nm Superluminescent Diodes with 20 nm full width at half maximum linewidth (SLD830S-A20, Thorlabs). The output end of the fiber is coupled to a collimator. A polarized beam splitter is used to transmit the majority of the forward light onto a quarter wave-plate, which transforms the linearly polarized light to circularly polarized light. The detection and excitation light are then combined using a dichroic mirror. The co-aligned beams are then directed toward a large beam galvanometer scanning mirror system (GVS012/M, Thorlabs, Inc.) driven by a two-channel function generator. The beams are then directed to a set of 1:1 telecentric pair that provides uniform image intensity and improves the effective FOV. A 0.26 NA refractive objective co-focused the beams onto the sample. The back-reflected light from the sample is collected via the same objective lens and guided towards the detection path. The quarter wave-plate transforms the reflected circularly polarized light back to linearly polarized light. This enables the polarized beam splitter to direct the back-reflected light towards the photodiode. A long-pass filter (FELH0800, Thorlabs Inc.) is used to block any residual 532 nm light. The 830 nm signal is then focused onto the photodiode with an aspherical lens. The photodiode is connected to a high-speed digitizer (CSE1442, Gage Applied, Lockport, IL, USA). A point acquisition is

acquired for each pixel and recorded by the digitizer. Each point acquisition is converted to an intensity value by computing its maximum amplitude and plotted at its respective location in the image.

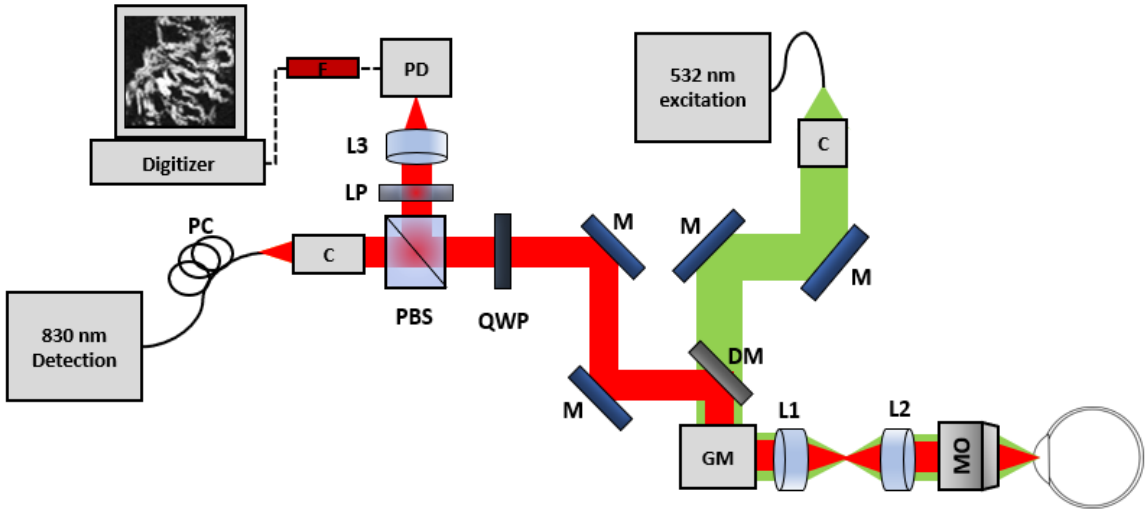

Figure 4-1. Schematic of the PARS microscopy system.

4.3. Results

The performance of the system was first tested on 7 µm carbon fiber networks at ~1 mm depth in water and representative images are shown in Figure **4-2** A-C. The images were acquired using ~ 900 pJ excitation pulse energy and ~ 2 mW interrogation power on the sample. The black strips in Figure **4-2**B&C is resulted from the shadow of the carbon fibers located on top of the depth of focus (white arrows). The signal-to-noise ratio (SNR), defined as the average of the maximum amplitude projection pixels in a region of interest (dashed yellow rectangles in Figure **4-2**A) over the standard deviation of the noise (dashed white rectangles in Figure **4-2**A), was quantified as 56 ± 3 dB. The SNR measurement was performed in four different regions of the image to quantify the deviation.

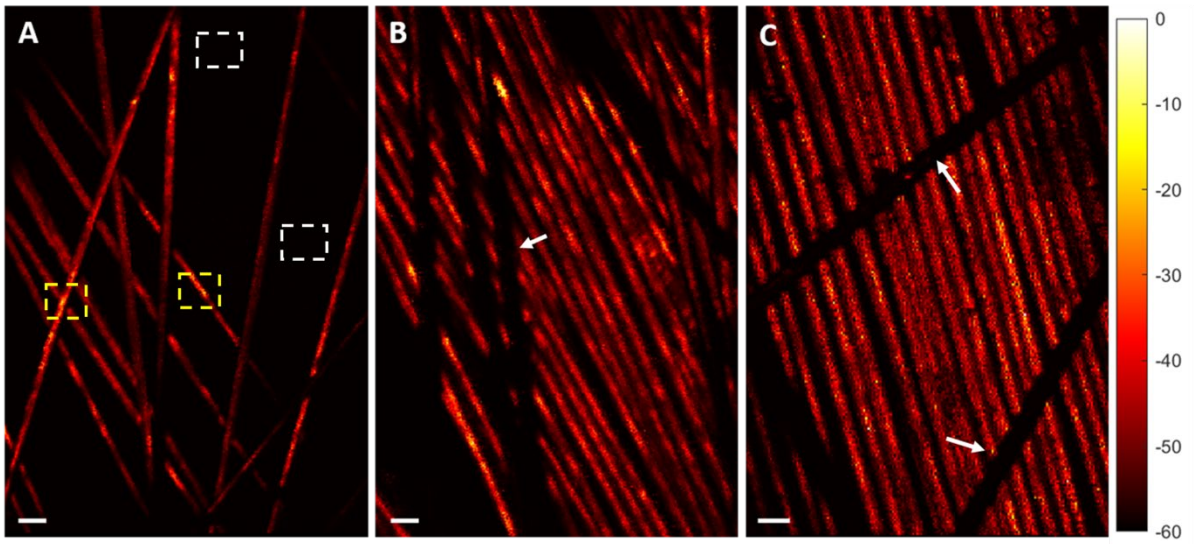

Figure 4-2 (A-C) Images of carbon fiber networks at ~1 mm depth in water acquired using PARS microscopy. The dashed yellow rectangles in (A) depict the regions for measuring the maximum amplitude and the dashed white rectangles show the region for measuring the standard deviation of the noise. Scale bar: 30 µm.

To demonstrate the *in-vivo* capabilities of the system the ear of a nude mouse (NU/NU, Charles River, MA, USA) was imaged. All of the experimental procedures were carried out in conformity with the laboratory animal protocol and was approved by the Research Ethics Committee at the University of Waterloo. A custom-made animal holder was used to restrain the animal. The base of the animal holder was lined with a thermal pad in order to keep the mouse body temperature between 36° and 38°C. Artificial tears were used frequently (~ every 5 minutes) to keep the cornea hydrated. Vital signs, such as respiration rates, heart rates and body temperature were monitored during the experiment. All of the 2D images shown in this manuscript were formed using a maximum amplitude projection (MAP) of each A-scan as a pixel in a C-scan en-face image. All images shown in this manuscript were produced by direct plotting from interpolated raw data using a Delaunay triangulation interpolation algorithm[351]. All images and signal processing steps were performed in the MATLAB

environment. Frangi vesselness filter was applied on the vasculature images[352]. Scale bars in the FOV were calibrated using a 1951 USAF resolution test target. Figure **4-3** demonstrates in-vivo PARS images of en-face microvasculature in the ear. Images were acquired with 20 kHz pulse repetition rate (PRR) of the excitation laser. The FOV covered in Figure **4-3**A is 1 mm × 1 mm, and it took ~7 seconds to acquire the image. Figure **4-3** B. was recorded from the same area with a smaller FOV of 500 µm × 500 µm, red blood cells within the capillaries can be clearly seen in this image (~ 7 seconds). The lateral resolution of the system for *in-vivo* experiment was measured ~ 2.6 µm. The lateral resolution of *in-vivo* ear and eye imaging was measured using edge spread function of the vessels as explained in [353]. The measured pulse energy at the sample surface was measured as ~ 50 nJ and the detection power was ~ 4 mW. The SNR of the large vessels was measured as approximately 41 ± 4 dB.

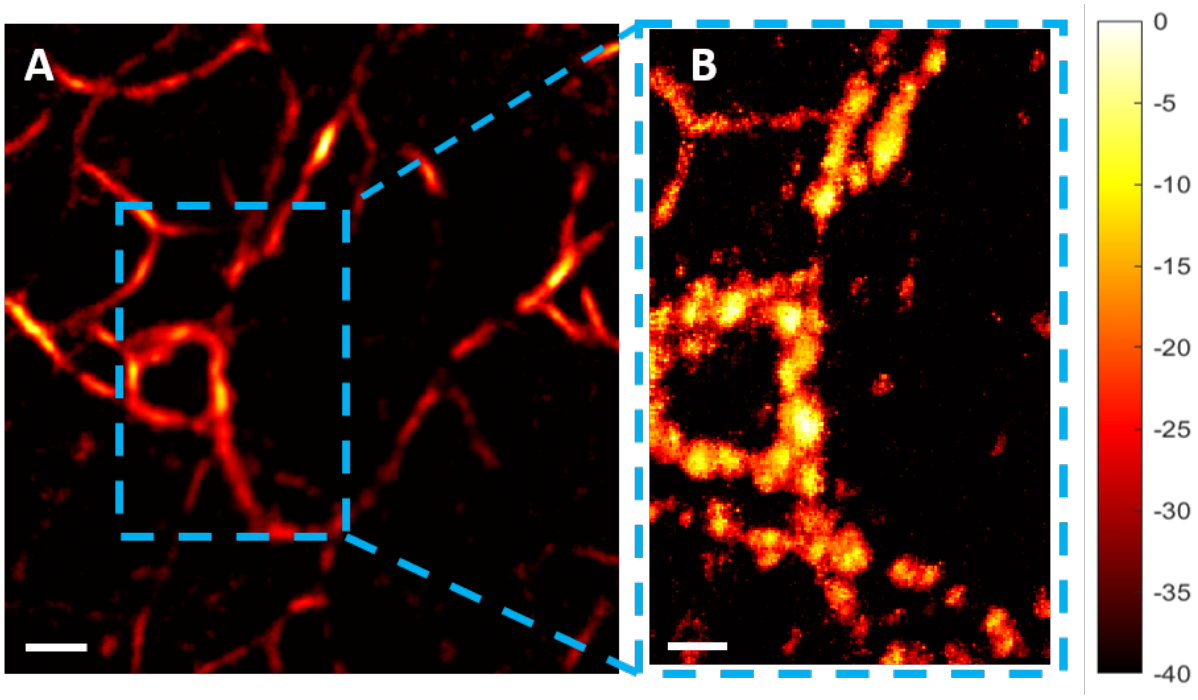

Figure 4-3 *In-vivo* imaging of mouse ear using PARS microscopy (A) Scale bar: 100 µm. (B) Scale bar: 15 µm.

For the eye imaging experiments, the repetition rate of the excitation laser was increased to 100 kHz to reduce the effect of motion artifacts. Both iris and retinal vasculature were imaged *in-vivo* in the mouse eye. The lateral resolution of the system for *in-vivo* eye imaging experiments was measured as ~ 2.6 μm. In the current design of PARS microscopy, the axial resolution is defined by optical sectioning. This has been measured to be equal to the depth of focus of imaging optics, which in this case is equal to ~ 40 μm. Since the ocular media are clear, optical scattering is not a major concern for imaging retinal vasculature in the mouse small eyeball. Therefore, imaging the retinal vasculature was possible with current setup and the imaging depth of the system was measured to be ~ 3 mm corresponding for the size of the mouse eyeball. The SNR of large vessels was measured as approximately 37 ± 3 dB. Figure **4-4** depicts representative images acquired from iris and retinal vasculature within different FOVs. Figure **4-4** A. represents an image acquired from the vasculature in the peripheral iris, covering an area of ~ 3 mm × 3 mm, and it took ~ 4 seconds to record the image. The enlarged capillary networks represented in the blue region is shown in Figure **4-4** B. Figure **4-4** C. is recorded from the vasculature of the inner iris, and Figure **4-4** E. shows the enlarged vessels of the area in the green rectangular region. Since the employed objective lens of the system has long enough working distance (~ 30 mm) compared to the diameter of mouse eyeball (~3 mm), imaging the retinal vasculature was also possible using the current setup. Figure **4-4** D & F show representative images acquired from retinal vasculature. Both detection and excitation beams were sent through the central part of the anterior segment to back of the eye. The reflected signals coming from the retinal vasculature were detected to form the images. Additionally, live imaging of vasculature near the limbal and episcleral region was acquired

during manual depth scanning over ~ 150μm imaging depth. Snapshots acquired from the video are presented in Figure **4-4**G. To maintain higher real-time speed, a more basic scatter point interpolation was used, which resulted in lower resolution compared to single captures. Currently, depending on the resolution and FOV, live imaging operates between 1-4 frames per second. The live imaging was used constantly during the imaging session to enable accurate alignment and focusing to select the right location. Unlike other pre-clinical imaging techniques[354], [355], in these experiments to mimic real world situation for clinical applications, the head of animal was not fixed and no tropical anesthesia or pupil dilation was applied to the eyeball. Therefore, motion artifacts are still presented in the images, for example, in Figure **4-4** A., these motion artifacts resulted in out of focus and losing PARS signal from part of the iris.

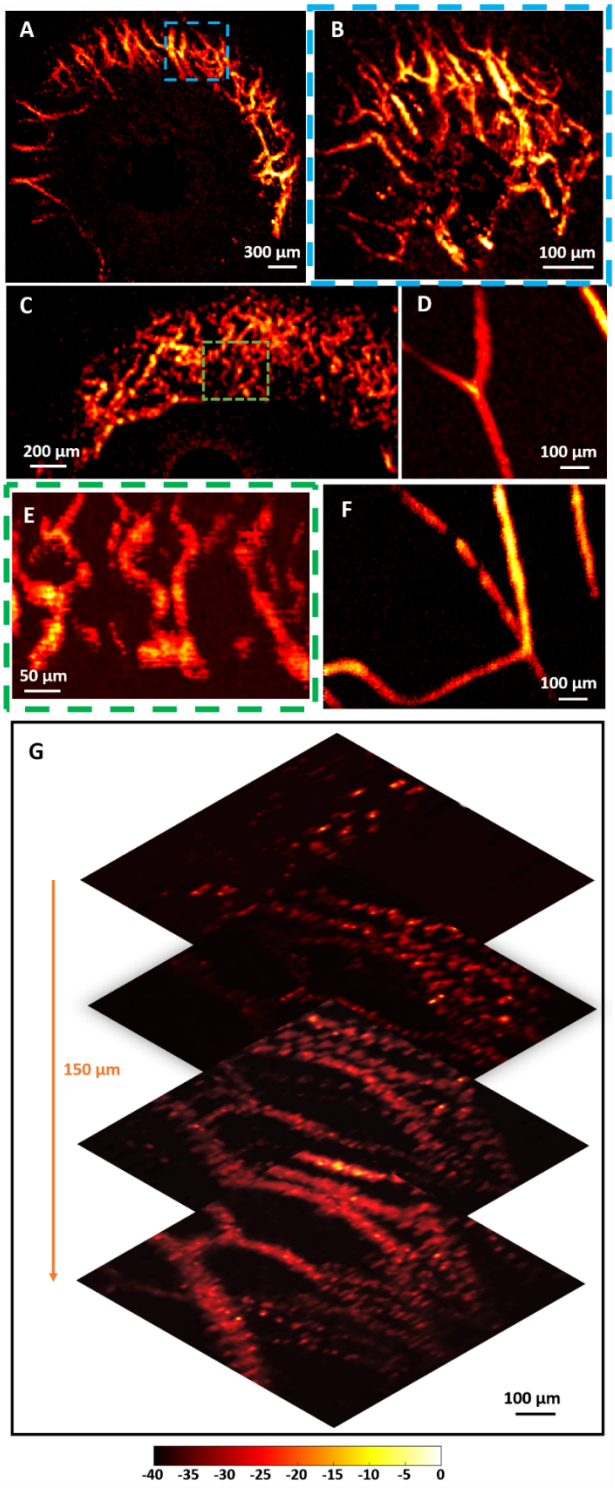

Figure 4-4 *In-vivo* imaging of ocular vasculature within different FOVs. (A) image acquired from the vasculature in the peripheral iris, covering an area of ~ 3 mm × 3 mm. (B) The enlarged capillary networks in the blue region. (C) Vasculature of the inner iris. (E) Enlarged vessels of the green rectangular area. (D & F) Images acquired from retinal vasculature. (G) Snapshots acquired from the live video acquired during imaging.

Light safety is an important factor to consider in ophthalmic imaging. In the eye imaging experiments, reasonably good images were formed with the minimum excitation pulse energy of ~ 50 nJ and ~ 4 mW detection beam power. The ocular maximum permissible exposure (MPE) depends on the optical wavelength, pulse duration, and exposure aperture. For a single laser pulse at 532 nm, the MPE should not exceed 5×10^{-7} J/cm^2; which corresponds to maximum pulse energy to be 200 nJ, assuming the size of a typical dilated human pupil to be 7 mm in diameter[356] . The 50 nJ laser pulse energy used in the experiment is well within the ANSI safety limits and the 160 nJ safety limit reported in [164]. The ~ 4 mW detection power is also within the ANSI safety limits for imaging human eye [357], [358]. In addition, for exposure duration longer than 1 seconds, eye movements redistribute the light over larger retinal areas, and decreases the retinal irradiance and thus the risk for injury [357]. In this study, depending on FOV, number of collected data points for each image, resolution, and duration of recorded PARS signal, the image acquisition time (different than live feedback speed) varies between 1 - 4 seconds. This helps to reduce the risk of ocular damage. Even though the employed values are within the ANSI safety limits of the previously reported methods, in the future an intensive study will be performed to analyze and improve the safety of the proposed system for clinical trials.

4.4. Discussion and Conclusion

There are several aspects that can be further refined for future studies. Unlike other OR-PAM systems that use mechanical scanning [359], [360] the reported system employs optical scanning using galvanometer mirrors. Even though, optical scanning enables the high imaging speed required for live feedback and real-world applications, the FOV of the current setup is

limited to 3 mm × 3 mm. The achieved FOV is not enough for capturing the full retina vasculature network in the rodent eye. To improve the FOV, we plan to employ customized scan lens. Moreover, we plan to apply multi-wavelength PARS to assess the blood oxygen saturation in both anterior and posterior segments of the eye in rodent models. Since PARS is an all-optical imaging system, it can naturally be combined with all other all-optical imaging systems such as OCT. We can potentially integrate optical coherence tomography to image with both scattering and absorption contrast and acquire volumetric images of the eye structure and vasculature.

To achieve functional PARS imaging combined with OCT, one of the important requirements is to provide a multiwavelength light source with enough pulse energy at each wavelength and high pulse repetition rates. Currently available multiwavelength light sources for functional photoacoustic studies are usually based on optical parametric oscillator (OPO) or dye lasers. Unfortunately, they are both expensive, bulky, and more importantly they have low pulse repetition rates (PRR) that severely compromise image acquisition speed for *in-vivo* imaging applications. In the next chapter, we propose a method for achieving temporally stable multiwavelength light source with enough pulse energy and high PRR for *in-vivo*, functional photoacoustic imaging applications and demonstrate the performance of the light source for functional PARS imaging.

Chapter 5
Functional photoacoustic remote sensing microscopy using stabilized temperature-regulated stimulated Raman scattering light source

Notes and Acknowledgement

This chapter summarizes results from investigation on the effect of temperature on the temporal stability and spectrum of stimulated Raman scattering (SRS) occurring inside single-mode silica fibers. The study is performed at temperature levels of 195 K, 273 K, and 300 K. The results suggest that a decrease in temperature causes an improvement of temporal stability of the output, considerable rise in the intensity of the SRS peaks, and significant increase of SRS cross section. The application of the method is shown for in vivo functional imaging of capillary networks in chicken embryo chorioallantois membrane using photoacoustic remote sensing microscopy. The content of this chapter is based on the following journal manuscript:

Zohreh Hosseinaee, Benjamin Ecclestone, Nicholas Pellegrino, Layla Khalili, Lyazzat Mukhangaliyeva, Paul Fieguth, and Parsin Haji Reza, "Functional photoacoustic remote sensing microscopy using a stabilized temperature-regulated stimulated Raman scattering light source," Opt. Express 29, 29745-29754 (2021)

Author contributions

Zohreh Hosseinaee co-designed with supervisor the optical system for PARS, collected background information on the topic, conducted the experiments, collected the data, processed the PARS data, prepared the figures, and wrote the main manuscript.

Benjamin Ecclestone helped with processing the data and conducting the experiments.

Nicholas Pellegrino developed and implemented the signal unmixing method.

Layla Khalili and **Lyazzat Mukhangaliyeva** developed the chicken embryo model.

Paul Fieguth contributed to the interpretation of the results and provide guidance.

Parsin Haji Reza proposed the idea, conceived the study, contributed to the interpretation of all results, and acted as the primary investigators.

All the authors reviewed the manuscript.

5.1. Introduction

Photoacoustic microscopy (PAM) is among the most rapidly growing optical imaging techniques. This modality is well-known for its practical functional and molecular imaging capabilities [202]. PAM has the unique imaging contrast of optical absorption and is the preferred modality for a wide range of biomedical applications [47], [186]. This technology has been applied to many clinical and pre-clinical applications including but not limited to functional brain imaging, measurement of the oxygen consumption rate of a tumor, imaging of lipid-rich samples [361], and detection of circulating melanoma cells[220], [362]. Functional photoacoustic measurements (e.g., blood oxygenation) require a tunable wavelength excitation laser that can target multiple chromophores inside the tissue [51]. Optical parametric oscillators (OPOs) and dye lasers are commonly used for functional photoacoustic studies [217], [363]. In addition to being expensive and bulky, these tunable laser systems typically have low pulse repetition rates (PRR) that severely compromise image acquisition speed for in vivo imaging applications (10 Hz – 10 kHz) [364]. For example, in ophthalmic applications, where functional imaging could help with early diagnosis of major blinding diseases, imaging speed is a critical parameter [11]. Conventionally, OPO lasers have been used for photoacoustic ophthalmoscopy, however, their low PRR would result in long acquisition time which is not compatible with clinical applications [165]. In contrast, the high speed offered by tunable SRS sources, may improve imaging time by several orders of magnitude, mitigating image artifacts due to involuntary eye motion [365].

Stimulated Raman scattering provides a simple, cost-effective technique that has been widely used to create multispectral pulsed sources with high PRR [366], [367]. SRS is a

nonlinear optical effect that generates one or more Stokes wavelengths downshifted from the frequency of the pump laser [368]. This phenomenon occurs when the light intensity inside a non-linear medium reaches a certain threshold level [369]. In multispectral photoacoustic imaging applications, silica fibers are typically used as the SRS medium. Here, if the peak power of the pump light is strong enough, cascading Raman shifts will occur (spaced at 13.2 THz), generating higher-order Stokes waves [362]. In 2011, Koeplinger et al. demonstrated the first application of the method for photoacoustic imaging [370]. The concept has been extended by other groups for generation of multispectral light sources with different pulse energies and pulse repetition rates [56], [371]. Free-space multiwavelength SRS light sources have been also developed for functional photoacoustic imaging. They are reported to have better monochromaticity compared to the fiber-based versions, however the cavity is more sensitive to environmental changes and misalignment compared to fiber-based SRS sources[372], [373]. Despite all the advantages provided by SRS sources, they suffer from pulse-to-pulse output energy fluctuations and power drift that will directly affect imaging quality [374], [375].

In this manuscript, we propose a new technique to improve the temporal stability of the SRS-based multispectral pulsed source. We achieve this by lowering the temperature of the SRS medium. There are two main reasons that temperature is an important factor in Raman-based optical components. First, Raman scattering involves nonlinear phonon-photon interactions. The characteristics of phonons, which are quantized lattice vibrations, are highly temperature-dependent [376], [377]. Second, Raman based devices may suffer from high operating temperatures, since they require high average intensity optical beams to produce

their nonlinear effects [378]. Therefore, temperature plays an important role in designing and/or operating Raman-based devices. The experiment is performed by keeping the optical fiber inside a temperature-controlled unit. The temperature of the unit is adjustable between 195 K and 300 K. It is shown that by controlling and decreasing the temperature, the temporal fluctuations of the generated output peaks are reduced. The proposed method is used to generate stable multiwavelength light at a high pulse repetition rate. The light source is used as the excitation laser for a photoacoustic remote sensing (PARS) microscope and applied to in vivo functional imaging of capillary networks in chicken embryo chorioallantois membrane (CAM). The proposed method offers a promising technology for creating reliable, cost-effective multiwavelength light sources with a sufficiently high pulse energy and PRR for a variety of photoacoustic imaging applications.

5.2. Methods

5.2.1. Temperature-controlled stimulated Raman scattering

The experimental setup used in this study is shown in Figure 5-1. A 532-nm 1.5 ns pulse-width, ytterbium-doped fiber laser (IPG Photonics) capable of PRRs from 20 to 600 kHz is used as the pump laser. To stabilize the laser output prior to the experiment, the source was continuously operated for 30 minutes at an output power of ~370 mW with 50 kHz PRR. The output of the laser was coupled to the fiber by a 10x microscope objective lens. The coupling efficiency for all the experiments was measured to be 63 ± 2%. The optical fiber (PM-460-HP, Thorlabs, Inc) used in this study is single-mode (SM) with 3 μm core diameter, and 6 m in length. Polarization maintaining (PM) fibers are selected for this study since they make SRS generation more efficient compared to non-PM SM fibers [379], [380]. The fiber is kept in a

custom-designed isolated passive temperature-controlled unit during the experiment. The temperature of the unit is adjusted at 300 K, 273 K, and 195 K, by adding water, mixture of water and ice, and dry ice. Once the temperature was stable at the required value, the experiments were conducted. The temperature of the unit stays stable over the several seconds data acquisition time since the thermal mass of the fiber is negligible relative to the cooling media. To prevent the effect of reduced temperature on the fiber coupling efficiency, the fiber coupler is kept outside of the temperature unit. SRS efficiency may also be affected by airflow which can cause random errors and long-term drift in the pulse energy[375]. To avoid this, the fiber was covered and placed at the bottom of the chamber and by sealing the unit, its airflow was isolated. The fiber output is coupled to a collimator, and spectral filters were used to select the SRS peak values. A measuring system made up of a beamsplitter, spectrometer, photodiode, power meter, data acquisition card and computer were used to collect and analyze the required information.

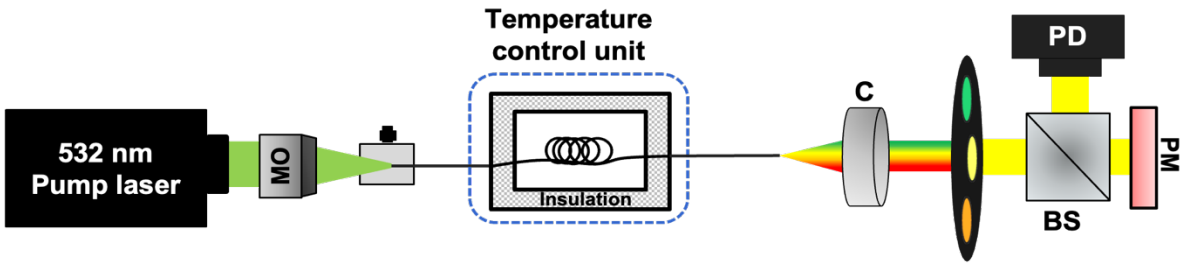

Figure 5-1. Schematic of the experimental setup. MO: microscope objective, C: collimator, BS: Beamsplitter, PD: Photodiode, PM: Power meter.

2.2. Multiwavelength photoacoustic remote sensing microscopy

The multiwavelength light source is applied in a functional photoacoustic imaging study. The imaging system used in this study is based on photoacoustic remote sensing microscopy,

previously described in[365], [381]. **Figure 5-2**A, shows the schematic of the PARS system. Briefly, the multispectral light source operates as the excitation laser for the setup. Concurrently, the detection light is provided by an 830-nm Superluminescent Diode (SLD830S-A20, Thorlabs). A polarized beam splitter is used to transmit most of the forward detection light onto a quarter wave-plate, which transforms the linearly polarized light into circularly polarized light. The detection and excitation beams are then combined using a dichroic mirror. The co-aligned beams are directed toward the sample using a large-beam galvanometer scanning mirror (GVS012/M, Thorlabs, Inc.), and are co-focused into the sample using an objective lens. The back-reflected light from the sample is collected via the same objective lens and guided towards a balanced photodiode. The photodiode outputs are connected to a high-speed digitizer (CSE1442, Gage Applied, Lockport, IL, USA) that performs analog to digital signal conversion. A point acquisition is made for each image pixel and is recorded by the digitizer. Each point acquisition is converted to an intensity value by computing its maximum amplitude and is plotted at its respective location in the image. All images and signal processing steps were performed in the MATLAB environment. **Figure 5-2**B shows the spectra of the individual SRS peaks acquired after spectral filters (FL532-1, FL543.5-10, FB560-10, FB570-10, FB590-10, Thorlabs, Inc.) and demonstrated the available wavelengths for the functional imaging. The spectral peaks at 573 nm and 588 nm wavelengths are broader compared to the other SRS peaks. This can be explained by the broadness of the Raman gain spectrum and also the existence of other non-linear effects such as four-wave-mixing [382]. When it comes to functional measurements, this type of spectral broadening should be considered in the unmixing model to maintain accuracy.

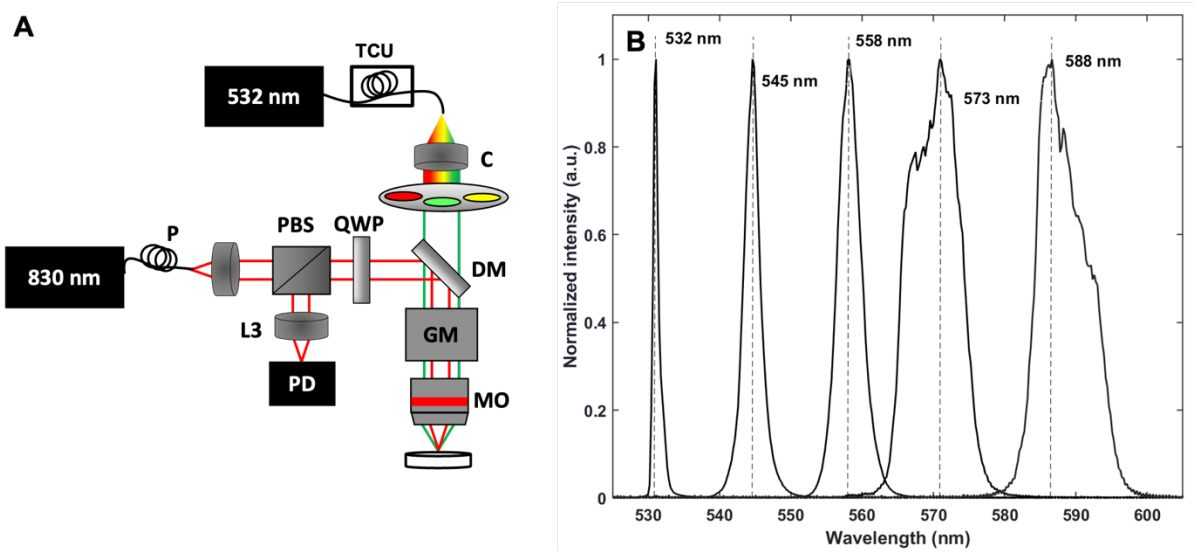

Figure 5-2. (A)Schematic of the PARS imaging system, P: polarizer, PBS: polarized beamsplitter, L: lens, PD: photodiode, GM: Galvanometer mirrors, QWP: quarter waveplate, MO: microscope objective, DM: dichroic mirror, C: collimator, TCU: temperature control unit. (B) Spectrum of the filter out wavelength acquired after spectral filters.

5.3. Results

5.3.1. Temperature-controlled stimulated Raman scattering

We first characterized the temporal stability of the laser itself. The root-mean-square (RMS) temporal fluctuation of the light source at an output power of ~ 370 mW was measured as ± 0.7%, which is in correspondence with the values reported by the manufacturer. The output of the laser was then coupled into the fiber and the spectrum of the generated SRS peaks were measured using the spectrometer. **Figure 5-3** shows the spectrum of SRS peaks acquired at different temperature levels. In this case, the coupling efficiency was ~ 62%, resulting in ~ 220 mW power coupled into the fiber. As the temperature increases, the bandwidth of the spectrum expands which is in agreement with previous reports [383]–[385]. This could be explained by decreasing of chromatic dispersion of the fiber with increasing temperature [386]. Raising the

temperature results in decreasing the phonon lifetime which leads to a broadening of the optical phonon spectrum [378]. Later it is shown that this temperature-dependent spectrum narrowing is accompanied with an increase in the output power intensity for the wavelengths at the higher end of the spectrum.

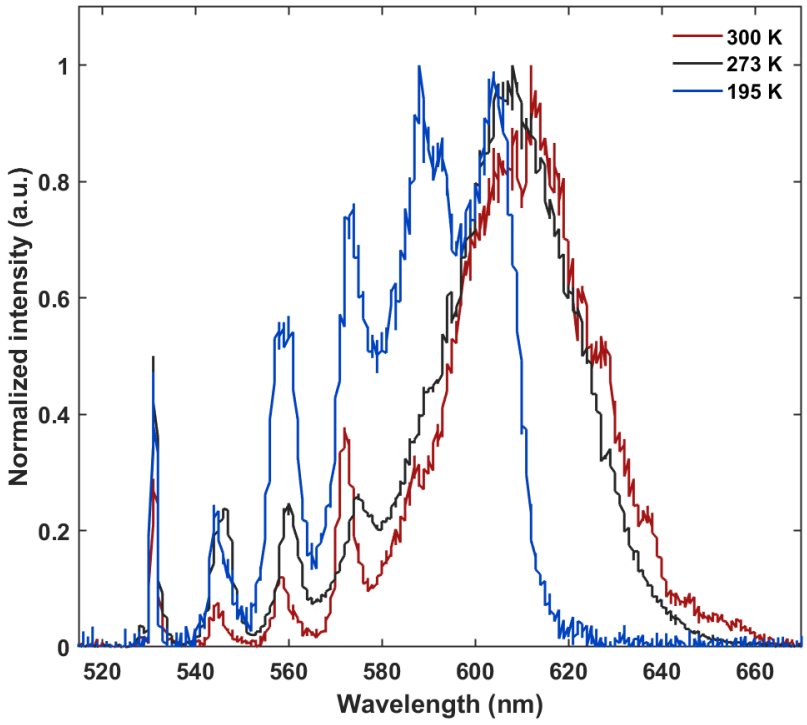

Figure 5-3. Spectrum of SRS peaks acquired at different temperature levels.

After evaluating the effect of temperature on the generated spectrums, we analyzed the temporal stability of the SRS peaks at different operating temperatures. We analyze the RMS stability using a photodiode to measure the SRS intensity generated by each laser pulse. To have high temporal resolution in the acquisitions, a 350 MHz-bandwidth silicon photodetector is used to collect the output pulses after the spectral filters. The timescale of the measurements is based on the potential photoacoustic imaging applications, thus the pulse-to-pulse fluctuations over several seconds are considered in this study. At selected temperature levels

and for each measurement 1000 datapoints are collected over ~ 6 seconds. Figure 5-4A-C shows an example of the light intensity measured using the photodetector, for the 558 nm Raman peak, which directly relates to the number of photons detected, at 300 K, 273K and 195 K, respectively. Here, if the 558 nm SRS peak is not generated (failed SRS event), it will cause a zero voltage on the detector output. The black arrows in Figure 5-4A-C refers to these failed SRS datapoints. In the graphs it can be observed that by reducing the temperature the number of datapoints contributing to SRS events increased, from ~ 690/1000 to ~ 999/1000, at 300K and 195 K, respectively. This represents a ~30% increase in the probability of the SRS event, corresponding to a significant improvement in the temporal stability of the source. This can be explained by the substantial growth of SRS cross section (i.e. the probability that the process will happen) and increase of SRS conversion coefficient as the temperature reduces [387].

In addition to the rate of failed SRS events, we also observe the variation in generated SRS peak intensity. We use the RMS deviation of the peak intensities in the acquired data as a stability metric. The dashed box in each figure highlights these corresponding SRS peaks. Here, the 300K temperature exhibits a large amount of peak variation in comparison to the 195K and 273K cases. Observing the inset figures, the standard deviation of the SRS pulses can be directly visualized. The differences in the variation at each temperature level, clearly shows the improvement in temporal stability with reduced temperature. In this case, both the peak variation, and the failed SRS events contribute greatly to the very large RMS deviation in the SRS peak at 300K. Conversely, the 273K and 195K each exhibit substantially improved pulse-to-pulse stability and substantially reduced SRS failures. Thus, corresponding to a significant improvement in the RMS stability.

We have also extended these measurements across each of the 545 nm 558nm, 573nm and 588nm SRS peaks. The relative power of individually filtered SRS peaks at different temperature levels is shown in Figure 5-4D. The bar chart presented here reveals the relative SRS intensity, while the error bars show the RMS fluctuations of the peaks. The results suggest that by lowering the temperature, the standard deviation of the pulse energy is reduced as well. As the temperature reduces, the generated SRS peak intensities become more uniform and their temporal power fluctuations decrease as well. Lowering the temperature improves the consistency of SRS events and might result in higher accuracy for applications such as photoacoustic microscopy.

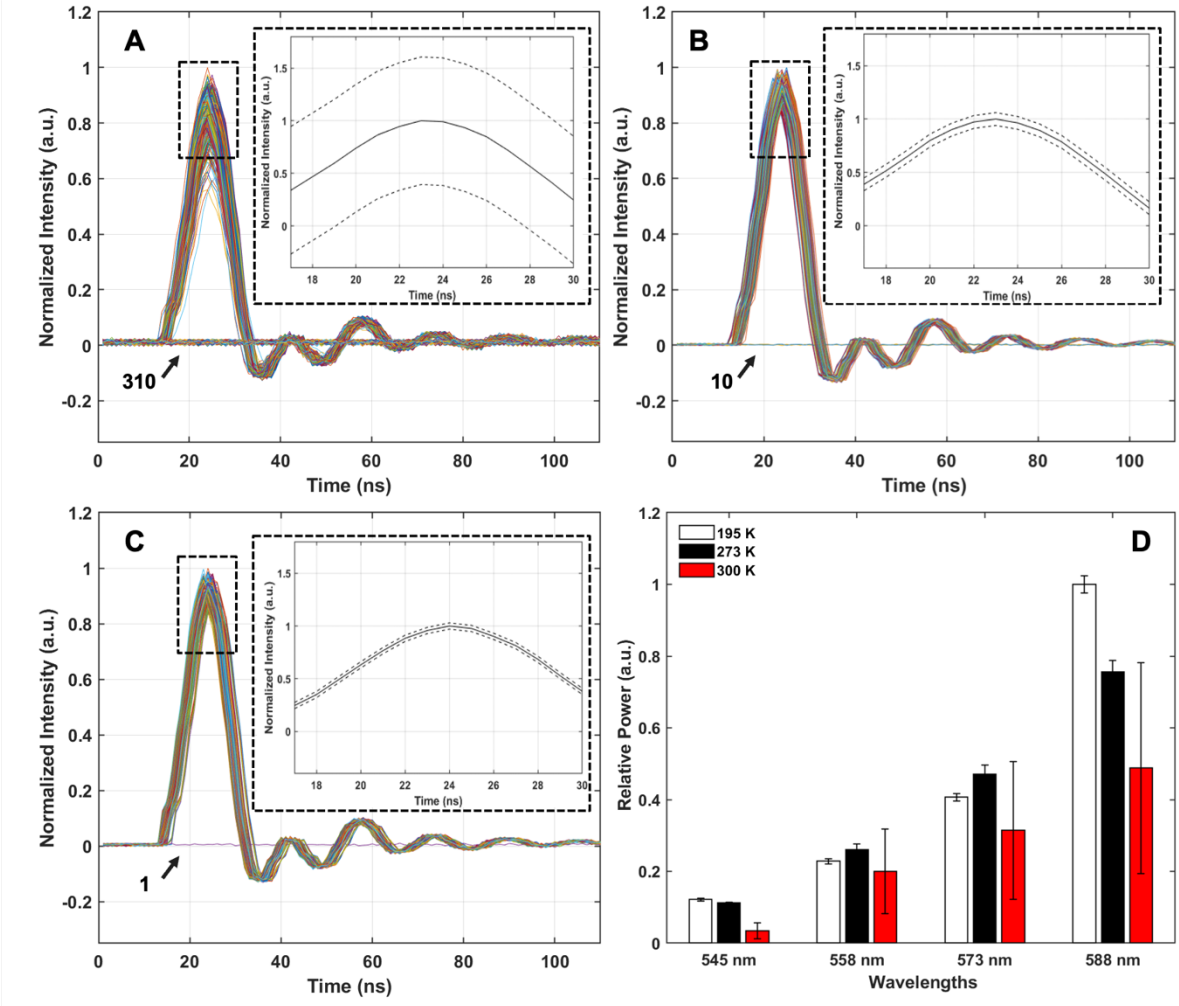

Figure 5-4 Temporal stability of SRS peaks at different temperature levels. (A) 300 K, (B) 273 K, (C) 195 K. Dashed boxes highlight the SRS peaks intensity. Inset figures show the deviation in SRS peak intensity. (D) Bar chart graph showing relative power of individual filtered out SRS peaks measured at different temperature levels. The error bars in this plot show the standard deviation of the SRS peaks.

Tables below summarize the numerical results of the graphs shown in **Figure 5-4** at each temperature level. Here, to decouple the SRS measurements from the fiber coupling efficiency, the results are shown in terms of the power coupled into the fiber. The stability is measured as the standard deviation of the pulse energies, and it is shown in term of nJ and the percentage of deviation (RMS). Based on the measured data, a significant difference was observed between the temporal stability of individual peaks at selected temperature levels. The

conversion efficiency, i.e., how much of the coupled light gets converted into each wavelength, is also improved by reducing the temperature of the SRS medium. This is in agreement with previous reports[378]. The total efficiency which is measured using cumulative energy converted from the 532 nm pump wavelength into other wavelength is also improved by lowering the temperature. We observed that higher pump powers lead to higher efficiency in all cases, which is to be expected. Additionally, the tables show that decreasing temperature causes a considerable rise in the intensity of the wavelengths at the higher end of the spectrum. This might be related to the rise in the Kerr constant by lowering the temperature which can affect the SRS intensity[388]. It is worthwhile to mention that the general effect of temperature was consistent for other stock configurations and input powers.

Table 5-1 SRS characteristics at 300 K temperature

	300 K			
Wavelength (nm)	**545**	**558**	**573**	**588**
Output Power (mW)	**0.92**	**5.46**	**8.58**	**13.34**
Output Pulse Energy (nJ)	**18.34**	**109.29**	**171.65**	**266.81**
Stability (±nJ)	**5.92**	**31.28**	**51.21**	**78.04**
Stability (%RMS)	**32.3**	**28.6**	**29.8**	**29.3**
Conversion Efficiency (%)	**0.52**	**3.07**	**4.82**	**7.50**
Total Efficiency (%)	**16**			

Table 5-2 SRS characteristics at 273 K temperature

	273 K			
Wavelength (nm)	**545**	**558**	**573**	**588**
Output Power (mW)	**3.06**	**7.13**	**12.88**	**20.68**
Output Pulse Energy (nJ)	**61.10**	**142.65**	**257.54**	**413.60**
Stability (±nJ)	**2.35**	**8.39**	**13.43**	**17.62**
Stability (%RMS)	**3.8**	**5.9**	**5.2**	**4.3**
Conversion Efficiency (%)	**1.65**	**3.85**	**6.96**	**11.17**
Total Efficiency (%)	**24**			

Table 5-3 SRS characteristics at 195 K temperature

	195 K

Wavelength (nm)	545	558	573	588
Output Power (mW)	3.32	6.23	11.11	27.34
Output Pulse Energy (nJ)	66.31	124.68	222.28	546.72
Stability (±nJ)	2.01	3.75	5.90	13.04
Stability (%RMS)	3.0	3.0	2.7	2.4
Conversion Efficiency (%)	1.79	3.37	6.00	14.77
Total Efficiency (%)	26			

5.3.2. Multiwavelength photoacoustic remote sensing microscopy

The PARS system with the stabilized SRS-based multispectral system was applied to *in-vivo* oxygen saturation measurement of a CAM model. Figure 5-5A shows a corresponding white light photograph of the CAM model. The temperature of the unit is set to 273 K to achieve temporally stable emissions with large enough pulse energies at 532 nm, 545 nm, and 558 nm spectral wavelengths. The output pulse energy measured on the sample was equal to 150 nJ, 100 nJ and 120 nJ at 558 nm, 545 nm, and 532 nm, respectively. Due to the motion of the CAM model, slight spatial shifts are observed between images. These shifts are corrected for using non-rigid image registration so that the spectral unmixing algorithm can subsequently be applied[389]. Briefly, the unmixing algorithm solves the inverse problem of estimating the relative concentrations of oxy- and deoxyhemoglobin, [HbO_2] and [Hb] respectively, on a per-pixel basis. The PARS response is linear with respect to hemoglobin concentration, and a regularized least-squares solution is used to estimate the relative concentrations. In addition to the effects of absorption at the excitation wavelengths, the reflectivity of the detection wavelength for both oxy- and deoxyhemoglobin must be considered due to its scaling effect on the detected PARS amplitude. To account for this, estimates of the relative concentrations are normalized by the associated reflectivity. Reflectivity is approximated as inverse absorption at the detection wavelength of 830 nm. In future works, the scattering information

provided through the probe beam of PARS can be used the same way as other scattering-based imaging modalities such as fundus photography or OCT to measure the amount of absorption inside the tissue. Figure 5-5 B-D shows capillary beds in the CAM model imaged with 532 nm, 545 nm, and 558 nm, respectively. Each image was acquired over 10 seconds and the temporal sequence between images is ~ 5-8 seconds. The oxygen saturation of the CAM model is presented in Figure 5-5E. Blood oxygenation saturation level is indicated using pseudocolor, ranging from blue to red in an ascending order.

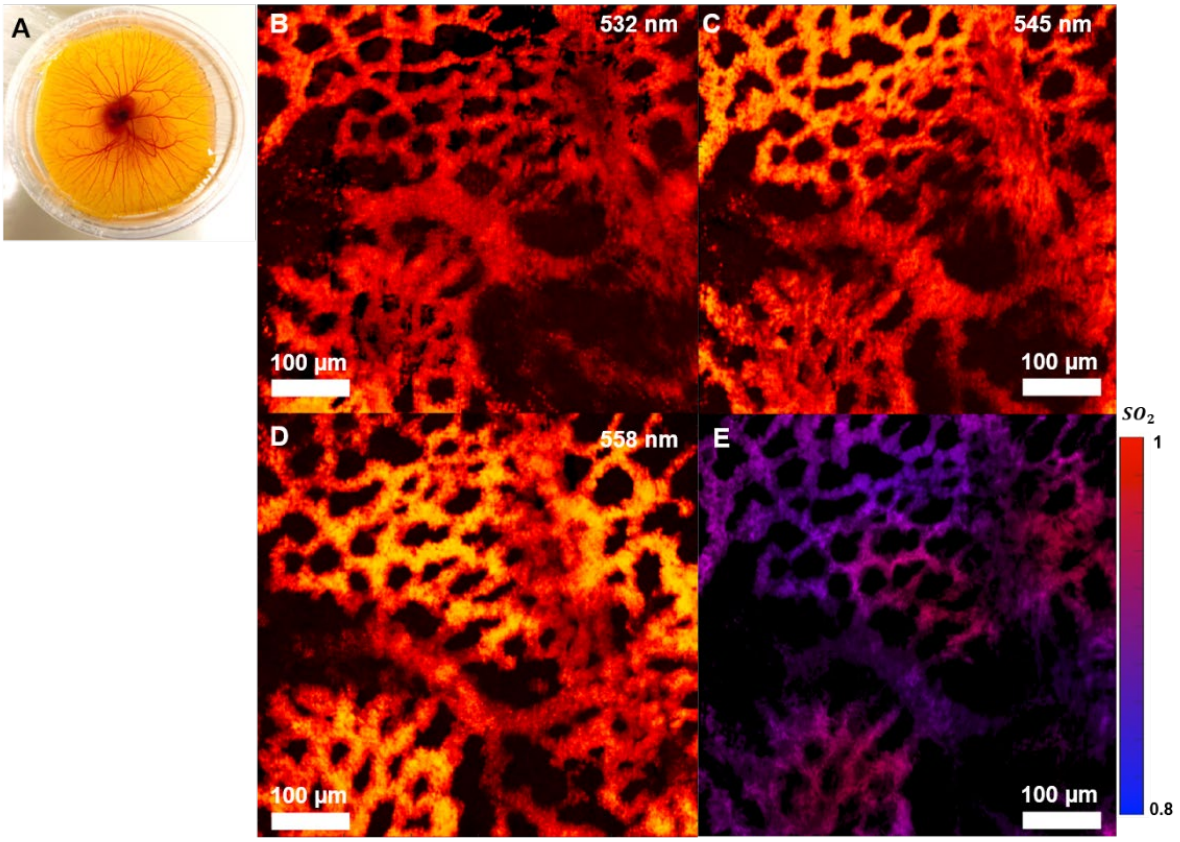

Figure 5-5. Functional oxygen saturation measurement of microvasculature in capillary beds. (A) Corresponding white light photograph of the CAM model. (B) PARS images acquired at 532 nm wavelength, (C) 545 nm, and (D) 558 nm. (E) Oxygen saturation map acquired using spectral unmixing.

5.4. Conclusion

To summarize, we have investigated the effects of temperature on the spectral shape and temporal stability of SRS peaks generated in single-mode silica fibers. In a temperature-controlled condition, with constant laser output, we observed that by lowering the temperature of the fiber the temporal stability of the SRS peaks increases by as much as 60%. This temporally stable multispectral light source could improve the repeatability and may lead to more accurate functional measurements. Therefore, it is expected that in a longitudinal SO_2 study, the temperature controlled multiwavelength light source will result in more accurate measurements. To test the full implications of the improved SRS will require a system capable of satisfying the simultaneity therefore reducing the systematic error in measuring functional information. Several groups have reported methods to achieve ultrashort switching time (a few hundred nanoseconds) among wavelengths [343], [375]. In future studies, similar methods can be used to evaluate the effect of light source stability on the accuracy of the measured values. This results in achieving a stable multispectral light source and improves the accuracy for functional photoacoustic imaging applications. It is also shown that as the temperature increases, the spectral bandwidth of the output beam broadens. Additionally, decreasing the temperature causes a considerable rise in the intensity of SRS peaks and significant growth of SRS cross section. The proposed method can be used to generate a cost-effective multiwavelength light source with high enough pulse energy and PRR for several imaging applications.

In the next chapters we show the application of the proposed stabilized multiwavelength light source for functional imaging of the ocular environment and combine it with OCT for acquiring complementary imaging contrast of depth-resolved optical scattering.

Chapter 6

Functional and structural ophthalmic imaging using noncontact multimodal photoacoustic remote sensing microscopy and optical coherence tomography.

Notes and Acknowledgement

This chapter summarizes results from a study that for the first time present a non-contact, multiwavelength photoacoustic remote sensing (PARS) microscopy combined with swept-source optical coherence tomography (SS-OCT) for *in-vivo* functional and structural imaging of the eye. The system provides complementary imaging contrasts of optical absorption and optical scattering, and is used for simultaneous, non-contact, *in-vivo* imaging of murine eye. The content of this chapter is based on the following journal manuscript:

Zohreh Hosseinaee, Nima Abbasi F., Nicholas Pellegrino, Layla Khalili, Lyazzat Mukhangaliyeva, Parsin Haji Reza, " Functional and structural ophthalmic imaging using noncontact multimodal photoacoustic remote sensing microscopy and optical coherence tomography " *Sci Rep* **11,** 11466 (2021).

Author contributions

Zohreh Hosseinaee co-designed with supervisor the optical system for PARS-OCT suitable for imaging the eye, investigated and lead the digital control requirements for the system, prepared and ordered the optical and digital components of the PARS-OCT system, constructed the PARS-OCT system, investigated and lead image processing for the SS-OCT system, conducted the experiments, processed the images, contributed to the interpretation the data, prepared the figures, and wrote the main manuscript.

Nima Abbasi constructed the software of the OCT system.

Nicholas Pellegrino developed and implemented the signal unmixing method.

Layla Khalili and **Lyazzat Mukhangaliyeva** assist with animal handling and conducting imaging experiments.

Parsin Haji Reza proposed the idea, conceived the study, contributed to the interpretation of all results, and acted as the primary investigators.

All the authors reviewed the manuscript.

6.1. Introduction

The ability to precisely detect and measure chromophore concentration in ocular tissue is crucial for improving investigations and diagnoses of major eye diseases. Several studies have demonstrated the vital role of ocular oxygen saturation (SO_2) and melanin concentration in various prevalent eye diseases[11]. For example, retinal oxygen saturation has been shown to be abnormal in diabetic retinopathy (DR)[390], [391], glaucoma diseases[392], [393], and retinal vein occlusions[394], [395]. In addition, melanin loss in the retinal pigment epithelium (RPE) layer is shown to be a major factor affecting the progression of age-related macular degeneration (AMD)[396], [397]. Therefore, accurate measurement of chromophore concentrations in the ocular environment could potentially enable improved measurement of biomarkers for early diagnosis of eye diseases[398]. In the past decades, extensive efforts have been made to accurately measure SO_2 and melanin concentration in the ocular environment. The gold standard for measuring retinal SO_2 in ophthalmic research uses intra-retinal electrodes to directly measure the oxygen tension[399], however, the invasive nature of the method limits its clinical applications, thus it can only be used in human subjects during surgical procedures[400]. Additionally, it is nearly impossible to map the amount of oxygenation over a large area using this method. Imaging-based methods are required to visualize the spatial distribution of oxygen in ocular blood vessels. Phosphorescence lifetime imaging has been used to map oxygenation in the mouse eye. Unfortunately, the need to introduce fluorescent probes into systematic circulation makes the method inappropriate for human practice[401]. Magnetic resonance imaging (MRI) can also detect retinal oxygen distribution non-invasively in humans, however, it has low resolution and offers only

qualitative measurement [402]. Recently, researchers are focused on optical imaging-based methods to extract blood oxygen saturation. Optical measurement of SO_2 is possible because the two forms of hemoglobin, oxy- and deoxyhemoglobin (HbO_2 and Hb), have distinct optical absorption properties. The differences in the absorption spectra of oxy- and deoxyhemoglobin can be utilized to quantify the relative amounts of HbO_2 and Hb in the blood[403]. Several optical imaging methods, including multiwavelength fundus imaging, scanning laser ophthalmoscopy and visible light optical coherence tomography (OCT), have all been investigated to measure ocular oxygen saturation[400]. These methods, however, rely on measuring the backscattered photons from blood vessels to quantify the absorption of specific chromophores inside the tissue[404], [405]. Therefore, they are sensitive to local geometrical parameters, such as retinal thickness, vessel diameters, and retinal pigmentation and may result in biased estimations[14].

Among various optical imaging modalities, photoacoustic microscopy (PAM) offers unique imaging contrast of optical absorption. In other words, any imaging target that absorbs light energy, can be imaged using PAM. Biological tissues have endogenous chromophores that can be exploited as imaging targets. For example, the absorption peak of DNA/RNA is in the ultraviolet spectral region, and hemoglobin and melanin mainly absorb light in the visible and near-infrared (NIR) spectral ranges[186]. This unique imaging ability makes PAM a favorable candidate for various functional and molecular imaging applications and measuring chromophore concentration[47]. Over the past decades, photoacoustic ophthalmoscopy has been applied for visualizing hemoglobin and melanin content in ocular tissue[348], quantifying ocular SO_2[406], and measuring the metabolic rate of oxygen consumption (MRO_2)[106].

Despite all these advantages offered by PAM devices, a major limitation arises from their need to be in contact with the ocular tissue[186]. This physical contact may increase the risk of infection and may cause patient discomfort. Furthermore, this contact-based imaging approach applies pressure to the eye and introduces barriers to oxygen diffusion. Thus, it has a crucial influence on the physiological and pathophysiological balance of ocular vasculature function, and it is not capable of studying dynamic processes under close conditions to normality[407]. In 2017 Haji Reza et al. developed photoacoustic remote sensing (PARS) microscopy for non-contact, non-interferometric detection of photoacoustic signals[335]. PARS microscopy can be considered as the non-contact, all-optical version of optical resolution PAM (OR-PAM), where the acoustically coupled ultrasound transducer is replaced with a co-focused probe beam. This all-optical detection scheme allows the system to measure the photoacoustic pressure waves at the subsurface origin where the pressure is maximum. Besides optical absorption imaging contrast, PARS also offers optical scattering contrast through its probe beam and can be considered as a dual-contrast imaging modality. Using only the probe beam, the PARS microscope can act as a confocal microscope to visualize scattering information of the tissue. In functional studies such as SO_2 measurement an additional advantage of PARS microscopy over other optical imaging modalities comes from its sensitivity to both optical absorption and optical scattering imaging contrasts. In other words, the scattering information provided through the probe beam of PARS microscopy can be used the same way as other scattering-based imaging modalities such as fundus photography or OCT to measure the amount of absorption inside the tissue. In addition, the wavelength of PARS excitation beam can be tuned to target a specific chromophore inside the tissue. The technology has proved its

potential over a short period of time in various biomedical applications, such as label-free histological imaging[340], [345], SO_2 mapping and angiogenesis imaging[339]. Very recently, our group demonstrated the first, non-contact, *in-vivo* photoacoustic imaging of ocular tissue using PARS microscopy[381].

In ophthalmic imaging applications, optical coherence tomography is a state-of-the-art imaging technique extensively used in preclinical and clinical applications for imaging both anterior and posterior parts of the eye[71]. Unlike photoacoustic imaging, OCT obtains its imaging contrast from optical scattering of internal tissue microstructures. Due to its interferometric nature, OCT provides depth-resolved scattering information and can be considered as an ideal companion for PARS microscopy for ophthalmic imaging applications. This combined multimodal imaging technology has the potential to provide chromophore selective absorption contrast in concert with depth-resolved scattering contrast in the ocular environment[408]. Recently, Martell et al.[409] reported a dual-modal PARS microscopy combined with spectral-domain OCT (SD-OCT) and applied it for *in-vivo* imaging of ear tissue.

To allow for *in-vivo,* non-contact, functional and structural ophthalmic imaging, here we have combined a multiwavelength PARS microscope with a swept source OCT system (SS-OCT). SS-OCT has been used in this study, as it provides extended imaging range, reduced sensitivity roll-off and improved light detection efficiency compared to SD-OCT counterparts. To the best of our knowledge, this is the first time that a swept-source OCT system is combined with an OR-PAM system in general (both contact-based OR-PAM and non-contact OR-PAM – i.e., PARS). In addition, for the first time we present dual-contrast PARS microscopy, where

multiwavelength excitation is used for targeting absorption contrast and the probe beam is used for targeting scattering imaging contrast. Additionally, here by capitalizing on the distinct differences in absorption spectra of oxy- and deoxyhemoglobin, oxygen saturation is estimated in the ocular tissue. To our knowledge, this is the first time a non-contact photoacoustic system is used for *in-vivo* SO_2 measurement in the ocular environment. This reported work has the potential to advance the diagnosis and treatment of major eye diseases.

6.2. Methods:

6.2.1. Stimulated Raman Scattering

Previous multiwavelength OR-PAM studies commonly used dye lasers or optical parametric oscillators to obtain multiple wavelengths required for oxygen saturation measurements[362], [410]. However, these sources suffer from low pulse repetition rates (PRR) of 10 Hz – 10 kHz and thus are not suitable for *in-vivo* ocular imaging applications. In this study to achieve multiwavelength PARS microscopy and provide a reasonable speed for eye imaging, the SRS effect is employed. SRS offers an effective approach for implementing high-speed and multiwavelength light sources [56]. Distinct SRS peaks are generated from inelastic nonlinear interactions between incoming photons and the molecules of the fiber itself [367]. Here, the output of the excitation laser was coupled into a 3.5-m polarization-maintaining single-mode fiber (PM-460 HP) using a fiber launch system. The coupling efficiency was ~65%, and four distinct optical wavelengths were observed at the output of the fiber. To evaluate the performance of the multiwavelength light source, a comprehensive study was conducted on the peak power values, damage threshold, and the temporal stability of the procedure [411]. Input power levels are limited by the fiber damage threshold. In our experiments, the input

power was varied between 1 mW- 800 mW. The fiber damage was first observed at 100-kHz pulse-repetition-rate and 800 mW average input power. SRS efficiency could be affected by temperature and airflow changes, and random errors and drift in pulse energy[375]. To improve the stability of the SRS peaks, the fiber was kept in a temperature-controlled unit (273 K) to isolate the airflow and the temperature. Additionally, at the output port of the fiber, which is connected to the collimator, the back-reflected light from the filter may also cause damage at the end of the fiber; this can be solved by introducing a small angle to the filter[56]. A fiber optic spectrometer measured the SRS peaks and confirmed the filtered wavelengths. Table 6-1shows maximum powers available for each wavelength at 100 kHz pulse-repetition-rate. These values are acquired by adjusting the input power of the fiber to find the maximum output power at each SRS wavelength.

Table 6-1 Measured power of SRS peaks generated in 3.5m fiber and at 100kHz PRR.

3.5-m fiber (100 kHz)				
Generated Wavelength (nm)	532	545	558	573
Output Energy (nJ)	250	230	230	180

6.2.2. System Architecture

Figure **6-1**A demonstrates the experimental setup of the multimodal PARS-OCT system. Details of the PARS subsystem was explained in the previous study published by our group for non-contact ophthalmic imaging[381]. Briefly, a 532-nm 1.5 ns pulse-width, ytterbium-doped fiber laser (IPG Photonics) is coupled to a single mode optical fiber to generate SRS peaks. The collimated excitation beam passes through bandpass filters to select the desired wavelength and is directed toward the sample. The detection arm uses an 830-nm Superluminescent Diode with 20 nm full width at half maximum linewidth (SLD830S-A20,

Thorlabs). A polarized beam splitter is used to transmit the majority of the forward light onto a quarter wave-plate, which transforms the linearly polarized light into circularly polarized light. The detection and excitation beams are then combined using a dichroic mirror. The co-aligned beams are directed toward a large-beam galvanometer scanning mirror system (GVS012/M, Thorlabs, Inc.). The beams are then directed to a telecentric pair set that provides uniform image intensity and improves the effective field-of-view. The excitation and detection beams are co-focused into the sample using a refractive objective lens (depending on the application the numerical aperture (NA) of the objective lens is switched between 0.26 and 0.4). The back-reflected light from the sample is collected via the same objective lens and guided towards the detection path. The quarter wave-plate transforms the reflected circularly polarized light back to linearly polarized light, which enables the polarized beam splitter to direct the back-reflected light towards the photodiode. A long-pass filter is used to block any residual 532 nm light. The 830 nm beam is then focused with an aspherical lens onto a balanced photodiode. The photodiode outputs are connected to a high-speed digitizer (CSE1442, Gage Applied, Lockport, IL, USA) that performs analog to digital signal conversion.

In the SS-OCT subsystem, a vertical cavity surface emitting laser (VCSEL) (Thorlabs, Inc.) is used as the light source. The laser is centered at ~1060 nm with 100 nm spectral bandwidth and frequency swept at 60 kHz which enables higher sensitivity compared to higher speed SS-OCT counterparts. A-line trigger, i. e. sweep trigger, was supplied by the light source and a K-linear sampling clock was provided by the Mach-Zehnder interferometer-based clock module integrated within the laser[412]. The output of the laser was connected to a custom fiber optic interferometer consisting of a circulator and a 50:50 fiber coupler that splits the

light into the reference and sample arms. The reference arm consists of BK7 dispersion compensating prisms in the optical path and a translating mirror to set the zero delay. In the sample arm the collimated light is combined with the PARS excitation and probe beams and together are directed to the sample. The returning light from the sample and reference arms were interfered at the coupler and detected by the built-in dual balanced photodetector. The OCT signal was digitized by a high-speed A/D card (ATS9351, Alazar Technologies Inc., Pointe-Claire, QC, Canada). The raw OCT data was transmitted to a host computer through a PCI-Express interface. The OCT system control was implemented in MATLAB platform to automatically control all the operations including system calibration, galvo-scanning, system synchronization, real-time imaging preview and data acquisition. The multimodal PARS-OCT system has two independent imaging modes. It can either performs as two standalone subsystems, or as a multimodal imaging unit to acquire simultaneous images. Figure **6-1**B demonstrates the timing chart of the multimodal imaging system. Briefly, in the simultaneous imaging mode, at each A-line, and for each rising edge of sweep trigger signal, the OCT digitizer collects data during the sampling clock of the K-clock, and it stops collecting data during the dummy clock (frequency ~ 250 MHz). The sweep-trigger signal also generates an auxiliary signal, and the falling edge of this auxiliary signal is used as the external trigger for PARS excitation and data acquisition. As a result, during the time that OCT system is collecting data, the PARS excitation is off and it turns on during the backward sweep of the swept source laser, where the OCT digitizer has stopped collecting signal. This will ensure that the photoacoustic pressure waves induced by PARS excitation, will not affect the quality of the OCT signal.

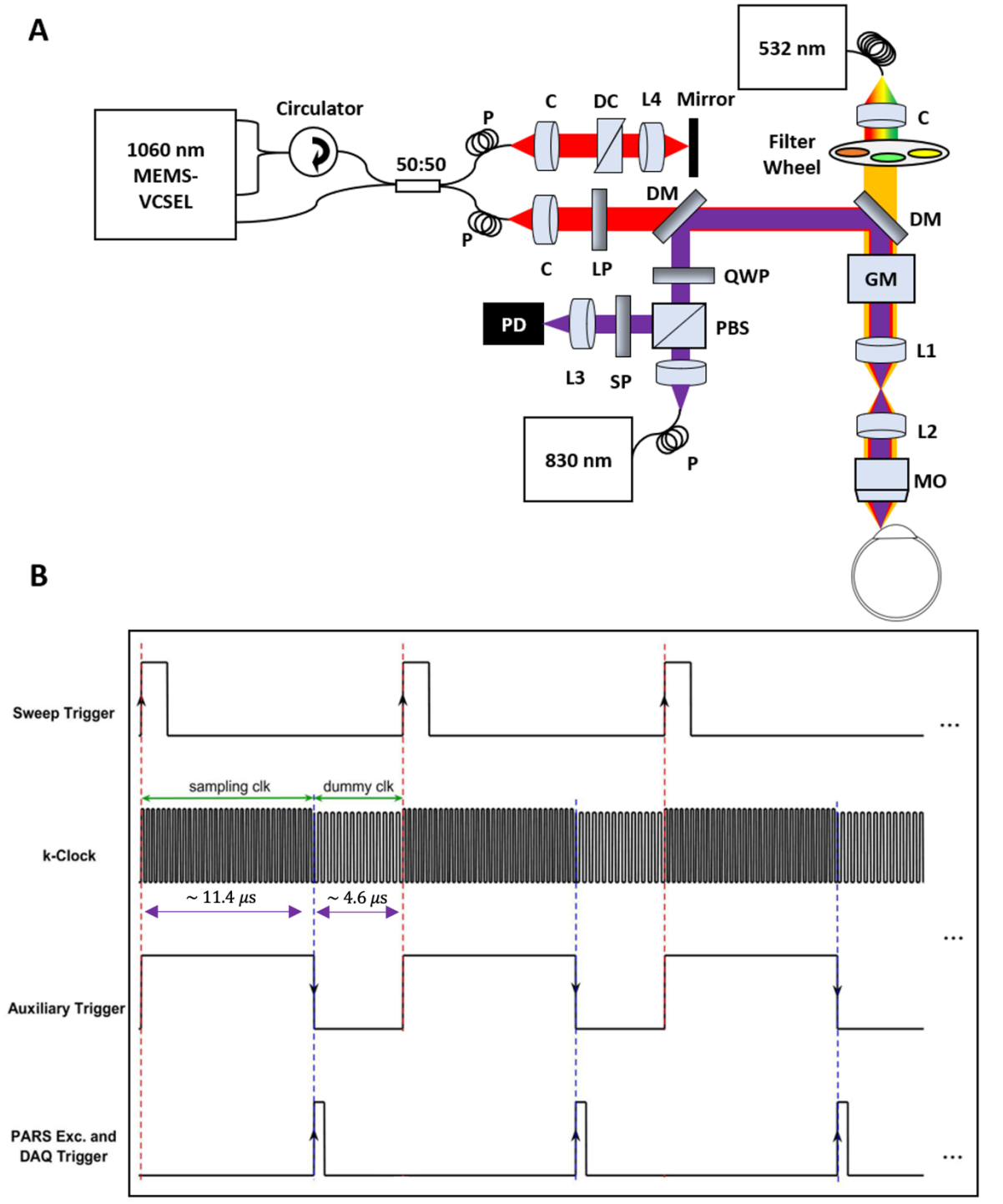

Figure 6-1. Simplified schematic and timing chart of the multimodal PARS-OCT system. Simplified system schematic. DM: Dichroic mirror, QWP: Quarter wave plate, PBS: Polarized beamsplitter, LP: Long pass filter, GM: Galvanometer mirrors, MO: microscope objective, L: Lens, C: Collimator, PD: Photodiode. DC: Dispersion compensation, P: Polarization controller (A). Multimodal imaging mode timing chart (B).

6.3. Image Reconstruction

All the PARS images shown in this manuscript were formed using a maximum amplitude projection (MAP) of each A-scan for each pixel of the *en-face* image. The images were produced by direct plotting from interpolated raw data using a Delaunay triangulation interpolation algorithm [351]. All images and signal processing steps were performed in the MATLAB environment. Scale bars in the field-of-view were calibrated using a 1951 USAF resolution test target.

For each OCT data set, 500 A-lines were acquired for each B-scan and on each cross-sectional position the slow scan axis traversed through 500 lateral positions. For each A-line trigger, 2448 sampling points were acquired to cover the resultant spectral interferogram, providing a depth ranging distance of ~12 mm. As a pre-processing step to extract complex data, the OCT reference spectrum was subtracted from the interference signal to remove DC bias, then Fourier transform was performed to extract the depth-resolved OCT signal. The top half of the Fourier transformed data was considered as valid complex data for further processing. Images were generated from the raw OCT data and numerically dispersion compensated up to the 5th order with a custom MATLAB algorithm[413]. No additional image post-processing was used for the OCT images presented in this thesis. The volumetric and *en-face* images were generated from the 3D data sets with ImageJ[414].

6.4. Animal Preparation

All of the experimental procedures were carried out in conformity with the laboratory animal protocol approved by the Research Ethics Committee at the University of Waterloo and adhered to the ARVO statement for use of animals in ophthalmic and vision research. All

sections of this report adhere to the ARRIVE Guidelines for reporting animal research. Nude mice and albino mice (NU/NU, Charles River, MA, USA) were imaged to demonstrate the *in-vivo* capabilities of the system. A custom-made animal holder was used to restrain the animal. The base of the animal holder was lined with a thermal pad in order to keep the animal body temperature between 36° and 38°C. Artificial tears were used frequently (~ every 5 minutes) to keep the cornea hydrated. Vital signs, such as respiration rates, heart rates and body temperature were monitored during the experiment.

6.5. Ocular Light Safety

Light safety is an important factor to consider in ocular imaging applications. In this study, the OCT light power on the cornea was measured to be ~1.5 mW centered at 1060 nm which is well within the ANSI safety limits for imaging human eye[415]. For the PARS system the detection power was ~ 2-3 mW which is in the range allowed by ANSI limits for imaging human eye. The PARS excitation pulse energy was in the range of 50-100 nJ. The ANSI standard was used to calculate the maximum permissible exposure (MPE) for ocular imaging [357], [415]. Based on the ANSI standard, the MPE for a single laser pulse can be measured as $MPE_{SP}=5.0\ CE\times10^{-7}=1.33\times10^{-4}$ J/cm^2, where C_E is a correction factor calculated as 267 according to the NA of the system. The repetitive pulse limit was then calculated as $MPE_{RP} = (n_{total})^{-0.25}\times MPE_{SP}= (5\times10^5)^{-0.25} \times1.33\times10^{-4}$ J/cm^2$=5.12\times10^{-6}$ J/cm^2, where n_{total} is the total number of pulses during imaging (500,000 pixels in the image). The maximum permissible single laser pulse energy in a typical human pupil of 7 mm[182] was then calculated as MPE_{RP} × pupil area=1.93 μJ, which is 19 times higher than the pulse energy used in this experiment.

6.6. Results and Discussion

The imaging performance of the multimodal PARS-OCT system was evaluated by measuring its spatial resolution and signal-to-noise ratio (SNR). These results are presented in Figure **6-2**. As mentioned earlier, PARS microscopy can be considered as a dual contrast imaging modality, providing both absorption and scattering imaging contrasts. The resolutions of both contrast mechanisms of PARS microscopy system were characterized by imaging 0.97 μm diameter microbead solution as explained in [353]. The lateral resolution provided by PARS absorption contrast with a 0.4 NA objective lens was measured to be ~ 1.5 ± 0.1 μm, as shown in Figure **6-2**A. The black line shows the raw data, and the red line represents the first order Gaussian curve fit using the MATLAB curve fitting toolbox. As mentioned earlier, in this chapter for the first time we showed the capability of PARS microscopy in providing scattering contrast. Basically, before applying an excitation beam, the probe beam has a constant intensity (effectively a DC signal). This constant light is due to the backscattering from the sample. This light can be collected to construct an image that represents the scattering contrast in PARS microscopy. The lateral resolution of PARS scattering contrast was characterized using microbead solution to be ~ 3.1 ± 0.1 μm (Figure **6-2**B). The difference between the absorption and scattering contrast lateral resolution, is induced by the different spectral ranges and slight variations in the beam size.

The OCT axial resolution was measured experimentally by using a mirror as the test sample. The result is shown in Figure **6-2**C. The red line point spread function (PSF) was measured after the coarse hardware dispersion compensation unit in the reference arm. The black line PSF in Figure **6-2**C was measured after numerical dispersion compensation up to the 5th order

using a custom MATLAB based algorithm. The full width half maximum of the axial PSF was 10.1 µm in free space, which corresponds to 7.3 µm in biological tissue, assuming an average refractive index of n = 1.38 and ignoring wavelength dependent local variation of the refractive index[416]. The SNR roll-off of the SS-OCT system was characterized by imaging a mirror in the sample arm at different positions. A neutral density filter with an optical density (OD) of 2.0 was used to reduce the signal intensity. The SNR in dB was calculated as the ratio of the A-scan peak height to the standard deviation of the noise floor. The maximum SNR of 100 dB was measured at ~ 100 µm away from the zero-delay line with incident power of ~ 1.5 mW. The SNR roll-off in free space was measured to be ~ 1dB over a scanning range of 1.3 mm Figure **6-2**D).

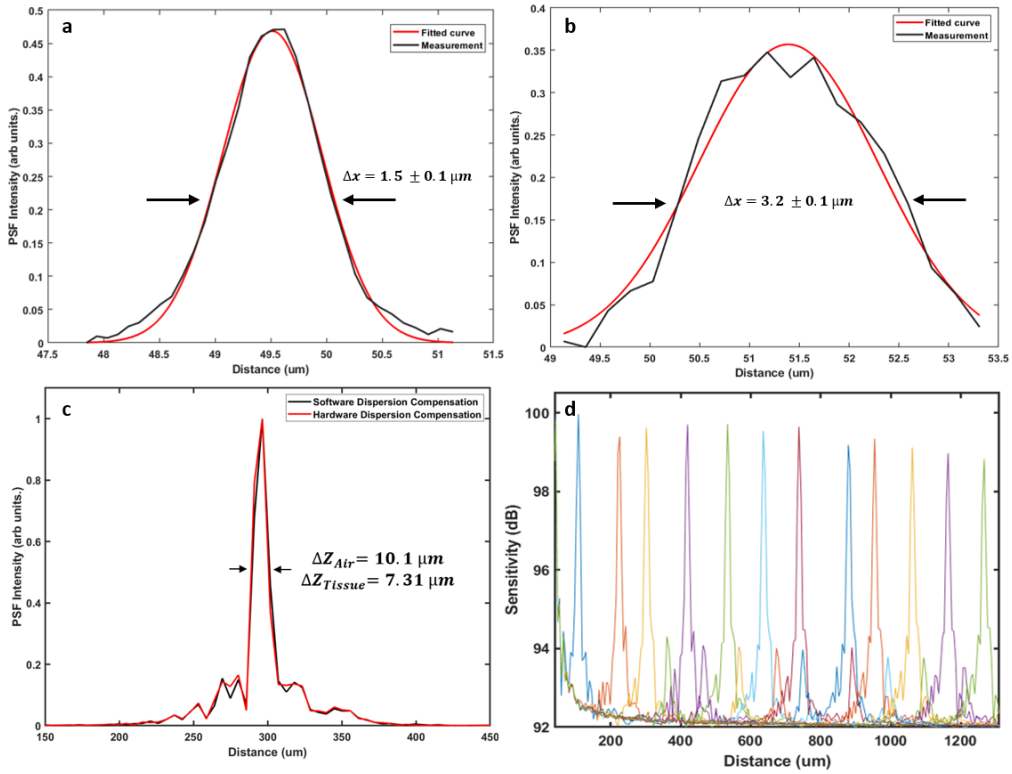

Figure 6-2. Imaging performance of the multimodal PARS-OCT system. PSF of PARS absorption contrast mechanism characterized by imaging 0.97 µm diameter microbead solution (A). PSF of PARS scattering contrast (B). Axial PSF of SS-OCT measured in free space (C). Sensitivity roll-off of SS-OCT (D)

To evaluate the *in-vivo* capabilities of our multimodal imaging system, we chose to first image mouse ear, a long-established animal model of cutaneous microcirculation that closely resembles that of human skin[417]. Since the multimodal system is configured similarly to a conventional optical microscope, it can be readily applied for studying other popular animal models such as zebra fish [154]. Figure **6-3**A shows white light photograph of the mouse ear. The dotted rectangles indicate the corresponding PARS and OCT imaging regions. Figure **6-3**B demonstrates a volumetric rendering of nude mouse ear covering ~ 2.5 mm × 2.5 mm area obtained *in-vivo* by SS-OCT system through a 0.26 NA microscope objective. The SS-OCT system provided a microanatomy of the avascular structures in the ear tissue (Figure **6-3**C). From the OCT cross-sectional images we were able to estimate that the imaged region had a thickness between 200 to 300 μm, which agreed well with previous reports[135]. The orthogonal view of the skin (Figure **6-3**D) clearly shows the structures of the ear due to the system's high resolution. The ear tissue consists of two skin layers separated by a layer of non-scattering cartilage, whereas, the epidermis, the outmost layer of the skin, tends to be more scattering. The junction between epidermis and dermis is clearly visible followed by the dermis where hair follicles, follicle shafts, follicle bulbs, and small blood and lymph vessels are located. The low-scattering regions embedded in the skin layers are most likely sebaceous glands. However, blood vessels are not evident on the OCT images. In contrast, the PARS absorption mechanism is good at locating vasculature with great details in the ear (Figure **6-3**E-G). For the mouse ear images the SNR, defined as the average of the maximum amplitude projection pixels in a region of interest over the standard deviation of the noise, was quantified as 36 ± 3 dB. The *in-vivo* resolution of the mouse ear images was measured as approximately

2.4 ± 0.5 µm. The *in-vivo* performance of the PARS scattering mechanism is presented in Figure **6-3**H. Due to its shorter central wavelength PARS scattering mechanism offers higher lateral resolution compared to the OCT system, and microscopic epidermal ridges are evident in the MAP image acquired using the PARS system.

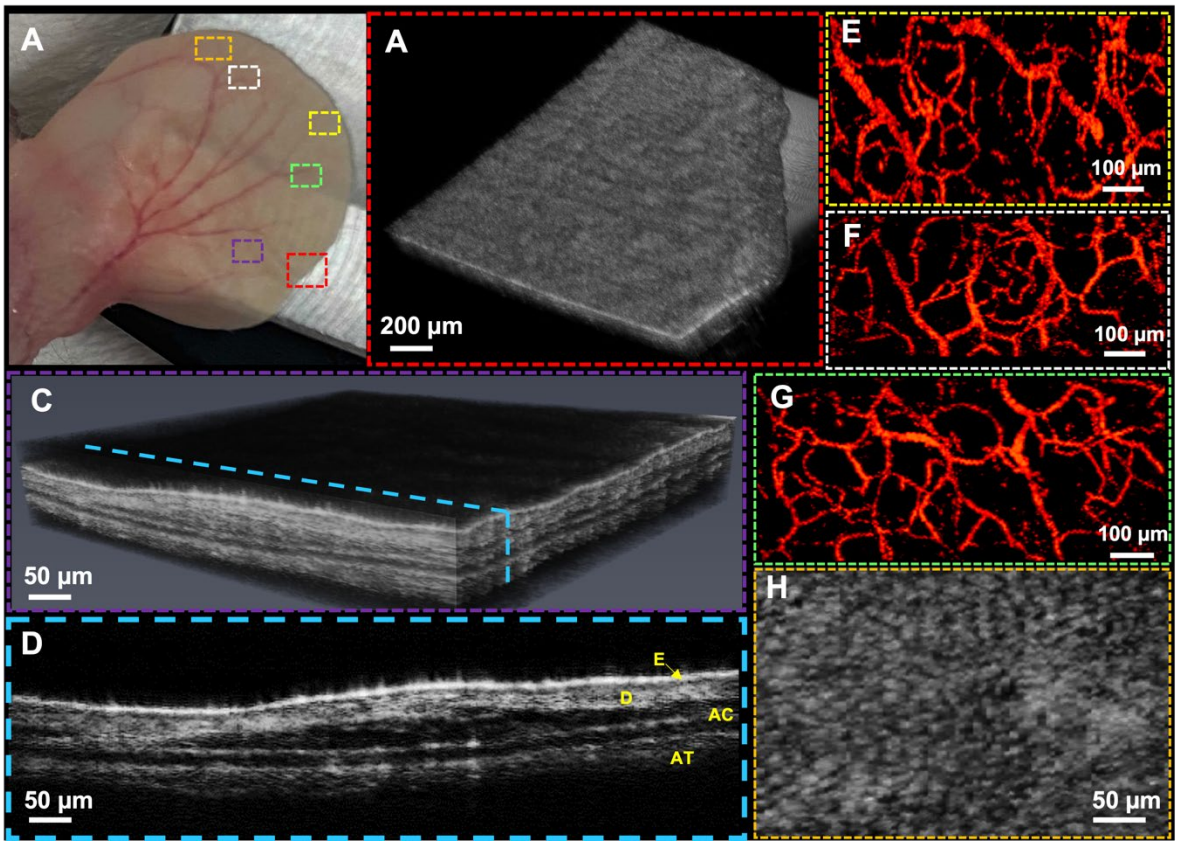

Figure 6-3. *In-vivo* imaging of mouse ear using multimodal PARS-OCT system. Corresponding white light photograph of the mouse ear, dotted rectangles indicate the PARS and OCT imaging regions (A). Volumetric rendering obtained by SS-OCT image(B). Volumetric OCT image showing different layers inside the ear tissue (C). Cross-sectional B-scan showing distinctive layers in the mouse ear tissue, E: Epidermis, D: Dermis, AC: Auricular cartilage, AT: Adipose Tissue (D). Vasculature of the ear obtained by PARS absorption mechanism (E-G). MAP image of the PARS scattering contrast showing epidermal ridges(H).

The multimodal imaging system was then applied to *in-vivo*, non-contact, structural and functional imaging of the ocular environment. First the performance of the system was tested as two standalone PARS and OCT subsystems for ocular imaging. Figure **6-4** shows representative images acquired using the SS-OCT system from the anterior segment of the

mouse eye. Figure **6-4** A demonstrates volumetric rendering of the entire eye, covering ~ 3.5 mm × 3.5 mm area obtained from albino mouse using a 0.26 NA microscope objective. Cross-sectional B-scans are shown in Figure **6-4** B&C, the resolution of the SS-OCT system allows for visualizing the anterior segment structures. To bring the lower part of the anterior segment into focus and increase its signal strength, the B-scan in Figure **6-4**C is flipped over the zero-delay line thus, iris, crystalline lens, iridocorneal angle and sclera are clearly visible. In Figure **6-4**B, cornea epithelium layer, Bowman's membrane and stroma can be distinguished.

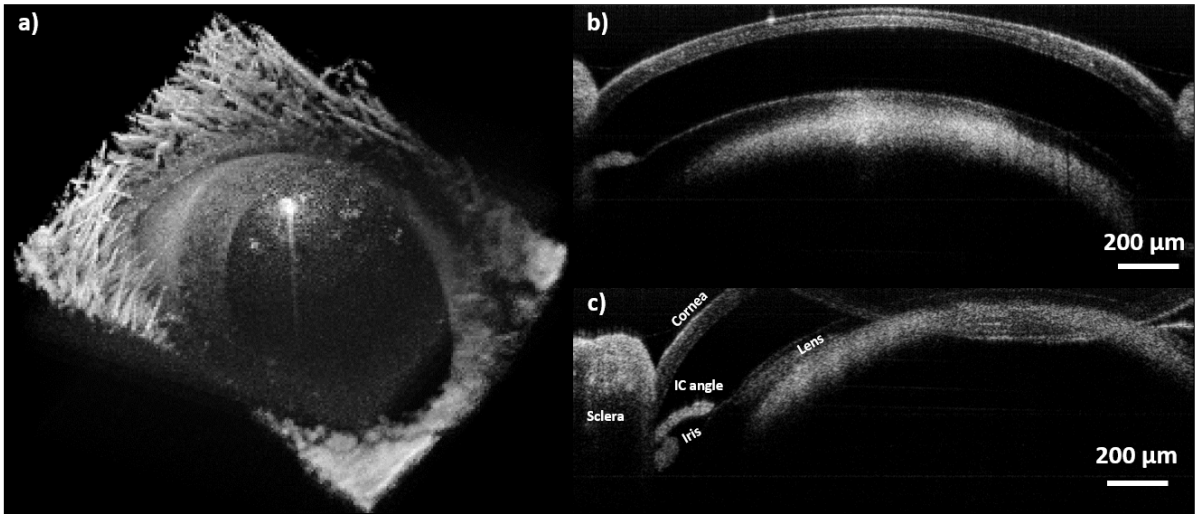

Figure 6-4. *In-vivo* imaging of ocular tissue using SS-OCT. Volumetric rendering acquired from the mouse eye (A). Cross-sectional OCT B-scan showing cornea and crystalline lens (B). Cross-sectional B-scan demonstrating cornea, sclera, crystalline lens, iris and iridocorneal angle (C).

The high-definition structural information provided by SS-OCT can be well complemented by high resolution vasculature images obtained from non-contact PARS microscopy. The potential of PARS microscopy for label-free, non-contact, *in-vivo* imaging of the iris and retinal vasculature was previously reported by our group[381]. Figure **6-5**A shows vasculature of the eye imaged with PARS microscope. The image was acquired using a 0.26 NA objective and the field of view was measured as ~ 2.5 mm × 2.5 mm. The boxes in this figure are not highlighting the exact structure and are only used to show the approximate region imaged in

Figure **6-5**B,D&E. Figure **6-5**B-F shown smaller field-of-views and are acquired using 20X microscope objective. The SNR of in-vivo eye images was measured ~ 35 ± 2 dB, and the *in-vivo* resolution of the mouse eye images was measured as 4.3 ± 0.6 μm. The mismatch between the *in-vivo* imaging resolution and the one measured using microbead solution can be explained by the presence of chromatic aberration and involuntary motion of the eye.

In this study, we also applied PARS microscopy for non-contact, *in-vivo* imaging of melanin which is another dominant light absorber in the ocular environment. In conventional photoacoustic imaging techniques, for *in-vivo* experiments, photoacoustic signals must propagate through various layers of the eye including the vitreous and lens which can significantly attenuate high frequency photoacoustic signals[418]. However, in PARS microscopy these pressure signals can be detected at the subsurface origin where the pressure is maximum, making PARS microscopy a great candidate for *in-vivo* ophthalmic imaging applications. Since the employed objective lens of the system has long enough working distance (~ 30 mm) compared to the diameter of mouse eyeball (~3 mm), therefore imaging the posterior segment of the eye was also possible using the current setup. The axial resolution of the PARS system (~ 100 μm), enables separating the signals of retinal blood vasculature from the RPE melanin given the retina thickness of ~ 200 μm[419]. The imaging depth of the system was measured to be ~ 3 mm corresponding for the size of the mouse eyeball. Figure **6-5**C demonstrates representative image acquired *in-vivo* from melanin content in RPE and choroid layers through PARS microscopy. In Figure **6-5**C, the honeycomb shaped RPE cells can be appreciated, however involuntary eye motion has distorted part of the image. Additionally, according to the Takekoshi et al. study[420], the RPE cells are more irregular in

albino mice compared to pigmented ones which can partially explain the irregularity present in the images.

Capitalizing on the distinct difference in the absorption spectra of oxyhemoglobin HbO_2 and deoxyhemoglobin Hb, we used two excitation wavelengths (532 nm and 558 nm) to estimate the concentration of HbO_2 and Hb. These two wavelengths have been successfully applied for measuring SO_2 in previous reports[421]. The 532-nm wavelength is close to an isosbestic point, and the 558-nm wavelength is more absorptive for Hb than HbO_2[422]. Figure **6-5** D&E show PARS images acquired from vasculature around the iris with 532 nm and 558 nm wavelengths, respectively. The different absorption coefficients at the two wavelengths make it possible to implement the linear SO_2 model. Briefly, an inverse problem is solved to estimate the relative concentrations of oxy- and deoxyhemoglobine on a per-pixel basis. The photoacoustic response is approximately linear with respect to hemoglobin concentration, and as such a regularized least squares algorithm can be used to solve for the relative concentrations. Once the relative concentrations of oxy- and deoxyhemoglobin, $[HbO_2]$ and $[Hb]$ respectively, have been obtained, oxygen saturation (SO_2) is estimated as $\frac{[HbO2]}{[HbO2] + [Hb]}$.

Blood oxygenation levels shown in Figure **6-5**F are pseudocolored from red to blue in an ascending order. The peripheral parts of the vessels have mainly lower oxygen saturation compared to the central regions which can be explained by oxygen uptake in the capillaries and delivery to the ocular cells[423]. The values measured in this study are an approximate estimation of blood oxygenation, and to further analyze the accuracy of PARS SO_2 measurement comprehensive phantom-based study using *in-vitro* blood will be conducted. In

addition, the method will be compared with other conventional techniques such as visible light OCT and multiwavelength fundus photography.

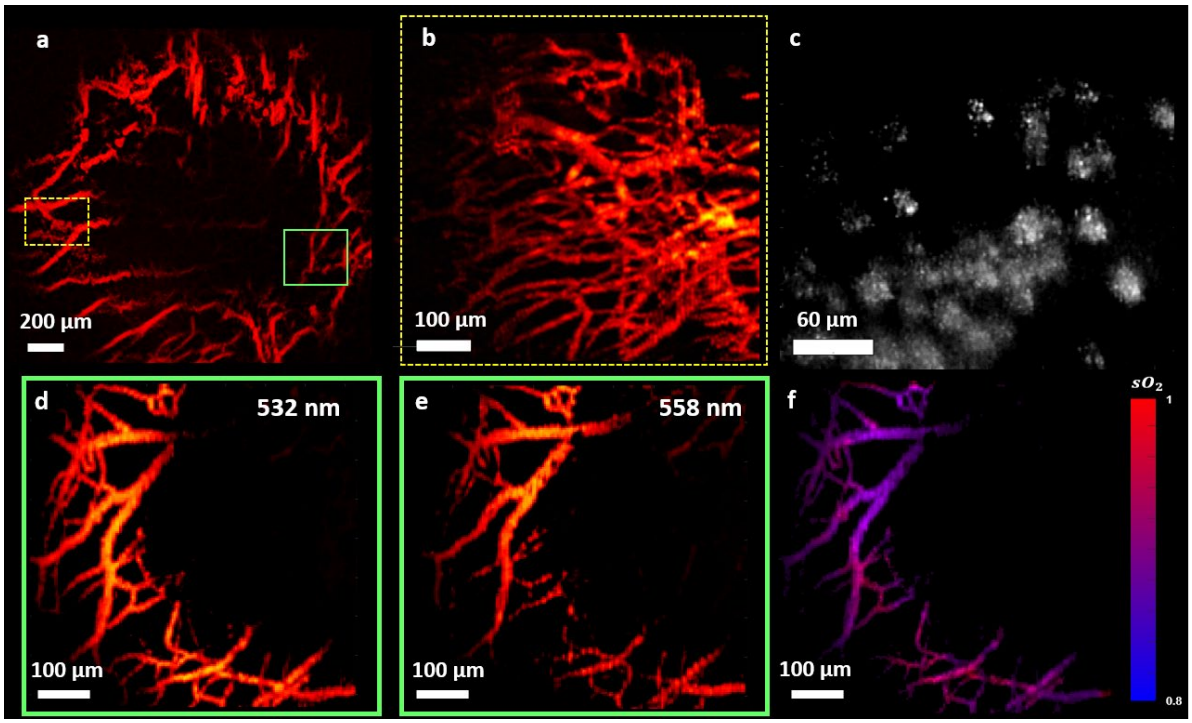

Figure 6-5. *In-vivo* imaging of ocular tissue using PARS. Vasculature of the iris imaged from ~ 2.5 mm × 2.5 mm area (A) Vasculature around the iris imaged with PARS (B) *In-vivo* images of melanin content in RPE and choroid layers (C) Images acquired using multiwavelength PARS system at 532 nm (D) 558 nm (E) and the corresponding SO_2 map (F).

Finally, the multimodal system is used for simultaneous imaging of the ocular tissue. Figure **6-6** shows representative images acquired using 0.4 NA microscope objective with the multimodal system. Figure **6-5**A depicts OCT volume rendering of a ~ 0.7 mm ×0.7 mm area. In Figure **6-5**B, cross-sectional B-Scan is presented, with iris tissue in focus. The focus of the system is adjusted to be on the iris and yellow arrows show cross-section of the iris vasculature. Figure **6-5**C represents e*n-face* OCT image generated from a single depth layer. The corresponding PARS image acquired simultaneously is presented in Figure **6-5**C, yellow spline in both images represent a large vessel which appeared in both images. The overlayed image

is presented in Figure **6-5**E. Involuntary eye and head motions have distorted parts of the image in both PARS and OCT. Since the lateral resolution of the PARS subsystem is ~ 2X higher than the OCT system, smaller vasculature can be seen in the PARS image which are not clear in the OCT image. Additionally, in the current PARS setup, the detected signal is from all depths withing the detection beam depth-of-focus [335], therefore, some of the vessels in the PARS image which are not visible in the OCT *en-face* image, could be located in upper/lower layers.

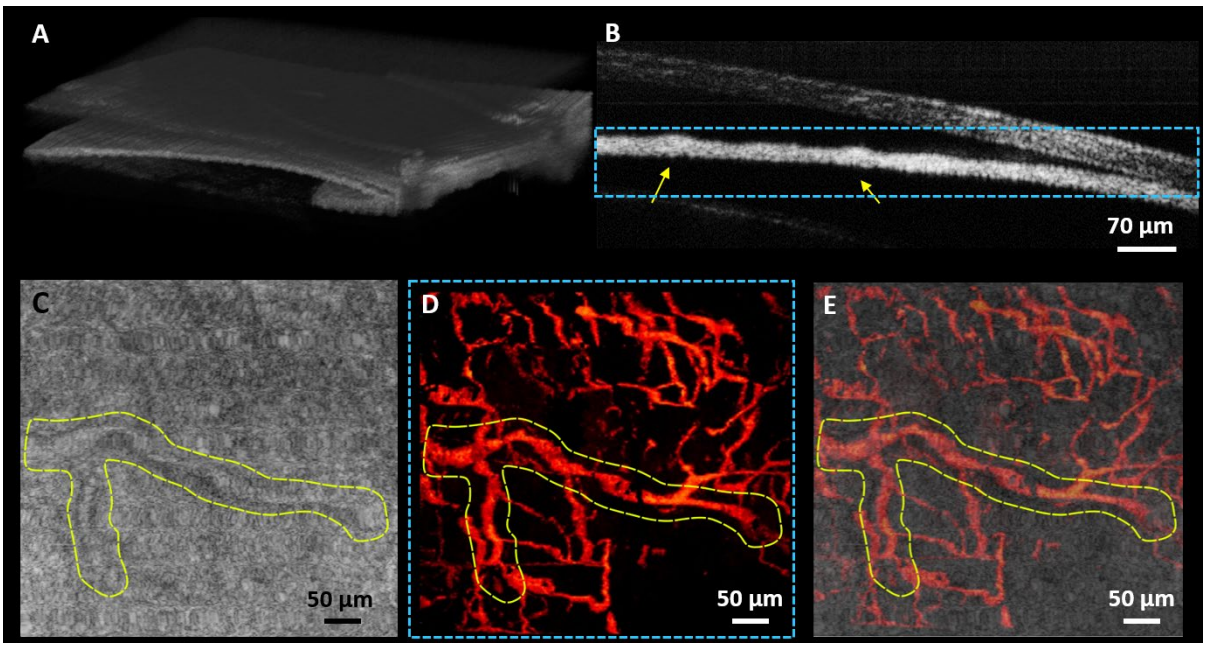

Figure 6-6. *In-vivo*, non-contact, simultaneous imaging of the ocular tissue using multimodal PARS-OCT system. Volume *OCT* rendering of the eye *(*A). OCT B-scan representing cross-section of the iris vasculature (yellow arrows) *(*B). *en-face* OCT image *(*C). vasculature of the iris imaged with the PARS subsystem *over the dashed area (*D). Overlayed PARS and OCT images *(*E).

There are several aspects that can be further studied in future works. We are planning to conduct a comprehensive study to evaluate the performance and sensitivity of the proposed multiwavelength PARS microscopy for accurate measurement of oxygen saturation and to compare it with other conventional techniques. Other animal models including rats and rabbits would be also employed to evaluate the performance of the system for imaging both anterior

and posterior parts of the eye. In addition, to improve the field-of-view of the system required for imaging larger eyeballs we plan to employ customized scan lens. Furthermore, we are planning to quantify ocular blood flow using Doppler-OCT and PARS microscopy. These capabilities will provide us with local SO_2 and blood flow that will lead to oxygen metabolic rate which is a potential biomarker for major eye diseases[424].

6.7. Conclusions

In summary, for the first time, we presented *in-vivo*, non-contact, simultaneous, functional and structural ophthalmic imaging using multiwavelength PARS microscopy combined with SS-OCT. The presented multimodal system provides complementary imaging contrasts of optical absorption and optical scattering. The capability of PARS microscopy for providing both absorption and scattering imaging contrasts was presented for the first time. The non-contact imaging ability offered by both systems makes them a favorable companion for clinical ophthalmic imaging applications. The reported system is a major step toward non-invasive, simultaneous, and accurate measurement of functional details in the ophthalmic tissue and can assist ophthalmologists with the diagnostics and treatment of major eye diseases.

Chapter 7

In vivo functional and structural retina imaging using multimodal photoacoustic remote sensing microscopy and optical coherence tomography

Notes and Acknowledgement

This chapter summarizes results from a study on the application multimodal PARS-OCT for *in vivo,* non-contact, functional and structural retinal imaging. To make system compatible for retina imaging, the microscope objective lens was removed. The optical power of the eye was used to focus the beams on the back of the eye. Additionally, the 50:50 telecentric pair was replaced with a 50:30 telescope to reduce the beam size. To our knowledge this is the first time a non-contact photoacoustic imaging technique is employed for *in vivo* oxygen saturation measurement in the retina. The content of this chapter is submitted to Scientific Reports journal:

Zohreh Hosseinaee, Nicholas Pellegrino, Nima Abbasi, Tara Amiri, James A. Tummon Simmons, Paul Fieguth, Parsin Haji Reza " *In vivo* functional and structural retina imaging using multimodal photoacoustic remote sensing microscopy and optical coherence tomography " (*submitted to Scientific Reports*)

Author contributions

Zohreh Hosseinaee studied and designed the modifications required for retina imaging, co-designed with supervisor the SO_2 accuracy experiments, conducted the experiments, processed the images, contributed to the interpretation the data, prepared the figures, and wrote the main manuscript.

Nicholas Pellegrino developed and implemented the signal unmixing method.

Nima Abbasi constructed the software of the OCT system.

Tara Amiri assisted with conducting SO_2 validation experiments.

Alexander James Tummon Simmons helped with designing the rat eye model phantom.

Paul Fieguth contributed to the interpretation of the results and provide guidance.

Parsin Haji Reza proposed the idea, conceived the study, contributed to the interpretation of all results, and acted as the primary investigators.

7.1. Introduction

Functional imaging techniques enable measuring alterations in biological function including metabolism, blood flow, regional chemical composition, and biochemical processes. These methods promise to dramatically improve the ability to study *in-situ* biochemistry and disease pathology[425]. In ophthalmology, functional changes most often precede structural changes in major eye diseases. Detecting these alterations aids in understanding pathogenesis, early diagnosis, and timely management of ophthalmic disorders. Retinal oxygen saturation (SO_2) and metabolic rate of oxygen consumption (MRO_2) are among the most important biomarkers characterizing the pathophysiological status of the posterior eye. Additionally, abnormal retinal SO_2 levels are believed to be involved in major eye diseases such as diabetic retinopathy (DR) and age-related macular degeneration (AMD) [426]–[428]. Therefore, the precise measurement of retinal oxygen saturation can be critical in investigating these blinding diseases. Additionally, since the retinal arterioles are derived from the central nervous system. Presuming the retinal arterial oxygen content is identical to the systemic circulation, retinal oximetry may provide relevant information on oxygen delivery to the central nervous system. Therefore, determination of oxygen saturation in the retinal vessels could enhance the monitoring and treatment of critically ill patients in the intensive care units[429]. Oxygen-sensitive electrodes and magnetic resonance imaging have been used to measure retinal SO_2, however these methods are usually restricted to terminal experiments and/or limited by low spatial resolution[427], [430]. Phosphorescence lifetime imaging has been also applied to map ocular oxygenation in animal models. Unfortunately, the need to inject fluorescent probes into systematic circulation makes the method inappropriate for human practice[401].

Recently, researchers are focused on optical imaging-based methods to evaluate retinal oxygenation. Optical imaging methods are capable of non-invasive SO_2 measurement and they can visualize the spatial distribution of oxygenation with high resolution in ocular environment[365]. Optical measurement of SO_2 is possible because the two forms of hemoglobin, oxy- and deoxyhemoglobin (HbO_2 and Hb), have distinct optical absorption properties. Owing to the differences in the absorption spectra of oxy- and deoxyhemoglobin, multi-wavelength imaging methods can assess the SO_2 in retinal vessels[431]. Currently available optical imaging modalities, such as fundus photography[432], scanning laser ophthalmoscope (SLO) [433], and optical coherence tomography (OCT) [30], [73], [79] are scattering based techniques and rely on the back-scattered light from the tissue to form an image. Despite the great progress in these optical imaging techniques, however, they use indirect methods to measure optical absorption. Therefore, the accuracy of these methods is affected by factors such as variation in vessel size[434], pigmentation[435], multiple light paths[419], and vessel wall thickness[431]. For example, in larger vessels the amount of detected backscattered light is much greater than in small vessels[419], hence the calculation of the optical density and SO_2 values can be affected in clinical trials[436],[437]. Additionally, it is shown that SO_2 variations, induce changes in vessel diameter[431], which may further alter the amount of backscattered light from the vessel and consequently the SO_2 measurements.

Photoacoustic microscopy (PAM), has the unique capability to map the direct optical absorption properties with high resolution in biological tissues[438]. The modality has the potential to overcome the limitations of current ocular imaging methods in functional

studies[439]. It has been shown in simulation studies that by increasing the vessel diameter and melanin concentration, the relative error of SO_2 measurement in the scattering-based method increases. However, the SO_2 measurement was insensitive to these parameters in PAM [436]. As these results suggest, PAM can be potentially a more accurate tool in quantifying retinal SO_2. However, the disadvantage of PAM in ophthalmic imaging arises from its need to be in contact with the ocular tissue[440]. This physical contact may increase the risk of infection and may cause patient discomfort. Additionally, it applies pressure to the eye and introduces barriers to oxygen diffusion and alter physiological and pathophysiological balance of ocular vasculature function[365]. Additionally, the use of ultrasonic signal detection scheme poses challenges in combining the technology with other imaging modalities[440].

Recently our group at PhotoMedicine Labs for the first time demonstrated non-contact photoacoustic imaging of the ocular tissue in murine eye using photoacoustic remote sensing (PARS) microscopy[381]. Later we combined the technology with OCT and applied it for *in-vivo* non-contact imaging of the anterior segment in the mouse eye[365]. We showed the potential of the system for estimation oxygen saturation in the iris vasculature and visualizing melanin content in the RPE. Building on the proven strength of PARS imaging, we further developed the technology to address the aforementioned need in retinal oximetry. In this paper we report our latest progress on *in-vivo* retinal imaging and present the capability of the reported non-contact multimodal imaging system for visualizing structural and functional information of the rodent retina. To our knowledge, this is the first time a non-contact photoacoustic imaging technique is applied for measuring oxygen saturation in the living

retina. This reported work has the potential to advance the diagnosis and treatment of major retinal disorders.

7.2. Method

7.2.1. System architecture

Figure 7-1 demonstrates the experimental setup of the multimodal PARS-OCT system. Briefly, the output beam of a 532-nm, ytterbium-doped laser (IPG Photonics) with 1.5 ns pulse-width is coupled to a single mode optical fiber. At the output end of the fiber multiwavelength spectral peaks are generated through stimulated Raman scattering (SRS). SRS efficiency could be affected by temperature and airflow changes, and random errors and drift in pulse energy[375]. To improve the stability of the SRS peaks, the fiber was kept in a temperature-controlled unit to isolate the airflow and the temperature[441]. The laser output was collimated into 2.1 mm diameter, then merged with the PARS probe beam centered at 830 (SLD830S-A20, Thorlabs) and the light of SS-OCT (center wavelength: 1060 nm; 100 nm spectral bandwidth, 60 kHz swept rate, Thorlabs). A two-dimensional galvanometer scanned the combined light beams (GVS012/M, Thorlabs) and relayed them to the eye through a telescopic lens (50:30 ratio) system. The pivot point of the telecentric pair is properly positioned to relay the galvanometer mirrors onto the entrance pupil of the eye, thereby minimizing vignetting. In PARS, pressure waves induced by light absorption were detected by the probe beam. The back-reflected light from the retina is directed towards the detection path. The quarter wave-plate transforms the reflected circularly polarized light back to linearly polarized light, which enables the polarized beam splitter to direct the back-reflected light towards the photodiode. The photodiode outputs are connected to a high-speed digitizer (CSE1442, Gage Applied,

Lockport, IL, USA) that performs analog to digital signal conversion. In SS-OCT, backscattered light from the retina first interfered with the reference arm beam, then detected by the built-in dual balanced photodetector. The OCT signal was digitized by a high-speed A/D card (ATS9351, Alazar Technologies Inc., Pointe-Claire, QC, Canada). The raw OCT data was transmitted to a host computer through a PCI-Express interface. OCT system control was implemented in MATLAB platform to automatically control all the operations including system calibration, galvo-scanning, system synchronization, real-time imaging preview and data acquisition. The lateral resolutions of both PARS and SS-OCT were around ~ 6 μm in the retina with a slight difference caused by the different spectral ranges. The axial resolutions of PARS and OCT were ~40 μm and ~7.3 μm, respectively.

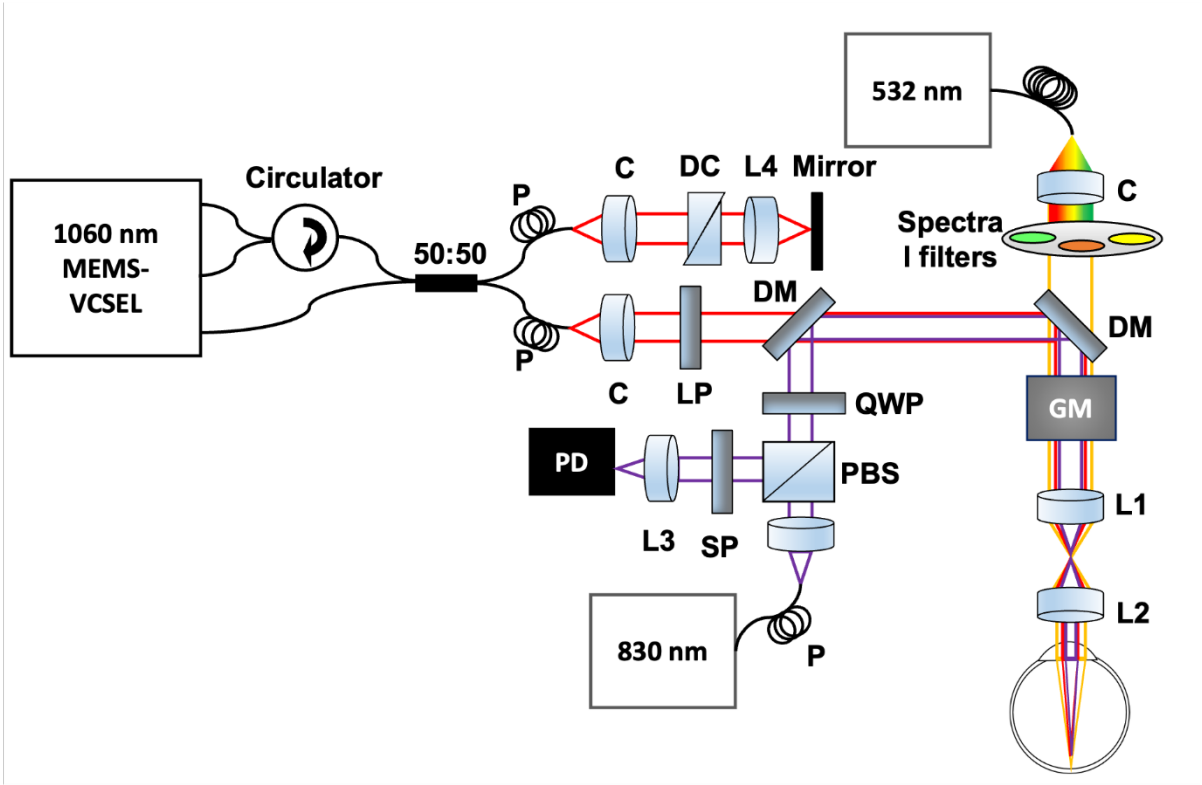

Figure 7-1 Simplified schematic of the multimodal PARS-OCT system. DM: Dichroic mirror, QWP: Quarter wave plate, PBS: Polarized beamsplitter, LP: Long pass filter, GM: Galvanometer mirrors, L: Lens, C: Collimator, PD: Photodiode. DC: Dispersion compensation, P: Polarization controller.

7.2.2. Image reconstruction

All the PARS images shown in this manuscript were formed using a maximum amplitude projection (MAP) of each A-scan for each pixel of the *en-face* image. The images were produced by direct plotting from interpolated raw data using a Delaunay triangulation interpolation algorithm[351]. All images and signal processing steps were performed in the MATLAB environment.

For each OCT data set, 500 A-lines were acquired for each B-scan. For each A-line trigger, 2448 sampling points were acquired to cover the resultant spectral interferogram, providing a depth ranging distance of ~ 12 mm. To extract the OCT complex data, reference spectrum was subtracted from the interference signal to remove DC bias, then Fourier transform was performed to extract the depth-resolved OCT signal. Images were generated from the raw OCT data and numerically dispersion compensated up to the 5th order with a custom MATLAB algorithm[413]. No additional image post-processing was used for the OCT images presented in this paper. The volumetric and en-face images were generated from the 3D data sets with ImageJ[414].

7.2.3. Animal preparation

All the experimental procedures were carried out in conformity with the laboratory animal protocol approved by the Research Ethics Committee at the University of Waterloo and adhered to the ARVO statement for use of animals in ophthalmic and vision research. All sections of this report adhere to the ARRIVE Guidelines for reporting animal research. Albino rats (NU/NU, Charles River, MA, USA) were imaged to demonstrate the *in vivo* capabilities of the system. A custom-made animal holder was used to restrain the animal. The base of the

animal holder was lined with a thermal pad to keep the animal body temperature between 36° and 38°C. One drop 0.5% proparacaine hydrochloride (topical anaesthetic; Alcaine, Alcon, Mississauga, ON, Canada) was applied to the eye, followed by one drop of 0.5% tropicamide (pupillary dilator; Alcon). Artificial tears were used frequently (~ every 2 minutes) to keep the cornea hydrated. Vital signs, such as respiration rates, heart rates and body temperature were monitored during the experiment.

7.3. Results

7.3.1. Phantom imaging

Initial calibration of the PARS sub-system was achieved through imaging phantom eye models. First, we used a realistic human eye model to test the feasibility of PARS on the retina. The phantom is shown in Figure 7-2a, and it was modified from a commercial product (OEM-7, Ocular Instruments, Bellevue, WA). The model consists of the cornea, crystalline lens, aqueous humor, vitreous humor, and artificial retina. Strings of 7 μm carbon fibers (CF) were placed at the bottom of the model where the artificial retina is located (Figure 7-2b), and they were imaged using the PARS system. Figure 7-2c shows representative PARS image acquired from CF at the back of the human eye model and Figure 7-2d shows corresponding image acquired using PARS scattering mechanism described in our previous report[365]. The PARS excitation and PARS detection are co-aligned, so that the same fibers are in focus in both absorption and scattering contrast images (white arrow).

Then a custom rat eye model was developed to help with the alignment of PARS excitation and detection beam for *in-vivo* trials. The eye model consisted of a single achromatic lens (63-817; Edmund Optics, Inc) with numerical aperture and curvature close to that of in the rat eye,

and a custom 3D printed plastic chamber. Strings of 7 μm carbon fibers were located at a fix distance from the lens (Figure 7-2e) corresponding to the focus of the lens and was approximately equal to the path length of a rat eye [442]. Representative images acquired using absorption and scattering contrast of PARS system are shown in Figure 7-2f-g. Similar to the human eye model, the excitation and detection beams were co-aligned so that the same CF are in focus in both images (white arrows).

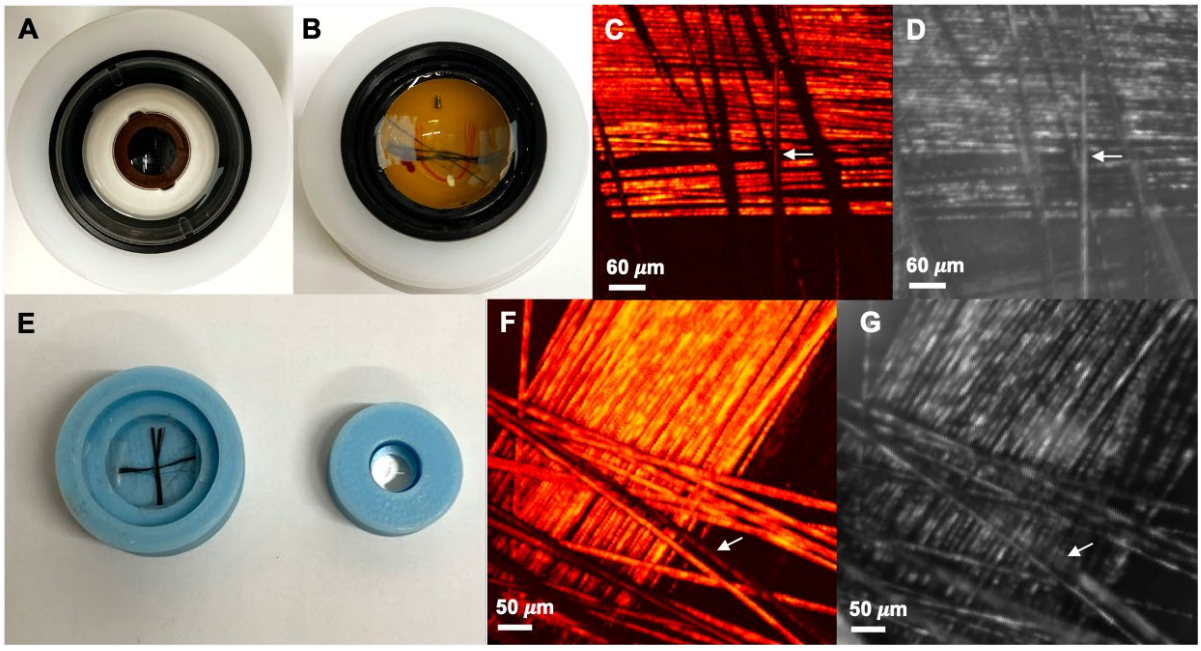

Figure 7-2. Imaging phantom eye models for human and rat. (A) Human eye model consisting of the cornea, crystalline lens, aqueous humor, vitreous humor, and artificial retina. (B) Strings of 7 µm carbon fibers are placed at the bottom of the eye model. (C) CF image acquired with PARS system. (D) CF image acquired using PARS scattering mechanism. (E) Custom rat eye model consisting of a single achromatic lens and a 3D printed plastic chamber and strings of carbon fibers. (F-G) PARS absorption and scattering contrast images, respectively. PARS excitation and detection beams are co-aligned so that the same CF are in focus in both images (white arrows).

7.3.2. SO_2 accuracy

The accuracy of the multiwavelength PARS sub-system in measuring oxygen saturation, was investigated by performing *in-vitro* phantom experiments using freshly collected bovine blood (Peel Sausage, Drayton, ON) with Sodium Citrated anticoagulant solution. Figure 7-3a shows the experimental setup. The setup included a blood reservoir, tubing, oxygen tank, oxygen

meter access points and a syringe pump (NE-4000, New Era Pump Systems, Inc.). Different levels of oxygen were delivered to the blood reservoir. Blood samples were drawn before and after image acquisition for CO-oximetry measurements. A clinical grade CO-oximeter (Avoximeter 4000, Instrumentation Laboratory LTD, Richmond Hill, Canada) served as a reference device for measuring blood oxygen saturation.

Images of glass capillary with flowing blood (20.00 ml/min), are acquired at 532 nm and 558 nm excitation wavelength (Figure 7-3b-c, shown from the top view in the X-Y plane). The depth of focus of the imaging system (~ 100 μm) was smaller compared to the size of the glass capillary (~ 200 μm). Therefore, to collect adequate data points, the focus is adjusted to the middle of the capillary which results in the black region in the center of the image (shadow effect from the higher depths blood absorption). The oval shape of the capillary can be resulted from the field curvature caused by the large field of view used to acquire signal from the full capillary. To estimate the SO_2, representative signal values were extracted from the two images. It is assumed that the SO_2 is homogeneous within the capillary and the mean values are extracted. Compared to the per-pixel basis estimation, the mean value method offers higher accuracy by reducing the impact of random errors. Here, rather than averaging the signal intensity over the entire image, only a sub-region where the target is adequately in-focus is used. The PARS signal intensity within the selected region is averaged to arrive at a representative value associated with each excitation wavelength. The relative concentrations of oxy- and deoxyhemoglobin and the corresponding SO_2 value is then calculated. The PARS measurements showed 40% and 60% oxygenation over 4 separate measurements, which were found to be within 6% accuracy (measured as standard deviation of the acquired data) with the

oximeter results. The value is in the range reported by other photoacoustic imaging studies [443], [444], and approaches the ISO-defined acceptable performance criterion for oximeters (< 4%) [445]. To further improve the accuracy several factors can be considered in future works. For example, nonlinear methods employing more than two optical wavelengths can be implemented to compensate for the absorption saturation effect [446]. Furthermore, to reduce the effect of laser pulse energy fluctuations, a more stable tunable source can be employed and ultrashort switching time (a few hundred nanoseconds) among wavelengths can be applied.

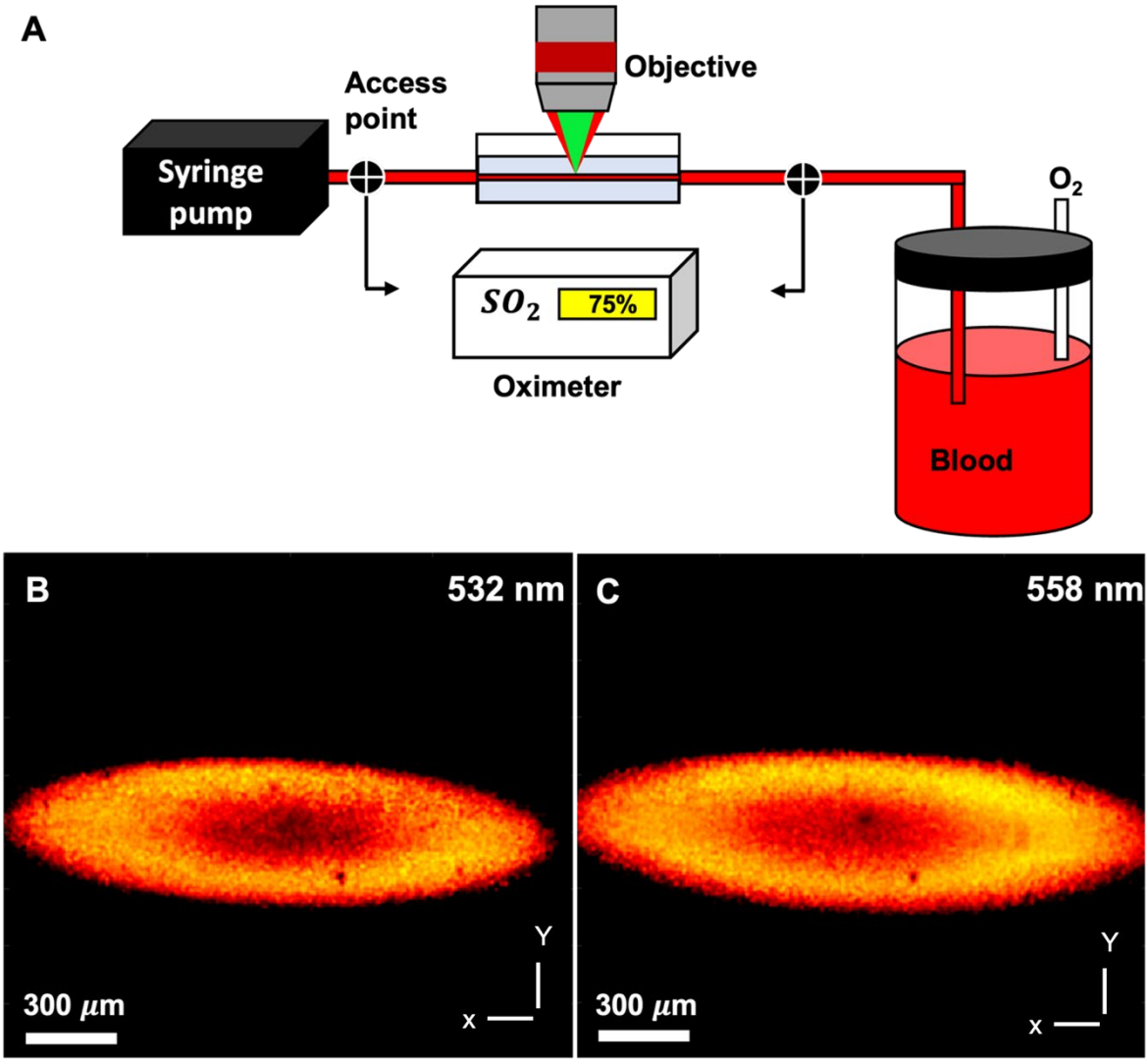

Figure 7-3. (A) Experimental setup of the in vitro phantom experiment using bovine blood. (B-C) Images of glass capillary with flowing blood acquired at 532 nm and 558 nm excitation wavelength, respectively.

7.3.3. Retina imaging

First the capability of the SS-OCT system was tested on the rat retina, and it was used to guide the PARS imaging system. Cross-sectional and volumetric OCT images of the rat retina are demonstrated in Figure 7-4. Each data set is acquired in ~10 seconds. Cross-sectional images enable visualization of major retinal layers. Retinal nerve fiber layer (NFL) and the retinal ganglion cell layer (GCL) form the innermost (top), highly reflective band. Beneath this are the inner plexiform (IPL), inner nuclear (INL), outer plexiform (OPL), and outer nuclear layer (ONL). In principle, those layers formed of nerve fibers, i.e., IPL and OPL, show high-backscattering, whereas the nuclear layers have low-backscattering. The junction between the inner segment and outer segment of the photoreceptors (I/OS PR) could be visualized, as well as the highly reflective band which comprises the RPE (Figure 7-4b). In the OCT images central retinal artery (CRA) remnant were also visible. (Figure 7-4a). OCT fundus views are also generated by axially summing the merged OCT data set (Figure 7-4c-e). From the OCT fundus image, as shown in Figure 7-4c, specific anatomy of the rat retina is visualized, including the optic nerve head, some large retinal vessels and optic nerve fiber bundles as indicated by the yellow arrows. Figure 7-4e shows the retinal microvasculature in the deeper retinal layer (Red arrows).

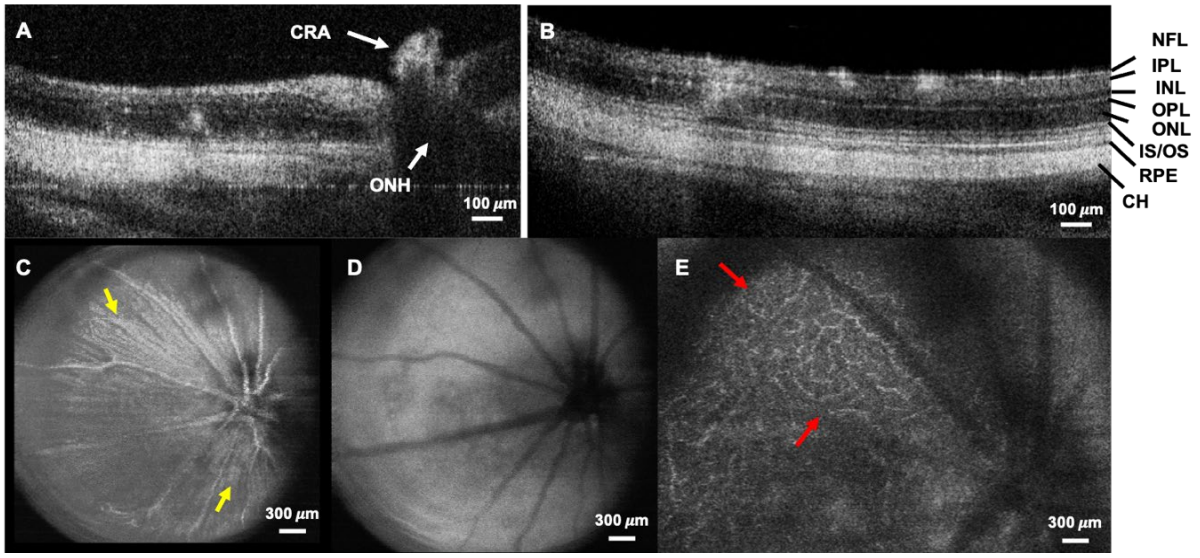

Figure 7-4. Volumetric and cross-sectional OCT images. (A-B) cross-sectional images acquired *in vivo* from rat retina showing distinct layers of the retina. NFL: nerve fiber layer, IPL: inner plexiform layer, INL: inner nuclear layer, OPL: outer plexiform layer, ONL: Outer nuclear layer, IS/OS junction of inner segment and outer segment layer. RPE retinal pigment epithelium layer, CH: choroid, CRA: central retinal artery, ONH: optic nerve head. (C-E). OCT fundus images visualizing optic nerve head, large retinal vessels, optic nerve fiber bundle (yellow arrows), deeper retinal layer microvasculature (red arrows).

These high-definition structural information of the SS-OCT subsystem can be well complemented by absorption based functional information obtained from PARS microscopy. The axial resolution of the PARS system (~ 40 μm), enables separating the signals of retinal blood vasculature from the RPE melanin given the retina thickness of ~ 200 μm[419]. As a result, PARS signals generated from major vessels can be considered to be mainly from hemoglobin. Figure 7-5a demonstrates fundus PARS image acquired from large vessels around ONH from a 2.6 mm × 2.6 mm area. Smaller vessels are also visible in the image; however, they are slightly distorted by motion artifacts. Figure 7-5b shows a zoomed-in section of one of the vessels acquired from a similar area where the smaller vasculature is more visible. In the previous report of PARS-OCT system[365], the PARS scattering contrast provided through the PARS detection beam was introduced. In retinal imaging applications, this capability allows the PARS microscope to be used the same way as fundus photography to image the

interior surface of the eye. Figure 7-5c, show a representative image acquired from the ONH using scattering contrast of the PARS system. Since 830 nm beam used in the proposed architecture, has different absorption coefficient for oxygenated and de-oxygenated hemoglobin (higher absorption for oxygenated hemoglobin); arteries appear dark (red arrows), and veins are light (blue arrows) in the image. Therefore, the scattering contrast of PARS microscope, can be used similar to retinal oximeters to measure oxygen saturation in the eye[447].

Relying on the proven strength of the PARS sub-system in providing functional information, the amplitude of multiwavelength PARS signals were employed to estimate SO_2 in every vessel (Figure 7-5d). The calculation is done based on the molecular extinction coefficients of HbO_2 and Hb at 532 nm and 558 nm optical wavelengths. The rodent's venous SO_2 measured with PARS was around 70% which agrees with previous reports [448]. Despite the good match between measured SO_2 by PARS and the preset SO_2 for blood experiments, the *in-vivo* rodent experiments conditions are different from those in *in vitro* experiments. For example, there are eye movements during imaging, notable chromatic aberration from the eyeball, etc. Whether such differences will affect the SO_2 quantification or not require future validation [449], [450]. Additionally, it is reported that visual stimulus might increase the retinal vessel diameter and blood flow, as well as affect the retinal SO_2 due to retinal neurovascular coupling[451]. These factors may affect the accuracy of the SO_2 measurements, and they need further investigation in the future. To our knowledge, this is the first report of optical absorption based retinal SO_2 demonstrated in the fundus view. It is important to note that PARS can provide two independent absorption contrast effect. First, is the absorption contrast provided by the

excitation laser. In this case, an isosbestic detection laser wavelength can be used to only visualize the excitation effect. Finally, PARS detection laser can also act as the secondary absorption contrast (Figure 7-5c.). The combination of these two effects, which is unique to PARS microscopy, can lead to more accurate measurements compared to current methods. This will be investigated further in the future.

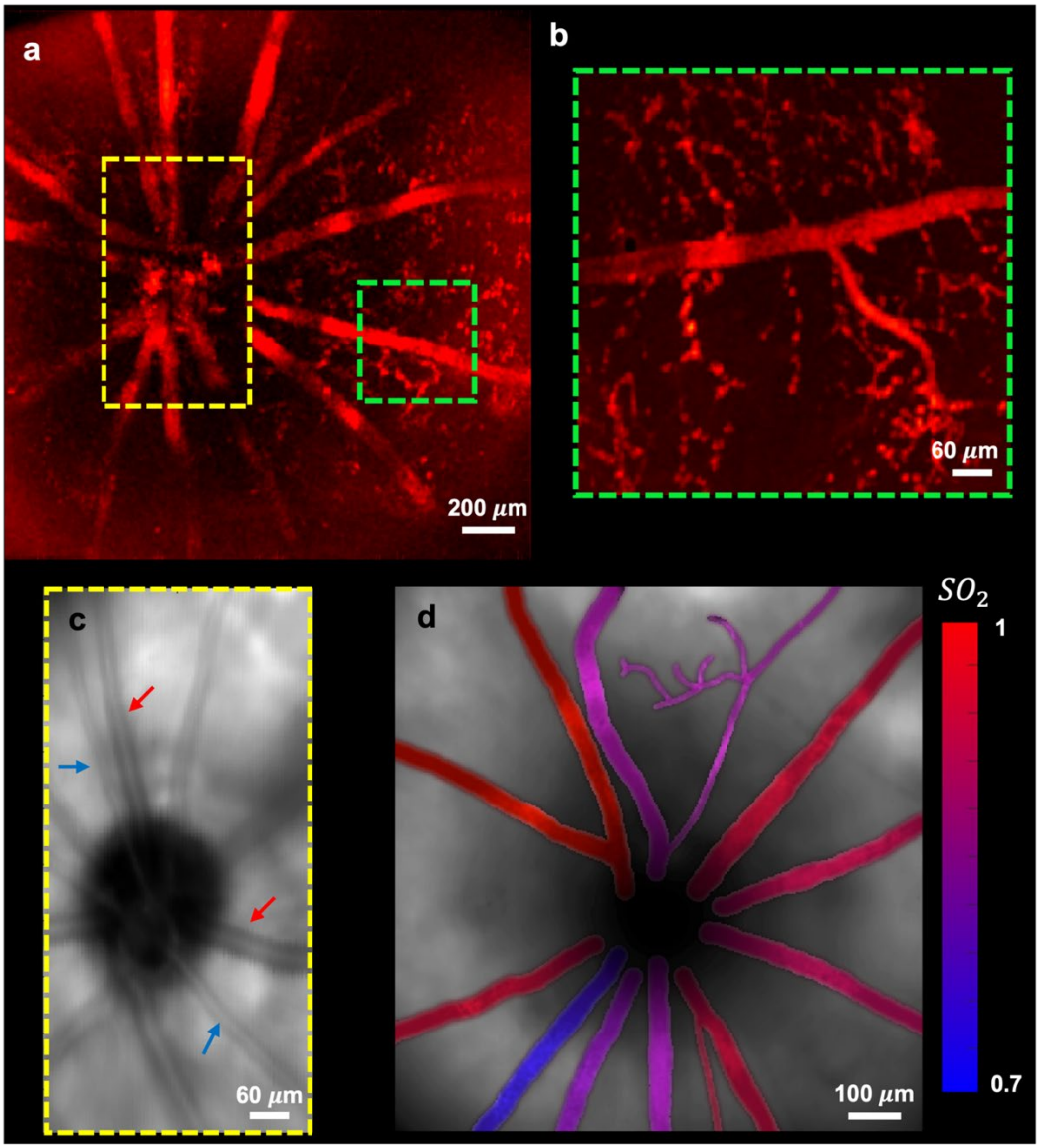

Figure 7-5. (A) Fundus PARS image acquired from large vessels around ONH from a 2.6 mm × 2.6 mm area. (B) zoomed-in section of one of the vessels acquired from a similar area with smaller vasculature. (C) Fundus image acquired using scattering contrast of PARS system. (D) Oxygen saturation map in the retina obtained using multiwavelength PARS imaging.

7.3.4. Ocular light Safety

Using ANSI standards, the ocular light safety for the developed multimodal PARS-OCT system can be calculated[357], [415]. First, the safety of PARS excitation laser is tested using the three ANSI rules: single pulse limit, average power limit, and multiple pulse limit. The pulse duration for the IPG laser used in this study is $t_1 = 1.5\,ns$. In the imaging setup, assuming that the collimated laser beam after being focused by the eye has a maximum diameter of 20 μm on the retina, the angular subtense of the source:

$$\boldsymbol{\alpha = \frac{20\,\mu m}{17\,mm} = 1.2\,mrad < \alpha_{min} = 1.5\,mrad}$$

Where 17 mm is the focal length of human eye. Therefore, the light source can be considered as a point source.

Rule 1 Since the pulse duration of the laser is $1.5\,ns$ only the thermal effect needs to be considered and the maximum permissible exposure (MPE) will be:

$$MPE_{SP} = 5 \times 10^{-7}\,J/cm^2$$

Rule 2 Since the exposure time ($\sim 10\,s$) is longer than the $0.7\,s$ and the wavelength is between 400 and 600 nm, dual limits due to both thermal and photochemical effects apply here. For the photochemical effect:

$$MPE_{ph} = 4.36 \times 10^{-2}\,J/cm^2$$

For the thermal effect:

$$MPE_{th} = 1.01 \times 10^{-2} J/cm^2$$

Rule 3 tests whether an exposure by a long pulse of duration $nt_1$is safe. Within a laser spot of 20 μm, there are at most two overlapping laser pulses (n = 2).

$$MPE_{rp} = n^{-0.25} \times MPE_{sp} = 0.84 \times 5 \times 10^{-7} = 4.2 \times 10^{-7} J/cm^2$$

Rule 3 is the most conservative of the three. Considering a pupil diameter of $D = 0.7\ cm$ MPE for a single pulse would be equal to $MPE_{rP} \times \left(\frac{D}{2}\right)^2 \times \pi \approx 160\ nJ$. The acquired value is in correspondence to the values reported by other groups[14], [452]. In this manuscript the energy of a single pulse is $<\ 150\ nJ$ which is below the allowed pulse exposure limit.

For λ=380 – 1400 nm, a spectrally flat limit was recently introduced that recommends MP corneal irradiances of $25t^{-0.75}$ W/cm^2 for $t\ <10\ s, (t = 10,\ MP = 4.4$ W/cm^2), and 4.0 W/cm^2 for $t\ >\ 10s$[453]. Based on the proposed limit the OCT light power on the cornea ($\sim 1.5\ mW$) and the PARS detection power ($\sim 2 - 3\ mW$) are well within the ANSI limits.

There are several aspects of the proposed system that can be further refined for future studies. The current PARS-OCT system was developed using visible excitation wavelength for targeting oxygenated and de-oxygenated hemoglobin in the blood. However, the laser safety threshold for ocular imaging is stricter in the visible than in the NIR spectral range. Additionally, the retina is sensitive to the visible light which poses challenges to eye fixation during imaging. Therefore, in future studies, the NIR spectral range can be examined as the excitation wavelength to overcome these issues. Additionally, the oxygen saturation measurement accuracy can be improved by using a more stable tunable light source and using nonlinear methods. In future, the scanning pattern of the SS-OCT system can be modified to enable Doppler OCT and OCT angiography and provide blood flow measurement and vasculature map, respectively. This information can be further combined with the non-contact oxygen saturation measurements of PARS to measure metabolic rate of oxygen consumption in the ocular environment in both small and large vessels. The system can be further applied

for evaluating the effects of visually evoked stimulus and how they could change this functional information. It can also be used in longitudinal studies on larger animal models like rabbit and monkeys with size of eyeballs closer to that of humans. Different eye disease models (such as Glaucoma, and DR) can be developed in these animals and the efficacy of the system be evaluated in diagnosis and monitoring of them.

7.4. Conclusion

In conclusion, for the first time, a non-contact photoacoustic imaging technique was applied for *in-vivo* measuring of retinal SO_2. It was also the first time multimodal *in-vivo* imaging of retina was demonstrated using multiwavelength PARS-OCT. The detailed structural information of OCT is well complemented with absorption-based functional information of PARS imaging. The proposed method can be a measure step toward non-invasive measurement of metabolic rate of oxygen consumption in retina, and it can further improve the diagnosis and treatment of important eye diseases.

Chapter 8
Ocular light safety

The invention and development of ophthalmic imaging instruments have increased our understanding of eye diseases and greatly improved the quality of treatments. Light safety is a major factor to consider when employing these devices. Studies to address safety concerns have been widely published over the past 40 years [357], [415]. The American National Standard Institute's (ANSI) Standard is among several safety standards that provide guidelines for the safe use of lasers in ophthalmic applications. Maximum permissible exposures (MPE) for different conditions in the ANSI Standard are derived on the foundation of animal (monkey, rabbit) testing to determine damage thresholds [453]. The MPE for a light source striking the retina in ANSI Standard is defined as the "level of laser radiation to which an unprotected person may be exposed without adverse biological changes in the eye"[412].

This chapter will discuss ocular safety of the developed multimodal PARS-OCT system and discuss important parameters that need to be considered for making the technology safe for clinical trials.

8.1. DAMAGE MECHANISMS AND EXPOSURE LIMITS

Retinal damage from light exposure occurs mainly from three main mechanisms:

a. ***Thermal damage*** is due to protein denaturation induced by temperature increases secondary to light absorption by melanin in the RPE. This form of damage can occur when the retina is exposed to laser light with a wavelength between 400 – 1400 nm for a duration longer than 20 μs [454]. For exposure durations longer than 20 μs, heat can dissipate out of the exposed area and the energy needed to produce retinal damage

increases with less than a linear dependence on exposure duration[455], [456]. For exposure durations shorter than ~20 μs, heat diffusion can be neglected, and the energy needed to produce retinal damage is independent of time.

b. ***Photochemical damage*** occurs at short visible wavelengths (400 – 600 nm), and it happens for exposure duration longer than ~ 1 second. It is associated with photo-oxidative damage to photoreceptors and lipofuscin pigments in the RPE. The energy needed to cause photochemical damage is independent of exposure duration[457].

c. ***Thermoacoustic damage*** occurs for pulses shorter than ~1 ns and is associated with various nonlinear mechanisms (laser-induced breakdown, self-focusing, etc.)[458]. Here less amount of energy is needed to cause retinal damage. Since the pulse duration and imaging time of our multimodal system is greater than 1 ns we do not consider it as a damage mechanism for our system.

Retinal irradiances or retinal radiant energies causing threshold retinal damage are converted into exposure limits that are generally expressed as maximum permissible (MP) radiant exposure (J/cm^2) for laser beams overfilling the pupil of the eye, which is the most common situation for accidental laser exposure.

8.2. Assumptions leading to exposure limits

The Standard's conversions of damage thresholds to exposure limits were based on several important assumptions as below:

8.2.1. Safety Factor and applicability

The exposure limits are set to be at least 10 times lower than the damage "threshold" expressed as a 50% probability of a minimum visible lesion. The Standard is derived for

healthy, alert individuals in occupational settings. Alert subjects exposed to bright light will either close their eyes or look away. This aversion reflex is not included in the Standard but can be accounted for by selecting the exposure duration of $0.25\ s$ for wavelengths in the 400–700 nm range[357].

8.2.2. Diameter of the Pupil

The Standard was developed under the assumption that the incident radiation overfills the natural pupil (iris) of the eye and that the pupil would constrict under bright lights in the visible spectrum. The duration of this pupil reflex is $0.2 - 1.0\ s$. Therefore, the pupil was assumed to be 7 mm in diameter (maximum natural dilation) for exposures shorter than $0.2 - 1.0\ s$. For longer exposures in the visible range, the pupil was assumed to constrict in response to bright light to a diameter of 3 mm. This protective effect of pupil constriction is included in the Standard[354].

8.2.3. Minimal Retinal Dimension

An underlying assumption in the Standard is that, for exposure by a collimated beam and durations less than ~1 s, the minimal retinal image is effectively ~25 μm in diameter (visual angle of 1.5 mrad). Although the point-spread function of the eye measured at half power is 4–6 μm wide[459], the sharp central peak is surrounded by a larger area containing substantial energy from small-angle forward scattering[459]. The resulting "thermal image" is ~25 μm, and the smallest observed thermal lesions were also of that order[460]. For exposure duration longer than ~1 s, eye movements redistribute the light over larger retinal areas, decreasing the retinal irradiance and thus the risk for injury compared with the instantaneous profile 25 μm in diameter[461]. For exposures of $100\ s$, the Standard uses a diameter of ~190 μm (visual

angle of 11 mrad) [462]. For even longer exposure durations, when task-determined eye and head movements dominate, the dimension of exposed retina is assumed to be ~1.7 mm in diameter (visual angle of 100 mrad or 5°).

8.2.4. Ocular Media

The retina is partially protected by absorption of light in the ocular media (cornea, crystalline lens, and vitreous). The crystalline lens absorbs light in $\lambda < 400$ nm, but the cornea and vitreous absorb for $\lambda <$ 300 nm, allowing harmful radiation (UV) to reach the retina if the lens is removed. Absorption by the ocular media of young adult subjects was incorporated into the Standard as well[463].

8.3. Concise presentation of the ANSI standard

The ANSI Standard gives the MP radiant exposure at the cornea ($MPH_C\ in\ J/cm^2$) (Table 8-1) for both small and extended sources. The MP levels for thermal and photochemical damage are dual limits for $\lambda \leq 600\ nm$ and $t \geq 0.7\ s$, and the smaller MP level is used. To use Table 8-1, first we must identify the cell that corresponds to our application. Then find the relevant parameters from Table 8-2 and calculate MPH_C. The MPH_C is the MP radiant exposure at the cornea for light overfilling the pupil.

Table 8-1 Maximum permissible radiant exposure MPH_c (in J/cm^2) at the cornea (Overfilling pupil) reproduced with permission from [357] © The Optical Society.

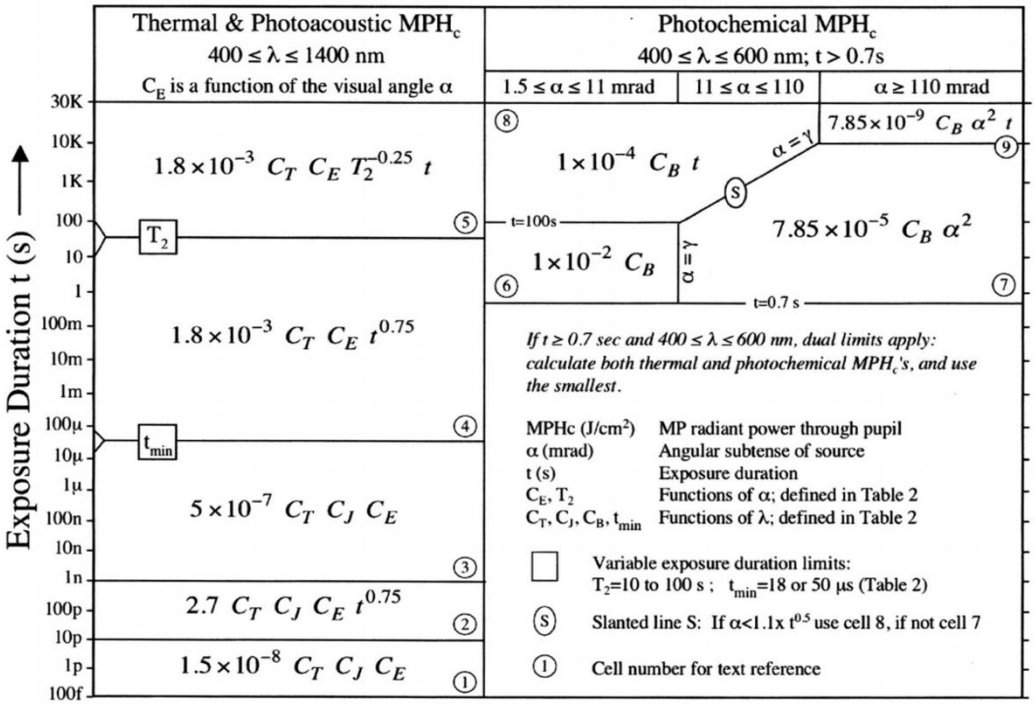

Table 8-2 Parameters to be used in Tables 8-1 and 8-3 reproduced with permission from [357] © The Optical Society.

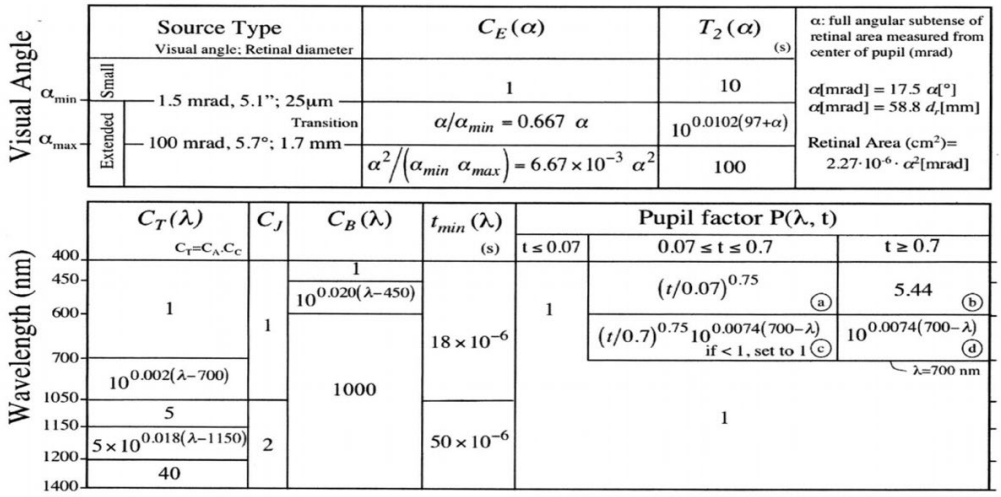

8.4. ANSI standard for ophthalmic applications

Optical devices that image the retina or perform diagnostic tests often bring light into the eye through a small area of the natural pupil (Maxwellian illumination). The exposure limits for ophthalmic applications in intrapupillary are expressed in radiant power ϕ (watts). Division by the exposure duration, t, converts energy to power. Table 8-3 together with the parameters defined in Table 8-2 gives the intrapupillary radiant power for light entering the pupil of the eye. The $MP\phi$'s in Table 8-3 were obtained by converting the MPH_c's of Table 8-1 using the area of 0.7 cm pupil and the pupil factor[357].

Table 8-3 Maximum permissible radiant power MPϕ (in watts) entering the natural or diluted pupil reproduced with permission from [357] © The Optical Society.

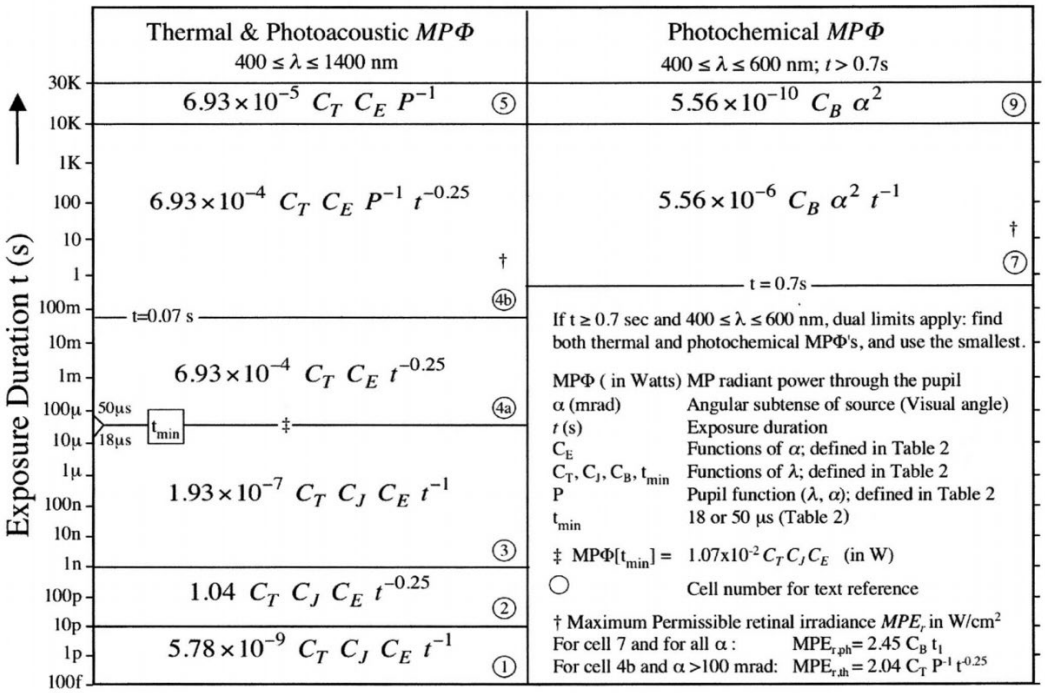

Table 8-3 can be used for most ophthalmic applications. If the wavelength (λ) and visual angle (α) of the retinal exposure duration (t) are known, then Table 8-3 shows which equations of

the thermal and photochemical limits are relevant. After eventual testing of the dual limits, one obtains the MP radiant power (in watts), for light entering the pupil of the eye.

The standards assume that the exposed retinal area is circular, if this is not the case, then an equivalent visual angle α_{eq}, is defined. The $MP\phi[\alpha = \alpha_{eq}]$ is the limiting power for an area corresponding to α_{eq}. Where the C'_E is defined as an effective scaling factor for use in computation of the $MP\phi$ for noncircular sources:

$$C'_E = C_E[\alpha = \alpha_{eq}] \times \frac{Area\ of\ noncircular\ field}{Area\ of\ circle\ subtended\ by\ \alpha_{eq}} \qquad \textbf{Equation 8-1}$$

Table 8-4 represents C'_E for rectangles of various dimensions as well as for squares and slits.

Table 8-4 Effective C'_E used in evaluating the $MP\phi$ for exposures in rectangular areas

Rectangle	Square	Slit
$\alpha_w < \alpha_{max}$ $\alpha_L < \alpha_{max}$ $\frac{8\alpha_L\alpha_w}{\pi\alpha_{min}(\alpha_L+\alpha_w)}$	$\alpha_w < \alpha_{max}$ $\frac{4\alpha}{\pi\alpha_{min}}$	$\alpha_w = \alpha_{min}$ $\alpha_L < \alpha_{max}$ $\frac{8\alpha_L}{\pi\,(\alpha_L+\alpha_{min})}$
$\alpha_w < \alpha_{max}$ $\alpha_L \geq \alpha_{max}$ $\frac{8\alpha_L\alpha_w}{\pi\alpha_{min}(\alpha_{max}+\alpha_w)}$	$\alpha_w \geq \alpha_{max}$ $\frac{4\alpha^2}{\pi\alpha_{min}\alpha_{max}}$	$\alpha_w = \alpha_{min}$ $\alpha_L \geq \alpha_{max}$ $\frac{8\alpha_L}{\pi\,(\alpha_{max}+\alpha_{min})}$
$\alpha_w \geq$ $\alpha_L \geq \alpha_{max}$ $\frac{4\alpha_L\alpha_w}{\pi\alpha_{min}\alpha_{max}}$		
α_L and α_w : visual angles subtending the length and the width of a rectangular field, respectively.		

8.5. Exposure by repetitive pulses

The material above describes safety limits for single-pulse exposures. The Standard also addresses the exposure by complex trains of pulses. Here we describe the case of evenly spaced pulses, each with the same energy. Such a pulse train is described by its pulse repetition frequency F, its total duration T, the number n of pulses $n = FT$, the duration t_1 and peak radiant power ϕ_1 of a single pulse, the energy per pulse Q_1 ($Q_1=\phi_1 t_1$), and the duty factor $\delta = Ft_1$. The ANSI Standard applies three "rules" that define three separate MP exposures (Table 8-5) and the rule that offers the highest protection is used. These MP levels are expressed in the same units so they can be easily compared with one another.

The first rule tests whether the radiant exposure of a single pulse (duration: t_1) exceeds the $MPH_c[t_1]$ at pulse duration t_1. In the more general form, it tests the safety of the brightest pulse in a train of uneven pulses, but this limit can also be applied for equally spaced equienergy pulses.

The second rule protects against average-power heat buildup in thermal injury and cumulative injury from the photochemical damage mechanism. It tests the safety of a continuous-wave (CW) equivalent exposure of duration T with a constant-power radiant power. The $MP\phi_{av}$ is then $MP\phi[T]$, and the corresponding radiant exposure per pulse is $(1/n)$ $MPH_c[T]$. Both thermal and photochemical limits must be tested separately.

The third rule protects against subthreshold pulse cumulative thermal injury and applies only to the thermal limits. It essentially tests whether the exposure by a long pulse of duration nt_1 is safe. The Standard formulation of rule 3 is as follows: "The exposure of any single pulse

within the group of pulses shall not exceed the single-pulse MPE (for $t_1 > t_{min}$) multiplied by $n^{-0.25}$.

Table 8-5 repetitive pulses (Evenly spaced pulsed of equal energy/pulse)

ANSI Rules		
	MP radiant exposure per pulse, $MPH_{c,1}$	MP radiant exposure per pulse, $MP\phi_{av}$
① Single Pulse Limit	$MPH_{c,1}[t_1]$	$\delta MP\phi[t_1]$
② Average Power Limit	$\frac{MPH_c[T]}{n}$	$MP\phi$[T]
③ Multiple Pulse Limit	$n^{-0.25}MPH_{c,1}[t_1]$	$n^{-0.25}\delta\ MP\phi[t_1]$

Which rules to test?			
	$t_1 < 1\ ns$	$t_1 < 1\ ns < t_{min}$	$t_1 \geq t_{min}$
$F < F_{cr}$	ⓐ 1th 2th 3*	ⓑ 2ph 3*	ⓒ 2ph 3
	* $t_1 = t_{min}$ and $\delta_{min} = Ft_{min}$		
$F \geq F_{cr}$	1th 2th 2ph ⓓ	2th 2ph ⓔ	

F Pulse Repetition Frequency
T Duration of pulse train (s)
n Number of pulses; n=FT

t_1 Duration of single pulse (s)
δ Duty factor
t_{min} 18μs ($400 < \lambda < 1050\ nm$)
50μs ($1050 < \lambda < 1400\ nm$)

MPH_c MP radiant exposure at cornea
$MP\phi$ MP radiant power through pupil
F_{cr}. Critical $PRF = 1/t_{min}$

Using these ANSI rules, the ocular light safety for the developed multimodal PARS-OCT system can be calculated. First, we start with the PARS excitation laser centered at $532\ nm$. The pulse duration for the IPG laser used in this study is $t_1 = 1.5\ ns$. In our imaging setup, assuming that the collimated laser beam after being focused by the eye has a diameter of 20 μm on the retina, the angular subtense of the source:

$$\boldsymbol{\alpha = \frac{20\ \mu m}{17\ mm} = 1.2\ mrad < \alpha_{min} = 1.5\ mrad}$$

Where 17 mm is the focal length of human eye. Therefore, the light source can be considered as a point source.

Rule 1 The MPE for single pulse exposure can be obtained based on Table 8-1. Since the pulse duration of the laser is 1.5 ns we only need to consider the thermal effect and the MP will be equal to:

$$MPE_{SP} = 5 \times 10^{-7} C_T C_E C_J = 5 \times 10^{-7}\ J/cm^2$$

Rule 2 For each PARS image, 600,000 pulses with PRR of 60 kHz are recorded. Since the exposure time ($\sim 10\ s$) is longer than the $0.7\ s$ and the wavelength is between 400 and 600 nm, dual limits due to both thermal and photochemical effects apply here. For the photochemical effect:

$$MPE_{ph} = 1\ \times 10^{-4} \times C_B \times t = 10^{-4} \times 43.65 \times 10 = 4.36 \times 10^{-2}\ J/cm^2$$

Where $C_B = 10^{0.020(\lambda - 450)} = 43.65$.

For the thermal effect:

$$MPE_{th} = 1.8\ \times 10^{-3} \times C_T \times C_E \times t^{0.75} = 1.8 \times 10^{-3} \times 1 \times 5.62 = 1.01 \times 10^{-2} J/cm^2$$

Rule 3 tests whether an exposure by a long pulse of duration nt_1 is safe. Within a laser spot of 20 μm, there are at most two overlapping laser pulses (n = 2).

$$MPE_{rp} = n^{-0.25} \times MPE_{sp} = 0.84 \times 5 \times 10^{-7} = 4.2 \times 10^{-7} J/cm^2$$

Rule 3 is the most conservative of the three. Considering a pupil diameter of $D = 0.7\ cm$ MPE for a single pulse would be equal to $MPE_{rP} \times \left(\frac{D}{2}\right)^2 \times \pi \approx 160\ nJ$. The acquired value is in correspondence to the values reported by other groups[14], [452]. In our imaging applications the energy of a single pulse is $<\ 150\ nJ$ which is below the allowed pulse exposure limit.

8.6. ANSI standard for scanning beam

To acquire one PARS image, the beam needs to be scanned over the field of view. Here, we show the safety calculation for the scanning beam. We can consider the $MP\phi_B$ beam power, the average power deposited over the region, for F frames/s, each frame having R horizontal lines ($R = 512$). The retinal field is square (visual angle of α_F), and we have a total exposure duration of $T = 10\ s$. Here we consider the $MP\phi_B$ for fields ranging from a visual angle (α_F)

from $1^{\circ}$to 50° ($\alpha_F = 17.5\ to\ 875\ mrad$), and $532\ nm$ wavelengths. These values are selected based on the conventional values used in our system. The visual scanning angle used in our study is between $15^{\circ}$to 30°($262\ to\ 525\ mrad$), and the frame rates is usually between 2-5 Hz. For the thermal limit, the equivalent continuous wavelength (CW) beam uniformly distributed over the entire field $MP\phi_B$ (in watts), for $\alpha_F < 100\,mrad$, $T = 10\,s$, and the C_E' corresponding to a square filed, is given by:

$$MP\phi_{B,CW,th} = \left\{6.93\ \times 10^{-4} C_T \left(\frac{4\alpha_F}{\pi\alpha_{min}}\right) P_{10}^{-1} t^{-0.25}\right\}$$

For example, in strict case of 1° ($\alpha_F = 17.5 \times 1 = 17.5\,mrad$) the value will become $\sim 1.064\,mW$.

and for $\alpha_F \geq 100\,mrad$:

$$MP\phi_{B,CW,th} = \left\{6.93\ \times 10^{-4} C_T \left(\frac{4\alpha_F^2}{\pi\alpha_{min}\alpha_{max}}\right) P_{10}^{-1} t^{-0.25}\right\}$$

Similarly, in a 50° ($\alpha_F = 17.5 \times 50 = 875\,mrad$) it will be $\sim 46\,mW$.

The photochemical limit (in watts) for the CW beam is given by:

$$MP\phi_{B,CW,ph} = \left\{5.56\ \times 10^{-6} C_B \frac{4}{\pi} \alpha_F^2 t^{-1}\right\}$$

Similarly, for the $\alpha_F = 1^{\circ}$, the limit will become $2.36\,mw$, and for $\alpha_F = 50^{\circ}$ $\sim 6\,watts$.

Figure 8-1 and Figure 8-2 represent MP (in watts) for both photochemical and thermal damages in a CW beam simulation, respectively. The plots show the values for 3 different PARS excitation wavelengths as a function of the visual angle.

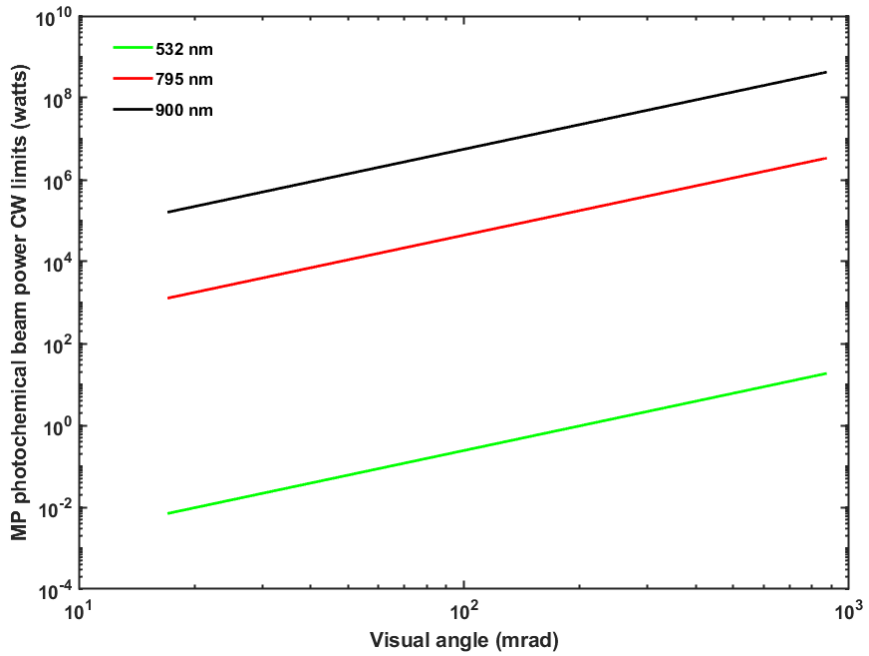

Figure 8-1 Maximum permissible beam power (in watts) for CW photochemical damage and 3 different PARS excitation wavelengths as a function of the visual angle.

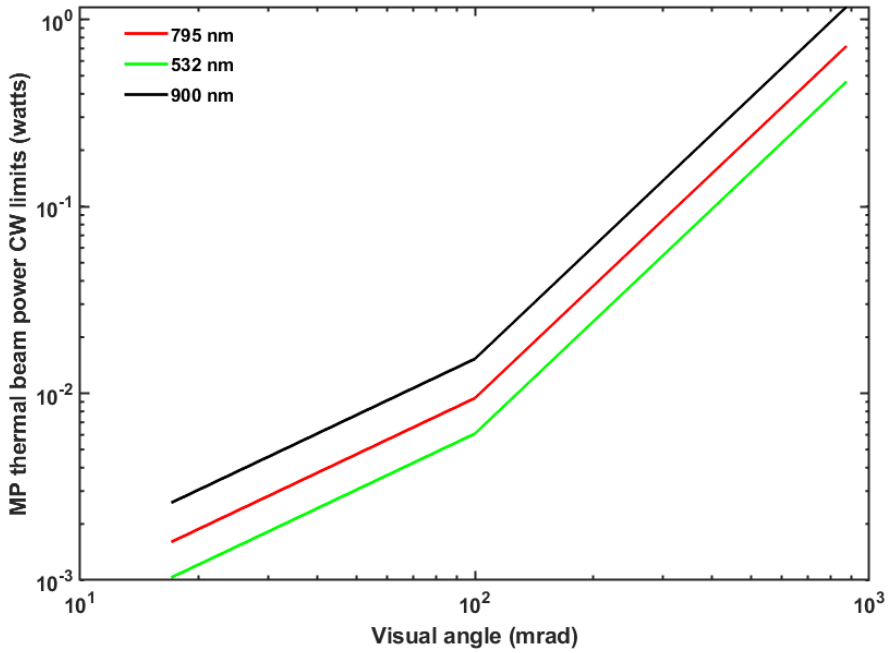

Figure 8-2 Maximum permissible beam power (in watts) for CW beam thermal damage and 3 different PARS excitation wavelengths as a function of the visual angle.

In general, the safety value of system is highly dependent on the visual field angle, wavelength, and duration of the imaging and will require careful consideration of the exposure limits. In

our simulations we have calculated the safety values for visible and NIR wavelengths. The laser safety threshold for ocular imaging is stricter in the visible spectrum than in the NIR spectral range. By moving to NIR region ($\lambda > 700\ nm$) , the absorption coefficients of blood will drop an order of magnitude[464], however, it would be possible to use higher amount of energy. In [465], 795 nm wavelength is applied for *in vivo* photoacoustic imaging of blood in human skin. Additionally, for ophthalmic imaging, since retina is sensitive to the visible light eye motion will cause challenges in eye fixations which will be mitigated by using NIR wavelengths [466].

8.7. Additional safety issues in the multimodal imaging system

The instrumentation for corneal and crystalline lens examination, often use high radiant exposures or irradiances in the anterior segment of the eye. Since the Standard was developed for light overfilling the pupil, it includes protection for light damage in the anterior segment in the visible spectrum, and the Standard extends to the UV and the IR, where damage is likely to occur. For λ=380–1400 nm, a spectrally flat limit was recently introduced that recommends MP corneal irradiances of $25t^{-0.75}$ W/cm^2 for $t < 10\ s$, and 4.0 W/cm^2 for $t > 10s$[453]. Based on the proposed limit the OCT light power on the cornea ($\sim 1.5\ mW$) and the PARS detection power ($\sim 2 - 3\ mW$) are well within the ANSI limits.

Chapter 9
Conclusion and future work

In this thesis dissertation several improvements over previous functional and structural ophthalmic imaging systems are reported. First, here, for the first time we applied a non-contact photoacoustic microscopy technique for imaging ocular tissue. Using PARS microscopy, we showed *in vivo* images acquired from both anterior and posterior segments of the murine eye. To make this possible, we made significant modifications to conventional PARS microscope. These modifications included employing, eye-friendly 830 nm detection wavelength, focusing optics and live feedback during *in vivo* imaging. The 830 nm probe beam improved PARS signal detection in the ocular environment by having lower absorption in water. Additionally, it reduced the amount of chromatic aberration in the system by having close spectral bandwidth to the 532 nm excitation beam. The PARS microscope used in this thesis, for the first time employed a telecentric pair, which provided a uniform image intensity and improved the effective imaging FOV. We have also showed the first live feedback in PARS imaging which is beneficial for accurate alignment and to select the right imaging location.

Second, we developed a method to generate stable multiwavelength light source with high pulse repetition rate. To this aim, stimulated Raman scattering happening inside a single mode fiber was employed and by controlling and decreasing the temperature, the temporal fluctuations of the generated output peaks were reduced. The light source was used as the excitation laser for a PARS microscope and applied to *in vivo* functional imaging of capillary networks in chicken embryo model. The method offered a promising technology for creating

reliable, cost-effective multiwavelength light sources with a sufficiently high pulse energy and PRR for a variety of photoacoustic imaging applications.

Third, using the temperature-regulated multiwavelength light source for the first time we showed *in vivo* functional imaging of the ocular tissue with a non-contact photoacoustic imaging modality. The multiwavelength PARS system is further combined with a swept-source OCT system and for the first time showed simultaneous, non-contact, *in vivo* imaging of murine eye. In addition, for the first time we presented dual-contrast PARS microscopy, where multiwavelength excitation was used for targeting absorption contrast and the PARS probe beam was used for targeting scattering imaging contrast. The reported system was a major step toward non-invasive, simultaneous, and accurate measurement of functional details in the ophthalmic tissue.

Finally, the multimodal PARS-OCT system were further modified and applied for non-contact imaging of the retina in living animal. Here, for the first time, non-contact oxygen saturation measurement was shown in *in vivo* using an absorption-based imaging technique in retinal tissue. The accuracy of PARS microscopy for oxygen saturation measurement was investigated using bovine blood. Furthermore, the system is evaluated in terms of ocular light safety offered by ANSI standards. The proposed technique offered a promising method for non-invasive measurement of metabolic rate of oxygen and improve diagnosis of major blinding eye diseases.

9.1. Future research

The technology developed and discussed in this PhD thesis leave plenty of room for future technological development, as well as pose questions that can before the center point of future animal and human studies.

First, the current PARS-OCT system was developed using visible excitation wavelength for targeting oxygenated and de-oxygenated hemoglobin in the blood. However, the laser safety threshold for ocular imaging is stricter in the visible spectrum than in the NIR spectral range. Additionally, the retina is sensitive to the visible light which poses challenges to eye fixation during imaging. Therefore, in future studies, the NIR spectral range can be examined as the excitation wavelength to overcome these issues.

Second, the imaging speed of the multimodal PARS-OCT system can be increased as well. The higher imaging speed may affect the SNR of the recorded images; however, it can reduce the challenges arising from involuntary eye motions.

Third, to improve the field of view of the system, scan lens can be employed in the imaging head of the system. By reducing the field of curvature, the scan lens optimizes the FOV and produce a flat imaging plane as the laser beam is scanned across the sample.

Forth, a fiber-based version of the system can be developed, which may offer easier alignment, and to make the system compact. Additionally, it can help with improving the SNR of the acquired images by acting as a pinhole in the detection end of the PARS system and eliminating specular reflections.

Fifth, the scanning pattern of the SS-OCT system can be modified to enable Doppler OCT and OCT angiography and provide blood flow measurement and vasculature map, respectively.

This information can be further combined with the non-contact oxygen saturation measurements of PARS to measure metabolic rate of oxygen consumption in the ocular environment in both small and large vessels. It can be further applied for evaluating the effects of visually evoked stimulus and how they could change this functional information.

Sixth, the application of light emitting diodes (LED) as an alternative excitation source for multiwavelength PARS imaging can be investigated in future studies.

Last, but not the least, the proposed multimodal ophthalmic imaging system can be employed for pre-clinical applications. The system can be used in longitudinal studies on larger animal models like rabbit and monkeys with size of eyeballs closer to that of humans. Different eye disease models (such as Glaucoma, and DR) can be developed in these animals and the efficacy of the system be evaluated in diagnosis and monitoring of them.

Bibliography

[1] S. Rowe, C. H. MacLean, and P. G. Shekelle, "Preventing visual loss from chronic eye disease in primary care: scientific review," *JAMA*, vol. 291, no. 12, pp. 1487–1495, Mar. 2004, doi: 10.1001/jama.291.12.1487.

[2] M. Ivanišević, "First look into the eye," *Eur J Ophthalmol*, vol. 29, no. 6, pp. 685–688, Nov. 2019, doi: 10.1177/1120672118804388.

[3] Curtin Robert, "Ophthalmic photography: retinal photography, angiography, and electronic imaging, second edition," *Ophthalmic Surgery, Lasers and Imaging Retina*, vol. 34, no. 1, pp. 79–80, Jan. 2003, doi: 10.3928/1542-8877-20030101-20.

[4] T. C. V. Cader, "History of Ophthalmic Photography," p. 3.

[5] S. Wolf, F. Jung, H. Kiesewetter, N. Körber, and M. Reim, "Video fluorescein angiography: method and clinical application," *Graefes Arch Clin Exp Ophthalmol*, vol. 227, no. 2, pp. 145–151, 1989, doi: 10.1007/BF02169788.

[6] R. H. Webb and G. W. Hughes, "Scanning laser ophthalmoscope," *IEEE Trans Biomed Eng*, vol. 28, no. 7, pp. 488–492, Jul. 1981, doi: 10.1109/TBME.1981.324734.

[7] R. H. Webb, G. W. Hughes, and F. C. Delori, "Confocal scanning laser ophthalmoscope," *Appl. Opt., AO*, vol. 26, no. 8, pp. 1492–1499, Apr. 1987, doi: 10.1364/AO.26.001492.

[8] C. J. Pavlin, K. Harasiewicz, M. D. Sherar, and F. S. Foster, "Clinical Use of Ultrasound Biomicroscopy," *Ophthalmology*, vol. 98, no. 3, pp. 287–295, Mar. 1991, doi: 10.1016/S0161-6420(91)32298-X.

[9] Masters, Barry R., ed. *Noninvasive diagnostic techniques in ophthalmology*. New York: Springer-Verlag, 1990.

[10] M. L. Gabriele *et al.*, "Optical Coherence Tomography: History, Current Status, and Laboratory Work," *Invest Ophthalmol Vis Sci*, vol. 52, no. 5, pp. 2425–2436, Apr. 2011, doi: 10.1167/iovs.10-6312.

[11] W. Liu and H. F. Zhang, "Photoacoustic imaging of the eye: A mini review," *Photoacoustics*, vol. 4, no. 3, pp. 112–123, Sep. 2016, doi: 10.1016/j.pacs.2016.05.001.

[12] N. D. Wangsa-Wirawan and R. A. Linsenmeier, "Retinal Oxygen: Fundamental and Clinical Aspects," *Arch Ophthalmol*, vol. 121, no. 4, pp. 547–557, Apr. 2003, doi: 10.1001/archopht.121.4.547.

[13] J. R. Sparrow, D. Hicks, and C. P. Hamel, "The Retinal Pigment Epithelium in Health and Disease," *Curr Mol Med*, vol. 10, no. 9, pp. 802–823, Dec. 2010, doi: 10.2174/156652410793937813.

[14] W. Liu and H. F. Zhang, "Photoacoustic imaging of the eye: A mini review," *Photoacoustics*, vol. 4, no. 3, pp. 112–123, Sep. 2016, doi: 10.1016/j.pacs.2016.05.001.

[15] C. M. C. Tempany *et al.*, "Multimodal imaging for improved diagnosis and treatment of cancers," *Cancer*, vol. 121, no. 6, pp. 817–827, 2015, doi: 10.1002/cncr.29012.

[16] M. Wu and J. Shu, "Multimodal Molecular Imaging: Current Status and Future Directions," *Contrast Media Mol Imaging*, vol. 2018, Jun. 2018, doi: 10.1155/2018/1382183.

[17] J. F. Rodríguez-Palomares, M. A. García Fernández, and J. Barba Cosials, "Integrating Multimodal Imaging in Clinical Practice: The Importance of a Multidisciplinary Approach," *Rev Esp Cardiol*, vol. 69, no. 5, pp. 477–479, May 2016, doi: 10.1016/j.rec.2016.01.019.

[18] H. Pan, J. Myerson, X. Yang, G. Lanza, and S. A. Wickline, "Atherosclerosis endothelial activation quantification in vivo with fluorine magnetic resonance imaging and spectroscopy," *Journal of Cardiovascular Magnetic Resonance*, vol. 16, no. 1, p. O91, Jan. 2014, doi: 10.1186/1532-429X-16-S1-O91.

[19] M. A. Bruckman *et al.*, “Dual-modal magnetic resonance and fluorescence imaging of atherosclerotic plaques in vivo using VCAM-1 targeted tobacco mosaic virus,” *Nano Lett.*, vol. 14, no. 3, pp. 1551–1558, Mar. 2014, doi: 10.1021/nl404816m.
[20] R. O’Halloran, B. H. Kopell, E. Sprooten, W. K. Goodman, and S. Frangou, “Multimodal Neuroimaging-Informed Clinical Applications in Neuropsychiatric Disorders,” *Frontiers in Psychiatry*, vol. 7, p. 63, 2016, doi: 10.3389/fpsyt.2016.00063.
[21] S. Teipel *et al.*, “Multimodal imaging in Alzheimer’s disease: validity and usefulness for early detection,” *Lancet Neurol*, vol. 14, no. 10, pp. 1037–1053, Oct. 2015, doi: 10.1016/S1474-4422(15)00093-9.
[22] M. F. Kircher *et al.*, “A brain tumor molecular imaging strategy using a new triple-modality MRI-photoacoustic-Raman nanoparticle,” *Nat. Med.*, vol. 18, no. 5, pp. 829–834, Apr. 2012, doi: 10.1038/nm.2721.
[23] J. Yao and L. V. Wang, “Photoacoustic microscopy: Photoacoustic microscopy,” *Laser & Photonics Reviews*, vol. 7, no. 5, pp. 758–778, Sep. 2013, doi: 10.1002/lpor.201200060.
[24] L. V. Wang and S. Hu, “Photoacoustic tomography: in vivo imaging from organelles to organs,” *science*, vol. 335, no. 6075, pp. 1458–1462, 2012.
[25] A. H. Kashani *et al.*, “Optical coherence tomography angiography: A comprehensive review of current methods and clinical applications,” *Progress in Retinal and Eye Research*, vol. 60, pp. 66–100, Sep. 2017, doi: 10.1016/j.preteyeres.2017.07.002.
[26] A. M. Zysk, F. T. Nguyen, A. L. Oldenburg, D. L. Marks, and S. A. Boppart, “Optical coherence tomography: a review of clinical development from bench to bedside,” *Journal of biomedical optics*, vol. 12, no. 5, p. 051403, 2007.
[27] A. C. S. Tan *et al.*, “An overview of the clinical applications of optical coherence tomography angiography,” *Eye*, vol. 32, no. 2, Art. no. 2, Feb. 2018, doi: 10.1038/eye.2017.181.
[28] X. Zhang, H. F. Zhang, and S. Jiao, “Optical coherence photoacoustic microscopy: accomplishing optical coherence tomography and photoacoustic microscopy with a single light source,” *J. Biomed. Opt.*, vol. 17, no. 3, p. 030502, 2012, doi: 10.1117/1.JBO.17.3.030502.
[29] Brunker, Joanna, Junjie Yao, Jan Laufer, and Sarah E. Bohndiek. "Photoacoustic imaging using genetically encoded reporters: a review." *Journal of biomedical optics* 22, no. 7 (2017): 070901.
[30] W. Drexler and J. G. Fujimoto, *Optical coherence tomography: technology and applications*. Springer Science & Business Media, 2008.
[31] X. Cai, B. S. Paratala, S. Hu, B. Sitharaman, and L. V. Wang, “Multiscale Photoacoustic Microscopy of Single-Walled Carbon Nanotube-Incorporated Tissue Engineering Scaffolds,” *Tissue Engineering Part C: Methods*, vol. 18, no. 4, pp. 310–317, Apr. 2012, doi: 10.1089/ten.tec.2011.0519.
[32] A. G. Bell, “On the production and reproduction of sound by light,” in *Proc. Am. Assoc. Adv. Sci.*, 1881, vol. 29, pp. 115–136.
[33] L. V. Wang and H.-I. Wu, *Biomedical Optics: Principles and Imaging*. Hoboken, NJ, USA: John Wiley & Sons, Inc., 2009. doi: 10.1002/9780470177013.
[34] L. V. Wang, *Photoacoustic Imaging and Spectroscopy*. CRC Press, 2017.
[35] P. Beard, “Biomedical photoacoustic imaging,” *Interface Focus*, vol. 1, no. 4, pp. 602–631, Aug. 2011, doi: 10.1098/rsfs.2011.0028.
[36] J. Chan, Z. Zheng, K. Bell, M. Le, P. H. Reza, and J. T. Yeow, “Photoacoustic Imaging with Capacitive Micromachined Ultrasound Transducers: Principles and Developments,” *Sensors*, vol. 19, no. 16, p. 3617, 2019.
[37] T. Bowen, “Radiation-Induced Thermoacoustic Soft Tissue Imaging,” in *1981 Ultrasonics Symposium*, 1981, pp. 817–822. doi: 10.1109/ULTSYM.1981.197737.

[38] R. G. M. Kolkman, E. Hondebrink, W. Steenbergen, and F. F. M. de Mul, “In vivo photoacoustic imaging of blood vessels using an extreme-narrow aperture sensor,” *IEEE J. Select. Topics Quantum Electron.*, vol. 9, no. 2, pp. 343–346, Mar. 2003, doi: 10.1109/JSTQE.2003.813302.
[39] P. Haji Reza, J. Sorge, M. Brett, and R. Zemp, “In vivo optical resolution photoacoustic microscopy using glancing angle-deposited nanostructured Fabry–Perot etalons,” *Optics letters*, vol. 40, no. 7, pp. 1350–1353, 2015.
[40] J. Xia *et al.*, “Whole-body ring-shaped confocal photoacoustic computed tomography of small animals in vivo,” *Journal of biomedical optics*, vol. 17, no. 5, p. 050506, 2012.
[41] L. Lin *et al.*, “Single-breath-hold photoacoustic computed tomography of the breast,” *Nat Commun*, vol. 9, no. 1, p. 2352, Dec. 2018, doi: 10.1038/s41467-018-04576-z.
[42] C. L. Bayer, G. P. Luke, and S. Y. Emelianov, “Photoacoustic Imaging for Medical Diagnostics,” *Acou. Today*, vol. 8, no. 4, p. 15, 2012, doi: 10.1121/1.4788648.
[43] E. W. Stein, K. I. Maslov, and L. V. Wang, “Noninvasive, in vivo imaging of blood-oxygenation dynamics within the mouse brain using photoacoustic microscopy,” *Journal of biomedical optics*, vol. 14, no. 2, p. 020502, 2009.
[44] J. Yao and L. V. Wang, “Photoacoustic microscopy,” *Laser & photonics reviews*, vol. 7, no. 5, pp. 758–778, 2013.
[45] S. Hu and L. V. Wang, “Photoacoustic imaging and characterization of the microvasculature,” *J. Biomed. Opt.*, vol. 15, no. 1, p. 011101, 2010, doi: 10.1117/1.3281673.
[46] H. Guo, Y. Li, W. Qi, and L. Xi, “Photoacoustic endoscopy: a progress review,” *Journal of Biophotonics*, vol. n/a, no. n/a, p. e202000217, doi: 10.1002/jbio.202000217.
[47] J. Yao and L. V. Wang, “Sensitivity of photoacoustic microscopy,” *Photoacoustics*, vol. 2, no. 2, pp. 87–101, 2014.
[48] S. Hu, “Emerging Concepts in Functional and Molecular Photoacoustic Imaging,” *Curr Opin Chem Biol*, vol. 33, pp. 25–31, Aug. 2016, doi: 10.1016/j.cbpa.2016.04.003.
[49] M. Moothanchery and M. Pramanik, “Performance Characterization of a Switchable Acoustic Resolution and Optical Resolution Photoacoustic Microscopy System,” *Sensors*, vol. 17, no. 2, p. 357, Feb. 2017, doi: 10.3390/s17020357.
[50] C. Zhang, K. Maslov, and L. V. Wang, “Subwavelength-resolution label-free photoacoustic microscopy of optical absorption in vivo,” *Opt. Lett.*, vol. 35, no. 19, p. 3195, Oct. 2010, doi: 10.1364/OL.35.003195.
[51] M. Li, Y. Tang, and J. Yao, “Photoacoustic tomography of blood oxygenation: A mini review,” *Photoacoustics*, vol. 10, pp. 65–73, May 2018, doi: 10.1016/j.pacs.2018.05.001.
[52] J. Yao, K. I. Maslov, Y. Shi, L. A. Taber, and L. V. Wang, “In vivo photoacoustic imaging of transverse blood flow by using Doppler broadening of bandwidth,” *Opt Lett*, vol. 35, no. 9, pp. 1419–1421, May 2010, doi: 10.1364/OL.35.001419.
[53] J. Yao and L. V. Wang, “Transverse flow imaging based on photoacoustic Doppler bandwidth broadening,” *JBO*, vol. 15, no. 2, p. 021304, Mar. 2010, doi: 10.1117/1.3339953.
[54] J. Yao, H. Ke, S. Tai, Y. Zhou, and L. V. Wang, “Absolute Photoacoustic Thermometry in Deep Tissue,” *Opt Lett*, vol. 38, no. 24, pp. 5228–5231, Dec. 2013.
[55] L. Gao *et al.*, “Single-cell photoacoustic thermometry,” *JBO*, vol. 18, no. 2, p. 026003, Feb. 2013, doi: 10.1117/1.JBO.18.2.026003.
[56] P. Haji Reza, A. Forbrich, and R. Zemp, “In-Vivo functional optical-resolution photoacoustic microscopy with stimulated Raman scattering fiber-laser source,” *Biomed. Opt. Express*, vol. 5, no. 2, p. 539, Feb. 2014, doi: 10.1364/BOE.5.000539.
[57] J. Yao *et al.*, “High-speed label-free functional photoacoustic microscopy of mouse brain in action,” *Nat Methods*, vol. 12, no. 5, pp. 407–410, May 2015, doi: 10.1038/nmeth.3336.

[58] Z. Chen *et al.*, "Non-invasive multimodal optical coherence and photoacoustic tomography for human skin imaging," *Scientific Reports*, vol. 7, no. 1, Art. no. 1, Dec. 2017, doi: 10.1038/s41598-017-18331-9.
[59] J. Laufer, E. Zhang, G. Raivich, and P. Beard, "Three-dimensional noninvasive imaging of the vasculature in the mouse brain using a high resolution photoacoustic scanner," *Applied optics*, vol. 48, no. 10, pp. D299–D306, 2009.
[60] R. J. Paproski, A. Heinmiller, K. Wachowicz, and R. J. Zemp, "Multi-wavelength photoacoustic imaging of inducible tyrosinase reporter gene expression in xenograft tumors," *Scientific reports*, vol. 4, p. 5329, 2014.
[61] S. Sethuraman, J. H. Amirian, S. H. Litovsky, R. W. Smalling, and S. Y. Emelianov, "Ex vivo Characterization of Atherosclerosis using Intravascular Photoacoustic Imaging," *Opt. Express*, vol. 15, no. 25, p. 16657, 2007, doi: 10.1364/OE.15.016657.
[62] J.-T. Oh, M.-L. Li, H. F. Zhang, K. Maslov, and L. V. Wang, "Three-dimensional imaging of skin melanoma in vivo by dual-wavelength photoacoustic microscopy," *Journal of biomedical optics*, vol. 11, no. 3, p. 034032, 2006.
[63] S. M. Maswadi *et al.*, "All-optical optoacoustic microscopy based on probe beam deflection technique," *Photoacoustics*, vol. 4, no. 3, pp. 91–101, 2016.
[64] T. T. Wong *et al.*, "Fast label-free multilayered histology-like imaging of human breast cancer by photoacoustic microscopy," *Science advances*, vol. 3, no. 5, p. e1602168, 2017.
[65] R. Lin, J. Chen, H. Wang, M. Yan, W. Zheng, and L. Song, "Longitudinal label-free optical-resolution photoacoustic microscopy of tumor angiogenesis in vivo," *Quant Imaging Med Surg*, vol. 5, no. 1, pp. 23–29, Feb. 2015, doi: 10.3978/j.issn.2223-4292.2014.11.08.
[66] L. Li *et al.*, "Small near-infrared photochromic protein for photoacoustic multi-contrast imaging and detection of protein interactions in vivo," *Nature Communications*, vol. 9, no. 1, Art. no. 1, Jul. 2018, doi: 10.1038/s41467-018-05231-3.
[67] V. Nguyen and Y. Paulus, "Photoacoustic Ophthalmoscopy: Principle, Application, and Future Directions," *J. Imaging*, vol. 4, no. 12, p. 149, Dec. 2018, doi: 10.3390/jimaging4120149.
[68] S. Y. Nam, L. M. Ricles, L. J. Suggs, and S. Y. Emelianov, "In vivo Ultrasound and Photoacoustic Monitoring of Mesenchymal Stem Cells Labeled with Gold Nanotracers," *PLoS ONE*, vol. 7, no. 5, p. e37267, May 2012, doi: 10.1371/journal.pone.0037267.
[69] D. Huang *et al.*, "Optical coherence tomography," *Science*, vol. 254, no. 5035, pp. 1178–1181, Nov. 1991, doi: 10.1126/science.1957169.
[70] C. A. de Amorim Garcia Filho, Z. Yehoshua, G. Gregori, C. A. Puliafito, and P. J. Rosenfeld, "Chapter 3 - Optical Coherence Tomography," in *Retina (Fifth Edition)*, S. J. Ryan, S. R. Sadda, D. R. Hinton, A. P. Schachat, S. R. Sadda, C. P. Wilkinson, P. Wiedemann, and A. P. Schachat, Eds. London: W.B. Saunders, 2013, pp. 82–110. doi: 10.1016/B978-1-4557-0737-9.00003-5.
[71] J. F. de Boer, R. Leitgeb, and M. Wojtkowski, "Twenty-five years of optical coherence tomography: the paradigm shift in sensitivity and speed provided by Fourier domain OCT [Invited]," *Biomed. Opt. Express*, vol. 8, no. 7, p. 3248, Jul. 2017, doi: 10.1364/BOE.8.003248.
[72] A. F. Fercher, R. Leitgeb, C. K. Hitzenberger, H. Sattmann, and M. Wojtkowski, "Complex spectral interferometry OCT," in *Medical Applications of Lasers in Dermatology, Cardiology, Ophthalmology, and Dentistry II*, Feb. 1999, vol. 3564, pp. 173–178. doi: 10.1117/12.339152.
[73] S. Aumann, S. Donner, J. Fischer, and F. Müller, "Optical Coherence Tomography (OCT): Principle and Technical Realization," in *High Resolution Imaging in Microscopy and Ophthalmology: New Frontiers in Biomedical Optics*, J. F. Bille, Ed. Cham: Springer International Publishing, 2019, pp. 59–85. doi: 10.1007/978-3-030-16638-0_3.

[74] Z. Yaqoob, J. Wu, and C. Yang, “Spectral domain optical coherence tomography: a better OCT imaging strategy,” *BioTechniques*, vol. 39, no. 6 Suppl, pp. S6-13, Dec. 2005, doi: 10.2144/000112090.
[75] P. Hahn, J. Migacz, R. O’Connell, R. S. Maldonado, J. A. Izatt, and C. A. Toth, “The use of optical coherence tomography in intraoperative ophthalmic imaging,” *Ophthalmic Surgery, Lasers and Imaging Retina*, vol. 42, no. 4, pp. S85–S94, 2011.
[76] M. Pircher and R. J. Zawadzki, “Review of adaptive optics OCT (AO-OCT): principles and applications for retinal imaging,” *Biomedical optics express*, vol. 8, no. 5, pp. 2536–2562, 2017.
[77] J. L. B. Ramos, Y. Li, and D. Huang, “Clinical and research applications of anterior segment optical coherence tomography–a review,” *Clinical & experimental ophthalmology*, vol. 37, no. 1, pp. 81–89, 2009.
[78] R. A. Leitgeb, R. M. Werkmeister, C. Blatter, and L. Schmetterer, “Doppler optical coherence tomography,” *Progress in retinal and eye research*, vol. 41, pp. 26–43, 2014.
[79] C.-L. Chen and R. K. Wang, “Optical coherence tomography based angiography [Invited],” *Biomed. Opt. Express, BOE*, vol. 8, no. 2, pp. 1056–1082, Feb. 2017, doi: 10.1364/BOE.8.001056.
[80] J. F. De Boer, C. K. Hitzenberger, and Y. Yasuno, “Polarization sensitive optical coherence tomography–a review,” *Biomedical optics express*, vol. 8, no. 3, pp. 1838–1873, 2017.
[81] X. Liang, V. Crecea, and S. A. Boppart, “Dynamic optical coherence elastography: a review,” *Journal of innovative optical health sciences*, vol. 3, no. 04, pp. 221–233, 2010.
[82] X. Shu, L. J. Beckmann, and H. F. Zhang, “Visible-light optical coherence tomography: a review,” *Journal of biomedical optics*, vol. 22, no. 12, p. 121707, 2017.
[83] P. J. Marchand, A. Bouwens, D. Szlag, T. Lasser, and J. Extermann, “Brain imaging with extended-focus optical coherence tomography at different scales and spectral ranges (Conference Presentation),” in *Optical Coherence Tomography and Coherence Domain Optical Methods in Biomedicine XXIII*, 2019, vol. 10867, p. 108671U.
[84] C. Magnain *et al.*, “Human Brain Imaging by Optical Coherence Tomography,” *Handbook of Neurophotonics*, p. 399, 2020.
[85] Y. Ling, C. Li, C. Purslow, Y. Yang, and Z. Huang, “Evaluation of human corneal ulcer healing process using optical coherence tomography: an in vitro study,” in *Optical Elastography and Tissue Biomechanics VI*, 2019, vol. 10880, p. 108801H.
[86] C. P. Hendon, T. H. Lye, X. Yao, Y. Gan, and C. C. Marboe, “Optical coherence tomography imaging of cardiac substrates,” *Quantitative imaging in medicine and surgery*, vol. 9, no. 5, p. 882, 2019.
[87] A. Rajabi-Estarabadi *et al.*, “Optical coherence tomography imaging of melanoma skin cancer,” *Lasers in medical science*, vol. 34, no. 2, pp. 411–420, 2019.
[88] A. Pinhas *et al.*, “Optical Coherence Tomography Angiography in Neurology and Neuro-Ophthalmology,” in *OCT and Imaging in Central Nervous System Diseases*, Springer, 2020, pp. 523–544.
[89] J. Malone *et al.*, “Endoscopic optical coherence tomography (OCT) and autofluorescence imaging (AFI) of ex vivo fallopian tubes,” in *Multimodal Biomedical Imaging XV*, 2020, vol. 11232, p. 1123202.
[90] J. E. Freund *et al.*, “Optical coherence tomography in urologic oncology: a comprehensive review,” *SN Comprehensive Clinical Medicine*, vol. 1, no. 2, pp. 67–84, 2019.
[91] D. Fried, “Optical Coherence Tomography for Imaging Dental Caries,” in *Detection and Assessment of Dental Caries*, Springer, 2019, pp. 199–208.

[92] E. Beaurepaire, L. Moreaux, F. Amblard, and J. Mertz, "Combined scanning optical coherence and two-photon-excited fluorescence microscopy," *Opt. Lett., OL*, vol. 24, no. 14, pp. 969–971, Jul. 1999, doi: 10.1364/OL.24.000969.
[93] J. P. Dunkers, M. T. Cicerone, and N. R. Washburn, "Collinear optical coherence and confocal fluorescence microscopies for tissue engineering," *Opt. Express, OE*, vol. 11, no. 23, pp. 3074–3079, Nov. 2003, doi: 10.1364/OE.11.003074.
[94] D. J. Harper *et al.*, "White Light Optical Coherence Tomography for Sub-Micron Resolution and Spectroscopic Imaging in the Mouse Retina," *Invest. Ophthalmol. Vis. Sci.*, vol. 59, no. 9, pp. 5826–5826, Jul. 2018.
[95] P. J. Marchand, D. Szlag, A. Bouwens, and T. Lasser, "In vivo high-resolution cortical imaging with extended-focus optical coherence microscopy in the visible-NIR wavelength range," *J Biomed Opt*, vol. 23, no. 3, pp. 1–7, 2018, doi: 10.1117/1.JBO.23.3.036012.
[96] L. V. Wang and J. Yao, "A practical guide to photoacoustic tomography in the life sciences," *Nat Methods*, vol. 13, no. 8, pp. 627–638, Aug. 2016, doi: 10.1038/nmeth.3925.
[97] B. Marsh-Armstrong, J. Migacz, R. Jonnal, and J. S. Werner, "Automated quantification of choriocapillaris anatomical features in ultrahigh-speed optical coherence tomography angiograms," *Biomed. Opt. Express, BOE*, vol. 10, no. 10, pp. 5337–5350, Oct. 2019, doi: 10.1364/BOE.10.005337.
[98] Z. Ma *et al.*, "Assessment of microvasculature flow state with a high speed all-optic dual-modal system of optical coherence tomography and photoacoustic imaging," *Biomedical optics express*, vol. 9, no. 12, pp. 6103–6115, 2018.
[99] E. Z. Zhang *et al.*, "Multimodal photoacoustic and optical coherence tomography scanner using an all optical detection scheme for 3D morphological skin imaging," *Biomed. Opt. Express*, vol. 2, no. 8, p. 2202, Aug. 2011, doi: 10.1364/BOE.2.002202.
[100] B. J. Vakoc *et al.*, "Three-dimensional microscopy of the tumor microenvironment in vivo using optical frequency domain imaging," *Nat. Med.*, vol. 15, no. 10, pp. 1219–1223, Oct. 2009, doi: 10.1038/nm.1971.
[101] H. S. Nam and H. Yoo, "Spectroscopic optical coherence tomography: A review of concepts and biomedical applications," *Applied Spectroscopy Reviews*, vol. 53, no. 2–4, pp. 91–111, Apr. 2018, doi: 10.1080/05704928.2017.1324876.
[102] U. Morgner *et al.*, "Spectroscopic optical coherence tomography," *Opt. Lett., OL*, vol. 25, no. 2, pp. 111–113, Jan. 2000, doi: 10.1364/OL.25.000111.
[103] N. D. Wangsa-Wirawan and R. A. Linsenmeier, "Retinal Oxygen: Fundamental and Clinical Aspects," *Arch Ophthalmol*, vol. 121, no. 4, pp. 547–557, Apr. 2003, doi: 10.1001/archopht.121.4.547.
[104] H.-P. Hammes, "Pericytes and the Pathogenesis of Diabetic Retinopathy," *Horm Metab Res*, vol. 37, no. S 1, pp. 39–43, Apr. 2005, doi: 10.1055/s-2005-861361.
[105] M. Mozaffarieh, M. C. Grieshaber, and J. Flammer, "Oxygen and blood flow: players in the pathogenesis of glaucoma," *Mol Vis*, vol. 14, pp. 224–233, Jan. 2008.
[106] W. Song *et al.*, "A combined method to quantify the retinal metabolic rate of oxygen using photoacoustic ophthalmoscopy and optical coherence tomography," *Sci Rep*, vol. 4, no. 1, p. 6525, May 2015, doi: 10.1038/srep06525.
[107] K. E. Wilson, S. V. Bachawal, L. Tian, and J. K. Willmann, "Multiparametric Spectroscopic Photoacoustic Imaging of Breast Cancer Development in a Transgenic Mouse Model," *Theranostics*, vol. 4, no. 11, pp. 1062–1071, Aug. 2014, doi: 10.7150/thno.9922.
[108] V. P. Nguyen *et al.*, "Contrast Agent Enhanced Multimodal Photoacoustic Microscopy and Optical Coherence Tomography for Imaging of Rabbit Choroidal and Retinal Vessels in vivo," *Sci Rep*, vol. 9, no. 1, p. 5945, Dec. 2019, doi: 10.1038/s41598-019-42324-5.

[109] J. Yao *et al.*, "Noninvasive photoacoustic computed tomography of mouse brain metabolism in vivo," *NeuroImage*, vol. 64, pp. 257–266, Jan. 2013, doi: 10.1016/j.neuroimage.2012.08.054.
[110] M. Nasiriavanaki, J. Xia, H. Wan, A. Q. Bauer, J. P. Culver, and L. V. Wang, "High-resolution photoacoustic tomography of resting-state functional connectivity in the mouse brain," *Proc Natl Acad Sci U S A*, vol. 111, no. 1, pp. 21–26, Jan. 2014, doi: 10.1073/pnas.1311868111.
[111] J. Jo and X. Yang, "Functional photoacoustic imaging to observe regional brain activation induced by cocaine hydrochloride," *J Biomed Opt*, vol. 16, no. 9, Sep. 2011, doi: 10.1117/1.3626576.
[112] P. J. Marchand *et al.*, "Visible spectrum extended-focus optical coherence microscopy for label-free sub-cellular tomography," *Biomed. Opt. Express*, vol. 8, no. 7, p. 3343, Jul. 2017, doi: 10.1364/BOE.8.003343.
[113] S. Hu, K. Maslov, V. Tsytsarev, and L. V. Wang, "Functional transcranial brain imaging by optical-resolution photoacoustic microscopy," *J Biomed Opt*, vol. 14, no. 4, p. 040503, 2009, doi: 10.1117/1.3194136.
[114] B. Zabihian *et al.*, "In vivo dual-modality photoacoustic and optical coherence tomography imaging of human dermatological pathologies," *Biomed. Opt. Express, BOE*, vol. 6, no. 9, pp. 3163–3178, Sep. 2015, doi: 10.1364/BOE.6.003163.
[115] D. Lee, C. Lee, S. Kim, Q. Zhou, J. Kim, and C. Kim, "In Vivo Near Infrared Virtual Intraoperative Surgical Photoacoustic Optical Coherence Tomography," *Sci Rep*, vol. 6, no. 1, p. 35176, Dec. 2016, doi: 10.1038/srep35176.
[116] K. J. Cash, C. Li, J. Xia, L. V. Wang, and H. A. Clark, "Optical Drug Monitoring: Photoacoustic Imaging of Nanosensors to Monitor Therapeutic Lithium in Vivo," *ACS Nano*, vol. 9, no. 2, pp. 1692–1698, Feb. 2015, doi: 10.1021/nn5064858.
[117] R. Pomerantz, D. Zell, G. McKenzie, and D. M. Siegel, "Optical Coherence Tomography Used as a Modality to Delineate Basal Cell Carcinoma prior to Mohs Micrographic Surgery," *CDE*, vol. 3, no. 3, pp. 212–218, 2011, doi: 10.1159/000333000.
[118] U. Dahlstrand *et al.*, "Photoacoustic imaging for three-dimensional visualization and delineation of basal cell carcinoma in patients," *Photoacoustics*, vol. 18, p. 100187, Jun. 2020, doi: 10.1016/j.pacs.2020.100187.
[119] M. Liu and W. Drexler, "Optical coherence tomography angiography and photoacoustic imaging in dermatology," *Photochem. Photobiol. Sci.*, vol. 18, no. 5, pp. 945–962, May 2019, doi: 10.1039/C8PP00471D.
[120] T.-J. Yoon and Y.-S. Cho, "Recent advances in photoacoustic endoscopy," *World J Gastrointest Endosc*, vol. 5, no. 11, pp. 534–539, Nov. 2013, doi: 10.4253/wjge.v5.i11.534.
[121] M. J. Gora, M. J. Suter, G. J. Tearney, and X. Li, "Endoscopic optical coherence tomography: technologies and clinical applications [Invited]," *Biomed. Opt. Express, BOE*, vol. 8, no. 5, pp. 2405–2444, May 2017, doi: 10.1364/BOE.8.002405.
[122] S. Zackrisson, S. M. W. Y. van de Ven, and S. S. Gambhir, "Light In and Sound Out: Emerging Translational Strategies for Photoacoustic Imaging," *Cancer Res*, vol. 74, no. 4, pp. 979–1004, Feb. 2014, doi: 10.1158/0008-5472.CAN-13-2387.
[123] M. Wu, A. FW van der Steen, E. Regar, and G. van Soest, "Emerging Technology Update Intravascular Photoacoustic Imaging of Vulnerable Atherosclerotic Plaque," *Interv Cardiol*, vol. 11, no. 2, pp. 120–123, Oct. 2016, doi: 10.15420/icr.2016:13:3.
[124] R. A. Leitgeb and B. Baumann, "Multimodal Optical Medical Imaging Concepts Based on Optical Coherence Tomography," *Front. Phys.*, vol. 6, p. 114, Oct. 2018, doi: 10.3389/fphy.2018.00114.

[125] M. Liu *et al.*, “Dual modality optical coherence and whole-body photoacoustic tomography imaging of chick embryos in multiple development stages,” *Biomed. Opt. Express, BOE*, vol. 5, no. 9, pp. 3150–3159, Sep. 2014, doi: 10.1364/BOE.5.003150.
[126] J. Xia and L. V. Wang, “Small-animal whole-body photoacoustic tomography: a review,” *IEEE Trans Biomed Eng*, vol. 61, no. 5, pp. 1380–1389, May 2014, doi: 10.1109/TBME.2013.2283507.
[127] M. Liu *et al.*, “Combined multi-modal photoacoustic tomography, optical coherence tomography (OCT) and OCT angiography system with an articulated probe for in vivo human skin structure and vasculature imaging,” *Biomed. Opt. Express, BOE*, vol. 7, no. 9, pp. 3390–3402, Sep. 2016, doi: 10.1364/BOE.7.003390.
[128] B. Zabihian *et al.*, “Comprehensive vascular imaging using optical coherence tomography-based angiography and photoacoustic tomography,” *J. Biomed. Opt*, vol. 21, no. 9, p. 096011, Sep. 2016, doi: 10.1117/1.JBO.21.9.096011.
[129] W. Zhou, Z. Chen, S. Yang, and D. Xing, “Optical biopsy approach to basal cell carcinoma and melanoma based on all-optically integrated photoacoustic and optical coherence tomography,” *Opt. Lett.*, vol. 42, no. 11, p. 2145, Jun. 2017, doi: 10.1364/OL.42.002145.
[130] K. Kratkiewicz *et al.*, “Photoacoustic/Ultrasound/Optical Coherence Tomography Evaluation of Melanoma Lesion and Healthy Skin in a Swine Model,” *Sensors*, vol. 19, no. 12, p. 2815, Jun. 2019, doi: 10.3390/s19122815.
[131] Y. Yang *et al.*, “Integrated optical coherence tomography, ultrasound and photoacoustic imaging for ovarian tissue characterization,” *Biomedical optics express*, vol. 2, no. 9, pp. 2551–2561, 2011.
[132] L. Xi, C. Duan, H. Xie, and H. Jiang, “Miniature probe combining optical-resolution photoacoustic microscopy and optical coherence tomography for in vivomicrocirculation study,” *Applied optics*, vol. 52, no. 9, pp. 1928–1931, 2013.
[133] X. Dai, L. Xi, C. Duan, H. Yang, H. Xie, and H. Jiang, “Miniature probe integrating optical-resolution photoacoustic microscopy, optical coherence tomography, and ultrasound imaging: proof-of-concept,” *Opt. Lett.*, vol. 40, no. 12, p. 2921, Jun. 2015, doi: 10.1364/OL.40.002921.
[134] S. J. Mathews *et al.*, “All-optical dual photoacoustic and optical coherence tomography intravascular probe,” *Photoacoustics*, vol. 11, pp. 65–70, Jul. 2018, doi: 10.1016/j.pacs.2018.07.002.
[135] L. Li, K. Maslov, G. Ku, and L. V. Wang, “Three-dimensional combined photoacoustic and optical coherence microscopy for in vivo microcirculation studies,” *Optics express*, vol. 17, no. 19, pp. 16450–16455, 2009.
[136] X. Cai *et al.*, “Investigation of neovascularization in three-dimensional porous scaffolds in vivo by a combination of multiscale photoacoustic microscopy and optical coherence tomography,” *Tissue Engineering Part C: Methods*, vol. 19, no. 3, pp. 196–204, 2013.
[137] S. Jiao, Z. Xie, H. F. Zhang, and C. A. Puliafito, “Simultaneous multimodal imaging with integrated photoacoustic microscopy and optical coherence tomography,” *Optics letters*, vol. 34, no. 19, pp. 2961–2963, 2009.
[138] T. Liu, Q. Wei, J. Wang, S. Jiao, and H. F. Zhang, “Combined photoacoustic microscopy and optical coherence tomography can measure metabolic rate of oxygen,” *Biomed Opt Express*, vol. 2, no. 5, pp. 1359–1365, Apr. 2011, doi: 10.1364/BOE.2.001359.
[139] V. Tsytsarev, B. Rao, K. I. Maslov, L. Li, and L. V. Wang, “Photoacoustic and optical coherence tomography of epilepsy with high temporal and spatial resolution and dual optical contrasts,” *Journal of Neuroscience Methods*, vol. 216, no. 2, pp. 142–145, Jun. 2013, doi: 10.1016/j.jneumeth.2013.04.001.

[140] M. Liu, “A study of spectral domain optical coherence tomography and photoacoustic microscopy for biometric and biomedical applications,” Thesis, University of Delaware, 2011. Accessed: May 20, 2020. [Online]. Available: http://udspace.udel.edu/handle/19716/10135
[141] X. Zhu *et al.*, “Resolution-matched reflection mode photoacoustic microscopy and optical coherence tomography dual modality system,” *Photoacoustics*, vol. 19, p. 100188, Sep. 2020, doi: 10.1016/j.pacs.2020.100188.
[142] W. Qin, W. Qi, T. Jin, H. Guo, and L. Xi, “*In vivo* oral imaging with integrated portable photoacoustic microscopy and optical coherence tomography,” *Appl. Phys. Lett.*, vol. 111, no. 26, p. 263704, Dec. 2017, doi: 10.1063/1.5006234.
[143] W. Qin, Q. Chen, and L. Xi, “A handheld microscope integrating photoacoustic microscopy and optical coherence tomography,” *Biomed. Opt. Express*, vol. 9, no. 5, p. 2205, May 2018, doi: 10.1364/BOE.9.002205.
[144] A. Dadkhah and S. Jiao, “Optical coherence tomography-guided dynamic focusing for combined optical and mechanical scanning multimodal photoacoustic microscopy,” *J. Biomed. Opt.*, vol. 24, no. 12, p. 1, Aug. 2019, doi: 10.1117/1.JBO.24.12.121906.
[145] Y. Liu *et al.*, “NIR-II Dual-Modal Optical Coherence Tomography and Photoacoustic Imaging-Guided Dose-Control Cancer Chemotherapy,” *ACS Appl. Polym. Mater.*, vol. 2, no. 5, pp. 1964–1973, May 2020, doi: 10.1021/acsapm.0c00155.
[146] B. Dong, C. Sun, and H. F. Zhang, “Optical detection of ultrasound in photoacoustic imaging,” *IEEE Transactions on Biomedical Engineering*, vol. 64, no. 1, pp. 4–15, 2016.
[147] C. Lee *et al.*, “Combined photoacoustic and optical coherence tomography using a single near-infrared supercontinuum laser source,” *Applied optics*, vol. 52, no. 9, pp. 1824–1828, 2013.
[148] B. Hermann *et al.*, “Hybrid ultrahigh resolution optical coherence / photoacoustic microscopy,” in *Photons Plus Ultrasound: Imaging and Sensing 2015*, Mar. 2015, vol. 9323, p. 93232N. doi: 10.1117/12.2079232.
[149] L. Li *et al.*, “Fast subcellular optical coherence photoacoustic microscopy for pigment cell imaging,” *Opt. Lett., OL*, vol. 40, no. 19, pp. 4448–4451, Oct. 2015, doi: 10.1364/OL.40.004448.
[150] S. Shang, Z. Chen, Y. Zhao, S. Yang, and D. Xing, “Simultaneous imaging of atherosclerotic plaque composition and structure with dual-mode photoacoustic and optical coherence tomography,” *Opt. Express, OE*, vol. 25, no. 2, pp. 530–539, Jan. 2017, doi: 10.1364/OE.25.000530.
[151] X. Shu, M. Bondu, B. Dong, A. Podoleanu, L. Leick, and H. F. Zhang, “Single all-fiber-based nanosecond-pulsed supercontinuum source for multispectral photoacoustic microscopy and optical coherence tomography,” *Opt. Lett.*, vol. 41, no. 12, p. 2743, Jun. 2016, doi: 10.1364/OL.41.002743.
[152] R. Haindl *et al.*, “Dual modality reflection mode optical coherence and photoacoustic microscopy using an akinetic sensor,” *Opt. Lett., OL*, vol. 42, no. 21, pp. 4319–4322, Nov. 2017, doi: 10.1364/OL.42.004319.
[153] S. Preisser *et al.*, “All-optical highly sensitive akinetic sensor for ultrasound detection and photoacoustic imaging,” *Biomedical optics express*, vol. 7, no. 10, pp. 4171–4186, 2016.
[154] R. Haindl *et al.*, “Functional optical coherence tomography and photoacoustic microscopy imaging for zebrafish larvae,” *Biomed. Opt. Express, BOE*, vol. 11, no. 4, pp. 2137–2151, Apr. 2020, doi: 10.1364/BOE.390410.
[155] L. V. Wang, “Multiscale photoacoustic microscopy and computed tomography,” *Nature Photon*, vol. 3, no. 9, pp. 503–509, Sep. 2009, doi: 10.1038/nphoton.2009.157.

[156] S. Pi *et al.*, "Rodent retinal circulation organization and oxygen metabolism revealed by visible-light optical coherence tomography," *Biomed. Opt. Express*, vol. 9, no. 11, p. 5851, Nov. 2018, doi: 10.1364/BOE.9.005851.
[157] J. Hui, R. Li, E. H. Phillips, C. J. Goergen, M. Sturek, and J.-X. Cheng, "Bond-selective photoacoustic imaging by converting molecular vibration into acoustic waves," *Photoacoustics*, vol. 4, no. 1, pp. 11–21, Mar. 2016, doi: 10.1016/j.pacs.2016.01.002.
[158] H. D. Lee, J. G. Shin, H. Hyun, B.-A. Yu, and T. J. Eom, "Label-free photoacoustic microscopy for in-vivo tendon imaging using a fiber-based pulse laser," *Sci Rep*, vol. 8, no. 1, p. 4805, Dec. 2018, doi: 10.1038/s41598-018-23113-y.
[159] M. Bondu, M. J. Marques, P. M. Moselund, G. Lall, A. Bradu, and A. Podoleanu, "Multispectral photoacoustic microscopy and optical coherence tomography using a single supercontinuum source," *Photoacoustics*, vol. 9, pp. 21–30, 2018.
[160] S. Jiao *et al.*, "Photoacoustic ophthalmoscopy for in vivo retinal imaging," *Opt. Express*, vol. 18, no. 4, p. 3967, Feb. 2010, doi: 10.1364/OE.18.003967.
[161] W. Song *et al.*, "Integrating photoacoustic ophthalmoscopy with scanning laser ophthalmoscopy, optical coherence tomography, and fluorescein angiography for a multimodal retinal imaging platform," *Journal of biomedical optics*, vol. 17, no. 6, p. 061206, 2012.
[162] X. Liu *et al.*, "Optical coherence photoacoustic microscopy for in vivo multimodal retinal imaging," *Opt. Lett.*, vol. 40, no. 7, p. 1370, Apr. 2015, doi: 10.1364/OL.40.001370.
[163] D. A. Robinson, "The mechanics of human saccadic eye movement," *The Journal of Physiology*, vol. 174, no. 2, pp. 245–264, 1964, doi: 10.1113/jphysiol.1964.sp007485.
[164] C. Tian, W. Zhang, A. Mordovanakis, X. Wang, and Y. M. Paulus, "Noninvasive chorioretinal imaging in living rabbits using integrated photoacoustic microscopy and optical coherence tomography," *Opt. Express*, vol. 25, no. 14, p. 15947, Jul. 2017, doi: 10.1364/OE.25.015947.
[165] W. Zhang *et al.*, "High-resolution, in vivo multimodal photoacoustic microscopy, optical coherence tomography, and fluorescence microscopy imaging of rabbit retinal neovascularization," *Light Sci Appl*, vol. 7, no. 1, p. 103, Dec. 2018, doi: 10.1038/s41377-018-0093-y.
[166] W. Zhang *et al.*, "Simultaneous photoacoustic microscopy, spectral-domain optical coherence tomography, and fluorescein microscopy multi-modality retinal imaging," *Photoacoustics*, vol. 20, p. 100194, Dec. 2020, doi: 10.1016/j.pacs.2020.100194.
[167] V. P. Nguyen, Y. Li, W. Zhang, X. Wang, and Y. M. Paulus, "Multi-wavelength, en-face photoacoustic microscopy and optical coherence tomography imaging for early and selective detection of laser induced retinal vein occlusion," *Biomed. Opt. Express*, vol. 9, no. 12, p. 5915, Dec. 2018, doi: 10.1364/BOE.9.005915.
[168] V. P. Nguyen, Y. Li, W. Zhang, X. Wang, and Y. M. Paulus, "High-resolution multimodal photoacoustic microscopy and optical coherence tomography image-guided laser induced branch retinal vein occlusion in living rabbits," *Sci Rep*, vol. 9, no. 1, p. 10560, Dec. 2019, doi: 10.1038/s41598-019-47062-2.
[169] L. Han, L. K. Chen, Z. Hosseinaee, and K. Bizheva, "In-vivo, non-contact, cellular resolution imaging of the human cornea with line-field SD-OCT at 2.5 kHz frame rate (Conference Presentation)," in *Optical Coherence Tomography and Coherence Domain Optical Methods in Biomedicine XXIV*, Mar. 2020, vol. 11228, p. 112280J. doi: 10.1117/12.2547884.
[170] K. Kawana, Y. Yasuno, T. Yatagai, and T. Oshika, "High-speed, swept-source optical coherence tomography: a 3-dimensional view of anterior chamber angle recession," *Acta Ophthalmologica Scandinavica*, vol. 85, no. 6, pp. 684–685, 2007.

[171] E. Auksorius *et al.*, “In vivo imaging of the human cornea with high-speed and high-resolution Fourier-domain full-field optical coherence tomography,” *Biomed. Opt. Express, BOE*, vol. 11, no. 5, pp. 2849–2865, May 2020, doi: 10.1364/BOE.393801.
[172] W. Drexler, M. Liu, A. Kumar, T. Kamali, A. Unterhuber, and R. A. Leitgeb, “Optical coherence tomography today: speed, contrast, and multimodality,” *Journal of biomedical optics*, vol. 19, no. 7, p. 071412, 2014.
[173] G. Held, S. Preisser, H. G. Akarçay, S. Peeters, M. Frenz, and M. Jaeger, “Effect of irradiation distance on image contrast in epi-optoacoustic imaging of human volunteers,” *Biomed. Opt. Express, BOE*, vol. 5, no. 11, pp. 3765–3780, Nov. 2014, doi: 10.1364/BOE.5.003765.
[174] C. Haisch, K. Eilert-Zell, M. M. Vogel, P. Menzenbach, and R. Niessner, “Combined optoacoustic/ultrasound system for tomographic absorption measurements: possibilities and limitations,” *Anal Bioanal Chem*, vol. 397, no. 4, pp. 1503–1510, Jun. 2010, doi: 10.1007/s00216-010-3685-9.
[175] G. S. Sangha, N. J. Hale, and C. J. Goergen, “Adjustable photoacoustic tomography probe improves light delivery and image quality,” *Photoacoustics*, vol. 12, pp. 6–13, Dec. 2018, doi: 10.1016/j.pacs.2018.08.002.
[176] Sowers, Timothy, Heechul Yoon, and Stanislav Emelianov. "Investigation of light delivery geometries for photoacoustic applications using Monte Carlo simulations with multiple wavelengths, tissue types, and species characteristics." *Journal of biomedical optics* 25, no. 1 (2020): 016005.
[177] K. Daoudi *et al.*, “Handheld probe integrating laser diode and ultrasound transducer array for ultrasound/photoacoustic dual modality imaging,” *Opt. Express, OE*, vol. 22, no. 21, pp. 26365–26374, Oct. 2014, doi: 10.1364/OE.22.026365.
[178] L. Zhao, M. Yang, Y. Jiang, and C. Li, “Optical fluence compensation for handheld photoacoustic probe: An in vivo human study case,” *J. Innov. Opt. Health Sci.*, vol. 10, no. 04, p. 1740002, Jun. 2017, doi: 10.1142/S1793545817400028.
[179] Y. Zhou, J. Liang, and L. V. Wang, “Cuffing-based photoacoustic flowmetry in humans in the optical diffusive regime,” *Journal of Biophotonics*, vol. 9, no. 3, pp. 208–212, 2016, doi: https://doi.org/10.1002/jbio.201500181.
[180] X. Zhang, X. Wu, O. J. Adelegan, F. Y. Yamaner, and Ö. Oralkan, “Backward-Mode Photoacoustic Imaging Using Illumination Through a CMUT With Improved Transparency,” *IEEE Transactions on Ultrasonics, Ferroelectrics, and Frequency Control*, vol. 65, no. 1, pp. 85–94, Jan. 2018, doi: 10.1109/TUFFC.2017.2774283.
[181] J. H. Uliana *et al.*, “Multiangle Long-Axis Lateral Illumination Photoacoustic Imaging Using Linear Array Transducer,” *Sensors*, vol. 20, no. 14, Art. no. 14, Jan. 2020, doi: 10.3390/s20144052.
[182] S. Jeon *et al.*, “In Vivo Photoacoustic Imaging of Anterior Ocular Vasculature: A Random Sample Consensus Approach,” *Sci Rep*, vol. 7, no. 1, p. 4318, Dec. 2017, doi: 10.1038/s41598-017-04334-z.
[183] S. Park, S. Rim, Y. Kim, and B. H. Lee, “Noncontact photoacoustic imaging based on optical quadrature detection with a multiport interferometer,” *Optics letters*, vol. 44, no. 10, pp. 2590–2593, 2019.
[184] Y. Wang, C. Li, and R. K. Wang, “Noncontact photoacoustic imaging achieved by using a low-coherence interferometer as the acoustic detector,” *Optics letters*, vol. 36, no. 20, pp. 3975–3977, 2011.
[185] Y. Wang, Y. Hu, B. Peng, H. Zhou, Y. Zhao, and Z. Ma, “Complete-noncontact photoacoustic microscopy by detection of initial pressures using a 3× 3 coupler-based fiber-optic interferometer,” *Biomedical Optics Express*, vol. 11, no. 1, pp. 505–516, 2020.

[186] Z. Hosseinaee, M. Le, K. Bell, and P. H. reza, "Towards non-contact photoacoustic imaging [Review]," *Photoacoustics*, p. 100207, Sep. 2020, doi: 10.1016/j.pacs.2020.100207.
[187] J. Eom, J. G. Shin, S. Park, S. Rim, and B. H. Lee, "An all-fiber-optic combined system of noncontact photoacoustic tomography and optical coherence tomography," *Sensors*, vol. 16, no. 5, p. 734, 2016.
[188] T. Berer, E. Leiss-Holzinger, A. Hochreiner, J. Bauer-Marschallinger, and A. Buchsbaum, "Multimodal noncontact photoacoustic and optical coherence tomography imaging using wavelength-division multiplexing," *Journal of biomedical optics*, vol. 20, no. 4, p. 046013, 2015.
[189] L. Amar, "Detection d'omes elastiques (ultrasonores) sur l'os occipital, induites par impulsions laser dans l'oeil d'un lapin," *CR Acad. Sc. Paris*, vol. 259, pp. 3653–3655, 1964.
[190] L. Amar, M. Bruma, M. Velghe, and P. Desvignes, "On the detection of laser induced ultrasonic waves in the human eye and the elaboration of a theory on the fundamental mechanism of vision," *Zeitschrift für angewandte Mathematik und Physik ZAMP*, vol. 16, no. 1, pp. 182–183, 1965.
[191] Q. X. Chen, A. Davies, R. J. Dewhurst, and P. A. Payne, "Photo-acoustic probe for intra-arterial imaging and therapy," *Electronics Letters*, vol. 29, no. 18, pp. 1632–1633, Sep. 1993, doi: 10.1049/el:19931087.
[192] V. Tsytsarev, K. I. Maslov, J. Yao, A. R. Parameswar, A. V. Demchenko, and L. V. Wang, "In vivo imaging of epileptic activity using 2-NBDG, a fluorescent deoxyglucose analog," *Journal of neuroscience methods*, vol. 203, no. 1, pp. 136–140, 2012.
[193] M. R. Kelly-Goss *et al.*, "Dynamic, heterogeneous endothelial Tie2 expression and capillary blood flow during microvascular remodeling," *Sci Rep*, vol. 7, no. 1, p. 9049, Dec. 2017, doi: 10.1038/s41598-017-08982-z.
[194] C. Tian, W. Zhang, V. P. Nguyen, X. Wang, Z. Huang, and Y. M. Paulus, "Integrated photoacoustic microscopy, optical coherence tomography, and fluorescence microscopy for multimodal chorioretinal imaging," in *Photons Plus Ultrasound: Imaging and Sensing 2018*, San Francisco, United States, Feb. 2018, p. 204. doi: 10.1117/12.2290594.
[195] L. Yan, C. Gao, B. Zhao, X. Ma, N. Zhuang, and H. Duan, "Non-destructive Imaging of Standard Cracks of Railway by Photoacoustic Piezoelectric Technology," *Int J Thermophys*, vol. 33, no. 10, pp. 2001–2005, Nov. 2012, doi: 10.1007/s10765-012-1253-6.
[196] M. Sun, X. Lin, Z. Wu, Y. Liu, Y. Shen, and N. Feng, "Non-destructive photoacoustic detecting method for high-speed rail surface defects," in *2014 IEEE International Instrumentation and Measurement Technology Conference (I2MTC) Proceedings*, May 2014, pp. 896–900. doi: 10.1109/I2MTC.2014.6860871.
[197] S. Jeon, J. Kim, J. P. Yun, and C. Kim, "Non-destructive photoacoustic imaging of metal surface defects," *J. Opt.*, vol. 18, no. 11, p. 114001, Nov. 2016, doi: 10.1088/2040-8978/18/11/114001.
[198] H. Wu *et al.*, "Beat frequency quartz-enhanced photoacoustic spectroscopy for fast and calibration-free continuous trace-gas monitoring," *Nature Communications*, vol. 8, no. 1, Art. no. 1, May 2017, doi: 10.1038/ncomms15331.
[199] P. Patimisco, G. Scamarcio, F. K. Tittel, and V. Spagnolo, "Quartz-Enhanced Photoacoustic Spectroscopy: A Review," *Sensors*, vol. 14, no. 4, Art. no. 4, Apr. 2014, doi: 10.3390/s140406165.
[200] G. J. Tserevelakis *et al.*, "Photoacoustic imaging reveals hidden underdrawings in paintings," *Sci Rep*, vol. 7, no. 1, p. 747, Dec. 2017, doi: 10.1038/s41598-017-00873-7.
[201] L. V. Wang and H. Wu, *Biomedical optics: principles and imaging*. John Wiley & Sons, 2012.

[202] M. Xu and L. V. Wang, “Photoacoustic imaging in biomedicine,” *Review of Scientific Instruments*, vol. 77, no. 4, p. 041101, Apr. 2006, doi: 10.1063/1.2195024.
[203] D.-K. Yao, C. Zhang, K. I. Maslov, and L. V. Wang, “Photoacoustic measurement of the Grüneisen parameter of tissue,” *Journal of biomedical optics*, vol. 19, no. 1, p. 017007, 2014.
[204] E. Petrova, S. Ermilov, R. Su, V. Nadvoretskiy, A. Conjusteau, and A. Oraevsky, “Using optoacoustic imaging for measuring the temperature dependence of Grüneisen parameter in optically absorbing solutions,” *Opt. Express*, vol. 21, no. 21, p. 25077, Oct. 2013, doi: 10.1364/OE.21.025077.
[205] L. V. Wang, “Tutorial on photoacoustic microscopy and computed tomography,” *IEEE Journal of Selected Topics in Quantum Electronics*, vol. 14, no. 1, pp. 171–179, 2008.
[206] Y. Liu, L. Nie, and X. Chen, “Photoacoustic Molecular Imaging: From Multiscale Biomedical Applications Towards Early-Stage Theranostics,” *Trends in Biotechnology*, vol. 34, no. 5, pp. 420–433, May 2016, doi: 10.1016/j.tibtech.2016.02.001.
[207] J. Xia, C. Huang, K. Maslov, M. A. Anastasio, and L. V. Wang, “Enhancement of photoacoustic tomography by ultrasonic computed tomography based on optical excitation of elements of a full-ring transducer array,” *Opt. Lett., OL*, vol. 38, no. 16, pp. 3140–3143, Aug. 2013, doi: 10.1364/OL.38.003140.
[208] H.-P. Brecht, R. Su, M. Fronheiser, S. A. Ermilov, A. Conjusteau, and A. A. Oraevsky, “Whole-body three-dimensional optoacoustic tomography system for small animals,” *J. Biomed. Opt.*, vol. 14, no. 6, p. 064007, 2009, doi: 10.1117/1.3259361.
[209] J. K. Gamelin *et al.*, “Curved array photoacoustic tomographic system for small animal imaging,” *JBO*, vol. 13, no. 2, p. 024007, Mar. 2008, doi: 10.1117/1.2907157.
[210] M. Toi *et al.*, “Visualization of tumor-related blood vessels in human breast by photoacoustic imaging system with a hemispherical detector array,” *Scientific Reports*, vol. 7, no. 1, Art. no. 1, Feb. 2017, doi: 10.1038/srep41970.
[211] J. Xia, J. Yao, and L. V. Wang, “Photoacoustic tomography: principles and advances,” *Electromagnetic waves (Cambridge, Mass.)*, vol. 147, p. 1, 2014.
[212] J. Xia *et al.*, “Whole-body ring-shaped confocal photoacoustic computed tomography of small animals in vivo,” *J. Biomed. Opt.*, vol. 17, no. 5, p. 050506, 2012, doi: 10.1117/1.JBO.17.5.050506.
[213] K. Maslov, G. Stoica, and L. V. Wang, “In vivo dark-field reflection-mode photoacoustic microscopy,” *Opt. Lett.*, vol. 30, no. 6, p. 625, Mar. 2005, doi: 10.1364/OL.30.000625.
[214] K. Maslov, H. F. Zhang, S. Hu, and L. V. Wang, “Optical-resolution photoacoustic microscopy for in vivo imaging of single capillaries,” *Opt. Lett.*, vol. 33, no. 9, p. 929, May 2008, doi: 10.1364/OL.33.000929.
[215] H. Azhari, *Basics of biomedical ultrasound for engineers*. John Wiley & Sons, 2010.
[216] C. Zhang, K. I. Maslov, J. Yao, and L. V. Wang, “In vivo photoacoustic microscopy with 7.6-μm axial resolution using a commercial 125-MHz ultrasonic transducer,” *JBO*, vol. 17, no. 11, p. 116016, Nov. 2012, doi: 10.1117/1.JBO.17.11.116016.
[217] H. F. Zhang, K. Maslov, G. Stoica, and L. V. Wang, “Functional photoacoustic microscopy for high-resolution and noninvasive in vivo imaging,” *Nat Biotechnol*, vol. 24, no. 7, pp. 848–851, Jul. 2006, doi: 10.1038/nbt1220.
[218] L.-D. Liao *et al.*, “Imaging brain hemodynamic changes during rat forepaw electrical stimulation using functional photoacoustic microscopy,” *NeuroImage*, vol. 52, no. 2, pp. 562–570, Aug. 2010, doi: 10.1016/j.neuroimage.2010.03.065.
[219] V. Periyasamy, N. Das, A. Sharma, and M. Pramanik, “1064 nm acoustic resolution photoacoustic microscopy,” *J. Biophotonics*, vol. 12, no. 5, May 2019, doi: 10.1002/jbio.201800357.

[220] S. Hu and L. V. Wang, "Optical-Resolution Photoacoustic Microscopy: Auscultation of Biological Systems at the Cellular Level," *Biophysical Journal*, vol. 105, no. 4, pp. 841–847, Aug. 2013, doi: 10.1016/j.bpj.2013.07.017.
[221] S.-L. Chen, L. J. Guo, and X. Wang, "All-optical photoacoustic microscopy," *Photoacoustics*, vol. 3, no. 4, pp. 143–150, 2015.
[222] M. Moothanchery, R. Bi, J. Y. Kim, S. Jeon, C. Kim, and M. Olivo, "Optical resolution photoacoustic microscopy based on multimode fibers," *Biomed Opt Express*, vol. 9, no. 3, pp. 1190–1197, Feb. 2018, doi: 10.1364/BOE.9.001190.
[223] D.-K. Yao, K. Maslov, K. K. Shung, Q. Zhou, and L. V. Wang, "In vivo label-free photoacoustic microscopy of cell nuclei by excitation of DNA and RNA," *Optics letters*, vol. 35, no. 24, pp. 4139–4141, 2010.
[224] Y. Zhou, G. Li, L. Zhu, C. Li, L. A. Cornelius, and L. V. Wang, "Handheld photoacoustic probe to detect both melanoma depth and volume at high speed *in vivo*," *J. Biophoton*, vol. 8, no. 11–12, pp. 961–967, Nov. 2015, doi: 10.1002/jbio.201400143.
[225] P. Wang *et al.*, "High-speed Intravascular Photoacoustic Imaging of Lipid-laden Atherosclerotic Plaque Enabled by a 2-kHz Barium Nitrite Raman Laser," *Sci Rep*, vol. 4, no. 1, p. 6889, May 2015, doi: 10.1038/srep06889.
[226] Z. Xu, Q. Zhu, and L. V. Wang, "In vivo photoacoustic tomography of mouse cerebral edema induced by cold injury," *J. Biomed. Opt.*, vol. 16, no. 6, p. 066020, 2011, doi: 10.1117/1.3584847.
[227] Y. Zhou, J. Yao, and L. V. Wang, "Tutorial on photoacoustic tomography," *J. Biomed. Opt*, vol. 21, no. 6, p. 061007, Apr. 2016, doi: 10.1117/1.JBO.21.6.061007.
[228] G. P. Luke, D. Yeager, and S. Y. Emelianov, "Biomedical applications of photoacoustic imaging with exogenous contrast agents," *Annals of biomedical engineering*, vol. 40, no. 2, pp. 422–437, 2012.
[229] E. M. Strohm, M. J. Moore, and M. C. Kolios, "Single Cell Photoacoustic Microscopy: A Review," *IEEE J. Select. Topics Quantum Electron.*, vol. 22, no. 3, pp. 137–151, May 2016, doi: 10.1109/JSTQE.2015.2497323.
[230] K. Homan, S. Mallidi, E. Cooley, and S. Emelianov, "Combined photoacoustic and ultrasound imaging of metal nanoparticles in vivo," *Nanoimaging*, vol. 3, 2010.
[231] S. Kim, Y.-S. Chen, G. P. Luke, M. Mehrmohammadi, J. R. Cook, and S. Y. Emelianov, "Ultrasound and photoacoustic image-guided photothermal therapy using silica-coated gold nanorods: in-vivo study," in *2010 IEEE International Ultrasonics Symposium*, 2010, pp. 233–236.
[232] X. Yang, S. E. Skrabalak, Z.-Y. Li, Y. Xia, and L. V. Wang, "Photoacoustic tomography of a rat cerebral cortex in vivo with Au nanocages as an optical contrast agent," *Nano letters*, vol. 7, no. 12, pp. 3798–3802, 2007.
[233] S. Yang *et al.*, "Noninvasive monitoring of traumatic brain injury and post-traumatic rehabilitation with laser-induced photoacoustic imaging," *Applied Physics Letters*, vol. 90, no. 24, p. 243902, 2007.
[234] J. L.-S. Su, B. Wang, and S. Y. Emelianov, "Photoacoustic imaging of coronary artery stents," *Optics Express*, vol. 17, no. 22, pp. 19894–19901, 2009.
[235] T. Sowers and S. Emelianov, "Exogenous imaging contrast and therapeutic agents for intravascular photoacoustic imaging and image-guided therapy," *Phys. Med. Biol.*, vol. 63, no. 22, p. 22TR01, Nov. 2018, doi: 10.1088/1361-6560/aae62b.
[236] D.-K. Yao, K. Maslov, K. K. Shung, Q. Zhou, and L. V. Wang, "In vivo label-free photoacoustic microscopy of cell nuclei by excitation of DNA and RNA," *Opt. Lett.*, vol. 35, no. 24, p. 4139, Dec. 2010, doi: 10.1364/OL.35.004139.

[237] C. Zhang, Y. S. Zhang, D.-K. Yao, Y. Xia, and L. V. Wang, "Label-free photoacoustic microscopy of cytochromes," *Journal of biomedical optics*, vol. 18, no. 2, p. 020504, 2013.
[238] B. Dong *et al.*, "Isometric multimodal photoacoustic microscopy based on optically transparent micro-ring ultrasonic detection," *Optica*, vol. 2, no. 2, pp. 169–176, 2015.
[239] K. Maslov and L. V. Wang, "Photoacoustic imaging of biological tissue with intensity-modulated continuous-wave laser," *J. Biomed. Opt.*, vol. 13, no. 2, p. 024006, 2008, doi: 10.1117/1.2904965.
[240] A. Petschke and P. J. La Rivière, "Comparison of intensity-modulated continuous-wave lasers with a chirped modulation frequency to pulsed lasers for photoacoustic imaging applications," *Biomed. Opt. Express*, vol. 1, no. 4, p. 1188, Nov. 2010, doi: 10.1364/BOE.1.001188.
[241] H. F. Zhang, C. A. Puliafito, and S. Jiao, "Photoacoustic Ophthalmoscopy for In Vivo Retinal Imaging: Current Status and Prospects," *Ophthalmic Surg Lasers Imaging*, vol. 42, no. 4, pp. S106–S115, Jul. 2011, doi: 10.3928/15428877-20110627-10.
[242] A. de La Zerda *et al.*, "Photoacoustic ocular imaging," *Optics letters*, vol. 35, no. 3, pp. 270–272, 2010.
[243] X. Wang, Y. Pang, G. Ku, X. Xie, G. Stoica, and L. V. Wang, "Noninvasive laser-induced photoacoustic tomography for structural and functional in vivo imaging of the brain," *Nature biotechnology*, vol. 21, no. 7, pp. 803–806, 2003.
[244] H. F. Zhang, K. Maslov, G. Stoica, and L. V. Wang, "Imaging acute thermal burns by photoacoustic microscopy," *Journal of biomedical optics*, vol. 11, no. 5, p. 054033, 2006.
[245] V. Ntziachristos, J. S. Yoo, and G. M. van Dam, "Current concepts and future perspectives on surgical optical imaging in cancer," *J. Biomed. Opt.*, vol. 15, no. 6, p. 066024, 2010, doi: 10.1117/1.3523364.
[246] G. Rousseau, A. Blouin, and J.-P. Monchalin, "Non-contact photoacoustic tomography and ultrasonography for tissue imaging," *Biomedical optics express*, vol. 3, no. 1, pp. 16–25, 2012.
[247] B. Lengenfelder *et al.*, "Contact-free endoscopic photoacoustic sensing using speckle analysis," *Journal of biophotonics*, vol. 12, no. 12, p. e201900130, 2019.
[248] M. Luukkala, P. Heikkila, and J. Surakka, "Plate wave resonance — a contactless test method," *Ultrasonics*, vol. 9, no. 4, pp. 201–208, Oct. 1971, doi: 10.1016/0041-624X(71)90387-8.
[249] W. A. Grandia and C. M. Fortunko, "NDE applications of air-coupled ultrasonic transducers," in *1995 IEEE Ultrasonics Symposium. Proceedings. An International Symposium*, 1995, vol. 1, pp. 697–709.
[250] D. K. Hsu, "Nondestructive testing using air-borne ultrasound," *Ultrasonics*, vol. 44, pp. e1019–e1024, 2006.
[251] A. J. Rogovsky, "Development and application of ultrasonic dry-contact and air-contact C-scan systems for nondestructive evaluation of aerospace composites," *Materials evaluation*, vol. 49, no. 12, pp. 1491–1497, 1991.
[252] T. E. Gómez Álvarez-Arenas, F. R. Montero de Espinosa, M. Moner-Girona, E. Rodríguez, A. Roig, and E. Molins, "Viscoelasticity of silica aerogels at ultrasonic frequencies," *Appl. Phys. Lett.*, vol. 81, no. 7, pp. 1198–1200, Aug. 2002, doi: 10.1063/1.1499225.
[253] D. A. Hutchins, W. M. D. Wright, and D. W. Schindel, "Ultrasonic measurements in polymeric materials using air-coupled capacitance transducers," *The Journal of the Acoustical Society of America*, vol. 96, no. 3, pp. 1634–1642, Sep. 1994, doi: 10.1121/1.410243.
[254] B. Hosten, D. A. Hutchins, and D. W. Schindel, "Measurement of elastic constants in composite materials using air-coupled ultrasonic bulk waves," *The Journal of the Acoustical Society of America*, vol. 99, no. 4, pp. 2116–2123, Apr. 1996, doi: 10.1121/1.415398.

[255] C. Li, D. A. Hutchins, and R. J. Green, “Short-range ultrasonic communications in air using quadrature modulation,” *IEEE transactions on ultrasonics, ferroelectrics, and frequency control*, vol. 56, no. 10, pp. 2060–2072, 2009.
[256] F.-J. García-Diego, J. M. Bravo, J. Pérez-Miralles, H. Estrada, and A. Fernández-Navajas, “Development of a Low-Cost Airborne Ultrasound Sensor for the Detection of Brick Joints behind a Wall Painting,” *Sensors*, vol. 12, no. 2, Art. no. 2, Feb. 2012, doi: 10.3390/s120201299.
[257] D. Sancho-Knapik, T. Gómez Álvarez-Arenas, J. J. Peguero-Pina, and E. Gil-Pelegrín, “Air-coupled broadband ultrasonic spectroscopy as a new non-invasive and non-contact method for the determination of leaf water status,” *J Exp Bot*, vol. 61, no. 5, pp. 1385–1391, Mar. 2010, doi: 10.1093/jxb/erq001.
[258] D. Sancho-Knapik, H. Calas, J. J. Peguero-Pina, A. Ramos Fernandez, E. Gil-Pelegrin, and T. E. Gomez Alvarez-Arenas, “Air-coupled ultrasonic resonant spectroscopy for the study of the relationship between plant leaves’ elasticity and their water content,” *IEEE Transactions on Ultrasonics, Ferroelectrics, and Frequency Control*, vol. 59, no. 2, pp. 319–325, Feb. 2012, doi: 10.1109/TUFFC.2012.2194.
[259] E. Corona, J. V. Garcia-Perez, T. E. Gomez Alvarez-Arenas, N. Watson, M. J. W. Povey, and J. Benedito, “Advances in the ultrasound characterization of dry-cured meat products,” *Journal of Food Engineering*, vol. 119, no. 3, pp. 464–470, Dec. 2013, doi: 10.1016/j.jfoodeng.2013.06.023.
[260] T.-I. Chiu, H.-C. Deng, S.-Y. Chang, and S.-B. Luo, “Implementation of ultrasonic touchless interactive panel using the polymer-based CMUT array,” in *2009 IEEE SENSORS*, Oct. 2009, pp. 625–630. doi: 10.1109/ICSENS.2009.5398325.
[261] G. R. McMillan, “The technology and applications of gesture-based control,” *NASA*, no. 19990007890, 1998.
[262] T. E. Gómez Álvarez-Arenas, J. Camacho, and C. Fritsch, “Passive focusing techniques for piezoelectric air-coupled ultrasonic transducers,” *Ultrasonics*, vol. 67, pp. 85–93, Apr. 2016, doi: 10.1016/j.ultras.2016.01.001.
[263] B. T. Khuri-Yakub, J. H. Kim, C.-H. Chou, P. Parent, and G. S. Kino, “A new design for air transducers,” in *IEEE 1988 Ultrasonics Symposium Proceedings.*, 1988, pp. 503–506.
[264] T. Yano, M. Tone, and A. Fukumoto, “Range finding and surface characterization using high-frequency air transducers,” *IEEE transactions on ultrasonics, ferroelectrics, and frequency control*, vol. 34, no. 2, pp. 232–236, 1987.
[265] W. Manthey, N. Kroemer, and V. Magori, “Ultrasonic transducers and transducer arrays for applications in air,” *Measurement Science and Technology*, vol. 3, no. 3, p. 249, 1992.
[266] D. W. Schindel, D. A. Hutchins, L. Zou, and M. Sayer, “The design and characterization of micromachined air-coupled capacitance transducers,” *IEEE Transactions on ultrasonics, ferroelectrics, and frequency control*, vol. 42, no. 1, pp. 42–50, 1995.
[267] L. Svilainis, A. Chaziachmetovas, and V. Dumbrava, “Efficient high voltage pulser for piezoelectric air coupled transducer,” *Ultrasonics*, vol. 53, no. 1, pp. 225–231, 2013.
[268] D. Hutchins, P. Burrascano, L. Davis, S. Laureti, and M. Ricci, “Coded waveforms for optimised air-coupled ultrasonic nondestructive evaluation,” *Ultrasonics*, vol. 54, no. 7, pp. 1745–1759, 2014.
[269] T. H. Gan, D. A. Hutchins, and R. J. Green, “Swept Frequency Multiplication (SFM) Techniques for Improved Air-Coupled Ultrasonic NDE,” in *AIP Conference Proceedings*, 2003, vol. 657, no. 1, pp. 620–627.
[270] A. Turo *et al.*, “Ultra-low noise front-end electronics for air-coupled ultrasonic non-destructive evaluation,” *NDT & e International*, vol. 36, no. 2, pp. 93–100, 2003.

[271] R. G. Kolkman *et al.*, “Feasibility of noncontact piezoelectric detection of photoacoustic signals in tissue-mimicking phantoms,” *Journal of biomedical optics*, vol. 15, no. 5, p. 055011, 2010.
[272] X. L. Deán-Ben, G. A. Pang, F. Montero de Espinosa, and D. Razansky, “Non-contact optoacoustic imaging with focused air-coupled transducers,” *Applied Physics Letters*, vol. 107, no. 5, p. 051105, 2015.
[273] K. Sathiyamoorthy, E. M. Strohm, and M. C. Kolios, “Low-power noncontact photoacoustic microscope for bioimaging applications,” *Journal of biomedical optics*, vol. 22, no. 4, p. 046001, 2017.
[274] J.-P. Monchalin, “Optical Detection of Ultrasound,” *IEEE Transactions on Ultrasonics, Ferroelectrics, and Frequency Control*, vol. 33, no. 5, pp. 485–499, Sep. 1986, doi: 10.1109/T-UFFC.1986.26860.
[275] S.-L. Chen, “Review of Laser-Generated Ultrasound Transmitters and Their Applications to All-Optical Ultrasound Transducers and Imaging,” *Applied Sciences*, vol. 7, no. 1, Art. no. 1, Jan. 2017, doi: 10.3390/app7010025.
[276] Z. Xie, S.-L. Chen, T. Ling, L. J. Guo, P. L. Carson, and X. Wang, “Pure optical photoacoustic microscopy,” *Optics express*, vol. 19, no. 10, pp. 9027–9034, 2011.
[277] E. Z. Zhang, J. G. Laufer, R. B. Pedley, and P. C. Beard, “In vivohigh-resolution 3D photoacoustic imaging of superficial vascular anatomy,” *Phys. Med. Biol.*, vol. 54, no. 4, pp. 1035–1046, Jan. 2009, doi: 10.1088/0031-9155/54/4/014.
[278] S.-L. Chen, Z. Xie, T. Ling, L. J. Guo, X. Wei, and X. Wang, “Miniaturized all-optical photoacoustic microscopy based on microelectromechanical systems mirror scanning,” *Opt. Lett., OL*, vol. 37, no. 20, pp. 4263–4265, Oct. 2012, doi: 10.1364/OL.37.004263.
[279] R. Ansari, E. Z. Zhang, A. E. Desjardins, and P. C. Beard, “All-optical forward-viewing photoacoustic probe for high-resolution 3D endoscopy,” *Light Sci Appl*, vol. 7, no. 1, p. 75, Dec. 2018, doi: 10.1038/s41377-018-0070-5.
[280] S.-L. Chen, Z. Xie, L. J. Guo, and X. Wang, “A fiber-optic system for dual-modality photoacoustic microscopy and confocal fluorescence microscopy using miniature components,” *Photoacoustics*, vol. 1, no. 2, pp. 30–35, May 2013, doi: 10.1016/j.pacs.2013.07.001.
[281] R. A. Barnes, S. Maswadi, R. Glickman, and M. Shadaram, “Probe beam deflection technique as acoustic emission directionality sensor with photoacoustic emission source,” *Appl. Opt.*, vol. 53, no. 3, p. 511, Jan. 2014, doi: 10.1364/AO.53.000511.
[282] R. Nuster, G. Zangerl, M. Haltmeier, and G. Paltauf, “Full field detection in photoacoustic tomography,” *Opt. Express, OE*, vol. 18, no. 6, pp. 6288–6299, Mar. 2010, doi: 10.1364/OE.18.006288.
[283] R. Nuster, P. Slezak, and G. Paltauf, “High resolution three-dimensional photoacoustic tomography with CCD-camera based ultrasound detection,” *Biomedical optics express*, vol. 5, no. 8, pp. 2635–2647, 2014.
[284] K. P. Köstli, M. Frenz, H. P. Weber, G. Paltauf, and H. Schmidt-Kloiber, “Optoacoustic tomography: time-gated measurement of pressure distributions and image reconstruction,” *Appl. Opt., AO*, vol. 40, no. 22, pp. 3800–3809, Aug. 2001, doi: 10.1364/AO.40.003800.
[285] E. Bossy and S. Gigan, “Photoacoustics with coherent light,” *Photoacoustics*, vol. 4, no. 1, pp. 22–35, Mar. 2016, doi: 10.1016/j.pacs.2016.01.003.
[286] D. A. Boas and A. K. Dunn, “Laser speckle contrast imaging in biomedical optics,” *J. Biomed. Opt.*, vol. 15, no. 1, p. 011109, 2010, doi: 10.1117/1.3285504.
[287] C. B. Burckhardt, “Speckle in ultrasound B-mode scans,” *IEEE Transactions on Sonics and ultrasonics*, vol. 25, no. 1, pp. 1–6, 1978.
[288] J.-S. Lee, “Speckle analysis and smoothing of synthetic aperture radar images,” *Computer graphics and image processing*, vol. 17, no. 1, pp. 24–32, 1981.

[289] J. M. Schmitt, S. H. Xiang, and K. M. Yung, “Speckle in optical coherence tomography,” *Journal of biomedical optics*, vol. 4, no. 1, pp. 95–106, 1999.
[290] B. Lengenfelder *et al.*, “Remote photoacoustic sensing using speckle-analysis,” *Scientific reports*, vol. 9, no. 1, pp. 1–11, 2019.
[291] M. Benyamin, H. Genish, R. Califa, A. Schwartz, Z. Zalevsky, and N. Ozana, “Non-contact photoacoustic imaging using laser speckle contrast analysis,” *Optics letters*, vol. 44, no. 12, pp. 3110–3113, 2019.
[292] C. Buj, J. Horstmann, M. Münter, and R. Brinkmann, “Speckle-based off-axis holographic detection for non-contact photoacoustic tomography,” *Current Directions in Biomedical Engineering*, vol. 1, no. 1, pp. 356–360, 2015.
[293] Z. Guo, L. Li, and L. V. Wang, “On the speckle-free nature of photoacoustic tomography,” *Medical physics*, vol. 36, no. 9Part1, pp. 4084–4088, 2009.
[294] Z. Zalevsky *et al.*, “Simultaneous remote extraction of multiple speech sources and heart beats from secondary speckles pattern,” *Optics express*, vol. 17, no. 24, pp. 21566–21580, 2009.
[295] S. Lévêque, A. C. Boccara, M. Lebec, and H. Saint-Jalmes, “Ultrasonic tagging of photon paths in scattering media:?parallel speckle modulation processing,” *Opt. Lett.*, vol. 24, no. 3, p. 181, Feb. 1999, doi: 10.1364/OL.24.000181.
[296] S. Lévêque-Fort, “Three-dimensional acousto-optic imaging in biological tissues with parallel signal processing,” *Applied Optics*, vol. 40, no. 7, pp. 1029–1036, 2001.
[297] G. Yao and L. V. Wang, “Theoretical and experimental studies of ultrasound-modulated optical tomography in biological tissue,” *Appl. Opt.*, vol. 39, no. 4, p. 659, Feb. 2000, doi: 10.1364/AO.39.000659.
[298] G. Yao, S. Jiao, and L. V. Wang, “Frequency-swept ultrasound-modulated optical tomography in biological tissue by use of parallel detection,” *Opt. Lett.*, vol. 25, no. 10, p. 734, May 2000, doi: 10.1364/OL.25.000734.
[299] J. Li and L. V. Wang, “Methods for parallel-detection-based ultrasound-modulated optical tomography,” *Applied optics*, vol. 41, no. 10, pp. 2079–2084, 2002.
[300] C. Buj, M. Münter, B. Schmarbeck, J. Horstmann, G. Hüttmann, and R. Brinkmann, “Noncontact holographic detection for photoacoustic tomography,” *JBO*, vol. 22, no. 10, p. 106007, Oct. 2017, doi: 10.1117/1.JBO.22.10.106007.
[301] J. Horstmann, H. Spahr, C. Buj, M. Münter, and R. Brinkmann, “Full-field speckle interferometry for non-contact photoacoustic tomography,” *Physics in Medicine & Biology*, vol. 60, no. 10, p. 4045, 2015.
[302] H. Li, F. Cao, and P. Lai, “Interferometry-free noncontact photoacoustic detection method based on speckle correlation change,” *Optics letters*, vol. 44, no. 22, pp. 5481–5484, 2019.
[303] U. Sangawa, T. Iwamoto, Y. Kaneko, and M. Hashimoto, “Palm sized airborne ultrasonic sensor with nanofoam acoustic lens and homodyne interferometer,” in *2010 IEEE International Ultrasonics Symposium*, Oct. 2010, pp. 1442–1445. doi: 10.1109/ULTSYM.2010.5935546.
[304] “Measurement of in-plane and out-of-plane ultrasonic displacements by optical heterodyne interferometry | SpringerLink.” https://link.springer.com/article/10.1007/BF00565636 (accessed May 13, 2020).
[305] W. Li, X. Yu, Z. Meng, Y. Jin, and J. Zhang, “Experimental study of balanced optical homodyne and heterodyne detection by controlling sideband modulation,” *Sci. China Phys. Mech. Astron.*, vol. 58, no. 10, p. 104201, Oct. 2015, doi: 10.1007/s11433-015-5718-z.
[306] M. J. Collett, R. Loudon, and C. W. Gardiner, “Quantum Theory of Optical Homodyne and Heterodyne Detection,” *Journal of Modern Optics*, vol. 34, no. 6–7, pp. 881–902, Jun. 1987, doi: 10.1080/09500348714550811.

[307] S. Jacob, C. Johansson, M. Ulfendahl, and A. Fridberger, “A digital heterodyne laser interferometer for studying cochlear mechanics,” *Journal of neuroscience methods*, vol. 179, no. 2, pp. 271–277, 2009.
[308] E. Zhang *et al.*, “Laser heterodyne interferometric signal processing method based on rising edge locking with high frequency clock signal,” *Optics express*, vol. 21, no. 4, pp. 4638–4652, 2013.
[309] G. De Vine *et al.*, “Picometer level displacement metrology with digitally enhanced heterodyne interferometry,” *Optics express*, vol. 17, no. 2, pp. 828–837, 2009.
[310] A. J. A. Bruinsma and J. A. Vogel, “Ultrasonic noncontact inspection system with optical fiber methods,” *Appl. Opt., AO*, vol. 27, no. 22, pp. 4690–4695, Nov. 1988, doi: 10.1364/AO.27.004690.
[311] G. A. Massey, “An optical heterodyne ultrasonic image converter,” *Proceedings of the IEEE*, vol. 56, no. 12, pp. 2157–2161, 1968.
[312] K. Krzempek *et al.*, “Multi-pass cell-assisted photoacoustic/photothermal spectroscopy of gases using quantum cascade laser excitation and heterodyne interferometric signal detection,” *Appl. Phys. B*, vol. 124, no. 5, p. 74, May 2018, doi: 10.1007/s00340-018-6941-x.
[313] K. Krzempek, G. Dudzik, K. Abramski, G. Wysocki, P. Jaworski, and M. Nikodem, “Heterodyne interferometric signal retrieval in photoacoustic spectroscopy,” *Opt. Express, OE*, vol. 26, no. 2, pp. 1125–1132, Jan. 2018, doi: 10.1364/OE.26.001125.
[314] J. Eom, S. J. Park, and B. H. Lee, “Noncontact photoacoustic tomography of in vivo chicken chorioallantoic membrane based on all-fiber heterodyne interferometry,” *Journal of biomedical optics*, vol. 20, no. 10, p. 106007, 2015.
[315] S. A. Carp, A. Guerra III, S. Q. Duque Jr, and V. Venugopalan, “Optoacoustic imaging using interferometric measurement of surface displacement,” *Applied Physics Letters*, vol. 85, no. 23, pp. 5772–5774, 2004.
[316] S. J. Park, J. Eom, Y. H. Kim, C. S. Lee, and B. H. Lee, “Noncontact photoacoustic imaging based on all-fiber heterodyne interferometer,” *Optics letters*, vol. 39, no. 16, pp. 4903–4906, 2014.
[317] C. Tian *et al.*, “Non-contact photoacoustic imaging using a commercial heterodyne interferometer,” *IEEE sensors journal*, vol. 16, no. 23, pp. 8381–8388, 2016.
[318] T. Berer, A. Hochreiner, S. Zamiri, and P. Burgholzer, “Remote photoacoustic imaging on solid material using a two-wave mixing interferometer,” *Optics letters*, vol. 35, no. 24, pp. 4151–4153, 2010.
[319] S. Zamiri, B. Reitinger, T. Berer, S. Bauer, and P. Burgholzer, “Determination of nanometer vibration amplitudes by using a homodyne photorefractive crystal interferometer,” *Procedia Engineering*, vol. 5, pp. 299–302, 2010.
[320] T. Honda, T. Yamashita, and H. Matsumoto, “Optical measurement of ultrasonic nanometer motion of rough surface by two-wave mixing in Bi12SiO20,” *Japanese journal of applied physics*, vol. 34, no. 7R, p. 3737, 1995.
[321] S. Luo, Y. Wang, Y. Luo, and C. Fan, “Study of two-wave-mixing interferometric method in ultrasonic detection using BSO crystal,” in *2012 IEEE International Conference on Mechatronics and Automation*, 2012, pp. 1938–1942.
[322] C. B. Scruby and L. E. Drain, *Laser ultrasonics techniques and applications*. CRC press, 1990.
[323] P. V. Chitnis, H. Lloyd, and R. H. Silverman, “An adaptive interferometric sensor for all-optical photoacoustic microscopy,” in *2014 IEEE International Ultrasonics Symposium*, Sep. 2014, pp. 353–356. doi: 10.1109/ULTSYM.2014.0087.

[324] A. Hochreiner, J. Bauer-Marschallinger, P. Burgholzer, B. Jakoby, and T. Berer, "Non-contact photoacoustic imaging using a fiber based interferometer with optical amplification," *Biomedical optics express*, vol. 4, no. 11, pp. 2322–2331, 2013.
[325] A. Hochreiner, T. Berer, H. Grün, M. Leitner, and P. Burgholzer, "Photoacoustic imaging using an adaptive interferometer with a photorefractive crystal," *Journal of biophotonics*, vol. 5, no. 7, pp. 508–517, 2012.
[326] D. George, H. Lloyd, R. H. Silverman, and P. V. Chitnis, "A frequency-domain non-contact photoacoustic microscope based on an adaptive interferometer," *Journal of biophotonics*, vol. 11, no. 6, p. e201700278, 2018.
[327] B. Yu and A. Wang, "Grating-assisted demodulation of interferometric optical sensors," *Applied optics*, vol. 42, no. 34, pp. 6824–6829, 2003.
[328] J. J. Alcoz, C. E. Lee, and H. F. Taylor, "Embedded fiber-optic Fabry-Perot ultrasound sensor," *IEEE Trans. Ultrason., Ferroelect., Freq. Contr.*, vol. 37, no. 4, pp. 302–306, Jul. 1990, doi: 10.1109/58.56491.
[329] Z. Chen, S. Yang, Y. Wang, and D. Xing, "Noncontact broadband all-optical photoacoustic microscopy based on a low-coherence interferometer," *Applied Physics Letters*, vol. 106, no. 4, p. 043701, 2015.
[330] J. Liu, Z. Tang, Y. Wu, and Y. Wang, "Rapid and noncontact photoacoustic tomography imaging system using an interferometer with high-speed phase modulation technique," *Review of Scientific Instruments*, vol. 86, no. 4, p. 044904, 2015.
[331] M. A. Choma, C. Yang, and J. A. Izatt, "Instantaneous quadrature low-coherence interferometry with 3×3 fiber-optic couplers," *Opt. Lett.*, vol. 28, no. 22, p. 2162, Nov. 2003, doi: 10.1364/OL.28.002162.
[332] S. Park, J. Lee, Y. Kim, and B. H. Lee, "Nanometer-Scale Vibration Measurement Using an Optical Quadrature Interferometer Based on 3 × 3 Fiber-Optic Coupler," *Sensors*, vol. 20, no. 9, Art. no. 9, Jan. 2020, doi: 10.3390/s20092665.
[333] J. Lu, Y. Gao, Z. Ma, H. Zhou, R. K. Wang, and Y. Wang, "In vivo photoacoustic imaging of blood vessels using a homodyne interferometer with zero-crossing triggering," *Journal of biomedical optics*, vol. 22, no. 3, p. 036002, 2017.
[334] J. Yao, "When pressure meets light: detecting the photoacoustic effect at the origin," *Light: Science & Applications*, vol. 6, no. 6, pp. e17062–e17062, 2017.
[335] P. Hajireza, W. Shi, K. Bell, R. J. Paproski, and R. J. Zemp, "Non-interferometric photoacoustic remote sensing microscopy," *Light: Science & Applications*, vol. 6, no. 6, pp. e16278–e16278, 2017.
[336] S. H. Jack, D. B. Hann, and C. A. Greated, "Influence of the acousto-optic effect on laser Doppler anemometry signals," *Review of Scientific Instruments*, vol. 69, no. 12, pp. 4074–4081, Dec. 1998, doi: 10.1063/1.1149253.
[337] K. L. Bell, P. Hajireza, W. Shi, and R. J. Zemp, "Temporal evolution of low-coherence reflectrometry signals in photoacoustic remote sensing microscopy," *Appl. Opt., AO*, vol. 56, no. 18, pp. 5172–5181, Jun. 2017, doi: 10.1364/AO.56.005172.
[338] K. Bell, P. Hajireza, and R. Zemp, "Scattering cross-sectional modulation in photoacoustic remote sensing microscopy," *Opt. Lett., OL*, vol. 43, no. 1, pp. 146–149, Jan. 2018, doi: 10.1364/OL.43.000146.
[339] P. H. Reza, K. Bell, W. Shi, J. Shapiro, and R. J. Zemp, "Deep non-contact photoacoustic initial pressure imaging," *Optica*, vol. 5, no. 7, pp. 814–820, 2018.
[340] B. R. Ecclestone *et al.*, "Towards virtual biopsies of gastrointestinal tissues using photoacoustic remote sensing microscopy," *Quantitative Imaging in Medicine and Surgery*, vol. 11, no. 3, pp. 1070077–1071077, Mar. 2021, doi: 10.21037/qims-20-722.

[341] S. Abbasi *et al.*, “All-optical Reflection-mode Microscopic Histology of Unstained Human Tissues,” *Scientific reports*, vol. 9, no. 1, pp. 1–11, 2019.
[342] S. Abbasi *et al.*, “Chromophore selective multi-wavelength photoacoustic remote sensing of unstained human tissues,” *Biomed. Opt. Express, BOE*, vol. 10, no. 11, pp. 5461–5469, Nov. 2019, doi: 10.1364/BOE.10.005461.
[343] K. L. Bell, P. H. Reza, and R. J. Zemp, “Real-time functional photoacoustic remote sensing microscopy,” *Optics letters*, vol. 44, no. 14, pp. 3466–3469, 2019.
[344] B. R. Ecclestone *et al.*, “Three-dimensional virtual histology in unprocessed resected tissues with photoacoustic remote sensing (PARS) microscopy and optical coherence tomography (OCT),” *Sci Rep*, vol. 11, no. 1, p. 13723, Jul. 2021, doi: 10.1038/s41598-021-93222-8.
[345] B. R. Ecclestone *et al.*, “Improving maximal safe brain tumor resection with photoacoustic remote sensing microscopy,” *Scientific Reports*, vol. 10, no. 1, Art. no. 1, Oct. 2020, doi: 10.1038/s41598-020-74160-3.
[346] S. Abbasi, K. Bell, and P. Haji Reza, “Rapid High-Resolution Mosaic Acquisition for Photoacoustic Remote Sensing,” *Sensors*, vol. 20, no. 4, p. 1027, 2020.
[347] S. Abbasi *et al.*, “Chromophore selective multi-wavelength photoacoustic remote sensing of unstained human tissues,” *Biomedical Optics Express*, vol. 10, no. 11, pp. 5461–5469, 2019.
[348] X. Shu, H. Li, B. Dong, C. Sun, and H. F. Zhang, “Quantifying melanin concentration in retinal pigment epithelium using broadband photoacoustic microscopy,” *Biomed. Opt. Express, BOE*, vol. 8, no. 6, pp. 2851–2865, Jun. 2017, doi: 10.1364/BOE.8.002851.
[349] S. N. Hennen *et al.*, “Photoacoustic tomography imaging and estimation of oxygen saturation of hemoglobin in ocular tissue of rabbits,” *Experimental Eye Research*, vol. 138, pp. 153–158, Sep. 2015, doi: 10.1016/j.exer.2015.05.022.
[350] S. Jeon *et al.*, “In Vivo Photoacoustic Imaging of Anterior Ocular Vasculature: A Random Sample Consensus Approach,” *Scientific Reports*, vol. 7, no. 1, Art. no. 1, Jun. 2017, doi: 10.1038/s41598-017-04334-z.
[351] L. Chen and J. Xu, “OPTIMAL DELAUNAY TRIANGULATIONS,” *Journal of Computational Mathematics*, vol. 22, no. 2, pp. 299–308, 2004.
[352] Frangi, Alejandro F., Wiro J. Niessen, Koen L. Vincken, and Max A. Viergever. "Multiscale vessel enhancement filtering." In *International conference on medical image computing and computer-assisted intervention*, pp. 130-137. Springer, Berlin, Heidelberg, 1998.
[353] Abbasi, Saad, Kevan Bell, Benjamin Ecclestone, and Parsin Haji Reza. "Live feedback and 3D photoacoustic remote sensing." *Quantitative Imaging in Medicine and Surgery* 11, no. 3 (2021): 1033.
[354] J. Min, Y. Lv, L. Mao, Y. Gong, Q. Gu, and F. Wei, “A rodent model of anterior ischemic optic neuropathy (AION) based on laser photoactivation of verteporfin,” *BMC Ophthalmol*, vol. 18, no. 1, p. 304, Nov. 2018, doi: 10.1186/s12886-018-0937-5.
[355] M. Augustin, S. Fialová, C. Fischak, L. Schmetterer, C. K. Hitzenberger, and B. Baumann, “Ocular fundus pulsations within the posterior rat eye: Chorioscleral motion and response to elevated intraocular pressure,” *Scientific Reports*, vol. 7, no. 1, Art. no. 1, Aug. 2017, doi: 10.1038/s41598-017-09310-1.
[356] S. Hu, B. Rao, K. Maslov, and L. V. Wang, “Label-free photoacoustic ophthalmic angiography,” p. 3.
[357] F. C. Delori, R. H. Webb, and D. H. Sliney, “Maximum permissible exposures for ocular safety (ANSI 2000), with emphasis on ophthalmic devices,” *J. Opt. Soc. Am. A, JOSAA*, vol. 24, no. 5, pp. 1250–1265, May 2007, doi: 10.1364/JOSAA.24.001250.
[358] N. Suehira *et al.*, “Three-beam spectral-domain optical coherence tomography for retinal imaging,” *JBO*, vol. 17, no. 10, p. 106001, Oct. 2012, doi: 10.1117/1.JBO.17.10.106001.

[359] R. H. Silverman *et al.*, "High-Resolution Photoacoustic Imaging of Ocular Tissues," *Ultrasound in Medicine & Biology*, vol. 36, no. 5, pp. 733–742, May 2010, doi: 10.1016/j.ultrasmedbio.2010.02.006.
[360] W. Liu *et al.*, "In vivo corneal neovascularization imaging by optical-resolution photoacoustic microscopy," *Photoacoustics*, vol. 2, no. 2, pp. 81–86, Jun. 2014, doi: 10.1016/j.pacs.2014.04.003.
[361] T. Buma, N. C. Conley, and S. W. Choi, "Multispectral photoacoustic microscopy of lipids using a pulsed supercontinuum laser," *Biomed. Opt. Express, BOE*, vol. 9, no. 1, pp. 276–288, Jan. 2018, doi: 10.1364/BOE.9.000276.
[362] S. M. Park *et al.*, "Quickly Alternating Green and Red Laser Source for Real-time Multispectral Photoacoustic Microscopy," *Photoacoustics*, vol. 20, p. 100204, Dec. 2020, doi: 10.1016/j.pacs.2020.100204.
[363] K. H. Song, E. W. Stein, J. A. Margenthaler, and L. V. Wang, "Noninvasive photoacoustic identification of sentinel lymph nodes containing methylene blue in vivo in a rat model," *J Biomed Opt*, vol. 13, no. 5, p. 054033, Oct. 2008, doi: 10.1117/1.2976427.
[364] G. Paltauf, R. Nuster, and M. Frenz, "Progress in biomedical photoacoustic imaging instrumentation toward clinical application," *Journal of Applied Physics*, vol. 128, no. 18, p. 180907, Nov. 2020, doi: 10.1063/5.0028190.
[365] Z. Hosseinaee, Nima Abbasi, N. Pellegrino, L. Khalili, L. Mukhangaliyeva, and P. Haji Reza, "Functional and structural ophthalmic imaging using noncontact multimodal photoacoustic remote sensing microscopy and optical coherence tomography," *Sci Rep*, vol. 11, no. 1, Art. no. 1, Jun. 2021, doi: 10.1038/s41598-021-90776-5.
[366] Y. Liang, L. Jin, B.-O. Guan, and L. Wang, "2 MHz multi-wavelength pulsed laser for functional photoacoustic microscopy," *Opt Lett*, vol. 42, no. 7, pp. 1452–1455, Apr. 2017, doi: 10.1364/OL.42.001452.
[367] P. Hajireza, A. Forbrich, and R. J. Zemp, "Multifocus optical-resolution photoacoustic microscopy using stimulated Raman scattering and chromatic aberration," *Opt. Lett., OL*, vol. 38, no. 15, pp. 2711–2713, Aug. 2013, doi: 10.1364/OL.38.002711.
[368] T. Cheng, W. Gao, X. Xue, T. Suzuki, and Y. Ohishi, "Experimental investigation of multiple Raman peak properties in a hundred-meter tellurite fiber," *Opt. Mater. Express, OME*, vol. 6, no. 11, pp. 3438–3445, Nov. 2016, doi: 10.1364/OME.6.003438.
[369] L. Sirleto and M. A. Ferrara, "Fiber Amplifiers and Fiber Lasers Based on Stimulated Raman Scattering: A Review," *Micromachines (Basel)*, vol. 11, no. 3, Feb. 2020, doi: 10.3390/mi11030247.
[370] D. Koeplinger, M. Liu, and T. Buma, "Photoacoustic microscopy with a pulsed multi-color source based on stimulated Raman scattering," in *2011 IEEE International Ultrasonics Symposium*, Oct. 2011, pp. 296–299. doi: 10.1109/ULTSYM.2011.0071.
[371] Y. Zhou, S. Liang, M. Li, C. Liu, P. Lai, and L. Wang, "Optical-resolution photoacoustic microscopy with ultrafast dual-wavelength excitation," *Journal of Biophotonics*, vol. 13, no. 6, p. e201960229, 2020, doi: https://doi.org/10.1002/jbio.201960229.
[372] Y. He, J. Shi, K. I. Maslov, R. Cao, and L. V. Wang, "Wave of single-impulse-stimulated fast initial dip in single vessels of mouse brains imaged by high-speed functional photoacoustic microscopy," *JBO*, vol. 25, no. 6, p. 066501, Jun. 2020, doi: 10.1117/1.JBO.25.6.066501.
[373] H. Linnenbank *et al.*, "Robust and rapidly tunable light source for SRS/CARS microscopy with low-intensity noise," *AP*, vol. 1, no. 5, p. 055001, Sep. 2019, doi: 10.1117/1.AP.1.5.055001.
[374] T. Buma, J. L. Farland, and M. R. Ferrari, "Near-infrared multispectral photoacoustic microscopy using a graded-index fiber amplifier," *Photoacoustics*, vol. 4, no. 3, pp. 83–90, Aug. 2016, doi: 10.1016/j.pacs.2016.08.002.

[375] C. Liu, J. Chen, Y. Zhang, J. Zhu, and L. Wang, “Five-wavelength optical-resolution photoacoustic microscopy of blood and lymphatic vessels,” *AP*, vol. 3, no. 1, p. 016002, Jan. 2021, doi: 10.1117/1.AP.3.1.016002.
[376] T. R. Hart, R. L. Aggarwal, and B. Lax, “Temperature Dependence of Raman Scattering in Silicon,” *Phys. Rev. B*, vol. 1, no. 2, pp. 638–642, Jan. 1970, doi: 10.1103/PhysRevB.1.638.
[377] M. Balkanski, R. F. Wallis, and E. Haro, “Anharmonic effects in light scattering due to optical phonons in silicon,” *Phys. Rev. B*, vol. 28, no. 4, pp. 1928–1934, Aug. 1983, doi: 10.1103/PhysRevB.28.1928.
[378] W.-C. Kim and D.-W. Park, “Analysis of Temperature Effects on Raman Silicon Photonic Devices,” *J. Opt. Soc. Korea, JOSK*, vol. 12, no. 4, pp. 288–297, Dec. 2008.
[379] S.-W. Cho *et al.*, “Optimal Generation of Ten Individual Green-to-Red Raman Source for Wavelength-Dependent Real-Time OR-PAM Images,” *IEEE Journal of Selected Topics in Quantum Electronics*, vol. 25, no. 1, pp. 1–9, Jan. 2019, doi: 10.1109/JSTQE.2018.2869646.
[380] R. Stolen, “Polarization effects in fiber Raman and Brillouin lasers,” *IEEE Journal of Quantum Electronics*, vol. 15, no. 10, pp. 1157–1160, Oct. 1979, doi: 10.1109/JQE.1979.1069913.
[381] Z. Hosseinaee, L. Khalili, J. A. T. Simmons, K. Bell, K. Bell, and P. H. Reza, “Label-free, non-contact, in vivo ophthalmic imaging using photoacoustic remote sensing microscopy,” *Opt. Lett., OL*, vol. 45, no. 22, pp. 6254–6257, Nov. 2020, doi: 10.1364/OL.410171.
[382] *Nonlinear Fiber Optics*. Elsevier, 2019. doi: 10.1016/C2018-0-01168-8.
[383] Arun, S., Vishal Choudhury, V. Balaswamy, and V. R. Supradeepa. "Stability analysis of high power, octave spanning, continuous-wave supercontinuum sources based on cascaded Raman scattering in standard telecom fibers." *OSA Continuum* 1, no. 4 (2018): 1267-1276.
[384] J. Suda and P. G. Zverev, “Temperature Dependence of Raman Frequency Shift in SrWO4 Crystal Studied by Lattice Dynamical Calculations,” *Crystals*, vol. 9, no. 4, Art. no. 4, Apr. 2019, doi: 10.3390/cryst9040197.
[385] M. Zhi-Wei *et al.*, “Influence of Temperature on Stimulated Raman Scattering in Single-Mode Silica Fibre,” *Chinese Physics Letters*, vol. 25, no. 11, pp. 3999–4002, 2008, doi: 10.1088/0256-307X/25/11/044.
[386] S. Martin-Lopez, M. Gonzalez-Herraez, P. Corredera, M. L. Hernanz, A. Carrasco, and J. A. Mendez, “Temperature effects on supercontinuum generation using a continuous-wave Raman fiber laser,” *Optics Communications*, vol. 267, no. 1, pp. 193–196, Nov. 2006, doi: 10.1016/j.optcom.2006.05.057.
[387] A. I. Sokolovskaya, A. D. Kudryavtseva, G. L. Brekhovskikh, and M. M. Suschinskiĭ, “Effect of Temperature on Stimulated Raman Scattering of Light in Substances with Various Kerr Constants,” *Soviet Journal of Experimental and Theoretical Physics*, vol. 30, p. 633, 1969.
[388] A. D. Kudryavtseva and A. I. Sokolovskaya, “Investigation of the self-focusing of light scattered in the stimulated Raman effect at different excitation levels,” *Sov. J. Quantum Electron.*, vol. 4, no. 4, p. 531, Apr. 1974, doi: 10.1070/QE1974v004n04ABEH006804.
[389] Y. WAN, H. HU, Y. XU, Q. CHEN, Y. WANG, and D. GAO, “A Robust and Accurate Non-rigid Medical Image Registration Algorithm Based on Multi-level Deformable Model,” *Iran J Public Health*, vol. 46, no. 12, pp. 1679–1689, Dec. 2017.
[390] M. Hammer *et al.*, “Diabetic patients with retinopathy show increased retinal venous oxygen saturation,” *Graefes Arch Clin Exp Ophthalmol*, vol. 247, no. 8, pp. 1025–1030, Aug. 2009, doi: 10.1007/s00417-009-1078-6.
[391] B. Khoobehi, K. Firn, H. Thompson, M. Reinoso, and J. Beach, “Retinal Arterial and Venous Oxygen Saturation Is Altered in Diabetic Patients,” *Invest. Ophthalmol. Vis. Sci.*, vol. 54, no. 10, pp. 7103–7106, Oct. 2013, doi: 10.1167/iovs.13-12723.

[392] E. Vandewalle *et al.*, “Oximetry in glaucoma: correlation of metabolic change with structural and functional damage,” *Acta Ophthalmologica*, vol. 92, no. 2, pp. 105–110, 2014, doi: https://doi.org/10.1111/aos.12011.
[393] O. B. Olafsdottir, S. H. Hardarson, M. S. Gottfredsdottir, A. Harris, and E. Stefánsson, “Retinal Oximetry in Primary Open-Angle Glaucoma,” *Invest. Ophthalmol. Vis. Sci.*, vol. 52, no. 9, pp. 6409–6413, Aug. 2011, doi: 10.1167/iovs.10-6985.
[394] S. H. Hardarson and E. Stefánsson, “Oxygen Saturation in Central Retinal Vein Occlusion,” *American Journal of Ophthalmology*, vol. 150, no. 6, pp. 871–875, Dec. 2010, doi: 10.1016/j.ajo.2010.06.020.
[395] T. Eliasdottir, D. Bragason, S. Hardarson, and E. Stefánsson, “Retinal Oxygen Saturation is Affected in Central Retinal Vein Occlusion,” *Invest. Ophthalmol. Vis. Sci.*, vol. 54, no. 15, pp. 46–46, Jun. 2013.
[396] L. G. HYMAN, A. M. LILIENFELD, F. L. FERRIS III, and S. L. FINE, “SENILE MACULAR DEGENERATION: A CASE-CONTROL STUDY,” *American Journal of Epidemiology*, vol. 118, no. 2, pp. 213–227, Aug. 1983, doi: 10.1093/oxfordjournals.aje.a113629.
[397] J. Landrum, R. Bone, and M. Kilburn, “The macular pigment: A possible role in protection from age-related macular degeneration,” vol. 38, pp. 537–538, 1997.
[398] J. Yi *et al.*, “Visible light optical coherence tomography measures retinal oxygen metabolic response to systemic oxygenation,” *Light: Science & Applications*, vol. 4, no. 9, Art. no. 9, Sep. 2015, doi: 10.1038/lsa.2015.107.
[399] J. C. M. Lau and R. A. Linsenmeier, “Increased intraretinal PO2 in short-term diabetic rats,” *Diabetes*, vol. 63, no. 12, pp. 4338–4342, Dec. 2014, doi: 10.2337/db14-0101.
[400] S. Chen, X. Shu, P. L. Nesper, W. Liu, A. A. Fawzi, and H. F. Zhang, “Retinal oximetry in humans using visible-light optical coherence tomography [Invited],” *Biomed Opt Express*, vol. 8, no. 3, pp. 1415–1429, Feb. 2017, doi: 10.1364/BOE.8.001415.
[401] O. S. Finikova *et al.*, “Oxygen microscopy by two-photon-excited phosphorescence,” *Chemphyschem*, vol. 9, no. 12, pp. 1673–1679, Aug. 2008, doi: 10.1002/cphc.200800296.
[402] Y. Ito and B. A. Berkowitz, “MR studies of retinal oxygenation,” *Vision Res*, vol. 41, no. 10–11, pp. 1307–1311, 2001, doi: 10.1016/s0042-6989(00)00258-3.
[403] R. N. Pittman, *Measurement of Oxygen*. Morgan & Claypool Life Sciences, 2011. Accessed: Feb. 18, 2021. [Online]. Available: http://www.ncbi.nlm.nih.gov/books/NBK54107/
[404] D. Schweitzer, E. Thamm, M. Hammer, and J. Kraft, “A new method for the measurement of oxygen saturation at the human ocular fundus,” *International Ophthalmology*, vol. 23, no. 4–6, pp. 347–353, 2001, doi: 10.1023/A:1014458815482.
[405] “Human macular pigment assessed by imaging fundus reflectometry,” *Vision Research*, vol. 29, no. 6, pp. 663–674, Jan. 1989, doi: 10.1016/0042-6989(89)90028-X.
[406] S. Chen, J. Yi, and H. F. Zhang, “Measuring oxygen saturation in retinal and choroidal circulations in rats using visible light optical coherence tomography angiography,” *Biomed Opt Express*, vol. 6, no. 8, pp. 2840–2853, Jul. 2015, doi: 10.1364/BOE.6.002840.
[407] D. Link *et al.*, “Novel non-contact retina camera for the rat and its application to dynamic retinal vessel analysis,” *Biomed Opt Express*, vol. 2, no. 11, pp. 3094–3108, Oct. 2011, doi: 10.1364/BOE.2.003094.
[408] Z. Hosseinaee, J. A. Tummon Simmons, and P. H. Reza, “Dual-Modal Photoacoustic Imaging and Optical Coherence Tomography [Review],” *Front. Phys.*, vol. 8, 2021, doi: 10.3389/fphy.2020.616618.
[409] Martell, Matthew T., Nathaniel JM Haven, and Roger J. Zemp. "Multimodal imaging with spectral-domain optical coherence tomography and photoacoustic remote sensing microscopy." *Optics Letters* 45, no. 17 (2020): 4859-4862.

[410] X. Wang, G. Ku, M. A. Wegiel, D. J. Bornhop, G. Stoica, and L. V. Wang, "Noninvasive photoacoustic angiography of animal brains in vivo with near-infrared light and an optical contrast agent," *Opt. Lett., OL*, vol. 29, no. 7, pp. 730–732, Apr. 2004, doi: 10.1364/OL.29.000730.
[411] S. O. Abu-Sardanah, C. Subramaniam, S. Abbasi, and P. H. Reza, "A comprehensive characterization of a stimulated Raman scattering fiber-laser source for multi-wavelength dependent photoacoustic microscopy techniques (Conference Presentation)," in *Photons Plus Ultrasound: Imaging and Sensing 2020*, Mar. 2020, vol. 11240, p. 1124024. doi: 10.1117/12.2545195.
[412] O. O. Ahsen *et al.*, "Swept source optical coherence microscopy using a 1310 nm VCSEL light source," *Opt. Express, OE*, vol. 21, no. 15, pp. 18021–18033, Jul. 2013, doi: 10.1364/OE.21.018021.
[413] B. Cense *et al.*, "Ultrahigh-resolution high-speed retinal imaging using spectral-domain optical coherence tomography," *Opt. Express, OE*, vol. 12, no. 11, pp. 2435–2447, May 2004, doi: 10.1364/OPEX.12.002435.
[414] C. A. Schneider, W. S. Rasband, and K. W. Eliceiri, "NIH Image to ImageJ: 25 years of image analysis," *Nature Methods*, vol. 9, no. 7, Art. no. 7, Jul. 2012, doi: 10.1038/nmeth.2089.
[415] "ANSI Z136.1-2014: Safe Use of Lasers - ANSI Blog," *The ANSI Blog*, Jul. 24, 2015. https://blog.ansi.org/2015/07/ansi-z1361-2014-safe-use-of-lasers/ (accessed Sep. 13, 2020).
[416] S. Hariri, A. A. Moayed, A. Dracopoulos, C. Hyun, S. Boyd, and K. Bizheva, "Limiting factors to the OCT axial resolution for in-vivo imaging of human and rodent retina in the 1060nm wavelength range," *Opt. Express*, vol. 17, no. 26, p. 24304, Dec. 2009, doi: 10.1364/OE.17.024304.
[417] E. Eriksson, J. V. Boykin, and R. N. Pittman, "Method for in vivo microscopy of the cutaneous microcirculation of the hairless mouse ear," *Microvasc Res*, vol. 19, no. 3, pp. 374–379, May 1980, doi: 10.1016/0026-2862(80)90056-4.
[418] S. G. Ye, K. A. Harasiewicz, C. J. Pavlin, and F. S. Foster, "Ultrasound characterization of normal ocular tissue in the frequency range from 50 MHz to 100 MHz," *IEEE Transactions on Ultrasonics, Ferroelectrics, and Frequency Control*, vol. 42, no. 1, pp. 8–14, Jan. 1995, doi: 10.1109/58.368319.
[419] M. Hammer, S. Leistritz, L. Leistritz, and D. Schweitzer, "Light paths in retinal vessel oxymetry," *IEEE Trans Biomed Eng*, vol. 48, no. 5, pp. 592–598, May 2001, doi: 10.1109/10.918598.
[420] I.-T. L, R. A, S. A, W. S, B. R, and M. C, "Retinal pigment epithelial integrity is compromised in the developing albino mouse retina.," *J Comp Neurol*, vol. 524, no. 18, pp. 3696–3716, May 2016, doi: 10.1002/cne.24025.
[421] R. Cao *et al.*, "Photoacoustic microscopy reveals the hemodynamic basis of sphingosine 1-phosphate-induced neuroprotection against ischemic stroke," *Theranostics*, vol. 8, no. 22, pp. 6111–6120, Nov. 2018, doi: 10.7150/thno.29435.
[422] C. Liu, Y. Liang, and L. Wang, "Optical-resolution photoacoustic microscopy of oxygen saturation with nonlinear compensation," *Biomed Opt Express*, vol. 10, no. 6, pp. 3061–3069, May 2019, doi: 10.1364/BOE.10.003061.
[423] I. M. Hogeboom van Buggenum, G. L. van der Heijde, G. J. Tangelder, and J. W. Reichert-Thoen, "Ocular oxygen measurement.," *Br J Ophthalmol*, vol. 80, no. 6, pp. 567–573, Jun. 1996.
[424] L. V. Wang, "Prospects of photoacoustic tomography," *Med Phys*, vol. 35, no. 12, pp. 5758–5767, Dec. 2008, doi: 10.1118/1.3013698.

[425] H. Chen, M. M. Rogalski, and J. N. Anker, “Advances in functional X-ray imaging techniques and contrast agents,” *Phys Chem Chem Phys*, vol. 14, no. 39, pp. 13469–13486, Oct. 2012, doi: 10.1039/c2cp41858d.
[426] D. A. Antonetti, R. Klein, and T. W. Gardner, “Diabetic retinopathy,” *N Engl J Med*, vol. 366, no. 13, pp. 1227–1239, Mar. 2012, doi: 10.1056/NEJMra1005073.
[427] N. D. Wangsa-Wirawan and R. A. Linsenmeier, “Retinal oxygen: fundamental and clinical aspects,” *Arch Ophthalmol*, vol. 121, no. 4, pp. 547–557, Apr. 2003, doi: 10.1001/archopht.121.4.547.
[428] T. A. Ciulla *et al.*, “Color Doppler imaging discloses reduced ocular blood flow velocities in nonexudative age-related macular degeneration,” *Am J Ophthalmol*, vol. 128, no. 1, pp. 75–80, Jul. 1999, doi: 10.1016/s0002-9394(99)00061-6.
[429] T. S. Eliasdottir, “Retinal oximetry and systemic arterial oxygen levels,” *Acta Ophthalmol*, vol. 96 Suppl A113, pp. 1–44, Nov. 2018, doi: 10.1111/aos.13932.
[430] B. A. Berkowitz and C. A. Wilson, “Quantitative mapping of ocular oxygenation using magnetic resonance imaging,” *Magn Reson Med*, vol. 33, no. 4, pp. 579–581, Apr. 1995, doi: 10.1002/mrm.1910330419.
[431] A. Harris, R. B. Dinn, L. Kagemann, and E. Rechtman, “A review of methods for human retinal oximetry,” *Ophthalmic Surg Lasers Imaging*, vol. 34, no. 2, pp. 152–164, Apr. 2003.
[432] Z. Huang *et al.*, “Retinal choroidal vessel imaging based on multi-wavelength fundus imaging with the guidance of optical coherence tomography,” *Biomed. Opt. Express, BOE*, vol. 11, no. 9, pp. 5212–5224, Sep. 2020, doi: 10.1364/BOE.397750.
[433] P. F. Sharp, A. Manivannan, H. Xu, and J. V. Forrester, “The scanning laser ophthalmoscope—a review of its role in bioscience and medicine,” *Phys. Med. Biol.*, vol. 49, no. 7, pp. 1085–1096, Mar. 2004, doi: 10.1088/0031-9155/49/7/001.
[434] D. G. Buerk, R. D. Shonat, C. E. Riva, and S. D. Cranstoun, “O2 gradients and countercurrent exchange in the cat vitreous humor near retinal arterioles and venules,” *Microvasc Res*, vol. 45, no. 2, pp. 134–148, Mar. 1993, doi: 10.1006/mvre.1993.1013.
[435] M. Hammer, W. Vilser, T. Riemer, and D. Schweitzer, “Retinal vessel oximetry-calibration, compensation for vessel diameter and fundus pigmentation, and reproducibility,” *J Biomed Opt*, vol. 13, no. 5, p. 054015, Oct. 2008, doi: 10.1117/1.2976032.
[436] W. Liu, S. Jiao, and H. F. Zhang, “Accuracy of retinal oximetry: a Monte Carlo investigation,” *J Biomed Opt*, vol. 18, no. 6, p. 066003, Jun. 2013, doi: 10.1117/1.JBO.18.6.066003.
[437] S. Jiao *et al.*, “Photoacoustic ophthalmoscopy for in vivo retinal imaging,” *Opt Express*, vol. 18, no. 4, pp. 3967–3972, Feb. 2010, doi: 10.1364/OE.18.003967.
[438] J. Yao and L. V. Wang, “Sensitivity of photoacoustic microscopy,” *Photoacoustics*, vol. 2, no. 2, pp. 87–101, Jun. 2014, doi: 10.1016/j.pacs.2014.04.002.
[439] W. Zhang *et al.*, “Simultaneous photoacoustic microscopy, spectral-domain optical coherence tomography, and fluorescein microscopy multi-modality retinal imaging,” *Photoacoustics*, vol. 20, p. 100194, Dec. 2020, doi: 10.1016/j.pacs.2020.100194.
[440] W. Song *et al.*, “A combined method to quantify the retinal metabolic rate of oxygen using photoacoustic ophthalmoscopy and optical coherence tomography,” *Scientific Reports*, vol. 4, no. 1, Art. no. 1, Oct. 2014, doi: 10.1038/srep06525.
[441] Z. Hosseinaee *et al.*, “Functional photoacoustic remote sensingmicroscopy using a stabilized temperature-regulated stimulated Raman scattering light source,” *Optics Express*, Aug. 2021, doi: 10.1364/OE.434004.
[442] D. C. Lozano and M. D. Twa, “Development of a Rat Schematic Eye From In Vivo Biometry and the Correction of Lateral Magnification in SD-OCT Imaging,” *Invest. Ophthalmol. Vis. Sci.*, vol. 54, no. 9, pp. 6446–6455, Sep. 2013, doi: 10.1167/iovs.13-12575.

[443] M. Gehrung, S. E. Bohndiek, and J. Brunker, “Development of a blood oxygenation phantom for photoacoustic tomography combined with online pO2 detection and flow spectrometry,” *JBO*, vol. 24, no. 12, p. 121908, Oct. 2019, doi: 10.1117/1.JBO.24.12.121908.
[444] R. Bulsink, M. Kuniyil Ajith Singh, M. Xavierselvan, S. Mallidi, W. Steenbergen, and K. J. Francis, “Oxygen Saturation Imaging Using LED-Based Photoacoustic System,” *Sensors (Basel)*, vol. 21, no. 1, p. 283, Jan. 2021, doi: 10.3390/s21010283.
[445] 14:00-17:00, “ISO 80601-2-61:2017,” *ISO*. https://www.iso.org/cms/render/live/en/sites/isoorg/contents/data/standard/06/79/67963.html (accessed Sep. 08, 2021).
[446] C. Liu, Y. Liang, and L. Wang, “Optical-resolution photoacoustic microscopy of oxygen saturation with nonlinear compensation,” *Biomed. Opt. Express*, vol. 10, no. 6, p. 3061, Jun. 2019, doi: 10.1364/BOE.10.003061.
[447] J. Beach, “Pathway to Retinal Oximetry,” *Transl Vis Sci Technol*, vol. 3, no. 5, p. 2, Sep. 2014, doi: 10.1167/tvst.3.5.2.
[448] Gray, L. H., and J. M. Steadman. "Determination of the oxyhaemoglobin dissociation curves for mouse and rat blood." *The Journal of physiology* 175, no. 2 (1964): 161-171.
[449] W. M. Harmening, P. Tiruveedhula, A. Roorda, and L. C. Sincich, “Measurement and correction of transverse chromatic offsets for multi-wavelength retinal microscopy in the living eye,” *Biomed Opt Express*, vol. 3, no. 9, pp. 2066–2077, Aug. 2012, doi: 10.1364/BOE.3.002066.
[450] S. Remtulla and P. E. Hallett, “A schematic eye for the mouse, and comparisons with the rat,” *Vision Res*, vol. 25, no. 1, pp. 21–31, 1985, doi: 10.1016/0042-6989(85)90076-8.
[451] H. Radhakrishnan and V. J. Srinivasan, “Multiparametric optical coherence tomography imaging of the inner retinal hemodynamic response to visual stimulation,” *J Biomed Opt*, vol. 18, no. 8, p. 86010, Aug. 2013, doi: 10.1117/1.JBO.18.8.086010.
[452] C. Tian, W. Zhang, A. Mordovanakis, X. Wang, and Y. M. Paulus, “Noninvasive chorioretinal imaging in living rabbits using integrated photoacoustic microscopy and optical coherence tomography,” *Opt. Express, OE*, vol. 25, no. 14, pp. 15947–15955, Jul. 2017, doi: 10.1364/OE.25.015947.
[453] D. Sliney *et al.*, “Adjustment of guidelines for exposure of the eye to optical radiation from ocular instruments: statement from a task group of the International Commission on Non-Ionizing Radiation Protection (ICNIRP),” *Appl. Opt., AO*, vol. 44, no. 11, pp. 2162–2176, Apr. 2005, doi: 10.1364/AO.44.002162.
[454] P. N. Youssef, N. Sheibani, and D. M. Albert, “Retinal light toxicity,” *Eye*, vol. 25, no. 1, pp. 1–14, Jan. 2011, doi: 10.1038/eye.2010.149.
[455] Lund, David J., and Peter R. Edsall. "Action spectrum for retinal thermal injury." In *Ophthalmic Technologies IX*, vol. 3591, pp. 324-334. International Society for Optics and Photonics, 1999.
[456] D. H. Sliney, “Retinal injury from laser radiation,” *Molecular Crystals and Liquid Crystals Science and Technology Section B: Nonlinear Optics*, vol. 21, no. 1–4, pp. 1–17, Jun. 1999.
[457] J. J. Hunter, J. I. W. Morgan, W. H. Merigan, D. H. Sliney, J. R. Sparrow, and D. R. Williams, “The susceptibility of the retina to photochemical damage from visible light,” *Progress in Retinal and Eye Research*, vol. 31, no. 1, pp. 28–42, Jan. 2012, doi: 10.1016/j.preteyeres.2011.11.001.
[458] Rockwell, Benjamin A., Daniel X. Hammer, Richard A. Hopkins, Dale J. Payne, Cynthia A. Toth, William P. Roach, Jeffrey J. Druessel et al. "Ultrashort laser pulse bioeffects and safety." *Journal of Laser Applications* 11, no. 1 (1999): 42-44.
[459] R. W. Gubisch, “Optical Performance of the Human Eye,” *J. Opt. Soc. Am., JOSA*, vol. 57, no. 3, pp. 407–415, Mar. 1967, doi: 10.1364/JOSA.57.000407.

[460] E. S. Beatrice, D. I. Randolph, H. Zwick, B. E. Stuck, and D. J. Lund, “Laser hazards: biomedical threshold level investigations,” *Mil Med*, vol. 142, no. 11, pp. 889–891, Nov. 1977.
[461] A. A. Skavenski, D. A. Robinson, R. M. Steinman, and G. T. Timberlake, “Miniature eye movements of fixation in rhesus monkey,” *Vision Research*, vol. 15, no. 11, pp. 1269-IN7, Nov. 1975, doi: 10.1016/0042-6989(75)90173-X.
[462] J. W. Ness *et al.*, “Retinal image motion during deliberate fixation: implications to laser safety for long duration viewing,” *Health Phys*, vol. 78, no. 2, pp. 131–142, Feb. 2000, doi: 10.1097/00004032-200002000-00002.
[463] W. J. Geeraets and E. R. Berry, “Ocular spectral characteristics as related to hazards from lasers and other light sources,” *Am J Ophthalmol*, vol. 66, no. 1, pp. 15–20, Jul. 1968, doi: 10.1016/0002-9394(68)91780-7.
[464] Bosschaart, Nienke, Gerda J. Edelman, Maurice CG Aalders, Ton G. van Leeuwen, and Dirk J. Faber. "A literature review and novel theoretical approach on the optical properties of whole blood." *Lasers in medical science* 29, no. 2 (2014): 453-479.
[465] Matsumoto, Y., Y. Asao, A. Yoshikawa, H. Sekiguchi, M. Takada, M. Furu, S. Saito et al. "Label-free photoacoustic imaging of human palmar vessels: a structural morphological analysis." *Scientific reports* 8, no. 1 (2018): 1-8.
[466] X. Shu *et al.*, “Designing visible-light optical coherence tomography towards clinics,” *Quant Imaging Med Surg*, vol. 9, no. 5, pp. 769–781, May 2019, doi: 10.21037/qims.2019.05.01.